Tailoring Biomaterials by Tuning Specific Peptide Interactions via Stereochemistry-Directed Interactions and Polymer-Peptide Conjugation

---

A
Dissertation
Presented to
the faculty of the School of Engineering and Applied Science
University of Virginia

---

in partial fulfillment
of the requirements for the degree

Doctor of Philosophy

by

Vincent P. Gray

December 2024

APPROVAL SHEET

This
Dissertation
is submitted in partial fulfillment of the requirements
for the degree of
Doctor of Philosophy

Author: Vincent P. Gray

This Dissertation has been read and approved by the examing committee:

Advisor: Rachel A. Letteri

Advisor:

Committee Member: Christopher B. Highley

Committee Member: Kyle J. Lampe

Committee Member: Camille Bilodeau

Committee Member: George S. Bloom

Committee Member:

Committee Member:

Accepted for the School of Engineering and Applied Science:

Jennifer L. West, School of Engineering and Applied Science

December 2024

Acknowledgements

Over the past several years, I have heard many friends and acquaintances who are PhDs and PhD candidates asked what getting a PhD is like. The vast majority have begun with talking about how long, arduous, and difficult it is, but for me it's a different story. As a product of the strong, positive culture that has surrounded me at UVA, what comes to mind when I think about my PhD is the exciting adventure that I have had spending time with great people and discovering science. I extend my heartfelt gratitude to all of the many people that have supported me throughout my PhD.

I gratefully acknowledge the financial sources that have supported my work in this thesis: the UVA Dean's Scholars Fellowship, the National Institute of Health's Biotechnology Training Program (T32GM136615), and the National Science Foundation (BMAT-2143647). I would also like to thank the UVA Dean's Scholars Fellowship and the UVA Distinguished Fellowship for financial support for travel to conferences.

To my committee members, Dr. Chris Highley, Dr. Kyle Lampe, Dr. George Bloom, Dr. Camille Bilodeau, and Dr. Rachel Letteri, thank you very much for your continuous support, mentorship, and intellectual contributions to my PhD work, it has been a pleasure working with you all. A special thank you to Chris for the opportunity to collaborate with you and Greg to submit a manuscript that started a whole new project for me, and to Kyle for regular mentorship during weekly collaborative meetings, where you taught me how to ask the right questions and gain a deeper understanding of the science.

To Rachel, thank you so much for being the most supportive and encouraging mentor one could ever ask for. Before I even joined the lab, your passion and excitement for science was immediately apparent and infectious. The fantastic culture of our group is a direct result of the supportive and collaborative environment that you foster and has been the best part of my PhD. You have taught me so much about being an amazing scientist, all the way from conceiving an idea to sharing the science with scientists and non-scientists alike; I will be forever grateful for your patience fostering these skills that I will carry with me for the rest of my life.

To the Letteri Lab, Mara, Israt, Mark, Zixian, Kelly, Aditi, Darren, Jerwin, Hadley, Mobina, thank you for the incredibly supportive culture that you have all had a hand in creating and carrying forward in the lab. You have all been amazing friends and it has been an incredible pleasure celebrating milestones together, getting lunch/dinner at Asado, and always having someone to turn to for advice. To Justin and Mack, it's been an honor working with such exceptionally intelligent and motivated undergraduate researchers. Thank you both for your contributions to this work and I can't wait to see your future successes! A special thank you to Mara, for always being there for me no matter what since the beginning of this journey, to Mark, for always being an incredible friend regardless of how many weird things I do or say, and to Aditi, for your constant support and positivity.

Thank you so much to all of the wonderful friends I have made here in Charlottesville for being a big part of what made my overall PhD experience more about the exciting journey than about the hardships. A special thank you to Colby, Will, and Eric, for all the fun years of board games and friendship that made the past several years go by in a flash.

To my friends from home, Nick, Allan, Ryan, Stefan, Rob, Tayah, Emily, Joey, and Isaac, thank you to each and every one of you for remaining such close friends over the years and for still hanging out together even though we are spread out all over the country.

Finally, I would like to thank my family for always being there throughout my PhD. Living within driving distance of home has been such a blessing, allowing me to easily be able to go home for a weekend and spend time together. Thank you for your undying support and love, for raising me with the values that made me the person I am today, and for always encouraging me to be the best that I can be.

Abstract

The complex, dynamic nature of native tissues requires next-generation biomaterials that are highly tunable and robust to address current engineering problems. Peptides are common key components of biomaterials as they undergo specific interactions that can be tailored by a wide sequence design space, but peptides are limited by a lack of *in vivo* stability. To overcome this instability and expand the tunability of biomaterials, we leveraged stereochemistry-directed interactions and polymer-peptide conjugation as tools to increase peptide stability and modulate specific interactions. In this thesis, we investigated the specific interactions of several peptides as therapeutics and biomaterials and expanded on the design rules that govern stereochemistry-directed interactions and polymer-peptide conjugate biomaterials. In *Chapter 2*, we utilized photochemistry and the specific, yet displaceable interactions between coiled coil peptides to develop a biomaterial with user-defined, spatiotemporal control over the presentation of biomolecules on the surface. Uniting specific coiled coil interactions with the benefits of stereochemistry-directed interactions, in *Chapter 3* we demonstrated that stereochemistry-directed interactions between coiled coils yields complexes that possess greater binding strength and are more enzymatically stable than analogous coiled coils composed of only L-peptides. In *Chapter 4* we further employed stereochemistry-directed interactions in the design of polymer-peptide conjugate biomaterials to disperse and prevent aggregates of toxic proteins implicated in amyotrophic lateral sclerosis (ALS), where both D- and L-conjugates successfully dispersed aggregates of a model toxic protein. To target another class of highly charged toxic proteins implicated in ALS, in *Chapter 5* we designed a set of peptides to interact electrostatically with these proteins and characterized their interactions using isothermal titration calorimetry to select candidates for conjugation to polymers as polymer-peptide therapeutics. Together, these studies enhance the tunability and functionality of biomaterials by leveraging specific peptide interactions and expanding the design rules for stereochemistry-directed interactions and polymer-peptide conjugates.

Table of Contents

List of Figures

Chapter 1. Introduction

The use of biomaterials to tackle engineering problems in the fields of regenerative medicine and therapeutics requires materials that are robust and highly tunable to recapitulate the highly specific interactions that drive the complex, dynamic nature of native tissues.[1] Peptides are widely used biomaterials that undergo specific biomimetic interactions and are relatively easy to synthesize, have a wide range of different functions due to a high degree of possible structural diversity, can easily be modified to incorporate non-native chemistries, and are composed of the same chemical building blocks as natural proteins, making them likely to be biocompatible.[2–4] While peptides have these advantages, they often suffer from a poor half-life *in vivo* due to a combination of low enzymatic stability and susceptibility to renal clearance.[5–7] This limits the application of peptides as therapeutics or biomaterials as they are often cleared from the body or broken down from the active form before they perform their intended functions. Two strategies to allay these concerns and make peptides more bioavailable are the use of stereochemistry-directed interactions and conjugation to polymers.

1.1 Stereochemistry-directed peptide interactions

All amino acids that comprise peptides and proteins occur in one of two stereochemistries, L or D, where the stereochemistry of an amino acid is dependent on the spatial arrangement of the side chain in 3D space (**Figure 1.1**). L-amino acids, and therefore L-peptides and L-proteins, are naturally occurring and therefore recognized by

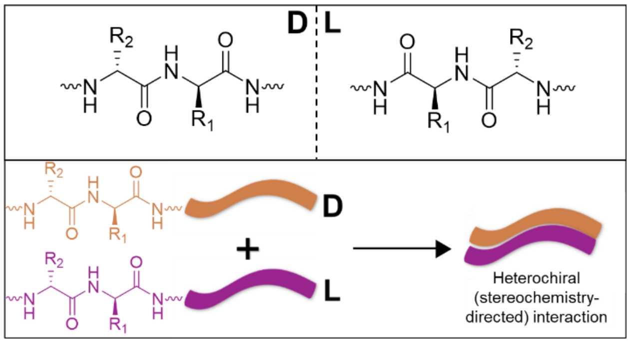

Figure 1.1. D- and L-peptides of the same sequence are chemically equivalent in every way except the direction that their side chains point, such that they are mirror images of each other. Blending D- and L-peptides yields heterochiral complexes with unique properties derived from stereochemistry-directed interactions.

enzymes, which cleave them by their amide bonds. On the other hand, D-amino acids, which are chemically equivalent to L-amino acids except by the direction the side chain points in 3D space, are unaffected by degrading enzymes as the enzymes do not recognize the amino acids in this spatial arrangement.[8–12] While we could use D-peptides for our biomaterials applications and not have to worry about degradation, tunability, cost, and specific interactions between D- and L-peptides provide compelling reasons to explore blending D- and L-peptides to take advantage of stereochemistry-directed interactions. For example, in regenerative medicine a scaffold needs to degrade or rearrange to allow for new tissue growth. If only D-peptides were used, the biomaterial would not degrade for a long time and may interfere with regrowing the desired tissue. Cost is also an important consideration, as D-amino acids cost more than L-amino acids, so using biomaterials prepared from a blend of D- and L-peptides would reduce costs significantly and increase the probability of commercial success, which in turn will make the biomaterial more likely to become available to patients. Finally, specific interactions between D- and L-peptides may contribute tunable control over both the degradation of peptide materials and peptide-peptide binding strengths.[13]

Stereochemistry-directed interactions offer tunable control over the degradation rate of L-peptides. One example is the degradation of the pentapeptide KYFIL (K = lysine, Y = tyrosine, F = phenylalanine, I = isoleucine, and L = leucine). When hydrogels composed of L-KYFIL are exposed to proteinase K, ~60% of the peptide is degraded after just one hour. However, >90% of the KYFIL peptide remains intact over 72 h when hydrogels composed of a 1:1 heterochiral mixture (50% L-KYFIL and 50% D-KYFIL) are exposed to the same enzyme.[12] In another example, hydrogels formed from the peptide L-Ac-$(FKFE)_2$ (E = glutamate) degrade by >95% after 5 days of incubation with each of three different enzymes, while hydrogels formed from a heterochiral mixture of Ac-$(FKFE)_2$ resist degradation by all three enzymes over the same time period. Of note, when hydrogels composed of 75% L-Ac-$(FKFE)_2$ and 25% D-Ac-$(FKFE)_2$ were exposed to the same enzymes, they degraded but at a much slower rate (after 5 days, about 50% of the peptide remains), demonstrating the high degree of tunability offered by stereochemistry-directed interactions.[14]

In addition to peptide degradation rate, stereochemistry-directed interactions also modulate the strength of the binding interaction between peptides and, by extension, macroscopic properties. For example, the β-sheet forming, self-assembling MAX1 peptide assembles to form fibrous hydrogels with storage modulus G' ~ 200 Pa in aqueous buffer. A 1:1 heterochiral mixture of D-MAX1 and L-MAX1 yields fibrous hydrogels with a 4x increase in modulus (G' ~ 800 Pa).[15] These results were attributed to stronger, more favorable packing interactions between the side chains of D- and L-MAX1 that were not possible in assemblies of MAX1 with only one stereochemistry.[16] Consistent with these findings for MAX1, hydrogels made from 1:1 blends of D- and L-Ac-$(FKFE)_2$ were stiffer than hydrogels prepared from L-Ac-$(FKFE)_2$. Moreover, the enthalpy of the interaction between D-$(FKFK)_2$ and L-$(FEFE)_2$ exceeds that between the same peptides in the L-configuration by nearly 10 kcal/mol.[17] However, blending D- and L-peptides that assemble into hydrogels does not always result in stronger mechanics. In fact, 1:1 heterochiral blends of KYFIL in 1X PBS result in a ~10x decrease in storage modulus (G' ~ 31 kPa for L-KYFIL vs. G' ~ 3 kPa for 1:1 L:D-KYFIL). This decrease is accompanied by a significant change in morphology from fibrous for L-KYFIL to plate-like structures for 1:1 L:D-KYFIL, suggesting that the drop in modulus is due to morphology rather than a loss of peptide interaction.[12] For the other examples with MAX1 and Ac-$(FKFE)_2$, the morphology of the peptide assemblies remained the same,[15–17] raising questions about what sequence differences contribute to this differential response to heterochiral assembly. The peptide Aβ(16-22) also undergoes a morphological change from fibrous to rigid, semi-crystalline structures in a heterochiral mixture. The heterochiral mixture was demonstrated to be more thermodynamically favorable than the homochiral mixture, but these peptides were not used to make hydrogels.[18] MAX1 and Ac-$(FKFE)_2$ both have alternating hydrophilic and hydrophobic amino acid sequences, whereas KYFIL and Aβ(16-22) contain longer stretches of hydrophobic amino acids. These sequence differences may begin to explain the differences in the outcomes of heterochiral assembly, but further work is needed to confirm this as a design rule. In another example, triple helices of the collagen-mimetic peptide $(PPG)_{10}$ are soluble but heterochiral mixtures precipitate, a result attributed to more favorable packing interactions for the heterochiral triple helices.[19] These findings are intriguing because typically, achieving large changes in the mechanical properties of peptide materials requires either changing the sequence of the peptide or changing the concentration, which can be time- and cost-intensive. Having the option to tune binding strength and therefore mechanical properties of peptide materials via stereochemistry-directed interactions provides another useful tool for preparing next-generation biomaterials.

As demonstrated by the examples above, stereochemistry-directed interactions have the potential to increase tunability in degradation profiles and peptide-peptide interaction strength, providing an exciting opportunity to introduce more tunability into the peptides we use in biomaterials. Of note, stereochemistry-directed interactions have only been shown to result in unique properties compared to homochiral interactions for peptides with β-sheet or α-helical secondary structure, which is an important design consideration when planning to implement stereochemistry-directed interactions in biomaterial design. Additionally, these heterochiral interactions have been explored in relatively few peptide sequences, leaving open questions about the design rules and outcomes of these interactions. To learn more about the design rules for stereochemistry-directed interactions, it will be important to generate a larger body of evidence with a wide variety of peptide sequences demonstrating that heterochiral peptides form complexes and modulate peptide properties. Thus far, heterochiral interactions have largely been studied in β-sheet peptides, with only a couple examples of helical peptides that undergo stereochemistry-directed interactions.[19–21] Even among helical peptide examples, these reports demonstrate that interaction occurs, but how they influence the properties of the peptide materials needs to be further explored. Further, neither the peptides K3 (SNFLSCYVSGFHPSDIEVDLLK) nor $L_4K_8L_4$ undergo stereochemistry-directed interactions, preferentially interacting with only peptides of the same stereochemistry when D- and L-peptides were mixed.[22,23] Of note, the $L_4K_8L_4$ peptide has a similar sequence pattern to the Aβ(16-22) peptide that did form heterochiral complexes. It has not yet been determined what differences between these peptides and the other peptides discussed above cause one set to undergo stereochemistry-directed interactions and not the other, but further exploration of this sequence space may unlock the full potential of stereochemistry-directed interactions in peptide-based biomaterials.

1.2 Polymer conjugation

Another method to address the existing drawbacks of peptide-based biomaterials surrounding enzymatic degradation and rapid renal clearance is to attach the peptides to polymers via conjugation reactions (**Figure 1.2**). Polymer-peptide conjugation not only increases the overall size of the material, sometimes through supramolecular assembly, to help it avoid renal clearance, but the polymer can also serve to increase the solubility of the peptide, slow enzymatic degradation, and reduce cytotoxicity.[24–27] Combining peptides and polymers marries the functional diversity and biocompatibility of peptides with the robust mechanics and wide range of compositions and architectures available to polymers.

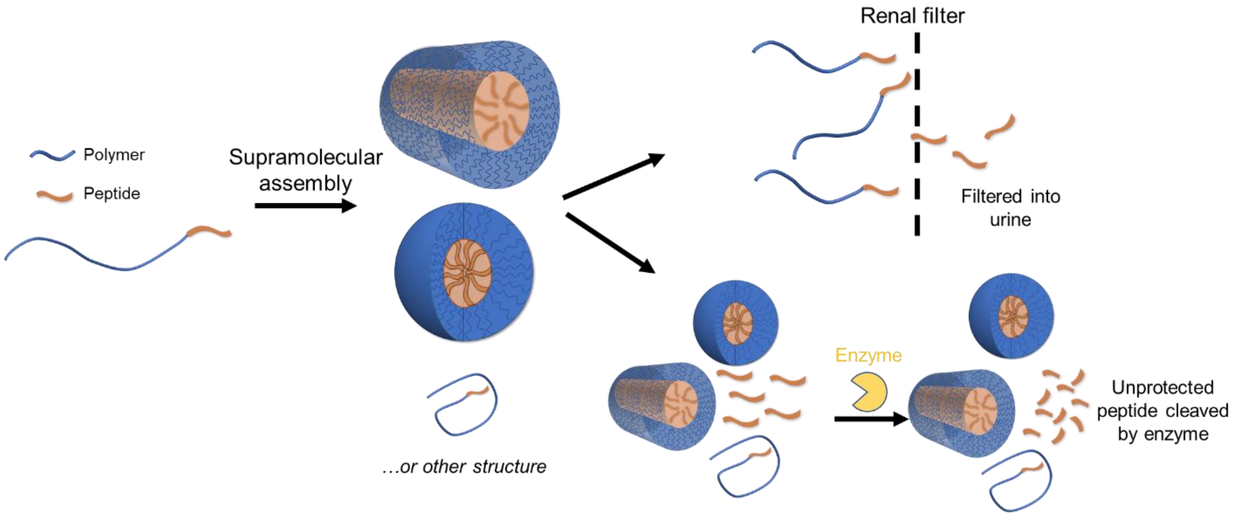

Figure 1.2. Conjugating peptides to polymers allows us to take advantage of the benefits of both components. Conjugates may assemble into micellar or other structures, dependent on the relative hydrophilicities of the polymer and peptide. The increase in size of conjugate structures protects the peptide from renal filtration and the polymer also protects the peptide from enzymes.

Polymer-peptide conjugates are used to protect peptides from premature clearance or breakdown, keep peptides soluble, and direct supramolecular assembly in a wide variety of applications. Antimicrobial peptides are among the most common classes of peptides conjugated to polymers, typically to avoid renal filtration and enzymatic degradation while increasing antimicrobial peptide solubility.[25,28] Antimicrobial peptides that are cytotoxic are often conjugated to neutral, hydrophilic polymers to avoid interactions with mammalian cells, but they typically also lose activity against bacteria. The structural diversity of polymers is crucial here, as changing the polymer architecture can balance antimicrobial activity and cytotoxicity.[25] In another example, polymer-peptide conjugates were used to disrupt aggregation of the amyloid beta (Aβ) peptide implicated in Alzheimer's disease.[29–31] The hydrophobic β-sheet breaker peptide iAβ5 (LPFFD) was conjugated to a comb-shaped (poly[N-(2-hydroxypropyl) methacrylamide]) (polyHPMA) polymer to yield a polyHPMA backbone with pendant iAβ5 peptide groups. Alone in 1X phosphate buffered saline (PBS) at 10 μM, the amyloid β fragment Aβ40 formed fibrillar aggregates hundreds of nanometers in size, but when incubated with the polyHPMA-iAβ5 comb-shaped conjugate, Aβ40 formed only small aggregates of a few nanometers. In this example, the polymer served as a carrier that solubilized the hydrophobic β-sheet breaker peptide to allow it to interact with Aβ40 without the treatment itself aggregating in solution. Further examples of polymer-peptide conjugates include drug delivery by polypeptide-PEG micelles, where the conjugate assembles into micelles that provide stability and controlled release for drugs encapsulated within the micelle.[24,32–34] These examples and more, highlighted in recent reviews,[24,25,27,35] underscore the benefits of preparing hybrid materials composed of polymers and peptides to benefit from the best properties of each material.

1.3 Thesis overview

In this thesis, we aim to design more tunable peptide biomaterials, gain further understanding of the design rules governing stereochemistry-directed interactions, and attach peptides to polymers to develop new therapeutics for amyotrophic lateral sclerosis. We break these goals into four chapters in this thesis (**Figure 1.3**). We first develop a tunable biomaterial scaffold with spatiotemporal control over the presentation of biomolecules in collaboration with Prof. Chris Highley's lab. We use a combination of photochemistry and specific, yet displaceable interactions between helical coiled coil peptides to provide spatial and temporal control, respectively, over biomolecule presentation on the scaffold (**Chapter 2**). To explore the knowledge gap in how stereochemistry-directed interactions affect the properties of helical peptide assemblies and leverage the benefits of stereochemistry-directed interactions in the same coiled coil system that provided spatiotemporal control over biomolecule display, we investigated heterochiral blends of coiled coils. We show that stereochemistry-directed interactions between coiled coils furnishes complexes that bind more strongly to each other and are more enzymatically stable than analogous coiled coils composed of only L-peptides (**Chapter 3**). We also leverage peptide self-assembly and stereochemistry-directed peptide interactions within a polymer-peptide conjugate biomaterial we developed to target and disperse aggregates of toxic proteins implicated in amyotrophic lateral sclerosis (ALS) (**Chapter 4**). Finally, to target a highly charged sub-class of these toxic proteins implicated in ALS, we designed a series of peptides to interact electrostatically with these proteins and characterized the interactions between peptide candidates and mimics of the toxic proteins using isothermal titration calorimetry (ITC). This study will be used to inform future studies and inform the best candidate peptides for attachment to polymers as toxic protein-sequestering polymer-peptide therapeutics (**Chapter 5**). Together, the work presented here contributes to the understanding and leveraging of peptide interactions to realize highly tunable biomaterials and new therapeutics, including highlighting the untapped potential of stereochemistry-directed interactions in the design of biomaterials.

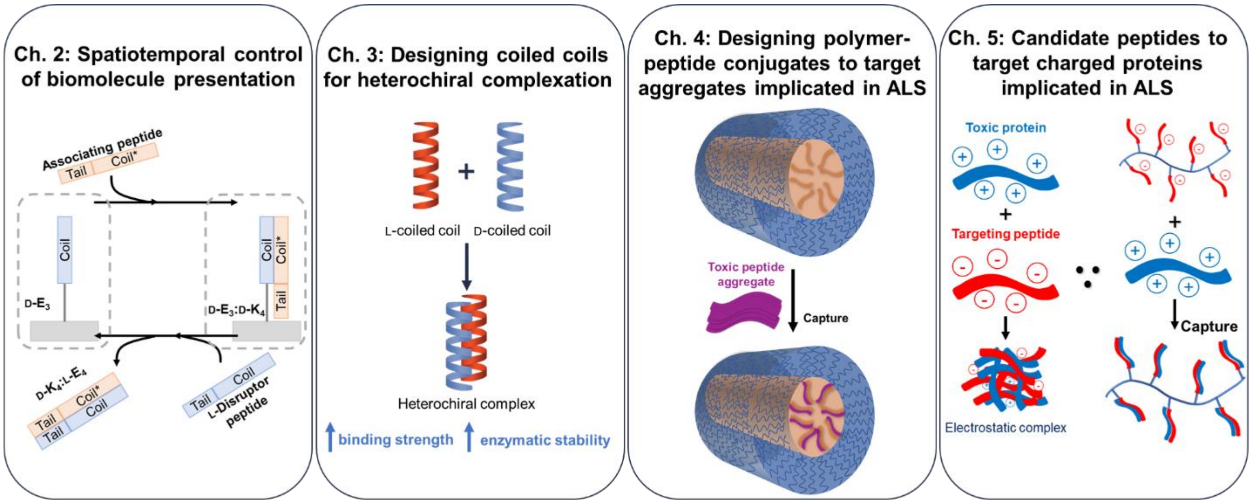

Figure 1.3. Thesis overview.

1.4 References

(1) Roach, P.; Eglin, D.; Rohde, K.; Perry, C. C. Modern Biomaterials: A Review - Bulk Properties and Implications of Surface Modifications. *J. Mater. Sci. Mater. Med.* **2007**, *18*,

1263–1277. https://doi.org/10.1007/s10856-006-0064-3.

(2) Hamley, I. W. Small Bioactive Peptides for Biomaterials Design and Therapeutics. *Chem. Rev.* **2017**, *117*, 14015–14041. https://doi.org/10.1021/acs.chemrev.7b00522.

(3) Collier, J. H.; Segura, T. Evolving the Use of Peptides as Components of Biomaterials. *Biomaterials* **2011**, *32* (18), 4198–4204. https://doi.org/10.1016/j.biomaterials.2011.02.030.

(4) Varanko, A.; Saha, S.; Chilkoti, A. Recent Trends in Protein and Peptide-Based Biomaterials for Advanced Drug Delivery. *Adv. Drug Deliv. Rev. 156*, 133–187.

(5) Boöttger, R.; Hoffmann, R.; Knappe, D. Differential Stability of Therapeutic Peptides with Different Proteolytic Cleavage Sites in Blood, Plasma and Serum. *PLoS One* **2017**, *12* (6), e0178943. https://doi.org/10.1371/journal.pone.0178943.

(6) Werle, M.; Bernkop-Schnürch, A. Strategies to Improve Plasma Half Life Time of Peptide and Protein Drugs. *Amino Acids* **2006**, *30*, 351–367. https://doi.org/10.1007/s00726-005-0289-3.

(7) Di, L. Strategic Approaches to Optimizing Peptide ADME Properties. *AAPS J.* **2015**, *17* (1), 134–143. https://doi.org/10.1208/s12248-014-9687-3.

(8) Bomb, K.; Zhang, Q.; Ford, E. M.; Fromen, C. A.; Kloxin, A. M. Systematic D-Amino Acid Substitutions to Control Peptide and Hydrogel Degradation in Cellular Microenvironments. *ACS Macro Lett.* **2023**, 725–732. https://doi.org/10.1021/acsmacrolett.3c00144.

(9) Li, X.; Du, X.; Li, J.; Gao, Y.; Pan, Y.; Shi, J.; Zhou, N.; Xu, B. Introducing d -Amino Acid or Simple Glycoside into Small Peptides to Enable Supramolecular Hydrogelators to Resist Proteolysis. *Langmuir* **2012**, *28*, 13512–13517. https://doi.org/10.1021/la302583a.

(10) Chen, X.; Fan, Z.; Chen, Y.; Fang, X.; Sha, X. Retro-Inverso Carbohydrate Mimetic Peptides with Annexin1-Binding Selectivity, Are Stable in Vivo, and Target Tumor Vasculature. *PLoS One* **2013**, *8* (12), e80390. https://doi.org/10.1371/journal.pone.0080390.

(11) Luo, Z.; Zhao, X.; Zhang, S. Self-Organization of a Chiral D-EAK16 Designer Peptide into a 3D Nanofiber Scaffold. *Macromol. Biosci.* **2008**, *8*, 785–791. https://doi.org/10.1002/mabi.200800003.

(12) Duti, I. J.; Florian, J. R.; Kittel, A. R.; Amelung, C. D.; Gray, V. P.; Lampe, K. J.; Letteri, R. A. Peptide Stereocomplexation Orchestrates Supramolecular Assembly of Hydrogel Biomaterials. *J. Am. Chem. Soc.* **2023**, *145*, 18468–18476. https://doi.org/10.1021/jacs.3c04872.

(13) Saklani, R.; Domb, A. J. Peptide and Protein Stereocomplexes. *ACS Omega* **2024**, *9*, 17726–17740. https://doi.org/10.1021/acsomega.4c00178.

(14) Swanekamp, R. J.; Welch, J. J.; Nilsson, B. L. Proteolytic Stability of Amphipathic Peptide Hydrogels Composed of Self-Assembled Pleated Β-Sheet or Coassembled Rippled Β-Sheet Fibrils. *Chem. Commun.* **2014**, *50*, 10133–10136. https://doi.org/10.1039/c4cc04644g.

(15) Nagy, K. J.; Giano, M. C.; Jin, A.; Pochan, D. J.; Schneider, J. P. Enhanced Mechanical Rigidity of Hydrogels Formed From Enantiomeric Peptide Assemblies. *J Am Chem Soc* **2011**, *133* (38), 14975–14977. https://doi.org/10.1158/0008-5472.CAN-10-4002.BONE.

(16) Nagy-Smith, K.; Beltramo, P. J.; Moore, E.; Tycko, R.; Furst, E. M.; Schneider, J. P. Molecular, Local, and Network-Level Basis for the Enhanced Stiffness of Hydrogel Networks Formed from Coassembled Racemic Peptides: Predictions from Pauling and Corey. *ACS Cent. Sci.* **2017**, *3*, 586–597. https://doi.org/10.1021/acscentsci.7b00115.

(17) Swanekamp, R. J.; Dimaio, J. T. M.; Bowerman, C. J.; Nilsson, B. L. Coassembly of Enantiomeric Amphipathic Peptides into Amyloid-Inspired Rippled β-Sheet Fibrils. *J. Am. Chem. Soc.* **2012**, *134*, 5556–5559. https://doi.org/10.1021/ja301642c.

(18) Urban, J. M.; Ho, J.; Piester, G.; Fu, R.; Nilsson, B. L. Rippled β-Sheet Formation by an Amyloid-β Fragment Indicates Expanded Scope of Sequence Space for Enantiomeric β-Sheet Peptide Coassembly. *Molecules* **2019**, *24*, 1983. https://doi.org/10.3390/molecules24101983.

(19) Xu, F.; Khan, I. J.; McGuinness, K.; Parmar, A. S.; Silva, T.; Murthy, N. S.; Nanda, V. Self-Assembly of Left- and Right-Handed Molecular Screws. *J. Am. Chem. Soc.* **2013**, *135* (50), 18762–18765. https://doi.org/10.1021/ja4106545.

(20) Mortenson, D. E.; Steinkruger, J. D.; Kreitler, D. F.; Perroni, D. V.; Sorenson, G. P.; Huang, L.; Mittal, R.; Yun, H. G.; Travis, B. R.; Mahanthappa, M. K.; Forest, K. T.; Gellman, S. H. High-Resolution Structures of a Heterochiral Coiled Coil. *Proc. Natl. Acad. Sci. U. S. A.* **2015**, *112* (43), 13144–13149. https://doi.org/10.1073/pnas.1507918112.

(21) Kreitler, D. F.; Yao, Z.; Steinkruger, J. D.; Mortenson, D. E.; Huang, L.; Mittal, R.; Travis, B. R.; Forest, K. T.; Gellman, S. H. A Hendecad Motif Is Preferred for Heterochiral Coiled-Coil Formation. *J. Am. Chem. Soc.* **2019**, *141* (4), 1583–1592. https://doi.org/10.1021/jacs.8b11246.

(22) Wadai, H.; Yamaguchi, K. I.; Takahashi, S.; Kanno, T.; Kawai, T.; Naiki, H.; Goto, Y. Stereospecific Amyloid-like Fibril Formation by a Peptide Fragment of B2-Microglobulin. *Biochemistry* **2005**, *44* (1), 157–164. https://doi.org/10.1021/bi0485880.

(23) Koga, T.; Matsuoka, M.; Higashi, N. Structural Control of Self-Assembled Nanofibers by Artificial β-Sheet Peptides Composed of D- or L-Isomer. *J. Am. Chem. Soc.* **2005**, *127* (50), 17596–17597. https://doi.org/10.1021/ja0558387.

(24) Shu, J. Y.; Panganiban, B.; Xu, T. Peptide-Polymer Conjugates: From Fundamental Science to Application. *Annu. Rev. Phys. Chem.* **2013**, *64*, 631–657. https://doi.org/10.1146/annurev-physchem-040412-110108.

(25) Cui, Z.; Luo, Q.; Bannon, M. S.; Gray, V. P.; Bloom, T. G.; Clore, M. F.; Hughes, M. A.; Crawford, M. A.; Letteri, R. A. Molecular Engineering of Antimicrobial Peptide (AMP)-Polymer Conjugates. *Biomater. Sci.* **2021**, *9* (15), 5069–5091. https://doi.org/10.1039/d1bm00423a.

(26) Liu, X. Y.; Nothias, J. M.; Scavone, A.; Garfinkel, M.; Millis, J. M. Biocompatibility Investigation of Polyethylene Glycol and Alginate-Poly-l-Lysine for Islet Encapsulation. *ASAIO J.* **2010**, *56* (3), 241–245. https://doi.org/10.1097/MAT.0b013e3181d7b8e3.

(27) Chen, C.; Ng, D. Y. W.; Weil, T. Polymer Bioconjugates: Modern Design Concepts toward Precision Hybrid Materials. *Prog. Polym. Sci.* **2020**, *105*, 101241. https://doi.org/10.1016/j.progpolymsci.2020.101241.

(28) Guiotto, A.; Pozzobon, M.; Canevari, M.; Manganelli, R.; Scarin, M.; Veronese, F. M. PEGylation of the Antimicrobial Peptide Nisin A: Problems and Perspectives. *Farmaco* **2003**, *58* (1), 45–50. https://doi.org/10.1016/S0014-827X(02)01301-0.

(29) Song, Y.; Cheng, P.-N.; Zhu, L.; Moore, E. G.; Moore, J. S. Multivalent Macromolecules Redirect Nucleation-Dependent Fibrillar Assembly into Discrete Nanostructures. *J. Am. Chem. Soc.* **2014**, *136*, 5233–5236. https://doi.org/10.1021/ja501102f.

(30) Song, Y.; Moore, E. G.; Guo, Y.; Moore, J. S. Polymer–Peptide Conjugates Disassemble Amyloid β Fibrils in a Molecular-Weight Dependent Manner. *J. Am. Chem. Soc.* **2017**, *139* (12), 4298–4301. https://doi.org/10.1021/jacs.7b00289.

(31) Jiang, X.; Halmes, A. J.; Licari, G.; Smith, J. W.; Song, Y.; Moore, E. G.; Chen, Q.;

Tajkhorshid, E.; Rienstra, C. M.; Moore, J. S. Multivalent Polymer − Peptide Conjugates: A General Platform for Inhibiting Amyloid Beta Peptide Aggregation. *ACS Macro Lett.* **2019**, *8*, 1365–1371. https://doi.org/10.1021/acsmacrolett.9b00559.

(32) Bae, Y.; Kataoka, K. Intelligent Polymeric Micelles from Functional Poly(Ethylene Glycol)-Poly(Amino Acid) Block Copolymers. *Adv. Drug Deliv. Rev.* **2009**, *61* (10), 768–784. https://doi.org/10.1016/j.addr.2009.04.016.

(33) Osada, K.; Christie, R. J.; Kataoka, K. Polymeric Micelles from Poly(Ethylene Glycol)-Poly(Amino Acid) Block Copolymer for Drug and Gene Delivery. *J. R. Soc. Interface* **2009**, *6*, S325–S339. https://doi.org/10.1098/rsif.2008.0547.focus.

(34) Otsuka, H.; Nagasaki, Y.; Kataoka, K. Self-Assembly of Poly(Ethylene Glycol)-Based Block Copolymers for Biomedical Applications. *Curr. Opin. Colloid Interface Sci.* **2001**, *6* (1), 3–10. https://doi.org/10.1016/S1359-0294(00)00082-0.

(35) Stevens, C. A.; Kaur, K.; Klok, H. A. Self-Assembly of Protein-Polymer Conjugates for Drug Delivery. *Adv. Drug Deliv. Rev.* **2021**, *174*, 447–460. https://doi.org/10.1016/j.addr.2021.05.002.

Chapter 2. Spatiotemporal control over biomolecule presentation *in vitro*

2.1 Introduction

In this chapter, we developed a biomaterial scaffold with the capability to present biomolecules with spatial and temporal control. This work was a collaborative effort with Greg Grewal and Chris Highley and was published in 2021 in *Biomaterials Science*. My contribution to this work was primarily in the characterization of the coiled coil peptide interactions, so that will be the focus of the results in this chapter.

The ability to spatiotemporally control the presentation of relevant biomolecules in synthetic culture systems has gained significant attention as researchers strive to recapitulate the complex, dynamic nature of the extracellular matrix (ECM) *in vitro*.[1,2] The ECM is the native tissue environment that plays a central role in regulating cellular fates through a combination of biophysical and biochemical processes.[3–6] In efforts to recapitulate microenvironmental features of the ECM *in vitro*, the dynamic nature of the ECM must be considered, with the presentation of cell fate cues in flux during continual restructuring.[6–9] To develop culture systems that influence cell migration, proliferation, and differentiation, approaches are needed to engineer the presentation of molecules involved in cell fate decisions.[10–12] Hydrogel biomaterials are advantageous in vitro platforms as they can replicate tissue-specific mechanics and be modified with biomolecules through numerous established strategies.[13–16]

The immobilization of biomolecules onto or within tissue culture substrates is important when engineering environments that mimic the ECM.[17–19] One successful approach for incorporating bioactive molecules into scaffolds is photo-mediated thiol–ene click conjugation.[20–22] Modifying hydrogel-forming polymers with norbornene groups enables spatial control over biomolecule presentation via photo-mediated thiol–ene click conjugation when used in conjunction with photomasks that selectively shield light.[3,17,18] Controlling the localization of molecules on tissue culture scaffolds affords the ability to establish a spatial distribution of bio-active cues and gradients of signaling molecules to better recapitulate physiological environments and potentiate downstream cellular fates.[23]

While providing spatial control, a drawback of these covalent methods for conjugation of biomolecules to hydrogels is that the resulting materials do not capture the dynamic nature of the ECM *in vivo*.[10,11] Cells continually transduce signals provided by biochemical and biophysical cues in their microenvironment,[24] and to achieve the dynamic characteristics of natural tissue in a biomaterial system, the ability to define the presentation of relevant signals, both spatially and temporally, is necessary.[19] To this end, there have been significant strides towards developing techniques to dynamically introduce bioactive cues into hydrogel systems.[25] For example, photo-mediated thiol–ene conjugation with subsequent photocleavage by means of o-nitrobenzyl-based ether linkers enabled reversible incorporation of bioactive compounds into hydrogel networks.[26] In a biologically inspired example, 3,4-dihydroxy-L-phenylalanine (DOPA), a catechol-containing amino acid present in mussels, facilitated reversible incorporation of biomolecules through dynamic-covalent esters formed between DOPA and phenylboronic acid.[27] These methods demonstrate efficacy in reversible incorporation of biomolecules; however, they primarily leverage covalent bonds when immobilizing bioactive molecules – thus motivating exploration into reversibility driven by noncovalent interactions.

Supramolecular interactions offer approaches for dynamic incorporation of biomolecules into hydrogel scaffolds to capture the dynamic biochemical and biophysical features of cellular microenvironments.[28,29] For example, host–guest pairs within hydrogels rapidly assemble, but can dissociate under externally applied forces.[30,31] Adhesive peptides appended to a naphthyl group achieve temporally controlled presentation within a hydrogel via interactions with a β-cyclodextrin host immobilized to alginate.[31] Subsequent addition of a bio-inert peptide attached to a higher affinity adamantane guest displaced the adhesive peptide and resulted in smaller 3T3 fibroblast cell areas. Additionally, oligonucleotides can be designed for reversible pairing through a similarly competitive process known as toehold-mediated strand displacement.[32–34] In toehold-mediated strand displacement, two complementary oligonucleotides pair, with one of the oligonucleotides designed with a longer 'toehold' region that can remain unpaired prior to introduction of a third, longer oligonucleotide designed to be fully complementary with the toehold-containing sequence and therefore a higher affinity binder. Adding the longer complementary strand displaces the shorter strand due to the higher affinity interaction between the two longer oligonucleotides. This non-covalent interaction facilitates reversible, repeatable, and specific addition or removal of biomolecules under short timescales through differences in association affinities on hydrogel scaffolds. This approach utilizes oligonucleotides and thus would require tagging proteins with oligonucleotides for specific interactions with proteins. The approach could be improved upon by substituting the need for oligonucleotides with peptides.

We sought here to adopt concepts from each platform to develop a new peptide-based method that affords reversible, dynamic incorporation of bioactive molecules into hydrogel networks with spatiotemporal control. We employ coiled coil-forming peptides that supramolecularly assemble in a specific manner in solution.[35–37] Like toehold-mediated strand displacement with DNA, Gröger et al. showed coiled coil peptides to undergo a similar process.[35] Introduction of a longer, higher affinity peptide to a lower affinity, toehold-containing coiled coil complex (dissociation constant, $K_D \sim 10^{-8}$ M) displaced the shorter, lower affinity component and yielded a high affinity coiled coil ($K_D \sim 10^{-9}$ M). These associations are similar in nature to other specific supramolecular assemblies, such as cyclodextrin-adamantane ($K_D \sim 10^{-5}$ M)[31] and cucurbituril host–guest systems ($K_D \sim 10^{-11}$–10^{-12} M).[29] We considered that the comparatively moderate affinities in the coiled coil system ($K_D \sim 10^{-8}$–10^{-9} M)[35] would allow for stable presentation of biomolecules over extended periods of time, with facile release potentiated via the addition of specific competitive molecules. Furthermore, while cyclodextrin and cucurbituril-based assemblies are reversible, the relatively straightforward synthesis of peptides and potential to reversibly trigger binding and release over multiple cycles under physiological conditions render coiled coil peptide platforms highly attractive for dynamic modulation of synthetic cellular microenvironments.

We sought to strategically design coiled coil-forming peptides to allow for both spatially-controlled conjugation via photo-mediated thiol–ene reactions and temporal control of biomolecule presentation via toehold-mediated strand displacement of coiled coil complexes. The ability to disrupt these associations in a temporally controlled way and remove the biomolecules provides the desired constitutive “on/off” functionality –

enabling facile reversible functionalization of in vitro culture systems. Herein, we describe the design, structural and thermodynamic characterization, and patterning of biomolecules using a coiled coil peptide-based system on both hyaluronic acid (HA) and fibrous poly(ethylene glycol) (PEG) hydrogel surfaces. Using the patterned substrates, we demonstrate temporal attachment and release of biomolecules. To showcase the potential of this system in modulating bioactivity in engineered microenvironments, we build on previous work studying supramolecular assemblies in reversible modulation of cell adhesion and morphology *in vitro*.[31,33] The reversible presentation of an adhesive sequence enables visual confirmation of changes occurring at the cellular level of *in vitro* models and may be of use in studies perturbing microenvironmental adhesion to ECM-derived peptide binding sequences to understand cell fate decisions.

Taken together, this coiled coil-forming peptide system represents a compelling platform for reversible, spatiotemporally controlled presentation of bioactive molecules. We note that this user-defined release process can be repeated over multiple cycles, lending itself to applications that require spatiotemporally controlled presentation of biomolecules that can be modulated through external cues as well as be reloaded for subsequent multi-stage release. In addition to the examples discussed here, this platform may be broadly applicable to understanding and controlling biomolecular composition in cellular microenvironments, for example to dynamically present growth factors and cytokines to modulate bioactivity *in vitro*.

2.2 Results and discussion

Towards introducing spatiotemporally controlled signals within model tissue-mimetic hydrogel environments, we investigated the ability of supramolecular coiled coil complexes to facilitate dynamic presentation of molecular adhesion motifs on or within both 2D HA hydrogels and fibrous PEG hydrogels. Many tissue-specific ECMs have fibrous components and thus fibrous hydrogels are of interest as *in vitro* models that recapitulate features of native ECM.[6,13] However, electrospinning PEG to prepare fibrous hydrogels is less reproducible than forming 2D HA hydrogels, so we investigated both hydrogel systems.

Hyaluronic acid is a hydrophilic, non-sulfated glycosaminoglycan that is ubiquitous in natural ECM, and thus intrinsically biocompatible.[15,16] PEG is a hydrophilic, biocompatible synthetic polymer used widely for biomedical applications, including for solubilization of therapeutics and as components of ECM-mimetic hydrogels.[13] Both HA and PEG are amenable to chemical modification either on the side chains or at the chain ends.[13] We installed norbornene moieties on both HA and PEG (NorHA and PEG-NB, respectively) to enable efficient, spatially controlled photo-mediated thiol–ene click reactions for addition of thiolated cross-linkers and biomolecules.[17,21] The resulting NorHA hydrogels and PEG-NB fibers were crosslinked using dithiothreitol (DTT) as a crosslinker, adjusting the stoichiometry to leave residual norbornene groups available for post-crosslinking photo-controlled addition of thiolated peptides.[3,17,21]

Coiled coil-forming peptides were designed as shown in **Figure 2.1** based on a previously described complementary glutamic acid/lysine (E/K)-rich peptide pairs that form heterodimeric coiled coils and undergo toehold-mediated strand displacement.[35,37,38] We modified the sequences with cysteine residues to facilitate thiol–ene conjugation to NorHA and PEG-NB and demonstrate the immobilization of fluorophore or adhesive motif-tagged complementary peptides via coiled coil formation. Specifically, for immobilization to the hydrogel surfaces, a tethered peptide ("T-peptide") was designed with a cysteine for conjugation, a glycine spacer, and three repeating heptads of EIAALEK as the glutamic acid (E)-rich coiled coil-forming motif (I = isoleucine, A = alanine, L = leucine). The complementary association peptide ("A-peptide") was designed with four repeating, lysine (K)-rich complementary KIAALKE heptads. The extra heptad repeat provides a toehold motif for triggered removal of the A peptide in the presence of the higher affinity disruptor peptide ("D-peptide") having four complementary repeating E-rich EIAALEK heptads. We

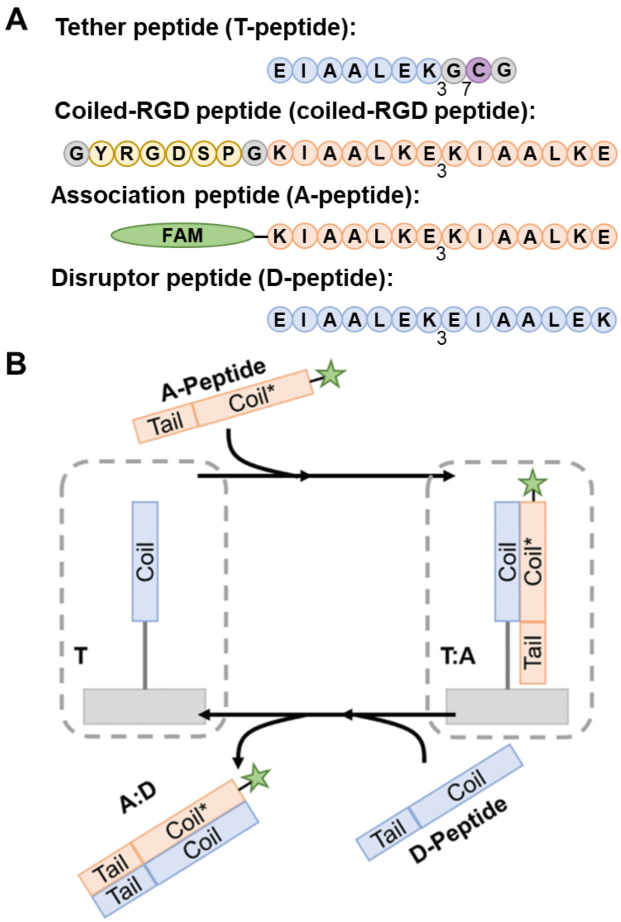

Figure 2.1. Coiled coil peptides and schematic of peptide association and subsequent removal from a surface via toehold-mediated strand displacement. A) Coiled coil peptides used in this study. Blue regions indicate E-rich coiled coil sequence repeats, orange regions indicate K-rich sequence repeats, the purple cysteine amino acid indicates the site where the coiled coil is bound to the hydrogel surface, and the yellow region indicates the RGD cell-binding motif representing a biomolecule attached to the coiled coil. B) Tethered peptides are covalently bound to NorHA/PEG-NB surfaces prior to incubation with A-peptide to form a T-peptide: A-peptide complex on the surface. The system is then incubated with D-peptide to interrupt the complex and preferentially form D-peptide: A-peptide complex, removing the A-peptide from the surface and leaving the T-peptide ready to form a new complex. Both the A-peptide and coiled-RGD peptide can fill the same role, as both have the same K-rich coiled coil structure, this example demonstrates the system with A-peptide.

hypothesized that this difference in affinities would facilitate removal of A-peptides from the hydrogels by disrupting the A-peptide: T-peptide coiled coils upon introduction of the D-peptide in solution. We further extend this platform for dynamic incorporation of adhesive ligands (here, the fibronectin-derived RGD motif) for use in cell culture systems. To accomplish this, we modified the A-peptide with an RGD sequence ("coiled-RGD") at the N-terminus. Successful synthesis of these four peptides was confirmed by electrospray ionization mass spectrometry (**Figure A1**), purity was determined by analytical-scale reverse-phase high performance liquid chromatography (**Figure A2**), and secondary structure was confirmed using circular dichroism spectroscopy (**Figure A3**).

2.2.1 Thermodynamic characterization of coiled coil peptide interactions using isothermal titration calorimetry (ITC)

Prior to applying these peptides to NorHA hydrogels and PEG-NB fibers for reversible biomolecule attachment, their interactions when forming complexes were characterized using ITC. ITC is a solution-based, label-free technique to acquire thermograms for biomolecular interactions that can be integrated and fit to thermodynamic models to obtain thermodynamic properties.[39,40] The coiled coil forming peptide pairs were analyzed in either NIH 3T3 fibroblast medium, PBS, or both, to obtain baseline-subtracted thermograms and integrated heats of interaction. Under the same conditions as the cell culture study (performed in NIH 3T3 fibroblast medium), the titrations of T-peptide into coiled-RGD peptide and coiled-RGD peptide into D-peptide were compared to a control titration of non-complementary T-peptide into D-peptide (**Figure 2.2**). The T-peptide: coiled-RGD peptide titration (**Figure 2.2A**) best fit a two-site binding model (giving two K_D

values, $K_{D,1} = 9.16 \times 10^{-9}$ M and $K_{D,2} = 3.81 \times 10^{-7}$ M) and did not fit well to a single-site binding model. This is consistent with the two-stage binding process reported for coiled coil dimerization.[35,41] However, for the titration of T-peptide into A-peptide (**Figure A7**), which has the same coiled coil sequence as the coiled-RGD peptide but with a fluorophore attached to the N-terminus rather than an RGD motif, we observe a good fit for a single-site binding model, so the two-site binding of the T-peptide and coiled-RGD peptide may instead be related to interactions with the RGD motif. The dissociation constants obtained from the two-site binding model indicate strong binding affinities, which is advantageous for the stable presentation of biomolecules over long periods of time.

Interestingly, the titration of coiled-RGD peptide into D-peptide also exhibits signs of a multi-stage binding process, but with both exothermic and endothermic heats of interaction (**Figure 2.2B**). We did not observe any switching from exothermic to endothermic heats of interaction for coiled coils with mismatched lengths, but this phenomenon did remain consistent for the same-length titration of A-peptide into D-peptide (**Figure A10**). This indicates that, for these coiled coils of the same length, peptide-peptide interactions are initially exothermic, but as the molar ratio of coiled-RGD peptide or A-peptide to D-peptide increases, molecular rearrangements which result in the endothermic (entropically favorable) release of ordered water molecules and exchange of excess coiled-RGD or A-peptide dominate the interaction.[42–45] This exothermic to endothermic switching precluded us from being able to fit the data with a binding model, but the larger magnitude of the heats of interaction from the coiled-RGD peptide: D-peptide interaction (~-80 kJ/mol, **Figure 2.2B**) compared to the heats associated with the T-peptide: coiled-RGD peptide interaction (~-30 kJ/mol, **Figure 2.2A**), indicate that the coiled-RGD peptide: D-peptide complex is thermodynamically favored over the T-peptide: coiled-RGD peptide complex. Therefore, we conclude that the coiled-RGD peptide will preferentially interact with the D-peptide in the presence of the T-peptide – facilitating reversibility in our system.

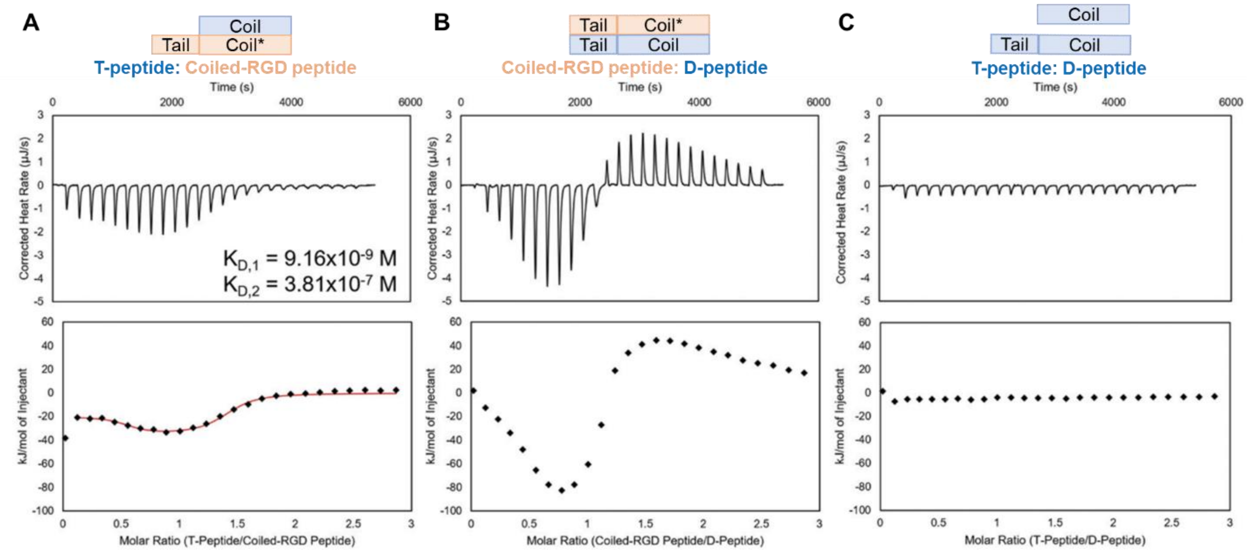

Figure 2.2. Baseline-subtracted thermograms (top) and integrated heats of interaction (bottom) for the titrations of A) T-peptide into coiled-RGD peptide, B) coiled-RGD peptide into D-peptide, and C) T-peptide into D-peptide. Where possible, the integrated heats of interaction were fit to a two-site binding model (red line) from which thermodynamic parameters were determined. The interaction between the T-peptide and the coiled-RGD peptide was high affinity, as evidenced by the K_D values on the order of 10^{-7}-10^{-9} M, indicating that the presentation of biomolecules on surfaces will be stable. The larger exothermic heats of interaction measured for the coiled-RGD peptide: D-peptide interaction demonstrates that these interactions between same-length coiled coils are stronger. No appreciable heats of interaction were observed for non-complementary T-peptide and D-peptide.

As expected, the titration of T-peptide into D-peptide results in little to no interaction (**Figure 2.2C**), as these peptides are non-complementary, both being E-rich. The heats of interaction are essentially 0 kJ/mol after subtracting out the heats of dilution of T-peptide into media and media into D-peptide. This confirms that there will be no off-target effects of the D-peptide interacting with T-peptide on the surface of our hydrogels.

These ITC experiments were also conducted in 1X PBS (pH 7.4 ± 0.05) to determine whether the NIH 3T3 fibroblast medium contributed to the results. We found that there were only marginal differences in the resultant heats of interaction (**Figures A7-A11**) when these coiled coils are titrated in 1X PBS compared to fibroblast medium. Additionally, all ITC experiments were replicable multiple times, as evidenced by the similarities between 2-5 replicates of each titration (**Figures A4-A11**).

2.2.2 Monitoring strand displacement by ITC

While the above ITC results suggest that strand displacement should occur for our coiled coil system, as the coiled coils with mismatched lengths have small heats of interaction than coiled coils of the same length, we sought to directly measure strand displacement using ITC. For this study, we used the coiled coil sequences without N- or C-terminal modifications: $(EIAALEK)_3$ (E_3) in place of the T-peptide, $(KIAALKE)_4$ (K_4) in place of the A-peptide or coiled-RGD peptide, and the D-peptide was unchanged as $(EIAALEK)_4$ $(E)_4$. We incubated K_4 with either E_3 or E_4 overnight in 1X PBS, then performed a titration of the remaining E coil into that complex (E_4 added to the K_4:E_3 complex and E_3 added to the K_4:E_4 complex) (**Figure 2.3**). We found that there were no observed heats of interaction when E_3 was titrated into K_4:E_4, which indicates that no strand displacement occurred. This was expected as we found that the K_4:E_4 interaction was stronger than the K_4:E_3 interaction, so E_3 was unable to displace E_4. However, when we titrated E_4 into the K_4:E_3 complex, we observed endothermic heats of interaction integrating to a maximum of ~20 kJ/mol. This again is consistent with entropically favorable molecular rearrangements from the release of both bound structured water and counterions from the free toehold region of the longer K_4 as it preferentially complexes with E_4. This titration provides a direct measurement of the thermodynamics of coiled coil strand displacement, corroborating our conclusions from the ITC data for the pairs of coiled coils.

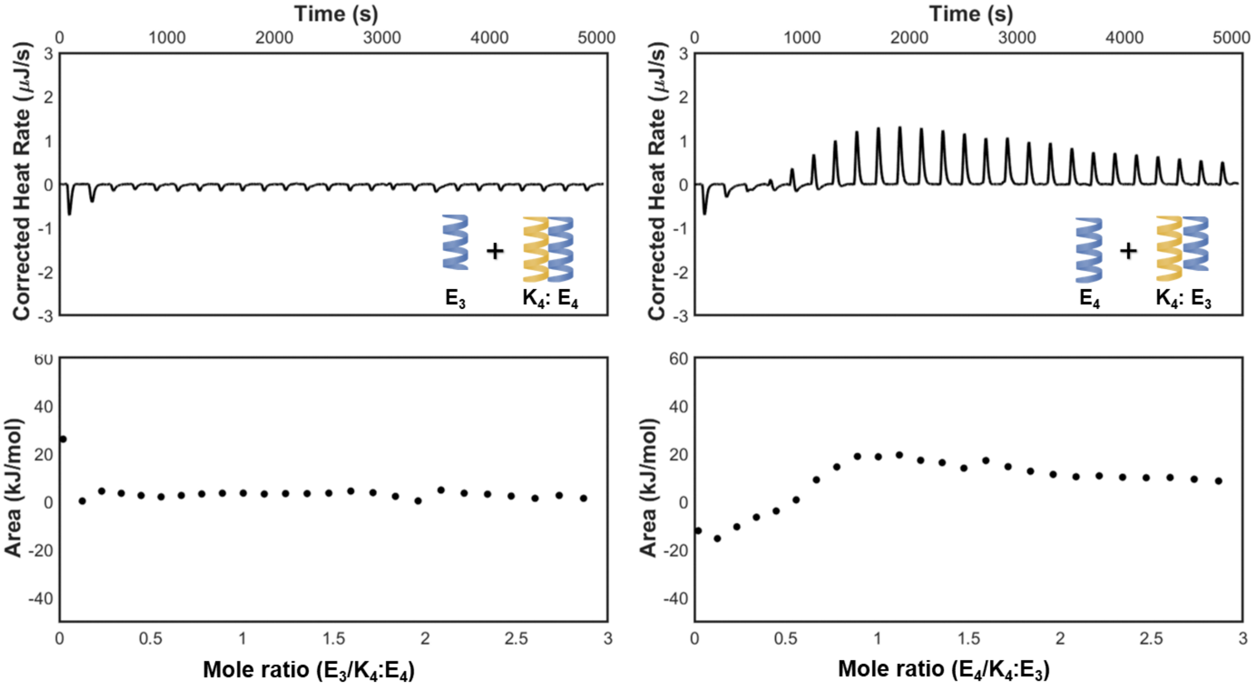

Figure 2.3. Baseline-subtracted thermograms and integrated heats of interactions for the titrations of A) E_3 into a pre-formed K_4:E_4 complex and B) E_4 into a pre-formed K_4:E_3 complex. No appreciable heats of interaction are observed for the titration of the shorter E_3 into the length-matched K_4:E_4 complex. However, endothermic heats of interaction are observed for the titration of the longer E_4 into the length-mismatched

K_4:E_3 complex where the K_4 has a toehold region, suggesting an entropically favorable molecular rearrangement. This offers a direct measurement of the thermodynamics of strand displacement.

2.2.3 Coiled coils photopatterned on a surface enable spatiotemporally controlled presentation of biomolecules on the surface

With the thermodynamic characterization of coiled coils showing promising results for the strand displacement potential for these coiled coils, we next moved to covalently binding the T-peptide to NorHA and PEG-NB surfaces with spatial control. T-peptides were attached to NorHA or PEG-NB surfaces via a photo-mediated thiol-ene reaction, with a photomask applied to generate 100 µm-wide stripes of T-peptides on the surface (**Figure 2.4A**). To demonstrate the ability to leverage coiled coil interactions to present a biomolecule on the surface, we swelled the surfaces with A-peptide, tagged with a fluorescein fluorophore (FAM), and imaged the surfaces using a Widefield microscope (**Figure 2.4B**). The micrographs of the FAM bound to the NorHA hydrogel and PEG-NB fiber surfaces demonstrate that not only is the FAM-tagged A-peptide present on the surfaces, but it is only present in the 100 µm stripes along which T-peptide was reacted.

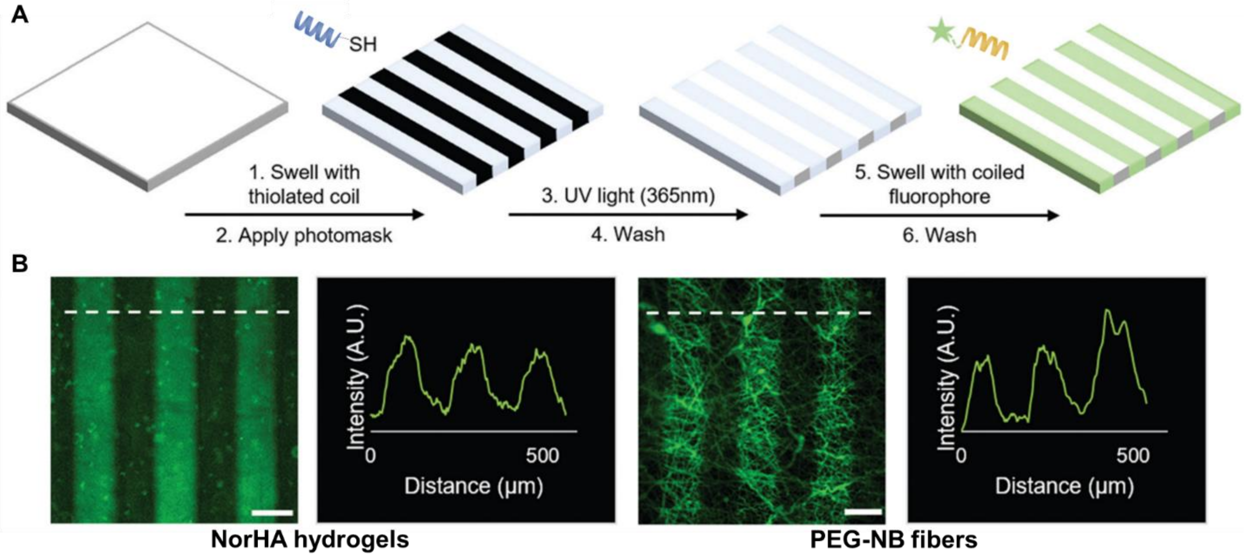

Figure 2.4. A) Schematic of the supramolecular, coiled coil-based FAM patterning process. The surface – either NorHA hydrogel or PEG-NB fibers – is swelled with thiolated T-peptide. A photomask is applied and the surface is irradiated with 365 nm light. The surface is then washed and swelled with FAM-tagged A-peptide. Finally, the surface is washed once more to remove unbound peptide. B) Representative micrographs and intensity profiles of FAM fluorescence on NorHA hydrogels and PEG-NB fibers. Scale bars = 100 µm. Dashed white lines indicate sample location of intensity profiles plotted for each micrograph. Credit to Greg Grewal for conducting these experiments and creating this figure.

With the spatial control over biomolecule presentation verified, we next demonstrated temporal control over biomolecule presentation by multiple cycles of release and loading of the FAM-tagged A-peptide on the surfaces (**Figure 2.5A**). By the ITC data we have analyzed for the coiled coil binding pairs, we expect that A-peptide bound to T-peptide on the surface will be released upon the introduction of D-peptide, with free T-peptide available on the surface, ready for another complementary coil with the same or a new biomolecule to be introduced. A NorHA hydrogel surface was loaded with FAM-tagged A-peptide and the fluorescence intensity of the outer swelling solution was monitored with time (**Figure 2.5B**). For the first 24 h, we held the hydrogels in 1X PBS. Over this time, we saw little to no fluorescence intensity in the outer solution, indicating that the peptides are stable on the hydrogel surface. After 24 h, D-peptide was introduced to trigger the release of the A-peptide. Over 8 h of release, we observed increasing FAM fluorescence in the outer solution, indicating that the A-peptide was being released from the surface. To demonstrate full temporal control, we sought to load and release over multiple cycles. After 8 h of release, the D-peptide was removed, and fresh A-peptide was introduced and held for another 24 h. Over this 24 h span, we observed no increase in FAM fluorescence, again supporting that our biomolecule-presenting peptides on the surface were stable. After this 24 h period, D-peptide was once again added to the hydrogel and FAM fluorescence was observed to increase, demonstrating that the A-peptide was again released.

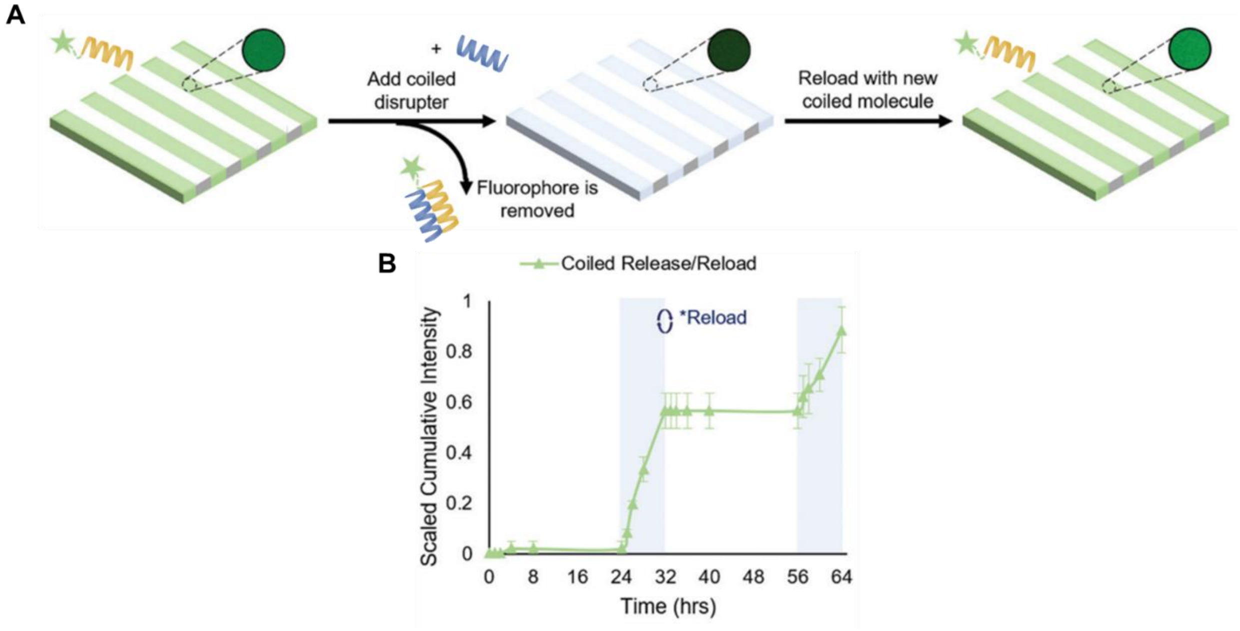

Figure 2.5. A) Schematic of FAM-tagged A-peptide release from surfaces via toehold-mediated strand displacement upon the addition of the complementary, length-matched D-peptide. After release of A-peptide from the surface, the surface can be reloaded with a new K_4 coiled coil, in this example it is reloaded

with another FAM-tagged A-peptide. B) Cumulative FAM fluorescence intensity of the outer swelling solution for over time to show repeated loading and release of FAM-tagged A-peptides from NorHA hydrogels. Hydrogels are loaded with FAM-tagged A-peptide then held in 1X PBS for 24 h, over which no fluorescence is observed, indicating that the A-peptide is stable on the surface over time. After 24 h, the A-peptide is released via addition of D-peptide for 8 h, over which the fluorescence intensity increases as A-peptide is released from the surface into the outer solution. Hydrogels were then reloaded with A-peptide for 24 h before the D-peptide disruption was repeated for 8 h. This experiment demonstrates that the surface can be loaded, released, reloaded, and released again over multiple cycles. Credit to Greg Grewal for conducting these experiments and creating this figure.

2.2.4 Fibroblast cells respond to the presentation and removal of RGD motifs on scaffolds

To test cell behavior on NorHA hydrogels and PEG-NB fibers displaying the RGD motif via coiled coil-mediated presentation, we cultured NIH 3T3 fibroblasts on both scaffolds after functionalizing the surface with coiled-RGD peptide. Cells adhered to and spread on the surface of scaffolds functionalized with coiled-RGD peptide (**Figure 2.6A,B**). The addition of D-peptide to remove the coiled-RGD peptide from the surface induced a significant change in cell adherence and area, with cell area being reduced by ~50% for cells seeded on NorHA hydrogels and for cell area decreasing on PEG-NB fibers to approximately the same sizes as observed on unmodified PEG-NB fibers (**Figure 2.6C**). These results demonstrate the temporal control that is possible over cellular growth and morphology by presentation of different cues over time using this system.

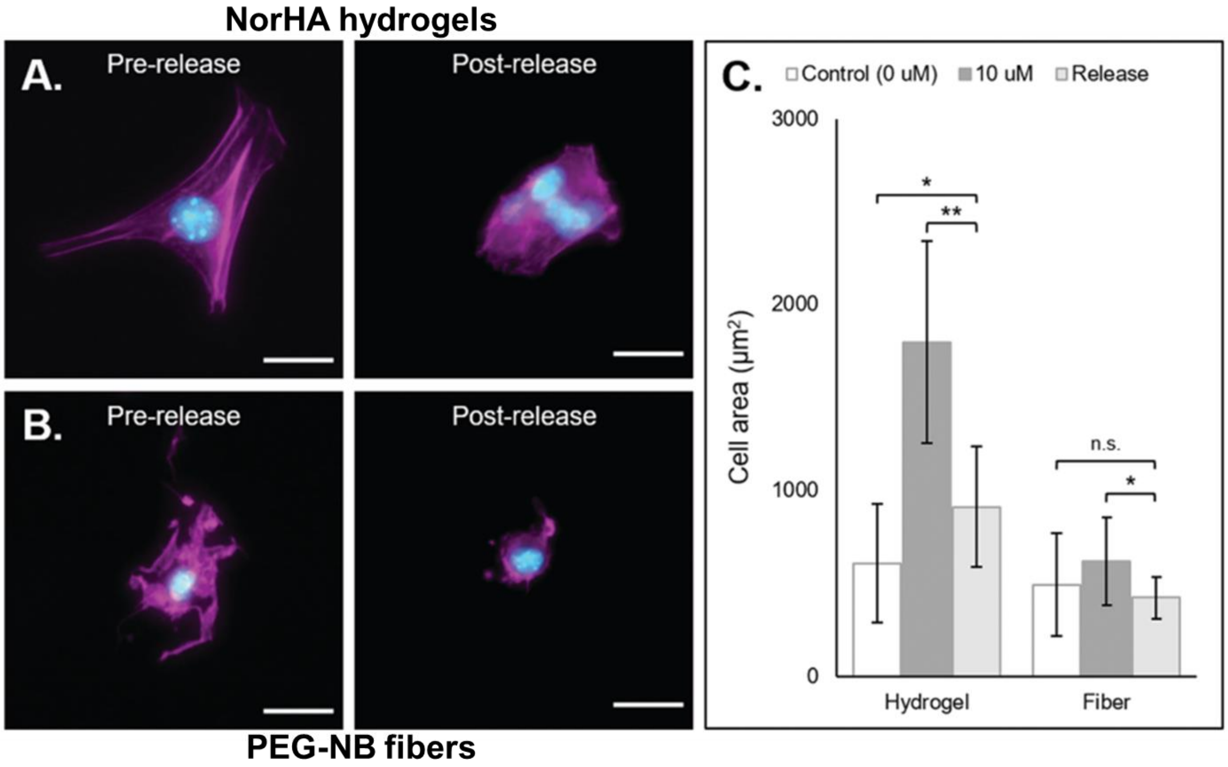

Figure 2.6. Effect of coiled-RGD peptide removal from A) NorHA hydrogel and B) PEG-NB fiber surfaces via addition of D-peptide on 3T3 fibroblast morphology. Surfaces were functionalized with 10 μM coiled-RGD peptide, then fibroblasts were seeded on the surface. Micrographs on the left show fibroblasts seeded on A) NorHA hydrogel and B) PEG-NB surfaces with coiled-RGD present. Micrographs on the right show fibroblasts on each surface after treated with 100 μM D-peptide. For both surfaces, cell exhibited fewer extensions and covered less surface area. C) Quantification of cell area across groups in the experiment. Statistics solely compared cell area after treatment with D-peptide to the control and 10 μM coiled-RGD groups prior to treatment with D-peptide. Scale bars = 25 μm, n.s. = no significance, *$p < 0.05$, **$p < 0.01$, error bars represent standard deviation. Credit to Greg Grewal for conducting these experiments and creating this figure.

2.3 Conclusions

Coiled coil peptides offer a versatile system for engineering spatial and temporal signals into hydrogel environments. Biofunctionality of a peptide can readily be altered through standard peptide synthesis techniques, and thiol groups in cysteine residues allow their incorporation via light-controlled reactions amenable to spatial patterning, as well as by other bioconjugation reactions, such as Michael additions. The supramolecular coiled coil interaction also presents a reversible platform that allows for the repeated introduction and removal of bioactivity within *in vitro* hydrogel and hydrogel fiber culture systems. Proof-of-concept experiments showing the reversible functionalization of the surface with FAM demonstrated the efficacy of this system to achieve high spatial and temporal control. Release was dependent on toehold-mediated strand displacement induced by addition of D-peptide and the process could be repeated by reloading with A-peptide. Using a version of the A-peptide modified with an RGD motif (coiled-RGD) for cell studies illustrated the ability to culture fibroblasts on materials functionalized with RGD via this coiled coil system. Removal of the coiled-RGD peptide via introduction of the D-peptide caused a statistically significant decrease in cell spread area on both hydrogels and fibers, indicating that the reversal of RGD presentation has a direct impact on fibroblast morphology. On the basis of these observations, future work should allow for the investigation of how dynamism in cell culture environments affects downstream cell behaviors. User-defined perturbations to these culture environments will enable fine-tuned control over the *in vitro* microenvironment. Future work will also consider differences in cell behaviors on hydrogels and hydrogel-based fibers, as well as differences between hydrogel backbone materials in this system. We believe this platform might be applied to many other areas of research that desire user-controlled addition and subsequent temporal release of bioactive compounds that can be reloaded for multiple release cycles.

2.4 Materials and methods

2.4.1 Synthesis of norbornene-functionalized hyaluronic acid (NorHA)

NorHA was synthesized as previously described.[17] Briefly, sodium hyaluronate (HA, Lifecore, 62 kDa) was dissolved in deionized (DI) water with Dowex 50 W × 8 ion-exchange resin (3 g resin per 1 g HA) for 2 h, and subsequently filtered, titrated to pH 7.02–7.05 with *tert*-butylammonium hydroxide (TBA, FisherSci) to yield HA-*tert*-butylammonium salt (HA-TBA). The final product was frozen at −80 °C, lyophilized, and stored under nitrogen. HA-TBA was then dissolved in anhydrous dimethyl sulfoxide (DMSO) and allowed to react with benzotriazole-1-yl-oxy-tris-(dimethylamino)-phosphonium hexafluorophosphate coupling reagent (BOP, Sigma, 0.3 mol equivalents relative to carboxylic acids on HA), and 5-norbornene-2-methylamine (nor-amine, Sigma, 1 mol equivalent relative to carboxylic acids on HA) to functionalize HA with norbornene groups. After ~2 h, the reaction was quenched with cold DI water, and the solution was transferred to a membrane (molecular weight cutoff: 6–8 kDa) and dialyzed against DI water for 5 d. Precipitate was removed by filtration, and the solution was re-dialyzed against DI water for 5 d prior to freezing at −80 °C, lyophilizing, purging with nitrogen, and storing at −20 °C until ready for use. The degree of modification was determined to be ~25% by ^{1}H nuclear magnetic resonance spectroscopy (^{1}H NMR, 500 MHz Varian Inova 500).

2.4.2 Peptide synthesis

All peptides used in this study were synthesized using a Liberty Blue (CEM) automated, microwave-assisted solid phase peptide synthesizer via Fmoc methods. Briefly, Rink amide resin (Advanced Chemtech, Rink Resin SS, 100–200 mesh, 1% DVB) was swollen with dimethylformamide (DMF, Aldrich, ACS reagent grade), and the immobilized Fmoc group removed with 20% (v/v) piperidine in dimethylformamide. Fmoc-protected amino acids (Advanced ChemTech, 0.2 M in DMF, 5 equivalents relative to theoretical available sites on the resin) and the coupling agents diisopropylcarbodiimide (DIC, Aldrich, 99%, 1 M in DMF) and Oxyma Pure (Advanced ChemTech, 1 M in DMF) were added to the reaction vessel and heated to 90 °C for 4 min. The Fmoc deprotection and coupling steps were repeated to build the peptide from the C-terminus to the N-terminus. For fluorescent peptides, 5(6)-carboxyfluorescein (Sigma Aldrich, ≥95%) was added last onto the N-terminus. The resultant peptides were cleaved from the resin with a cocktail of 92.5% trifluoroacetic acid (TFA, Aldrich, 99%), 2.5% triisopropylsilane (TIPS, Aldrich, 99%), 2.5% 2,2′-(ethylenedioxy) diethanethiol (DODT, Aldrich, 95%), and 2.5% DI water, and then isolated by precipitation into cold diethyl ether (Aldrich, ACS reagent, contains butylated hydroxytoluene as inhibitor) and centrifugation. After removal of ether under vacuum, the peptides were resuspended in DI water, frozen in liquid nitrogen, lyophilized, and stored at −20 °C as powders until ready for use. High performance liquid chromatography (HPLC) was used to determine peptide purity; since we noted no appreciable byproduct species, the peptides were used without further purification (**Figure A2**). Peptide primary structure was confirmed *via* electrospray ionization mass spectrometry (**Figure A1**). Secondary structures were determined by circular dichroism (CD) spectroscopy (**Figure A3**).

2.4.3 Isothermal titration calorimetry

Experiments were performed using a standard volume affinity isothermal titration calorimeter (TA Instruments, New Castle, DE) with peptide solutions prepared in either 1X phosphate buffered saline (PBS) or NIH 3T3 fibroblast culture medium at indicated concentrations. Peptide solutions were adjusted to pH 7.4 using NaOH or HCl and then degassed for 10 min at 25 °C. Titrations consisted of an initial 2 µL injection, followed by 24 or 49 injections (10 µL each) of one peptide solution (150–200 µM) into 1.3 mL of a second peptide solution (10–20 µM). Following an initial delay of 200 s, injections were separated by 200 s. Experiments were performed at 25 °C with the stirring speed set to 125 rpm and the cooling rate set to medium. The reference cell was filled with 1.3 mL of degassed, deionized water. The thermograms were analyzed using NanoAnalyze software (TA Instruments) and heats of binding (in kJ/mol) were obtained by integrating the area under each injection peak in the baseline-subtracted thermograms, then dividing by moles of each injected volume. When possible, the resultant curves were then fit to either the independent (one site) or multiple sites (two site) binding models to obtain K_D values. Heats of dilution from blank injections – either peptide (150–200 µM) into 1X PBS/fibroblast medium or 1X PBS/fibroblast medium into peptide (10–20 µM) – were subtracted from experimental heats to yield the blank-corrected data.[39] In all analyses, we neglected the heats from the initial 2 µL injection.

2.4.4 Fabrication of NorHA hydrogels

Prior to formation of NorHA hydrogels, glass coverslips (22 × 22 mm) were functionalized with 3-(mercaptopropyl) trimethoxysilane (MTS, Sigma Aldrich, 95%) to present pendant sulfhydryl groups as follows. Briefly, glass coverslips were plasma treated (Harrick Plasma) for 3 min, and MTS was added dropwise to plasma treated surface prior to being baked at 100 °C for 1 h, and 120 °C for 10 min in an exhausted oven. The coverslips were washed sequentially in dichloromethane (DCM), 70% ethanol in water, and DI water, then stored under inert atmosphere until ready for use. NorHA hydrogels were synthesized from a solution consisting of 5% (w/v) NorHA, 1 mM lithium phenyl-2,4,6-trimethyl benzoylphosphinate (LAP) photoinitiator to induce thiyl radicals, and dithiothreitol (DTT) for crosslinking ([thiol]: [norbornene] = 0.6) in PBS. For each hydrogel, 50 μL of the NorHA solution was pipetted onto a thiol-functionalized glass coverslip (22 × 22 mm), sandwiched with an 18 × 18 mm coverslip, and crosslinked by irradiation for 2 min at 365 nm (10 mW cm^{-2}, Omnicure) to covalently stabilize the gel network. NorHA hydrogels to be used in spatial patterning experiments were incubated in a 1% (w/v) bovine serum albumin (BSA) solution in PBS for 30 min to limit nonspecific binding prior to subsequent experiments; NorHA hydrogels to be uniformly patterned were incubated solely in PBS prior to use in experiments.

2.4.5 Preparation of norbornene-functionalized poly(ethylene glycol) (PEG-NB) electrospun fibers

The electrospinning protocol was adapted from Sharma and coworkers[21] and all fibers were collected on thiolated coverslips – identical to those used for preparing the 2D

NorHA hydrogels. Solutions consisting of 8-arm PEG-NB (10% w/v, ~20 kDa, JenKem Technology, USA), polyethylene oxide (5% w/v, ~400 kDa, carrier polymer), DTT ([thiol] : [norbornene] = 0.6), and 2-hydroxy-4′-(2-hydroxyethoxy)-2-methylpropiophenone (I2959, 0.05% w/v) were mixed for at least 24 h in PBS. Electrospinning was conducted on a custom setup with the following parameters: 16-gauge needle; ~15 cm between the needle and collection surface; 0.8 mL h^{-1} flow rate; 10–14 kV positive voltage applied to the needle; and 6 kV negative voltage applied to the collection surface. Fibers were collected for at least 10 min and crosslinked for 15 min (365 nm, 10 mW cm^{-2}, Omnicure) under nitrogen. Fibers were then incubated in a 1% (w/v) BSA/PBS solution if they were to be spatially patterned or in PBS alone if they were to be uniformly patterned prior to subsequent experimentation.

2.4.6 Photoligation of peptides to hydrogels and fibers

NorHA hydrogels and PEG-NB fibers were fabricated with a 0.6 thiol: norbornene ratio to avail norbornene groups for photo-patterned attachment of thiolated peptides after crosslinking. For fluorescent-based experiments, solutions of thiolated peptides (20 μM, T-peptide or thiolated fluorophore), BSA (1% w/v), and LAP (1 mM) in PBS were added dropwise to the surface of the hydrogels/fibers, covered with photomasks (CAD/Art Services), and irradiated (365 nm, 10 mW cm^{-2}) for 2 min. For cell-based experiments, a 100 μM solution of the T-peptide with 1 mM LAP in PBS was added dropwise to the surface of the hydrogels/fibers and irradiated with light (365 nm, 10 mW cm^{-2}) for 2 min. Following radical-induced thiol–ene coupling of the peptides to the hydrogel/fiber surfaces, samples were washed 3x in PBS for at least 30 min per wash to remove unreacted peptide and stored at room temperature until further use. Hydrogels/fibers with covalently tethered fluorophores were imaged directly after the wash steps, while other samples were used in coiled coil experiments as described below.

2.4.7 Formation of coiled coil complexes and subsequent peptide release

To induce coiled coil peptide complex formation on NorHA hydrogels and PEG-NB fibers, the scaffolds with tethered T-peptide were swollen with a 20 µM solution of the complementary A-peptide (2 mL per well) for 3 min prior to washing 3x with PBS for at least 30 min per wash to remove unbound peptide. To release the A-peptide, D-peptide was introduced into the system (3 mL per well, 20 µM for fluorescence experiments) at multiple time points. During the disruption process, the higher affinity D-peptide binds A-peptides, disrupting the A-peptide: T-peptide coiled coil and removing the A-peptides from the surface. Solution (1 mL) was removed at predetermined timepoints and the remaining 2 mL were aspirated off and replaced with fresh D-peptide solution. Aliquots collected at each time point were stored at 4 °C until analysis.

To introduce an Arg-Gly-Asp (RGD) cell adhesion motif into hydrogels and fibers for cell culture, 100 µM of the T-peptide was tethered to the substrates by the radical-induced thiol–ene click reaction as described above. Subsequently, following the same protocol as above, solutions of either 0 µM, 10 µM, or 100 µM of a complementary peptide containing an RGD sequence (coiled-RGD peptide, GYGRGDSPG(KIAALKE)$_4$) were added to supramolecularly attach the adhesion motif to the surface. For disruption of this complex and removal of RGD from the system, 100 µM solutions of the D-peptide were used.

2.4.8 Determination of peptide release

Kinetics of peptide release from NorHA hydrogels were indirectly assessed using plate reader measurements of fluorophore intensity in the supernatant at time points during disruption. Briefly, the A-peptide was synthesized as described above with 5(6)-carboxyfluorescein (FAM) included on the N-terminus during peptide synthesis, and the fluorescence of the disruption solution at each time point was determined via a BioTek Synergy 4 fluorescence spectrophotometer (excitation: 495 nm; emission: 518 nm). Three hydrogels were assessed for each experimental group.

Peptide release was further assessed visually using fluorescence microscopy (Leica DMi8 Widefield) during disruption. At each time point, fluorescent images (20x, dry) were taken of each NorHA hydrogel and the average intensity of photopatterned stripes was determined via ImageJ pixel intensity analysis. Three stripes per hydrogel were measured across three hydrogels for each experimental group.

2.4.9 Cell culture

NIH 3T3 fibroblasts (kindly provided by Dr Steven Caliari at the University of Virginia) were used for all cell experiments (passages 4–8). Cells were cultured in Dulbecco's modified Eagle's medium (DMEM) fortified with 10% (v/v) calf bovine serum (ATCC) and 1X antibiotic-antimycotic (Gibco). Prior to seeding cells on 2D NorHA hydrogels or PEG-NB fibers, hydrogels and fibers were sterilized with germicidal light for 2 h and swelled with culture medium for at least 30 min. Cells suspended in culture medium were seeded at a density of 5×10^4 cells per hydrogel or fiber sample and allowed 24 h to adhere to the surface. Cells were then fixed for subsequent analysis, as described below.

For release experiments, hydrogel/fibrous scaffolds were similarly seeded at a density of 5 × 10^4 cells per scaffold, and cells were allowed to adhere for 24 h. Following the 24 h window, the medium was removed and replaced with culture medium containing D-peptide (2 mL, supplemented with 100 µM of the D-peptide) to induce release of the A-peptide. The D-peptide-containing medium was exchanged a total of two times, with exchanges at 1 h intervals, to facilitate displacement of coiled-RGD peptide. An incubation time of 1 h was allowed after the second treatment for a cumulative 3 h window. Following this release cycle, cells were fixed and treated for subsequent analysis.

2.4.10 Cell staining

For analysis of cell experiments, fibroblasts were fixed in a 10% (v/v) solution of neutral buffered formalin for 15 min before permeabilization with a 0.1% (v/v) Triton X-100/PBS solution for 10 min. Samples were then blocked by incubation in a 3% (w/v) BSA solution for at least 1 h to prevent nonspecific binding. F-actin was visualized by staining with Alexa Fluor-488-phalloidin (Thermofisher, 1 : 600 dilution) for at least 1 h and nuclei were visualized by staining with DAPI (ThermoFisher, 1 : 1 × 10^4 dilution) for 1 min. Samples were washed once with PBS, once with 0.1% (v/v) TWEEN-20 in PBS, and again in PBS after the staining steps to remove unbound fluorophore. All samples were protected from light and stored at 4 °C until imaging.

2.4.11 Imaging and image analysis

All imaging was conducted on a Leica DMi8 Widefield microscope. Coverslips with NorHA hydrogels or PEG-NB fibers were placed on microscope slides, sandwiched with a 25 × 25 mm coverslip, and inverted for imaging. Imaging settings (exposure time and light intensity) were held constant for all imaging where fluorescence intensities were compared across multiple samples. For imaging of hydrogels containing fluorescent peptides, three distinct photopatterned stripes per scaffold from three scaffolds were imaged for analysis. Images acquired with the 20× dry objective were used for intensity comparisons. To evaluate pattern fidelity, we plotted the normalized intensity line profiles across 3 stripes on each sample; all intensity profiles were normalized to the lowest intensity value corresponding to each representative image.

For cellular experiments, at least three distinct areas per scaffold for three hydrogel and three fibrous scaffolds were imaged for cell spread area analyses. A 40x dry objective was used for cell area measurements, while a 100x oil immersion objective was used to visualize F-actin formation.

2.4.12 Statistical analyses

For quantitative comparisons between two experimental groups, independent *t*-tests were used; for comparisons with more than two experimental groups, a one-way ANOVA was leveraged in conjunction with a Tukey HSD *post-hoc* test with an *α* value of 0.95 indicating statistical significance.

2.5 References

(1) Wade, R. J.; Burdick, J. A. Engineering ECM Signals into Biomaterials. *Mater. Today* **2012**, *15*, 454–459. https://doi.org/10.1016/S1369-7021(12)70197-9.

(2) Velasco-Hogan, A.; Xu, J.; Meyers, M. A. Additive Manufacturing as a Method to

Design and Optimize Bioinspired Structures. *Adv. Mater.* **2018**, *30* (52), e1800940. https://doi.org/10.1002/adma.201800940.

(3) Wade, R. J.; Bassin, E. J.; Gramlich, W. M.; Burdick, J. A. Nanofibrous Hydrogels with Spatially Patterned Biochemical Signals to Control Cell Behavior. *Adv. Mater.* **2015**, *27* (8), 1356–1362. https://doi.org/10.1002/adma.201404993.

(4) Baker, B. M.; Trappmann, B.; Wang, W. Y.; Sakar, M. S.; Kim, I. L.; Shenoy, V. B.; Burdick, J. A.; Chen, C. S. Cell-Mediated Fibre Recruitment Drives Extracellular Matrix Mechanosensing in Engineered Fibrillar Microenvironments. *Nat. Mater.* **2015**, *14* (12), 1282–1268. https://doi.org/10.1038/nmat4444.

(5) Davidson, C. D.; Wang, W. Y.; Zaimi, I.; Jayco, D. K. P.; Baker, B. M. Cell Force-Mediated Matrix Reorganization Underlies Multicellular Network Assembly. *Sci. Rep.* **2019**, *9* (1), 12. https://doi.org/10.1038/s41598-018-37044-1.

(6) Baker, B. M. Deconstructing the Third Dimension - How 3D Culture Microenvironments Alter Cellular Cues. *J. Cell Sci.* **2012**, *125* (13), 3015–3024. https://doi.org/10.1242/jcs.079509.

(7) Frantz, C.; Stewart, K. M.; Weaver, V. M. The Extracellular Matrix at a Glance. *J. Cell Sci.* **2010**, *123*, 4195–4200.

(8) Lutolf, M. P.; Hubbell, J. A. Synthetic Biomaterials as Instructive Extracellular Microenvironments for Morphogenesis in Tissue Engineering. *Nat. Biotechnol.* **2005**, *23* (1), 47–55. https://doi.org/10.1038/nbt1055.

(9) Wade, R. J.; Bassin, E. J.; Rodell, C. B.; Burdick, J. A. Protease-Degradable

Electrospun Fibrous Hydrogels. *Nat. Commun.* **2015**, *6*, 6639. https://doi.org/10.1038/ncomms7639.

(10) DeForest, C. A.; Anseth, K. S. Photoreversible Patterning of Biomolecules within Click-Based Hydrogels. *Angew. Chemie - Int. Ed.* **2012**, *51* (8), 1816–1819. https://doi.org/10.1002/anie.201106463.

(11) Grim, J. C.; Marozas, I. A.; Anseth, K. S. Thiol-Ene and Photo-Cleavage Chemistry for Controlled Presentation of Biomolecules in Hydrogels. *J. Control. Release* **2015**, *219*, 95–106. https://doi.org/10.1016/j.jconrel.2015.08.040.

(12) Stevens, M. M.; George, J. H. Exploring and Engineering the Cell Surface Interface. *Science (80-.).* **2005**, *310* (5751), 1135–1138. https://doi.org/10.1126/science.1106587.

(13) Caliari, S. R.; Burdick, J. A. A Practical Guide to Hydrogels for Cell Culture. *Nat. Methods* **2016**, *13* (5), 405–414. https://doi.org/10.1038/nmeth.3839.

(14) Anseth, K. S.; Tibbitt, M. W. Hydrogels as Extracellular Matrix Mimics for 3D Cell Culture. *Biotechnol. Bioeng.* **2009**, *103* (4), 655–663. https://doi.org/10.1002/bit.22361.

(15) Highley, C. B.; Prestwich, G. D.; Burdick, J. A. Recent Advances in Hyaluronic Acid Hydrogels for Biomedical Applications. *Curr. Opin. Biotechnol.* **2016**, *40*, 35–40. https://doi.org/10.1016/j.copbio.2016.02.008.

(16) Burdick, J. A.; Prestwich, G. D. Hyaluronic Acid Hydrogels for Biomedical Applications. *Adv. Mater.* **2011**, *23* (12), 41–56.

https://doi.org/10.1002/adma.201003963.

(17) Gramlich, W. M.; Kim, I. L.; Burdick, J. A. Synthesis and Orthogonal Photopatterning of Hyaluronic Acid Hydrogels with Thiol-Norbornene Chemistry. *Biomaterials* **2013**, *34* (38), 9803–9811. https://doi.org/10.1016/j.biomaterials.2013.08.089.

(18) Hui, E.; Gimeno, K. I.; Guan, G.; Caliari, S. R. Spatiotemporal Control of Viscoelasticity in Phototunable Hyaluronic Acid Hydrogels. *Biomacromolecules* **2019**, *20* (11), 4126–4134. https://doi.org/10.1021/acs.biomac.9b00965.

(19) Burdick, J. A.; Murphy, W. L. Moving from Static to Dynamic Complexity in Hydrogel Design. *Nat. Commun.* **2012**, *3*, 1269. https://doi.org/10.1038/ncomms2271.

(20) Hoyle, C. E.; Bowman, C. N. Thiol-Ene Click Chemistry. *Angew. Chemie - Int. Ed.* **2010**, *49* (9), 1540–1573. https://doi.org/10.1002/anie.200903924.

(21) Sharma, S.; Floren, M.; Ding, Y.; Stenmark, K. R.; Tan, W.; Bryant, S. J. A Photoclickable Peptide Microarray Platform for Facile and Rapid Screening of 3-D Tissue Microenvironments. *Biomaterials* **2017**, *143*, 17–28. https://doi.org/10.1016/j.biomaterials.2017.07.025.

(22) Tam, R. Y.; Smith, L. J.; Shoichet, M. S. Engineering Cellular Microenvironments with Photo- and Enzymatically Responsive Hydrogels: Toward Biomimetic 3D Cell Culture Models. *Acc. Chem. Res.* **2017**, *50* (4), 703–713. https://doi.org/10.1021/acs.accounts.6b00543.

(23) Fisher, S. A.; Tam, R. Y.; Fokina, A.; Mahmoodi, M. M.; Distefano, M. D.; Shoichet, M. S. Photo-Immobilized EGF Chemical Gradients Differentially Impact Breast Cancer Cell Invasion and Drug Response in Defined 3D Hydrogels. *Biomaterials* **2018**, *178*, 751–766. https://doi.org/10.1016/j.biomaterials.2018.01.032.

(24) Weng, G.; Bhalla, U. S.; Iyengar, R. Complexity in Biological Signaling Systems. *Science (80-.).* **1999**, *284* (5411), 92–96. https://doi.org/10.1126/science.284.5411.92.

(25) Fumasi, F. M.; Stephanopoulos, N.; Holloway, J. L. Reversible Control of Biomaterial Properties for Dynamically Tuning Cell Behavior. *J. Appl. Polym. Sci.* **2020**, *137* (25), 49058. https://doi.org/10.1002/app.49058.

(26) DeForest, C. A.; Tirrell, D. A. A Photoreversible Protein-Patterning Approach for Guiding Stem Cell Fate in Three-Dimensional Gels. *Nat. Mater.* **2015**, *14*, 523–531. https://doi.org/10.1038/nmat4219.

(27) Liu, L.; Tian, X.; Ma, Y.; Duan, Y.; Zhao, X.; Pan, G. A Versatile Dynamic Mussel-Inspired Biointerface: From Specific Cell Behavior Modulation to Selective Cell Isolation. *Angew. Chemie - Int. Ed.* **2018**, *57* (26), 7878–7882. https://doi.org/10.1002/anie.201804802.

(28) Mann, J. L.; Yu, A. C.; Agmon, G.; Appel, E. A. Supramolecular Polymeric Biomaterials. *Biomater. Sci.* **2018**, *6*, 10–37. https://doi.org/10.1039/C7BM00780A.

(29) Appel, E. A.; Biedermann, F.; Rauwald, U.; Jones, S. T.; Zayed, J. M.; Scherman,

O. A. Supramolecular Cross-Linked Networks via Host-Guest Complexation with Cucurbit[8]Uril. *J. Am. Chem. Soc.* **2010**, *132* (40), 14251–14260. https://doi.org/10.1021/ja106362w.

(30) Highley, C. B.; Rodell, C. B.; Burdick, J. A. Direct 3D Printing of Shear-Thinning Hydrogels into Self-Healing Hydrogels. *Adv. Mater.* **2015**, *27* (34), 5075–5079. https://doi.org/10.1002/adma.201501234.

(31) Boekhoven, J.; Pérez, C. M. R.; Sur, S.; Worthy, A.; Stupp, S. I. Dynamic Display of Bioactivity through Host-Guest Chemistry. *Angew. Chemie - Int. Ed.* **2013**, *52* (46), 12077–12080. https://doi.org/10.1002/anie.201306278.

(32) McNamara, S. L.; Brudno, Y.; Miller, A. B.; Ham, H. O.; Aizenberg, M.; Chaikof, E. L.; Mooney, D. J. Regenerating Antithrombotic Surfaces through Nucleic Acid Displacement. *ACS Biomater. Sci. Eng.* **2020**, *6* (4), 2159–2166. https://doi.org/10.1021/acsbiomaterials.0c00038.

(33) Freeman, R.; Stephanopoulos, N.; Álvarez, Z.; Lewis, J. A.; Sur, S.; Serrano, C. M.; Boekhoven, J.; Lee, S. S.; Stupp, S. I. Instructing Cells with Programmable Peptide DNA Hybrids. *Nat. Commun.* **2017**, *8*, 15982. https://doi.org/10.1038/ncomms15982.

(34) Freeman, R.; Han, M.; Álvarez, Z.; Lewis, J. A.; Wester, J. R.; Stephanopoulos, N.; McClendon, M. T.; Lynsky, C.; Godbe, J. M.; Sangji, H.; Luijten, E.; Stupp, S. I. Reversible Self-Assembly of Superstructured Networks. *Science (80-.).* **2018**, *362* (6416), 808–813. https://doi.org/10.1126/science.aat6141.

(35) Gröger, K.; Gavins, G.; Seitz, O. Strand Displacement in Coiled-Coil Structures:

Controlled Induction and Reversal of Proximity. *Angew. Chemie - Int. Ed.* **2017**, *56* (45), 14217–14221. https://doi.org/10.1002/anie.201705339.

(36) Lupas, A. N.; Gruber, M. The Structure of α-Helical Coiled Coils. *Adv. Protein Chem.* **2005**, *70* (04), 37–38. https://doi.org/10.1016/S0065-3233(05)70003-6.

(37) Litowski, J. R.; Hodges, R. S. Designing Heterodimeric Two-Stranded Alpha-Helical Coiled-Coils. *J. Biol. Chem.* **2002**, *277* (40), 37272–37279. https://doi.org/10.1074/jbc.M204257200.

(38) Litowski, J. R.; Hodges, R. S. Designing Heterodimeric Two-Stranded a -Helical Coiled-Coils : The Effect of Chain Length on Protein Folding , Stability and Specificity. *J. Pept. Res.* **2001**, *58*, 477–492.

(39) Archer, W. R.; Schulz, M. D. Isothermal Titration Calorimetry: Practical Approaches and Current Applications in Soft Matter. *Soft Matter* **2020**, *16*, 8760–8774. https://doi.org/10.1039/d0sm01345e.

(40) Kabiri, M.; Unsworth, L. D. Application of Isothermal Titration Calorimetry for Characterizing Thermodynamic Parameters of Biomolecular Interactions: Peptide Self-Assembly and Protein Adsorption Case Studies. *Biomacromolecules* **2014**, *15*, 3463–3473. https://doi.org/10.1021/bm5004515.

(41) De Crescenzo, G.; Litowski, J. R.; Hodges, R. S.; O'Connor-McCourt, M. D. Real-Time Monitoring of the Interactions of Two-Stranded de Novo Designed Coiled-Coils: Effect of Chain Length on the Kinetic and Thermodynamic Constants of Binding. *Biochemistry* **2003**, *42*, 1754–1763. https://doi.org/10.1021/bi0268450.

(42) Kabiri, M.; Bushnak, I.; McDermot, M. T.; Unsworth, L. D. Toward a Mechanistic Understanding of Ionic Self-Complementary Peptide Self-Assembly: Role of Water Molecules and Ions. *Biomacromolecules* **2013**, *14* (11), 3943–3950. https://doi.org/10.1021/bm401077b.

(43) Archer, W. R.; Fiorito, A.; Heinz-Kunert, S. L.; Macnicol, P. L.; Winn, S. A.; Schulz, M. D. Synthesis and Rare-Earth-Element Chelation Properties of Linear Poly(Ethylenimine Methylenephosphonate). *Macromolecules* **2020**, *53*, 2061–2068. https://doi.org/10.1021/acs.macromol.9b02472.

(44) Darby, S. J.; Platts, L.; Daniel, M. S.; Cowieson, A. J.; Falconer, R. J. An Isothermal Titration Calorimetry Study of Phytate Binding to Lysozyme: A Multisite Electrostatic Binding Reaction. *J. Therm. Anal. Calorim.* **2017**, *127* (2), 1201–1208. https://doi.org/10.1007/s10973-016-5487-6.

(45) Liang, H.; Lin, F.; Zhang, Z.; Liu, B.; Jiang, S.; Yuan, Q.; Liu, J. Multicopper Laccase Mimicking Nanozymes with Nucleotides as Ligands. *ACS Appl. Mater. Interfaces* **2017**, *9*, 1352–1360. https://doi.org/10.1021/acsami.6b15124.

Chapter 3. Designing coiled coils for heterochiral complexation to enhance binding and enzymatic stability

3.1 Introduction

In this chapter, we built upon our knowledge of the specific biomolecular interactions between coiled coils that we leveraged in Chapter 2 to explore stereochemistry-directed interactions in these coiled coil systems. This work represents an important advance bringing together the specific, complementary biomolecular interactions of coiled coils with the advantages in enzymatic stability and stronger binding interactions for stereochemistry-directed interactions.

Coiled coils are common helical structural motifs estimated to be found in approximately 10% of all eukaryotic proteins.[1,2] Specifically, coiled coils mediate interactions between proteins, operating, for example, in the regulation of DNA transcription and muscle contraction.[3,4] These functions are possible in complex biological environments as coiled coils have strong binding with a high degree of specificity.[4,5] Coiled coil specificity and affinity are derived from a combination of hydrophobic, electrostatic, and hydrogen bonding interactions, arising from conserved regions within coiled coil sequences. Typically, coiled coils are composed of repeating patterns of seven amino acids (*i.e.*, a heptad), labeled *abcdefg*, where amino acids in the *a* and *d* positions are hydrophobic and often those in the *e* and *g* positions are charged (**Figure 3.1A**).[3,6–9] While the strong affinity and high specificity of coiled coils make them attractive for use in biomaterials applications,[10–16] the lifetime of peptides *in vivo* is limited by poor enzymatic stability.[17–20]

One strategy to make peptide materials more stable is to alter stereochemistry, as D-amino acids resist degradation by enzymes.[21–25] While we could certainly improve the enzymatic stability of coiled coil biomaterials by making them entirely of D-amino acids, recent reports suggest that invoking stereochemistry-directed interactions between entirely L-peptides and entirely D-peptides gives rise to properties unique to those of naturally occurring L-peptides, including enhanced mechanics, stronger peptide-peptide interactions, and greater enzymatic stability. For example, 1:1 heterochiral blends of the D- and L-forms of the β-sheet forming peptide 'MAX1' result in hydrogels with a stiffness four times greater than those formed from homochiral D- or L-MAX1.[26,27] In another example, homochiral triple helices of the collagen-mimetic peptide $(PPG)_{10}$ are soluble but heterochiral mixtures precipitate, a result attributed to more favorable packing interactions for the heterochiral triple helices compared to homochiral.[28] Moreover, the enthalpy of interaction is stronger between heterochiral blends of peptides $Ac\text{-}(FKFK)_2\text{-}NH_2$ and Ac-(FEFE)2-NH2 as compared to homochiral peptide interactions.[29] With respect to enzymatic stability, the L-form of the peptide $Ac\text{-}(FKFE)_2\text{-}NH_2$ degrades within a day upon incubation with protease, while 1:1 blends of D- and L-$(FKFE)_2$ remain stable for at least 5 days, similar to the D-form of the peptide.[30] We sought to combine the enhanced interactions and enzymatic stability of heterochiral mixtures with the specific, strong binding of coiled coils into components of next-generation biomaterials.

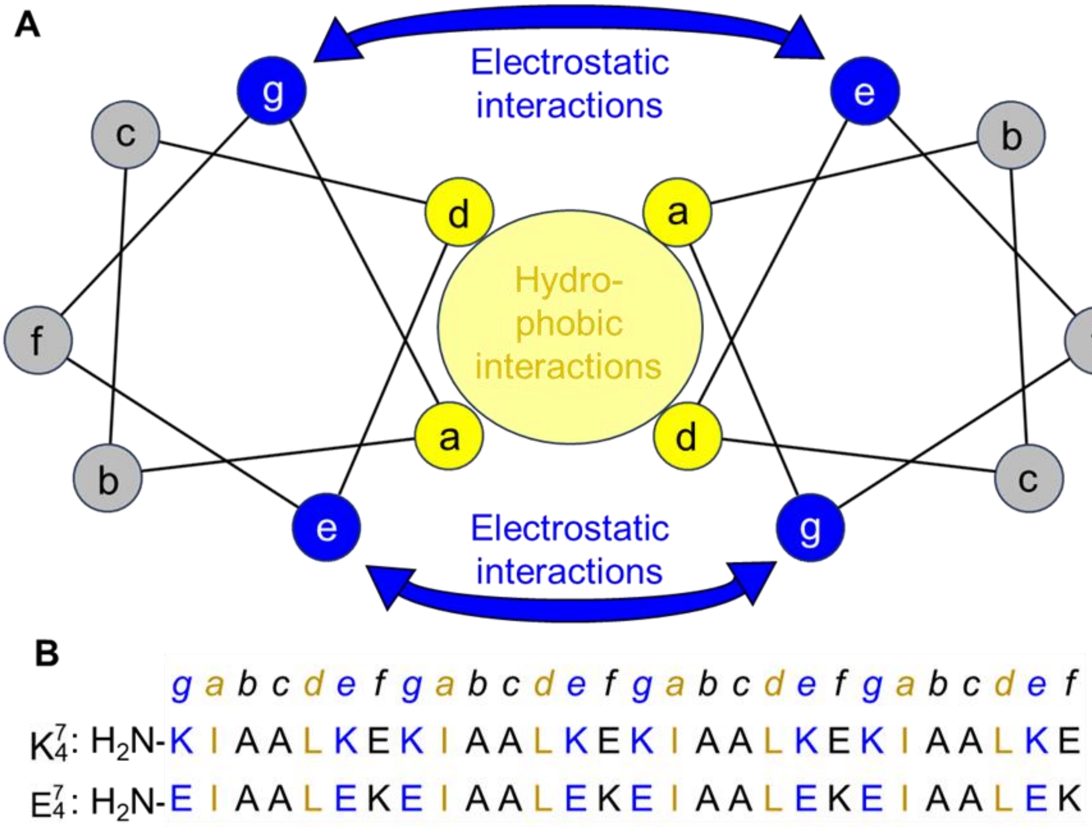

g a b c d e f g a b c d e f g a b c d e f g a b c d e f

K_4^7: H_2N-K I A A L K E K I A A L K E K I A A L K E K I A A L K E

E_4^7: H_2N-E I A A L E K E I A A L E K E I A A L E K E I A A L E K

Figure 3.1. (A) Helical wheel diagram of the heptad repeat abcdefg, with hydrophobic interactions between complementary coils highlighted in yellow and electrostatic interactions between complementary coils highlighted in blue. (B) Sequences of K_4^7 and E_4^7 aligned with the heptad abcdefg registry.

Interest in heterochiral assemblies of coiled coil peptides stems back to early structural considerations for proteins.[31,32] Reports include a tetramer formed from heterochiral heptads,[33] yet more recent work by Gellman and coworkers highlighted that heptads may not be the most ideal sequence pattern for heterochiral assembly. Crystal structures revealed that side chain interactions between hydrophobic residues on heterochiral peptides occurred in a repeating pattern of residues spaced 3, 4, and 4 residues apart, rather than with a 3 and 4 residue spacing typical of the heptad repeating structure. The 3,4,4 spacing is consistent with a noncanonical repeating sequence pattern of eleven amino acids (*i.e.*, a hendecad), labeled *abcdefghijk*, where the hydrophobic amino acids are in positions *a*, *d*, and *h*.[34,35] In this case, the hendecad structure is preferred because coiled coils of opposing stereochemistry are unable to supercoil, a correction which aligns the hydrophobic faces of the coiled coils in conventional homochiral heptads. Rather, the hydrophobic faces of hendecads align without a need for supercoiling, making them amenable to any combination of stereochemistry. While these reports provide a good basis for the structural considerations of heterochiral coiled coils, the potentially unique properties of the resulting heterochiral complexes have not yet been studied.

Here, we redesign the complementary glutamic acid/lysine (E/K)-rich coiled coil sequences (**Figure 3.1B**) ubiquitously employed as components in previously reported biomaterials[10,13,14] to promote heterochiral complexation and compare the intermolecular interactions and enzymatic stability of the resulting complexes to those of analogous homochiral coiled coils. We found that, to allow for heterochiral complexation and the possibility of accessing unique heterochiral blend properties, we needed to redesign the original heptad repeat sequences of the E/K coils as hendecad repeat sequences. The heterochiral hendecad repeat complexes exhibit higher binding strength and greater enzymatic stability than analogous all L hendecad complexes. Unlocking the benefits of stereochemistry-directed interactions in widely used biomaterial motifs such as coiled coils has the potential to greatly extend the lifetime of and tailor intermolecular interactions for next-generation materials.

3.2 Results and discussion

Here we investigate the effects of stereochemistry-driven interactions on the affinity and stability of coiled coil complexes. Using isothermal titration calorimetry and high performance liquid chromatography-based enzymatic stability measurements, we compare the affinities and enzymatic stabilities of analogous homochiral and heterochiral coiled coils composed of either repeating heptads or hendecads. This study demonstrates the advantages of heterochiral coiled coil complexes and provides a template for modifying existing heptad coiled coils to accommodate heterochiral coiled coil formation.

3.2.1. Heptad coiled coil formation: homochiral vs. heterochiral

The anion-rich coiled coil (EIAALEK)$_n$ (E_n^7, where n is the number of heptad repeats and the 7 superscript indicates a heptad repeat) and cation-rich coiled coil (KIAALKE)$_n$ (K_n^7) are known to form homochiral complexes when n≥3.[14] The secondary structure of these coiled coils was confirmed to be α-helical by circular dichroism (CD) spectroscopy (**Figure B27**). We used isothermal titration calorimetry (ITC), a label-free, solution-based technique used to study interactions between biomolecules,[36] to assess the thermodynamics of heptad coiled coil complex formation. The homochiral titration of L-K_4^7: L-E_4^7 in 1X PBS at pH 7.4 results in heats of interaction that are initially exothermic (with a maximum binding heat of -98 ± 4 kJ/mol) until reaching a molar ratio of ~0.8:1 L-K_4^7: L-E_4^7, after which endothermic heats of interaction (with a maximum of binding heat of 63 ± 0.6 kJ/mol) are observed (**Figure 3.2A**). This may indicate that coiled coil interactions are initially exothermic due to enthalpically favorable electrostatic interactions between complementary coils, but as binding partners are consumed, molecular rearrangements which result in the endothermic (entropically-favorable) release of ordered water molecules dominate the heats of interaction.[37–39] These thermograms were reproducible (**Figure B21**), yet did not fit well to single-site or multisite binding models that would allow us to obtain a binding constant to compare to other pairs. The 1:1 mixture of L-K_4^7 and L-E_4^7 yields blends that are also helical, having a stronger helical CD signal than the individual coiled coils (**Figure B28A**). In contrast to the homochiral titration, the heterochiral titration of D-K_4^7 (designed by simply switching the chirality of all amino acids in the peptide from L to D) into L-E_4^7 produces only endothermic binding heats smaller in magnitude (having a maximum binding heat of 48 ± 0.3 kJ/mol) than the corresponding homochiral pair (**Figure 3.2B**). This finding may indicate that interactions between the heterochiral heptad coils are dominated by endothermic hydrophobic interactions, with little contribution from electrostatic interactions. To test this, we repeated the homochiral titration of L-K_4^7 into L-E_4^7 in 10X PBS, where we expected the excess salt to screen electrostatic interactions. Supporting our hypothesis, we found the heats of interaction in 10X PBS to be endothermic in contrast to the exothermic and endothermic heats of interaction that we observed in 1X PBS (**Figure 3.2C**). Additionally, the CD signal of the 1:1 mixture of D-K_4^7 into L-E_4^7 is very close to zero at all wavelengths between 200 nm and 250 nm, indicating that the CD is simply the sum of the equimolar D- and L-coils (**Figure B28C**). Together, these findings indicate that simply inverting the stereochemistry of one peptide in heptad-based coiled coils disrupts complex formation to some degree, ablating any potential for stronger interactions in heterochiral complexes compared to homochiral complexes in this heptad configuration, which is consistent with previous reports of non-ideality for heterochiral complexation of heptad-based coiled coils.

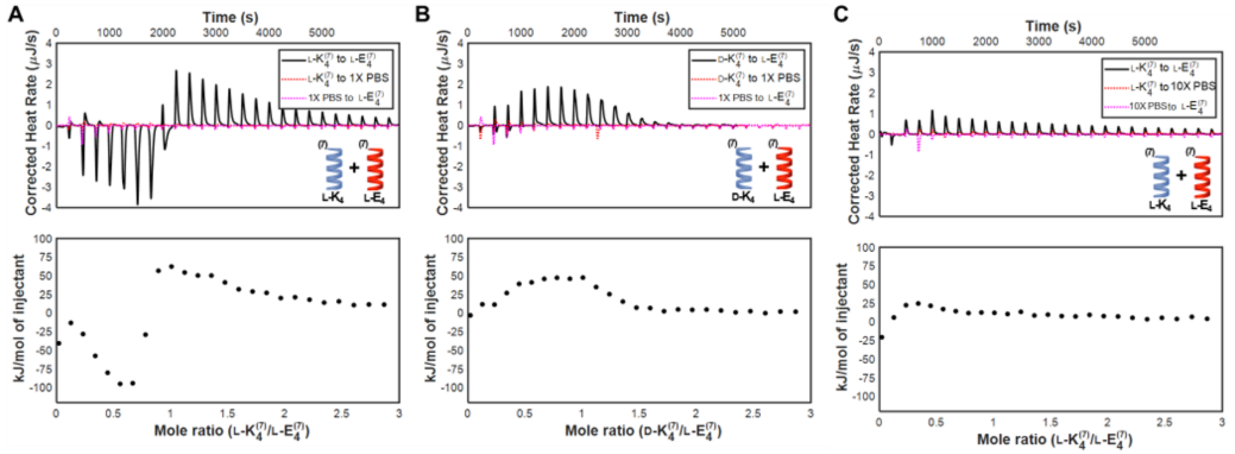

Figure 3.2. Thermograms and integrated binding heats of: (a) homochiral heptad coiled coils L-K$_4^7$ and L-E$_4^7$ in 1X PBS; (b) heterochiral heptad coiled coils D-K$_4^7$ and L-E$_4^7$ in 1X PBS; and (c) homochiral heptad coiled coils L-K$_4^7$ and L-E$_4^7$ in 10X PBS. While both exothermic and endothermic binding heats are observed for interactions between homochiral coils in 1X PBS, only endothermic binding heats are observed for interactions between heterochiral coils in 1X PBS and interactions between homochiral coils in 10X PBS.

3.2.2. Enzymatic degradation of heptad coiled coils

While we did not observe stronger binding for heterochiral heptads, knowing that stereochemistry-driven interactions are expected to provide both binding strength and enzymatic stability advantages, we next examined whether these heptads would exhibit more enzymatic stability in a heterochiral mixture compared to homochiral. Solutions of K$_4^7$ and E$_4^7$ (200 µM in 1X PBS at pH 7.4) were blended as homochiral (L-K$_4^7$: L-E$_4^7$) or heterochiral (D-K$_4^7$: L-E$_4^7$) mixtures. These blends were then incubated with 5 µg/mL Proteinase K, an enzyme known for its broad-spectrum activity and expected to cleave after the I, A, L, and E residues of these peptides. Immediately after adding Proteinase K, as well as after 1, 3, 6, 12, and 24 h incubations, we used high performance liquid chromatography (HPLC) to monitor the degradation of the coiled coils. In the HPLC eluent (low pH and in the presence of an organic solvent, acetonitrile), the coiled coil complex does not remain bound, resulting in two peaks corresponding to intact, K_4^7 (eluting at 5.7 min) and intact E_4^7 (eluting at 6.9 min). In the absence of Proteinase K, K_4^7 and E_4^7 exhibit little to no degradation over 24 h in the homochiral or heterochiral blends (**Figure B31**). In the presence of Proteinase K, we observe that ~50% of the coiled coils degrade after 6 h and none of the intact coiled coils remain after just 24 h (**Figure 3.3A**). For the heterochiral blend, the D-K_4^7 coil experiences little to no degradation, as expected. However, the L-E_4^7 coil in the heterochiral complex degrades more rapidly than it did in the homochiral complex, as the peak at 6.9 min disappears completely within 12 h (**Figure 3.3B**). This is consistent with the lower heats of binding that we observe in heterochiral heptads, as the L-coil in the homochiral complex is better protected from the protease, perhaps due to shielding from the complex. The mere presence of a D-peptide in the material is insufficient to slow enzymatic degradation. These results further motivated us to design coiled coils with a hendecad repeating pattern and repeat these experiments.

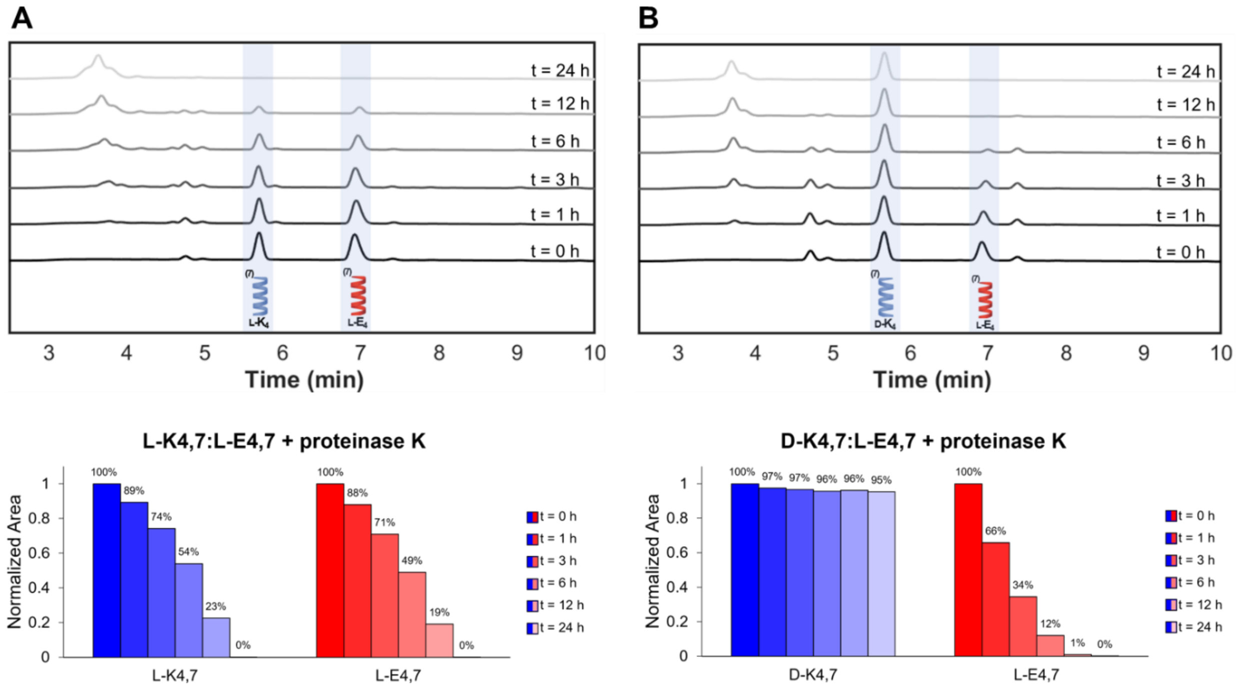

Figure 3.3. Enzymatic stability of heptad coiled coils in the presence of 5 µg/mL Proteinase K. HPLC chromatograms and percent intact K_4^7 and E_4^7 by peak area immediately after addition of and upon incubation for 1, 3, 6, 12, and 24 h with Proteinase K in A) a homochiral blend and B) a heterochiral blend.

3.2.3. Design of hendecad coiled coils

From Gellman and coworkers' work, we know that a hendecad repeating structure (*abcdefghijk*), where *a*, *d*, and *h* are hydrophobic residues, is favorable for heterochiral coil formation.[34,35] To assist with the redesign of the heptad coiled coils to a repeating hendecad structure based on E_n^7 and K_n^7, we employed helical wheel diagrams to visualize potential sequences. We observed that, as expected, the hydrophobic residues in the *a* and *d* positions of the heptad are gathered on one face of the helix, with charged residues, in the case of K_4^7, cationic residues specifically, flanking on either side (**Figure 3.4A**). With this knowledge, we used the same amino acids from K_n^7 to design a coiled coil with hendecad repeat structure. We first placed isoleucines and leucines in the *a*, *d*, and *h* positions, then cationic lysine residues in the *e*, *g*, and *k* positions to place them on either side of the hydrophobic face of the helix (**Figure 3.4B**), matching the placement of amino acids around the helix that we observed in the heptad repeat structure. The *b*, *c*, *i*, and *j* positions were filled with alanines, similar to the heptad structure, and the *f* position was filled with glutamic acid, serving the same role as in the heptad to provide solubility while being on the opposite side from the interacting face of the helix. For the E-rich hendecad, we used the same sequence except with all lysines exchanged for glutamic acids and vice versa. Using this newly designed hendecad-based coiled coil sequence, we again investigated complex formation and enzymatic stability of homochiral and heterochiral coils.

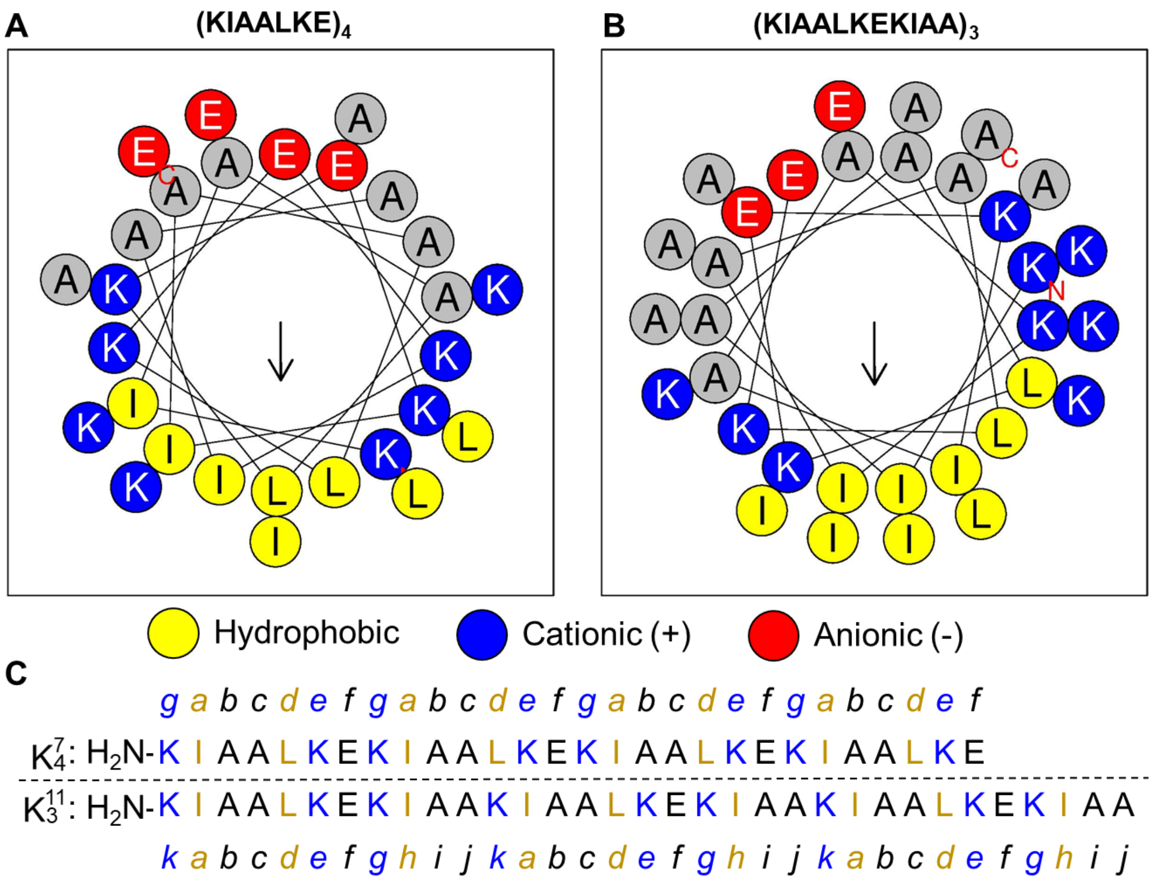

Figure 3.4. Helical wheel diagrams of: (A) K_4^7; and (B) K_3^{11}. Helical wheels generated using HeliQuest (*https://heliquest.ipmc.cnrs.fr/*). (C) Sequences of K_4^7 and K_3^{11} aligned with the heptad abcdefg and hendecad abcdefghijk registers.

3.2.4. Hendecad coiled coil formation: homochiral vs. heterochiral

To elucidate whether the change from a heptad to a hendecad repeating structure affords stronger heterochiral complex affinity compared to homochiral, we examined hendecad complex formation using ITC. We investigated hendecad coiled coils with a length of three repeats (K_3^{11} and E_3^{11}) as they have a similar number of amino acids to the heptad coiled coils we used previously (33 amino acids for three repeats of the hendecad and 28 amino acids for four repeats of the heptad). First, we confirmed the helical secondary structure of these newly designed hendecad coiled coils using CD spectroscopy (**Figure B27B**). The homochiral titration of L-K_3^{11} into L-E_3^{11} in 1X PBS at pH 7.4 results in an interaction that is initially exothermic (with a maximum binding heat of --46 ± 8 kJ/mol) and becomes endothermic (with a maximum binding heat of 26 ± 1 kJ/mol) at a molar ratio of ~0.5 L-K_3^{11}: L-E_3^{11} (**Figure 3.5A**), similar to the profile observed for the homochiral interaction of the heptad coils L-K_4^7 and L-E_4^7. The binding heats then trend to zero (after subtracting the dilution heats of injectant into buffer and buffer into titrand) for all molar ratios > 1.6 L-K_3^{11}: L-E_3^{11}, indicating no further interaction. Blending these coiled coils at a 1:1 ratio yields a mixture with a stronger α-helical signal by CD spectroscopy than either individual coiled coil (**Figure B28B**). The heterochiral titration also begins with exothermic binding heats that become endothermic, but this titration has a second exothermically dominated domain at molar ratios > 1.2 D-K_3^{11}: L-E_3^{11} and the binding heats don't trend to zero until molar ratios > 2.5 D-K_3^{11}: L-E_3^{11} (**Figure 3.5B**). While the maximum exothermic binding heats for the homochiral titration and the two exothermic domains of the heterochiral interaction are similar in magnitude (-46 ± 8 kJ/mol for the homochiral interaction and -46 ± 1 kJ/mol and -44 ± 0.7 kJ/mol for the first and second exothermic domains of the heterochiral interaction), the maximum endothermic binding heats for the heterochiral interaction are much greater than the homochiral interaction (26 ± 0.7 kJ/mol for the homochiral titration and 88 ± 5 kJ/mol for the heterochiral titration). This indicates a stronger binding affinity for the heterochiral interaction of these hendecad coiled coils that mirrors what has been previously reported for Ac-$(FKFE)_2$.[29] Similarly to heterochiral heptad coiled coils, the CD signal for 1:1 D-K_3^{11}: L-E_3^{11} (**Figure B28D**) is close to zero for the wavelength range from 200 nm to 250 nm, due to opposing stereochemistries of the equimolar blend of peptides.

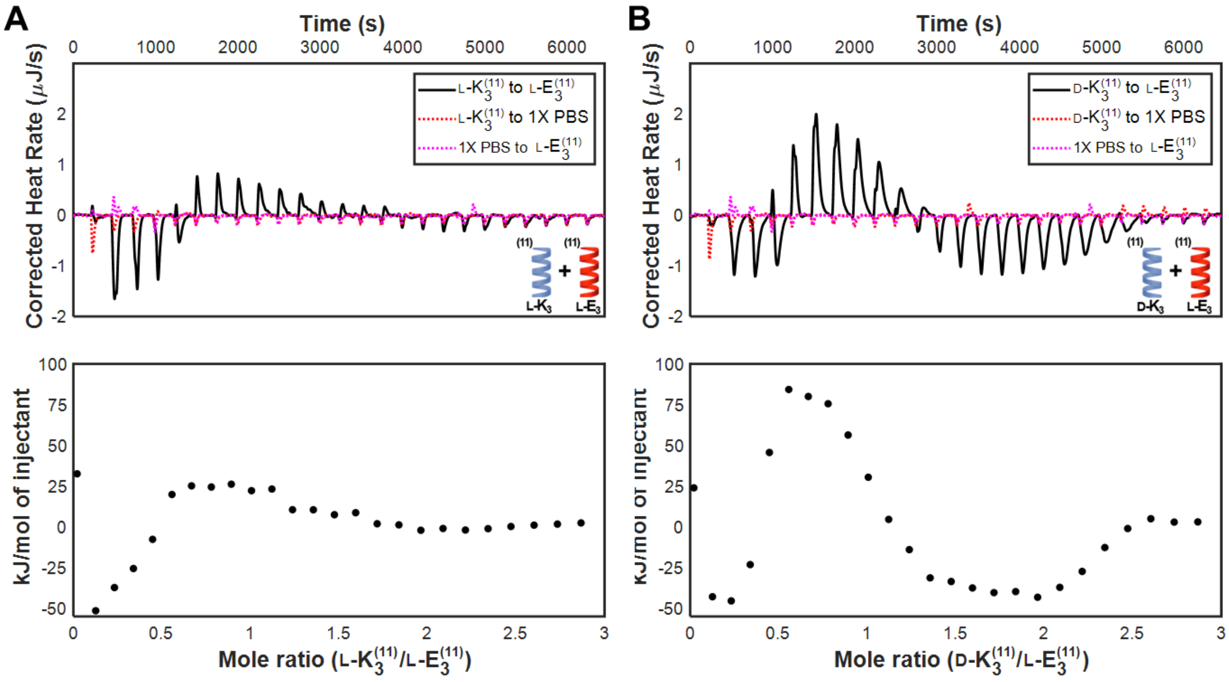

Figure 3.5. Thermograms and integrated binding heats of: (a) homochiral hendecad coiled coils L-K_3^{11} and L-E_3^{11} in 1X PBS; and (b) heterochiral hendecad coiled coils D-K_3^{11} and L-E_3^{11} in 1X PBS. Larger heats of interaction are observed for the heterochiral complex than for the homochiral complex.

3.2.5. Enzymatic degradation of hendecad coiled coils

Encouraged by the stronger binding affinity we observed for heterochiral hendecad coiled coils compared to homochiral, we next investigated the enzymatic stability of our designed hendecad coiled coils. We incubated solutions of homochiral (L-K_3^{11}: L-E_3^{11}) or heterochiral (D-K_3^{11}: L-E_3^{11}) hendecad coiled coils with 5 µg/mL Proteinase K as we did for the heptad coiled coils (200 µM each in 1X PBS at pH 7.4). Similar to the heptad coiled coils, the hendecad coiled coils elute as two separate peaks, one for K_3^{11} (eluting at 5.9

min) and one for E_3^{11} (eluting at 7.9 min). When incubated in buffer alone without Proteinase K, both the homochiral and heterochiral complexes remain stable over 30 h (**Figure B32**). In the presence of Proteinase K, both L-K_3^{11} and L-E_3^{11} in the homochiral complex degrade completely in under 6 h, with only 11% and 7% of the peak area for each, respectively, remaining after 3 h (**Figure 3.6A**). On the other hand, 44% of the L-E_3^{11} in the heterochiral complex remains after 30 h of incubation (**Figure 3.6B**), and we found that even after 7 days of incubation, L-E_3^{11} did not completely degrade as 23% of the peptide still remains (**Figure B33**). As expected, the D-K_3^{11} in the heterochiral complex remains largely stable over the 30 h incubation with Proteinase K. These results demonstrate that forming a heterochiral complex using our designed hendecad coiled coils is an effective strategy to protect a coiled coil in the natural L stereochemistry from degradation.

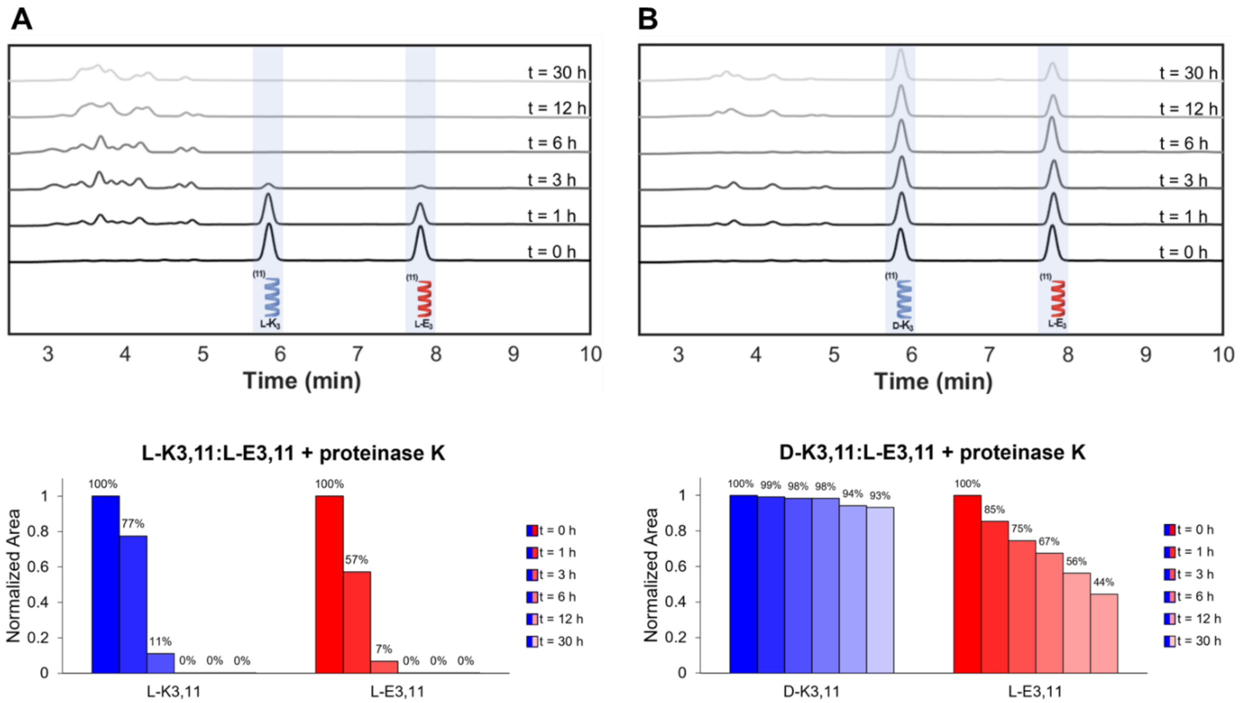

Figure 3.6. Enzymatic stability of hendecad coiled coils in the presence of 5 μg/mL Proteinase K. HPLC chromatograms and percent intact K_3^{11} and E_3^{11} by peak area immediately after addition of and upon incubation for 1, 3, 6, 12, and 30 h with Proteinase K in A) a homochiral blend and B) a heterochiral blend.

3.3 Conclusions

This work highlights that peptides can be rationally designed to undergo heterochiral interactions and thereby unlock a larger range of binding affinities and better control over enzymatic stability. Experiments with coiled coils featuring the canonical heptad repeat pattern reveal that they bind stronger as homochiral compared to heterochiral mixtures, but with limited enzymatic stability. Redesigning these heptad coiled coils into noncanonical hendecad repeat patterns enables complexation from both homochiral and heterochiral mixtures, with greater binding strength and enzymatic stability observed for the latter. The consistency between the binding heats observed in ITC and the enzymatic degradation profiles from HPLC throughout the manuscript corroborated the ITC results we observed despite not fitting the ITC data to binding models. We observed that, in cases where the binding heats for one complex were smaller than another, the L-peptides in that complex degraded more quickly in the presence of enzyme, suggesting that such enzymatic stability measurements are a useful tool to assess intermolecular interactions. Going forward, while the design rules for homochiral coiled coils with heptad repeating patterns are relatively well known, continuing to correlate peptide sequence design in both homochiral and heterochiral mixtures of hendecad coiled coils to properties of the resulting complexes will provide important insights that enrich our molecular toolkit for engineering tunable materials.

3.4 Materials and methods

3.4.1. Materials

Phosphate-buffered saline (PBS) pellets, sodium hydroxide (NaOH, 97%) pellets, acetonitrile (HPLC grade), trifluoracetic acid (TFA, 99%), dimethyl sulfoxide (99.9%), hydrochloric acid (37 wt%), dimethylformamide (DMF, ≥99.8%), diethyl ether (≥99.0%, contains butylated hydroxytoluene as inhibitor), triisopropylsilane (98%), piperidine (≥99%), 2,2′-(ethylenedioxy)diethanethiol (95%), diisopropyl carbodiimde (99%), and Proteinase K (from Tritirachium album) were purchased from Sigma-Aldrich. Ultrapure water (18.2 MΩ cm) was obtained from a Thermo Scientific Smart2Pure water purification system. All chemicals were used without further purification. We note that each PBS pellet, when dissolved in 200 mL of DI water yields 1X PBS (137 mM NaCl, 2.7 mM KCl, 10 mM Na_2HPO_4, 1.8 mM KH_2PO_4). To prepare 10X PBS, we dissolved each PBS pellet in 20 mL of DI water.

3.4.2. Coiled coil synthesis

Coiled coils were synthesized in-house using a CEM Corporation Liberty Blue automated, microwave-assisted solid phase peptide synthesizer via Fmoc methods on Rink amide resin SS (0.5 mmol/g substitution, 100-200 mesh, 1% divinylbenzene, Advanced ChemTech). All syntheses began with swelling the resin in dimethylformamide (DMF) then two "dummy" coupling steps, where DMF is added to the reaction vessel alone and is heated to 90 °C like a normal coupling method. These "dummy" coupling steps serve to allow the instrument to fully warm up and consistently hit the target temperature before starting the synthesis. Fmoc-protected amino acids (Fmoc-Lys(Boc)-OH, Fmoc-Ile-OH, Fmoc-Leu-OH, Fmoc-Ala-OH, and Fmoc-Glu(OBut)-OH) were used to grow the amino acid chain. Fmoc protecting group removal was performed using 20% (v/v) piperdine in DMF and coupling reactions were performed with amino acids in the presence of the coupling agents diisopropylcarbodiimide (1 M in DMF) and Oxyma Pure (1 M in DMF) at 90 °C for 2 min. The Fmoc removal and amino acid coupling steps were repeated to build the peptide from C-terminus to N-terminus. The peptides were cleaved from the resin and side chain protecting groups (Boc and OBut) were removed via a 3 h, room temperature reaction in a cleavage cocktail containing 92.5% (v/v) trifluoroacetic acid, 2.5% triisopropylsilane, 2.5% 2,2'- (ethylenedioxy)diethanethiol, and 2.5% water purified by reverse osmosis (RO water). The peptides were precipitated in cold ether and centrifuged (4816 x g for 5 min at 4 °C) to isolate a peptide pellet. The peptide pellets were washed once more in cold ether and centrifuged under the same conditions to re-isolate peptide pellets. The pellets were dried under vacuum for 45 min before being suspended in RO water, frozen in liquid nitrogen, lyophilized, and stored as powders at -20 °C.

3.4.3. Analytical-scale high performance liquid chromatography (HPLC)

Peptide samples were dissolved at 1-2 mg/mL in HPLC solvent (95% ultrapure water + 0.1% TFA, 5% acetonitrile + 0.1% TFA) and filtered through 13 mm syringe filters with 0.45 µm polytetrafluoroethylene membranes (VWR) into 2 mL vials. HPLC was performed on a Waters Alliance e2695 HPLC system with a 2998 photodiode array detector with separation achieved using an XBridge C18 reverse-phase column (4.6 x 75 mm, 3.5 µm particle size). For crude and purified peptide samples, a 1 mL/min linear gradient from 5-95% (v/v) acetonitrile in water + 0.1% TFA over 9 min was employed to elute the peptides from the column operating at 35 °C. The only exceptions were l-E$_4^7$ and d-E$_4^7$, which were eluted on a 1 mL/min gradient from 5-62% (v/v) acetonitrile in water + 0.1% TFA over 17 min to better separate the peaks. Elution was monitored by absorbance at 214 nm.

3.4.4. Peptide purification by preparative-scale high performance liquid chromatography (HPLC)

To purify peptides, 30-40 mg of peptide was dissolved in 10 mL of HPLC solvent (95% ultrapure water + 0.1% TFA, 5% acetonitrile + 0.1% TFA) and twice filtered through 25 mm syringe filters with 0.45 µm polytetrafluoroethylene membranes. The filtered solution was loaded into the injection loop of a Waters 2545 HPLC system with an attached 2489 photodiode array detector and Waters Fraction Collector III collection system. The sample was separated on an XBridge C18 reverse-phase column (30 x 150 mm, 5 μm particle size). The gradients used to achieve separation are listed in Table B1. Eluent was collected in 13 x 100 mm glass culture tubes (VWR) and the fractions of eluent that eluted from the desired product peak were combined and lyophilized. The lyophilized powders were used to obtain HPLC chromatograms and mass spectra of purified peptides and then were stored as powders at -20 °C.

3.4.5. Matrix-assisted laser desorption/ionization (MALDI) time-of-flight (TOF) mass spectrometry

MALDI-TOF mass spectrometry was used to verify the mass of the purified peptides. Samples were prepared at ~1 mg/mL in RO water. These samples were mixed 1:1 with a solution of cyano-4-hydroxycinnamic acid (CHCA) matrix prepared in 70% (v/v) acetonitrile in water + 0.1% TFA (2 μL of sample + 2 μL of CHCA solution) by pipetting up and down 6 times. Upon mixing, a 2 μL aliquot was pipetted onto a FlexiMass SR48 target plate (Shimadzu) and left at room temperature to dry. MALDI-TOF was performed on a Shimadzu 8030 MALDI-TOF using MALDI TOFMix (LaserBio Labs) as a calibrant.

3.4.6. Isothermal titration calorimetry

ITC experiments were performed on a standard volume Affinity ITC (TA Instruments). All peptide solutions were prepared at 200 μM in 1X or 10X PBS, pH corrected to 7.40 ± 0.05 by adding 1-5 μL of 1 M NaOH and degassed for 5-10 min using a TA Instruments degassing station at 400 mm Hg. The solution to be loaded into the syringe (the titrant) was used as prepared, whereas the solution to be loaded into the sample cell (the titrand) was diluted to 20 μM by adding 9 μL of 1X or 10X PBS to 1 μL of 200 μM sample. The pH of the 20 μM sample was checked and always found to be within pH 7.40 ± 0.05. The titrant and titrand pH were always checked to ensure they were with pH 7.40 ± 0.05 immediately prior to experiments to avoid substantial heat contributions from the heat of mixing of solutions with different pH. The 20 μM sample was also degassed before use. Titrations consisted of an initial 2 μL injection followed by 24 10 μL injections of 200 μM titrant solution injected into 1.3 mL of 20 μM titrand solution. Following an initial delay of 200 s, injections were separated by 250 s, unless otherwise noted. Experiments were performed at 25 °C with a stirring rate of 125 rpm. The reference cell was filled with 1.3 mL of degassed, deionized water that is exchanged weekly. The resulting thermograms were baseline-subtracted and heats of binding were obtained by integrating the area under each injection peak using NanoAnalyze (TA Instruments). The obtained heats of binding were then divided by moles of injectant. Heats of dilution (titrations of titrant into buffer and buffer into titrand) were analyzed similarly, and the molar heats of dilution were subtracted from the molar heats of binding to yield the final plots of kJ/mol of injectant vs. mole ratio for each titration. Reported values for maximum exothermic and endothermic heats of interaction are the average of two separate experiments, with standard deviation reported.

3.4.7. Coiled coil degradation

Degradation was monitored by HPLC. Solutions of individual coiled coils were prepared at 200 µM in 1X PBS and pH corrected to 7.40 ± 0.05 using 1-15 µL of 1 M NaOH. A stock solution of Proteinase K enzyme was prepared at 0.5 mg/mL. For each pair of peptides, 1.5 mL of each 200 µM solution was mixed, then 30 µL of 0.5 mg/mL Proteinase K was added to the 3 mL total mixed solution to obtain a final concentration of 5 µg/mL Proteinase K. Each degradation solution was stirred at 250 rpm for the duration of the experiment. For each timepoint, a 1 mL aliquot of degradation solution was added to an HPLC vial, a 100 µL injection was performed on HPLC, and the remaining 900 µL was returned to the bulk degradation solution. To normalize for slight shifts in elution time due to changing solvent or environmental conditions, a MATLAB script (included in SI) was used to align all K_4^7 (for heptad degradation) or K_3^{11} (for hendecad degradation) peaks to the same elution time as the elution at t = 0 h.

3.4.8. Circular dichroism (CD) spectroscopy

To confirm coiled coil stereochemistry and secondary structure, we measured CD spectra for individual and mixtures of coiled coils. Unless otherwise noted, samples were prepared at 100 µM in 1X PBS (pH 7.4). For measurement of coiled coil complexes, individual coiled coils were prepared at 200 µM in 1X PBS, then mixed in equal volumes. Measurements were performed on a Jasco J-1500 CD spectrophotometer at 20 °C using a 1 mm path length quartz cuvette from 250 nm to 200 nm at a scanning speed of 50 nm/min. In Section 4.1, we provide details on how we optimized these conditions. For temperature-dependent studies, spectra were taken at 5 °C intervals from 5 °C to 95 °C using a heating rate of 5 °C/min.

3.5 References

(1) Liu, J.; Rost, B. Comparing Function and Structure between Entire Proteomes. *Protein Sci.* **2001**, *10*, 1970–1979. https://doi.org/10.1110/ps.10101.

(2) Rackham, O. J. L.; Madera, M.; Armstrong, C. T.; Vincent, T. L.; Woolfson, D. N.; Gough, J. The Evolution and Structure Prediction of Coiled Coils across All Genomes. *J. Mol. Biol.* **2010**, *403*, 480–493. https://doi.org/10.1016/j.jmb.2010.08.032.

(3) Lupas, A. N.; Gruber, M. The Structure of α-Helical Coiled Coils. *Adv. Protein Chem.* **2005**, *70* (04), 37–38. https://doi.org/10.1016/S0065-3233(05)70003-6.

(4) Marsden, H. R.; Kros, A. Coiled Coils Self-Assembly of Coiled Coils in Synthetic Biology : Inspiration and Progress. *Angew. Chemie* **2010**, *49*, 2988–3005. https://doi.org/10.1002/anie.200904943.

(5) Truebestein, L.; Leonard, T. A. Coiled-Coils: The Long and Short of It. *BioEssays* **2016**, *38*, 903–916. https://doi.org/10.1002/bies.201600062.

(6) Lupas, A. N.; Bassler, J.; Dunin-Horkawicz, S. The Structure and Topology of α-Helical Coiled Coils. In *Fibrous Proteins: Structures and Mechanisms*; Parry, D. A. D., Squire, J. M., Eds.; Springer Chem, 2017; Vol. 82, pp 95–129. https://doi.org/10.1007/978-3-319-49674-0_4.

(7) Cohen, C.; Parry, D. A. D. A-Helical Coiled Coils and Bundles: How to Design an

A-helical Protein. *Proteins Struct. Funct. Genet.* **1990**, *7*, 1–15. https://doi.org/10.1002/prot.340070102.

(8) Woolfson, D. N. THE DESIGN OF COILED-COIL STRUCTURES AND ASSEMBLIES. *Adv. Protein Chem.* **2005**, *70* (04), 79–112. https://doi.org/10.1016/S0065-3233(04)70004-2.

(9) Mason, J. M.; Arndt, K. M. Coiled Coil Domains: Stability, Specificity, and Biological Implications. *ChemBioChem* **2004**, *5*, 170–176. https://doi.org/10.1002/cbic.200300781.

(10) Wu, Y.; Collier, J. H. α-Helical Coiled-Coil Peptide Materials for Biomedical Applications. *Wiley Interdiscip. Rev. Nanomedicine Nanobiotechnology* **2017**, *9* (2), 1–17. https://doi.org/10.1002/wnan.1424.

(11) Grewal, M. G.; Gray, V. P.; Letteri, R. A.; Highley, C. B. User-Defined, Temporal Presentation of Bioactive Molecules on Hydrogel Substrates Using Supramolecular Coiled Coil Complexes. *Biomater. Sci.* **2021**, *9* (12), 4374–4387. https://doi.org/10.1039/d1bm00016k.

(12) Jing, P.; Rudra, J. S.; Herr, A. B.; Collier, J. H. Self-Assembling Peptide-Polymer Hydrogels Designed from the Coiled Coil Region of Fibrin. *Biomacromolecules* **2008**, *9* (9), 2438–2446. https://doi.org/10.1021/bm800459v.

(13) Apostolovic, B.; Danial, M.; Klok, H. A. Coiled Coils: Attractive Protein Folding Motifs for the Fabrication of Self-Assembled, Responsive and Bioactive Materials. *Chem. Soc. Rev.* **2010**, *39* (9), 3541–3575. https://doi.org/10.1039/b914339b.

(14) Litowski, J. R.; Hodges, R. S. Designing Heterodimeric Two-Stranded Alpha-Helical Coiled-Coils. *J. Biol. Chem.* **2002**, *277* (40), 37272–37279. https://doi.org/10.1074/jbc.M204257200.

(15) Wu, D.; Sinha, N.; Lee, J.; Sutherland, B. P.; Halaszynski, N. I.; Tian, Y.; Caplan, J.; Zhang, H. V.; Saven, J. G.; Kloxin, C. J.; Pochan, D. J. Polymers with Controlled Assembly and Rigidity Made with Click-Functional Peptide Bundles. *Nature* **2019**, *574*, 658–662. https://doi.org/10.1038/s41586-019-1683-4.

(16) Paloni, J. M.; Olsen, B. D. Coiled-Coil Domains for Self-Assembly and Sensitivity Enhancement of Protein-Polymer Conjugate Biosensors. *ACS Appl. Polym. Mater.* **2020**, *2*, 1114–1123. https://doi.org/10.1021/acsapm.9b01061.

(17) Huet, T.; Kerbarh, O.; Schols, D.; Clayette, P.; Gauchet, C.; Dubreucq, G.; Vincent, L.; Bompais, H.; Mazinghien, R.; Querolle, O.; Salvador, A.; Lemoine, J.; Lucidi, B.; Balzarini, J.; Petitou, M. Long-Lasting Enfuvirtide Carrier Pentasaccharide Conjugates with Potent Anti-Human Immunodeficiency Virus Type 1 Activity. *Antimicrob. Agents Chemother.* **2010**, *54* (1), 134–142. https://doi.org/10.1128/AAC.00827-09.

(18) Boöttger, R.; Hoffmann, R.; Knappe, D. Differential Stability of Therapeutic Peptides with Different Proteolytic Cleavage Sites in Blood, Plasma and Serum. *PLoS One* **2017**, *12* (6), e0178943. https://doi.org/10.1371/journal.pone.0178943.

(19) Werle, M.; Bernkop-Schnürch, A. Strategies to Improve Plasma Half Life Time of Peptide and Protein Drugs. *Amino Acids* **2006**, *30*, 351–367. https://doi.org/10.1007/s00726-005-0289-3.

(20) Di, L. Strategic Approaches to Optimizing Peptide ADME Properties. *AAPS J.* **2015**, *17* (1), 134–143. https://doi.org/10.1208/s12248-014-9687-3.

(21) Bomb, K.; Zhang, Q.; Ford, E. M.; Fromen, C. A.; Kloxin, A. M. Systematic D-Amino Acid Substitutions to Control Peptide and Hydrogel Degradation in Cellular Microenvironments. *ACS Macro Lett.* **2023**, 725–732. https://doi.org/10.1021/acsmacrolett.3c00144.

(22) Li, X.; Du, X.; Li, J.; Gao, Y.; Pan, Y.; Shi, J.; Zhou, N.; Xu, B. Introducing d -Amino Acid or Simple Glycoside into Small Peptides to Enable Supramolecular Hydrogelators to Resist Proteolysis. *Langmuir* **2012**, *28*, 13512–13517. https://doi.org/10.1021/la302583a.

(23) Chen, X.; Fan, Z.; Chen, Y.; Fang, X.; Sha, X. Retro-Inverso Carbohydrate Mimetic Peptides with Annexin1-Binding Selectivity, Are Stable in Vivo, and Target Tumor Vasculature. *PLoS One* **2013**, *8* (12), e80390. https://doi.org/10.1371/journal.pone.0080390.

(24) Luo, Z.; Zhao, X.; Zhang, S. Self-Organization of a Chiral D-EAK16 Designer Peptide into a 3D Nanofiber Scaffold. *Macromol. Biosci.* **2008**, *8*, 785–791. https://doi.org/10.1002/mabi.200800003.

(25) Duti, I. J.; Florian, J. R.; Kittel, A. R.; Amelung, C. D.; Gray, V. P.; Lampe, K. J.; Letteri, R. A. Peptide Stereocomplexation Orchestrates Supramolecular Assembly of Hydrogel Biomaterials. *J. Am. Chem. Soc.* **2023**, *145*, 18468–18476. https://doi.org/10.1021/jacs.3c04872.

(26) Nagy, K. J.; Giano, M. C.; Jin, A.; Pochan, D. J.; Schneider, J. P. Enhanced

Mechanical Rigidity of Hydrogels Formed From Enantiomeric Peptide Assemblies. *J Am Chem Soc* **2011**, *133* (38), 14975–14977. https://doi.org/10.1158/0008-5472.CAN-10-4002.BONE.

(27) Nagy-Smith, K.; Beltramo, P. J.; Moore, E.; Tycko, R.; Furst, E. M.; Schneider, J. P. Molecular, Local, and Network-Level Basis for the Enhanced Stiffness of Hydrogel Networks Formed from Coassembled Racemic Peptides: Predictions from Pauling and Corey. *ACS Cent. Sci.* **2017**, *3*, 586–597. https://doi.org/10.1021/acscentsci.7b00115.

(28) Xu, F.; Khan, I. J.; McGuinness, K.; Parmar, A. S.; Silva, T.; Murthy, N. S.; Nanda, V. Self-Assembly of Left- and Right-Handed Molecular Screws. *J. Am. Chem. Soc.* **2013**, *135* (50), 18762–18765. https://doi.org/10.1021/ja4106545.

(29) Swanekamp, R. J.; Dimaio, J. T. M.; Bowerman, C. J.; Nilsson, B. L. Coassembly of Enantiomeric Amphipathic Peptides into Amyloid-Inspired Rippled β-Sheet Fibrils. *J. Am. Chem. Soc.* **2012**, *134*, 5556–5559. https://doi.org/10.1021/ja301642c.

(30) Swanekamp, R. J.; Welch, J. J.; Nilsson, B. L. Proteolytic Stability of Amphipathic Peptide Hydrogels Composed of Self-Assembled Pleated β-Sheet or Coassembled Rippled β-Sheet Fibrils. *Chem. Commun.* **2014**, *50* (70), 10133–10136. https://doi.org/10.1039/c4cc04644g.

(31) Crick, F. H. C. Is A-Keratin a Coiled Coil ? *Nature* **1952**, *170*, 882–883.

(32) Crick, F. H. C. The Packing of α-Helices: Simple Coiled-Coils. *Acta Crystallogr.* **1953**, *6*, 689–697. https://doi.org/10.1107/s0365110x53001964.

(33) Sia, S. K.; Kim, P. S. A Designed Protein with Packing between Left-Handed and Right-Handed Helices. *Biochemistry* **2001**, *40*, 8981–8989. https://doi.org/10.1021/bi010725v.

(34) Kreitler, D. F.; Yao, Z.; Steinkruger, J. D.; Mortenson, D. E.; Huang, L.; Mittal, R.; Travis, B. R.; Forest, K. T.; Gellman, S. H. A Hendecad Motif Is Preferred for Heterochiral Coiled-Coil Formation. *J. Am. Chem. Soc.* **2019**, *141* (4), 1583–1592. https://doi.org/10.1021/jacs.8b11246.

(35) Mortenson, D. E.; Steinkruger, J. D.; Kreitler, D. F.; Perroni, D. V.; Sorenson, G. P.; Huang, L.; Mittal, R.; Yun, H. G.; Travis, B. R.; Mahanthappa, M. K.; Forest, K. T.; Gellman, S. H. High-Resolution Structures of a Heterochiral Coiled Coil. *Proc. Natl. Acad. Sci.* **2015**, *112* (43), 13144–13149. https://doi.org/10.1073/PNAS.1507918112.

(36) Archer, W. R.; Schulz, M. D. Isothermal Titration Calorimetry: Practical Approaches and Current Applications in Soft Matter. *Soft Matter* **2020**, *16*, 8760–8774. https://doi.org/10.1039/d0sm01345e.

(37) Archer, W. R.; Fiorito, A.; Heinz-Kunert, S. L.; Macnicol, P. L.; Winn, S. A.; Schulz, M. D. Synthesis and Rare-Earth-Element Chelation Properties of Linear Poly(Ethylenimine Methylenephosphonate). *Macromolecules* **2020**, *53*, 2061–2068. https://doi.org/10.1021/acs.macromol.9b02472.

(38) Darby, S. J.; Platts, L.; Daniel, M. S.; Cowieson, A. J.; Falconer, R. J. An Isothermal Titration Calorimetry Study of Phytate Binding to Lysozyme: A Multisite Electrostatic Binding Reaction. *J. Therm. Anal. Calorim.* **2017**, *127* (2), 1201–1208.

https://doi.org/10.1007/s10973-016-5487-6.

(39) Liang, H.; Lin, F.; Zhang, Z.; Liu, B.; Jiang, S.; Yuan, Q.; Liu, J. Multicopper Laccase Mimicking Nanozymes with Nucleotides as Ligands. *ACS Appl. Mater. Interfaces* **2017**, *9*, 1352–1360. https://doi.org/10.1021/acsami.6b15124.

Chapter 4. Designing polymer-peptide conjugates to target aggregates that are implicated in ALS

4.1 Introduction

In this chapter, we designed polymer-peptide conjugates to sequester toxic aggregating proteins implicated in amyotrophic lateral sclerosis (ALS). We investigated both D- and L-peptides as components of the polymer-peptide conjugate to further explore the design rules of stereochemistry-directed interactions.

ALS, also known as Lou Gehrig's disease, is a lethal neuromuscular disease.[1–3] There were approximately 222,000 cases of ALS worldwide in 2015 and that number is estimated to increase by 69% to 376,000 cases by 2040.[4] Current treatment options include the drugs riluzole[5] and edaravone[6], which slow ALS progression but fail to significantly extend patient survival,[5,7] highlighting the urgent need for new ALS therapies.

In 40-50% of familial and 5-10% of sporadic cases of ALS,[8] a mutation of the *C9orf72* gene results in a hexanucleotide expansion of guanine and cytosine. This particular hexanucleotide, GGGGCC, is typically repeated up to 23 times in healthy patients, but in patients with ALS it is repeated hundreds or thousands of times.[9,10] Following transcription in this repeat expansion region, repeat-associated non-ATG (RAN) translation occurs, resulting in erroneous protein production (**Figure 4.1**).[11,12] This results in the accumulation of repeating

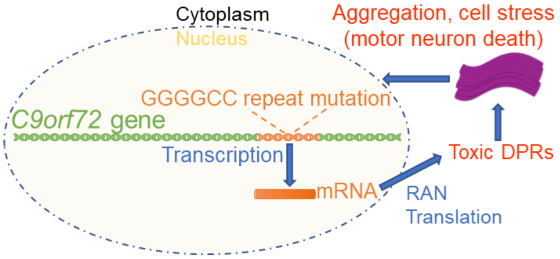

Figure 4.1. *C9orf72* gene mutation in ALS. A hexanucleotide expansion of GGGGCC occurs within the gene, which, upon transcription, results in aggregation of repeating hexanucleotide RNA foci, loss of C9orf72 protein, and RAN translation of toxic DPRs. Toxic DPRs aggregate, capture proteins, and cause cellular stress, leading to motor neuron death.

hexanucleotide RNA foci,[10] a loss of the C9orf72 protein,[13] and the production of five dipeptide repeat proteins (DPRs): glycine-alanine $(GA)_n$, glycine-arginine $(GR)_n$, proline-arginine $(PR)_n$, glycine-proline $(GP)_n$, and proline-alanine $(PA)_n$.[12,14] The pathogenic mechanism of the *C9orf72* mutation is not yet fully understood, and likely results from a combination of these three mutation effects, but it is known that $(GA)_n$, is toxic in cell culture[15,16] and is present in characteristic inclusions in the affected brain regions of patients with ALS.[17] The $(GA)_n$ DPR, in a manner somewhat similar to the amyloid β protein implicated in Alzheimer's disease, is an aggregating protein.[16] $(GA)_n$ DPRs form insoluble cytoplasmic aggregates that transmit between cells[18] and are toxic to cultured cells and primary neurons, including toxic mechanisms such as autophagy abnormalities and endoplasmic reticulum (ER) stress.[16,19,20] Therefore, a method of alleviating $(GA)_n$ toxicity provides a therapeutic opportunity.

Recent reports indicate that biologics designed to sequester or prevent the production of DPRs have had success in mitigating the deleterious hallmarks of ALS.[18,21,22] For example, antibodies engineered to target $(GA)_n$ reduced $(GA)_n$ aggregation both *in vitro* and *in vivo*[18,21] and, more recently, afforded favorable behavioral outcomes in ALS mouse models.[21] In fact, in the ALS mouse model, mice that were treated with antibodies had a significant increase in survival compared to mice that received no treatment.[21] Antisense oligonucleotides targeting the DPR-coding RNAs reduced levels of RNA foci and DPRs, changes which resulted in recovery from cognitive deficits in a mouse model.[22]

While the above examples highlight the transformative therapeutic potential of DPR sequestration for ALS patients, the use of biologics presents several key challenges including: the time- and cost-intensive production processes; susceptibility to physicochemical alterations during manufacture and transport;[23] enzymatic degradation;[23] undesirable immunogenic effects;[24] and the need for extensive use of cold-chain to deploy these treatments in developing countries.[25] It will be very important to consider the deployment of therapeutics in developing countries moving forward, as the cases of ALS are predicted to shift from predominantly developed countries to developing countries over the next 15 years.[4] To address these limitations, we seek to engineer synthetic therapeutics targeting $(GA)_n$ DPRs that will be easier to produce, less susceptible to physiochemical changes, and can be designed to eliminate the need for cold chain.

For our synthetic design to target $(GA)_n$, we designed a polymer-peptide conjugate with two components: a $(GA)_n$-binding peptide and a hydrophilic, biocompatible polymer (**Figure 4.2**). We expect that the peptide will target the $(GA)_n$ DPRs in solution, while the polymer component will keep the conjugate and targeted DPR soluble to prevent and/or reverse aggregation. A similar strategy has been reported for targeting amyloid β.[26–28] Treatment of $A\beta_{40}$ with a comb-shaped conjugate of the β-sheet breaker $iA\beta_5$ conjugated to a backbone of poly[N-(2-hydroxypropyl) methacrylamide]) leads to dispersal of $A\beta_{40}$ aggregates. To determine whether a similar approach would similarly disperse $(GA)_n$ aggregates, we sought to design a similar system. For the binding peptide, we selected $(GA)_{10}$, matching the structure of the aggregating DPR. This peptide was chosen to promote interactions with the full length $(GA)_n$ protein while remaining hydrophilic enough to be processable and dynamic enough to be available to interact with outside $(GA)_n$. The $iA\beta_5$ peptide used to target $A\beta_{40}$ was designed by a similar approach, as it is a short peptide that was taken from the full length protein.[28,29] We examined both L-$(GA)_{10}$ and

D-$(GA)_{10}$, as recent work with β-sheet forming peptides suggests that stereochemistry-directed interactions between an L-peptide (the stereochemical configuration that is naturally occurring, so the configuration that the $(GA)_n$ DPR will be in) and a D-peptide (does not occur naturally) lead to stronger binding between the peptides.[30–32] If this holds true for $(GA)_n$, then the D-$(GA)_{10}$ may target the $(GA)_n$ DPRs more strongly than L-$(GA)_{10}$.

In this chapter, we sought to fill two knowledge gaps. First, we wanted to determine whether attaching a peptide designed to interact with $(GA)_n$ to a hydrophilic polymer would effectively disperse $(GA)_n$ aggregates in a similar manner to the approach that was previously shown to be effective against aggregates of $Aβ_{40}$.[26–28] While this polymer-peptide approach was successful for $Aβ_{40}$, the degree to which this approach is broadly applicable is not yet known. The success of the polymer-peptide conjugate may be dependent on the choice of the peptide component in the conjugate, which we also investigated. To better understand the extent to which stereochemistry-directed interactions affect peptide-peptide interactions, we compared D- and L-conjugates to determine whether there was a difference in their ability to disperse aggregates of L-$(GA)_n$. Here we report the effects our designed polymer-peptide conjugates have on the aggregation of model toxic $(GA)_n$ proteins using solution turbidity and transmission electron microscopy (TEM) studies.

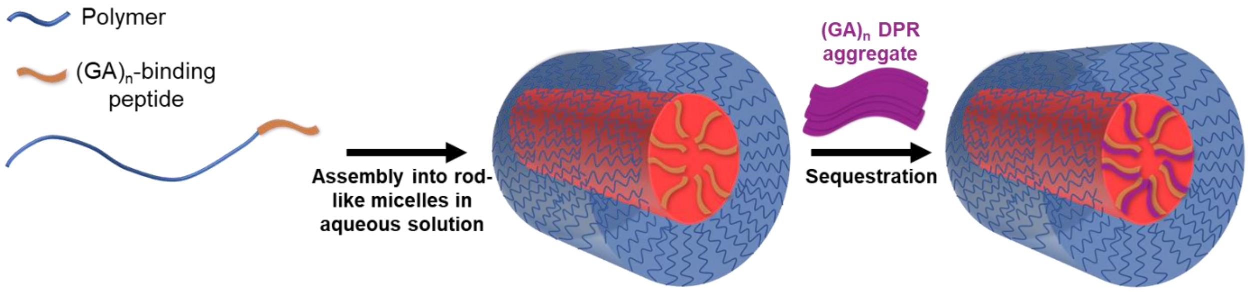

Figure 4.2. Proposed method of targeting $(GA)_n$ DPRs.

4.2 Results and discussion

4.2.1. $(GA)_{10}$ recapitulates the features of toxic $(GA)_n$ and is a suitable model toxic DPR

We began by investigating $(GA)_{10}$ as a model $(GA)_n$ DPR. We selected n = 10 repeats initially as this length was just soluble enough in the presence of aqueous solvent to allow for solution characterization. We confirmed the primary structure and purity of $(GA)_{10}$ using NMR spectroscopy, MALDI-TOF mass spectrometry, and HPLC (**Figure C1**). To confirm that $(GA)_{10}$ is of sufficient length to recapitulate the physical properties observed in native $(GA)_n$ species, we verified the β-sheet secondary structure and the aggregation behavior of $(GA)_{10}$. Fourier-transform infrared spectroscopy (FTIR) of $(GA)_{10}$ in both powder form (**Figure C2**) and in 10 mM phosphate buffer (**Figure 4.3A**) shows a strong peak characteristic of β-sheet formation at 1624 cm^{-1}.[33] The β-sheet secondary structure is further confirmed by the concentration-dependent fluorescence of the amyloid dye

Thioflavin T in the presence of $(GA)_{10}$ (**Figure 4.3B**). As for aggregation, $(GA)_{10}$ at 2.1 mM (3 mg/mL) in 10 mM phosphate buffer results in a visually turbid solution seconds after dissolution (**Figure C3**) and after incubation overnight shows signs of aggregation by transmission electron microscopy (TEM) (**Figure 4.3C, Figures C5-C6**). The combination of retaining the same secondary structure and aggregating in aqueous solution make $(GA)_{10}$ a suitable model for the toxic $(GA)_n$ DPRs in this study, as it will allow us to test methods of preventing aggregation and dispersing pre-formed aggregates.

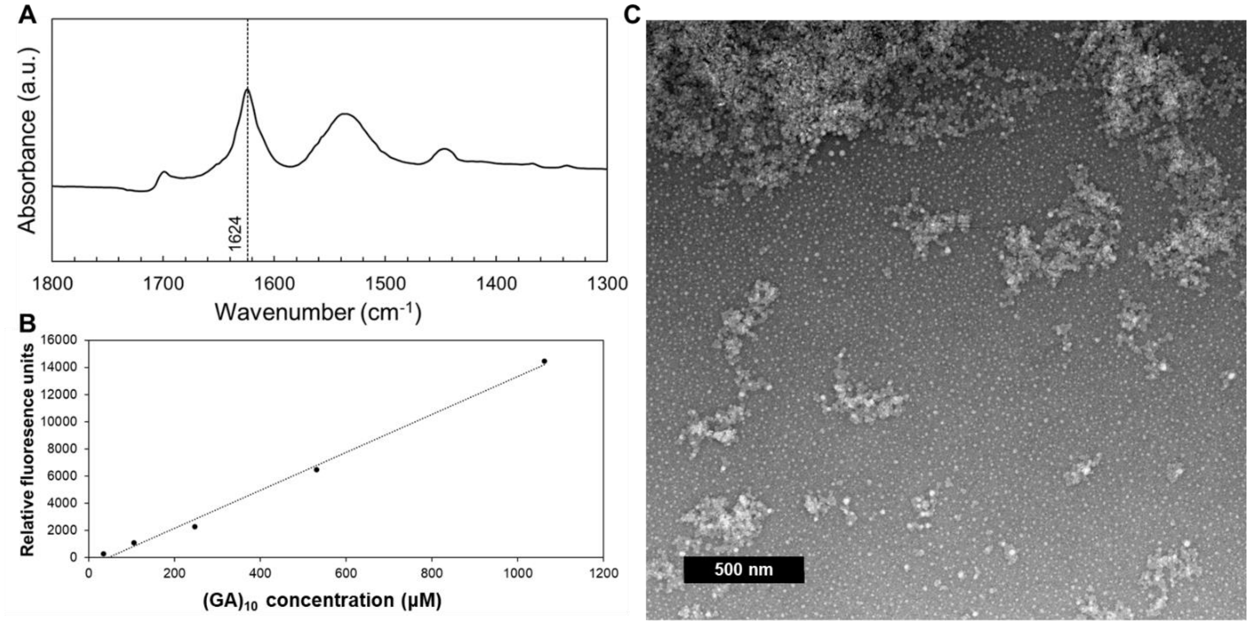

Figure 4.3. Characterization of $(GA)_{10}$ features. A) IR spectrum of 3 mg/mL $(GA)_{10}$ in 10 mM phosphate buffer, with a characteristic β-sheet peak at 1624 cm^{-1} highlighted. B) Thioflavin T fluorescence as a function of $(GA)_{10}$ concentration in 10 mM phosphate buffer. The dotted line is meant as a linear guide for the eye. C) TEM image of $(GA)_{10}$ after overnight incubation in 10 mM phosphate buffer. Scale bar is 500 nm. Multiple levels of aggregation are observed, with small aggregates coming together to form larger aggregates.

4.2.2. Design, synthesis, and characterization of $(GA)_n$-targeting polymer-peptide conjugates

Similarly to the design of the amyloid β breaker iAβ5,[29] which was directly inspired by the hydrophobic region of the N-terminal domain of amyloid β, we directly modeled our $(GA)_n$-binding peptide off $(GA)_n$ itself, using $(GA)_{10}$ as the $(GA)_n$-binding peptide in our polymer-peptide conjugate. We selected poly(ethylene glycol) (PEG) as the polymer component of our polymer-peptide conjugate for its significant aqueous solubility and demonstrated biocompatibility.[34] As the $(GA)_{10}$ in the peptide component of the conjugate is expected to interact with $(GA)_n$ DPRs, we need a polymer with high solubility to prevent the conjugate from becoming too hydrophobic and participating in aggregation itself. Additionally, PEG is widely used in biomaterials and FDA-approved, making it a logical choice for a potential therapeutic.[35]

To conjugate $(GA)_{10}$ to PEG, we used thiol-maleimide chemistry. A thiol was added to the $(GA)_{10}$ sequence via addition of a cysteine residue, and we also included three glycine residues as a spacer to separate the $(GA)_{10}$ from the polymer and allow it to be more flexible. This resulted in a final sequence of CGGG-$(GA)_{10}$. The $(GA)_{10}$ peptide was dissolved at 1 mM in an aqueous 7 M urea solution, where the presence of urea (a known denaturant)[36] supports solubilization, and stirred at a 2:1 volume ratio with a 1 mM solution of methoxypolyethylene glycol maleimide (mPEG-mal) (5000) at room temperature for 1 h (**Figure 4.4A**). A 1.25:1 ratio of peptide: polymer was not sufficient to drive the reaction of the polymer to completion, so a 2:1 molar ratio of thiol (peptide): maleimide (polymer) was used (**Figure C7**). After an hour, HPLC shows a reduction in the size of the peptide peak, the disappearance of the polymer peak, and the appearance of two new peaks (**Figure 4.4B**), one corresponding to the conjugate and one broad peak hypothesized to be conjugate that has begun interacting with free CGGG-$(GA)_{10}$ peptide in solution. This would make sense as the conjugate is designed to target $(GA)_n$ proteins and is corroborated by the fact that a 2:1 excess of CGGG-$(GA)_{10}$: mPEG-mal is required to react all of the polymer (**Figure C7**), likely because some of the peptide is being sequestered by the conjugates as they are formed. To separate the conjugate from the excess peptide and the conjugate already containing sequestered peptide, we used preparative-scale HPLC to isolate the peak corresponding to the conjugate. The product obtained from this purification was confirmed to be mPEG-CGGG-$(GA)_{10}$ conjugate by NMR spectroscopy (**Figure C8)** and the purity was confirmed by size exclusion chromatography (SEC) (**Figure C8**) and HPLC (**Figure C8**). We produced both L- and D-CGGG-$(GA)_{10}$ conjugates in this manner and further characterized them by TEM following overnight incubation in 10 mM phosphate buffer (**Figure 4.4C, Figures C9-C10**). We observe the presence of rod-like morphology throughout the sample, suggesting assembly of the conjugates into cylindrical micelles with a hydrophilic PEG exterior and a hydrophobic $(GA)_{10}$ interior.

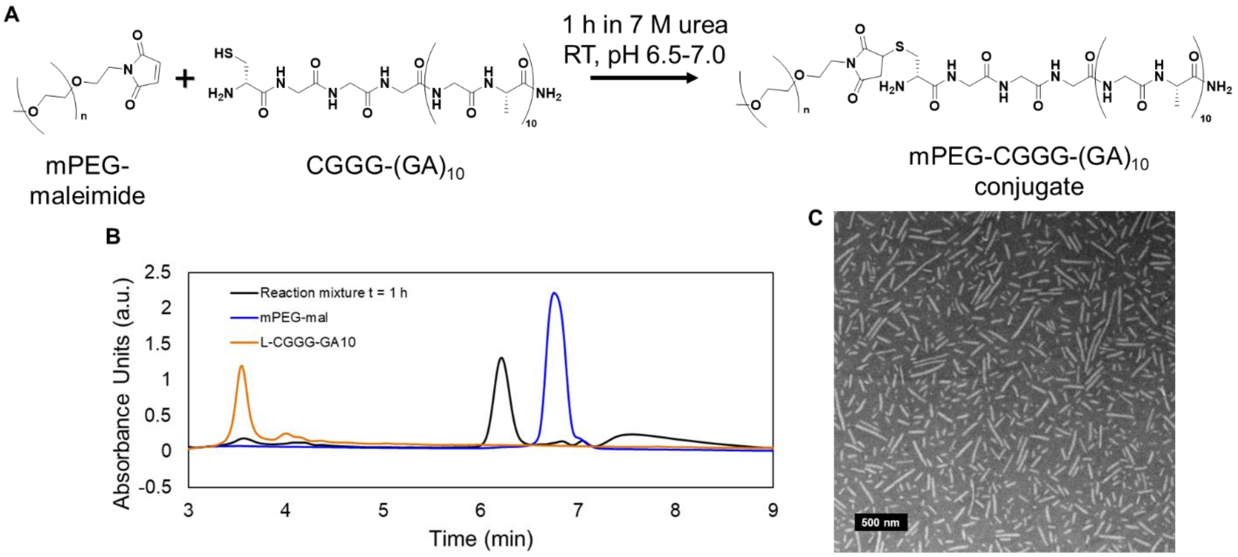

Figure 4.4. Synthesis and characterization of mPEG-CGGG-$(GA)_{10}$ conjugates. A) Synthesis of mPEG-CGGG-$(GA)_{10}$ conjugates via thiol-maleimide chemistry. B) HPLC chromatogram showing the reaction mixture after 1 h (black trace), mPEG-mal alone (blue trace), and L-CGGG-$(GA)_{10}$ alone (orange trace). After 1 h of reaction, the largest peak in the reaction mixture (at 6.1 min) is a new peak, attributed to the newly formed conjugate, and elutes between the polymer peak and the peptide peak. The other major peak in the chromatogram, a very broad peak that elutes from 7.2 to 9 min, is attributed to conjugate product that interacts with peptide reactant. C) TEM image of mPEG-L-CGGG-$(GA)_{10}$ after overnight incubation in 10 mM phosphate buffer. A rod-like morphology is observed throughout the sample, suggesting a cylindrical micelle morphology for the conjugate. Scale bar is 500 nm.

4.2.3. Co-incubation of $(GA)_{10}$ with mPEG-CGGG-$(GA)_{10}$ conjugates

To test the efficacy of the mPEG-CGGG-$(GA)_{10}$ conjugates in preventing aggregation of the $(GA)_{10}$ model toxic DPR, we incubated $(GA)_{10}$ in 10 mM phosphate buffer containing either mPEG-L-CGGG-$(GA)_{10}$, mPEG-D-CGGG-$(GA)_{10}$, the mPEG-mal we used for conjugation as a control, or with no additives, just $(GA)_{10}$ in buffer alone. As a measure of aggregation, we observed the turbidities of solutions from each treatment group over time by monitoring absorbance at 550 nm and plotting absorbance units with the absorbance of the buffer subtracted out (**Figure 4.5**). The absorbance of the conjugates alone in buffer is similar to the absorbance of buffer alone (**Figure C11**), so the addition of conjugate to the solution does not artificially increase turbidity. The $(GA)_{10}$ in each condition was incubated at 3 mg/mL (2.1 mM), a concentration at which we have observed $(GA)_{10}$ to be insoluble. We dissolved the conjugates and mPEG-mal control at 7 mg/mL, which for the conjugates is approximately 1 mM conjugate and 0.25 mM peptide content on the conjugate. The duration of this experiment was 14 days, over which bacteria may be expected to grow in aqueous conditions. To determine whether bacterial growth contributes to a rise in turbidity, we monitored the turbidity of a solution of 10 mM phosphate buffer for a duration of 28 days and did not observe any increase in turbidity (**Figure C12**). The experiment was performed with three separately prepared vials for each condition, and each timepoint is plotted with a bar to show the average turbidity as well as individual data points corresponding to each individual vial in the treatment group. We observe that the control condition where buffer alone is added to $(GA)_{10}$ continually increases in turbidity and heterogeneity between vials over time. Unexpectedly, the control condition where we added mPEG-mal to $(GA)_{10}$ has an increase in turbidity over the first day, then remains stable, rather than continuing to increase like the buffer alone. mPEG-mal has a functional reactive group, so it is possible that the maleimide is reacting with the free amine on the $(GA)_{10}$, leading to less aggregation. We further tested this in a second turbidity study by comparing a PEG (5000)-methyl ether (PEG-ME) without a reactive group against the mPEG-mal (**Figure C13**). We found that the aggregation behavior of $(GA)_{10}$ treated with PEG-ME is similar to $(GA)_{10}$ treated with buffer alone, supporting that the maleimide group is interacting with $(GA)_{10}$ and preventing aggregation. As the conjugates we are using are purified and do not contain PEG with free reactive units, the best control treatment group is PEG-ME, so we used that going forward in future experiments.

For the $(GA)_{10}$ treated with the mPEG-L-CGGG-$(GA)_{10}$ conjugate, there is a sharp drop in turbidity over the first day, followed by sustained incremental decreases in turbidity over the 14 days of this experiment, demonstrating the ability of the conjugate to not only prevent aggregation, but also reverse the initial aggregation that occurred. Finally, co-incubation of $(GA)_{10}$ with the mPEG-D-CGGG-$(GA)_{10}$ conjugate leads to higher average turbidities than the mPEG-L-CGGG-$(GA)_{10}$ conjugate at the t = 0 days time point taken just after adding the conjugate to $(GA)_{10}$, but we note that this is at least partially due to one vial that had a much higher turbidity than the others in the group. Interestingly, we find that over time that high turbidity vial becomes less turbid to the point where it is similar in turbidity to the other two vials in the sample group after 10 days. Similarly to the mPEG-L-CGGG-$(GA)_{10}$ conjugate group, we observe that the mPEG-D-CGGG-$(GA)_{10}$ decreases in turbidity over time, albeit with a more gradual decrease than for the mPEG-L-CGGG-$(GA)_{10}$ group. This result may indicate that the opposite stereochemistries pack together differently, causing a difference in the rate at which $(GA)_{10}$ is targeted by the mPEG-D-CGGG-$(GA)_{10}$ conjugate, but further studies would be needed to confirm this. Overall, both conjugate treatment groups have a marked effect of not only preventing aggregation but also reversing it, even with an order of magnitude less peptide content present in the conjugate (~0.25 mM) compared to the free $(GA)_{10}$ (~2.1 mM).

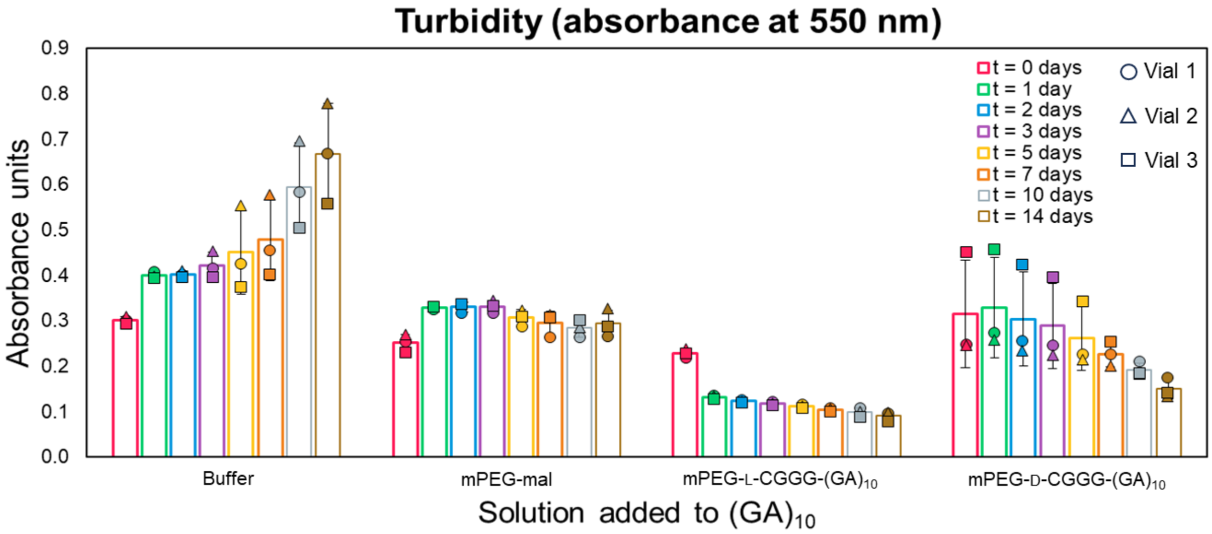

Figure 4.5. Turbidity over time for $(GA)_{10}$ treated with four different conditions: 10 mM phosphate buffer alone, 7 mg/mL mPEG-mal, 7 mg/mL mPEG-L-CGGG-$(GA)_{10}$, and 7 mg/mL mPEG-D-CGGG-$(GA)_{10}$. When incubated in buffer alone, the $(GA)_{10}$ increases in turbidity over time. However, when incubated with just polymer (mPEG-mal), the turbidity initially increases then remains stable, indicating that the polymer alone prevented further aggregation. This result was attributed to the presence of a reactive group on mPEG-mal. The mPEG-L-CGGG-$(GA)_{10}$ treatment group led to a decrease in $(GA)_{10}$ turbidity with a sharp drop over the first day, then steadily decreased throughout the remainder of the experiment. Finally, the mPEG-D-CGGG-$(GA)_{10}$ treatment group initially did not lead to a decrease in $(GA)_{10}$ aggregation, but over time did decrease in turbidity.

In addition to turbidity, we monitored thioflavin T fluorescence as a measure of aggregation. However, we observed trends that were not at all similar to the trends observed for the turbidity experiment. While there were some changes in the first couple days, from 2 days to 14 days there was little to no change in fluorescence, with the fluorescence values being very similar across all conditions tested (**Figure C14**). These results indicate that either the thioflavin T was able to diffuse into the conjugates and stain both free, aggregated $(GA)_{10}$ and $(GA)_{10}$ taken up by the conjugates, leading to a constant level of fluorescence at most time points, or the $(GA)_{10}$ concentration in the outside solution does not change but the level of aggregation of the $(GA)_{10}$ changes.

4.2.4. Morphological behavior of $(GA)_{10}$ incubated in buffer and with conjugates

At the beginning and end of the turbidity experiment performed above, small aliquots of each solution were examined by TEM to examine changes in the morphological characteristics of the $(GA)_{10}$ under different conditions (**Figure 4.6, Figures C15-C20**). Immediately after adding $(GA)_{10}$ to buffer alone (t = 0 days), we already observed aggregation beginning to occur, with a mixture of small, independent aggregates and larger structures that seem to be made up of groups of those smaller aggregates. To rule out the possibility of the 10 mM phosphate buffer contributing to the structures that we observed, we took TEM images of the buffer alone and saw no evidence of any structures formed (**Figure C4**). After 14 days of incubation in buffer, we observe the formation of much larger aggregates, which aligns with the turbidity data indicating that the solution became more turbid over time. For both groups of $(GA)_{10}$ treated with conjugate at t = 0 days, we observed both cylindrical structures that are consistent with the structures of the conjugates and some small aggregates. After 14 days of incubation, we still observe a mixture of both conjugates and small aggregates for both L- and D-conjugates, but there is nothing similar to the large aggregation observed for the $(GA)_{10}$ incubated in buffer alone. These data taken together with the turbidity data indicate that the mPEG-L-CGGG-$(GA)_{10}$ and mPEG-D-CGGG-$(GA)_{10}$ conjugates may have some therapeutic potential as they prevent $(GA)_n$ aggregation.

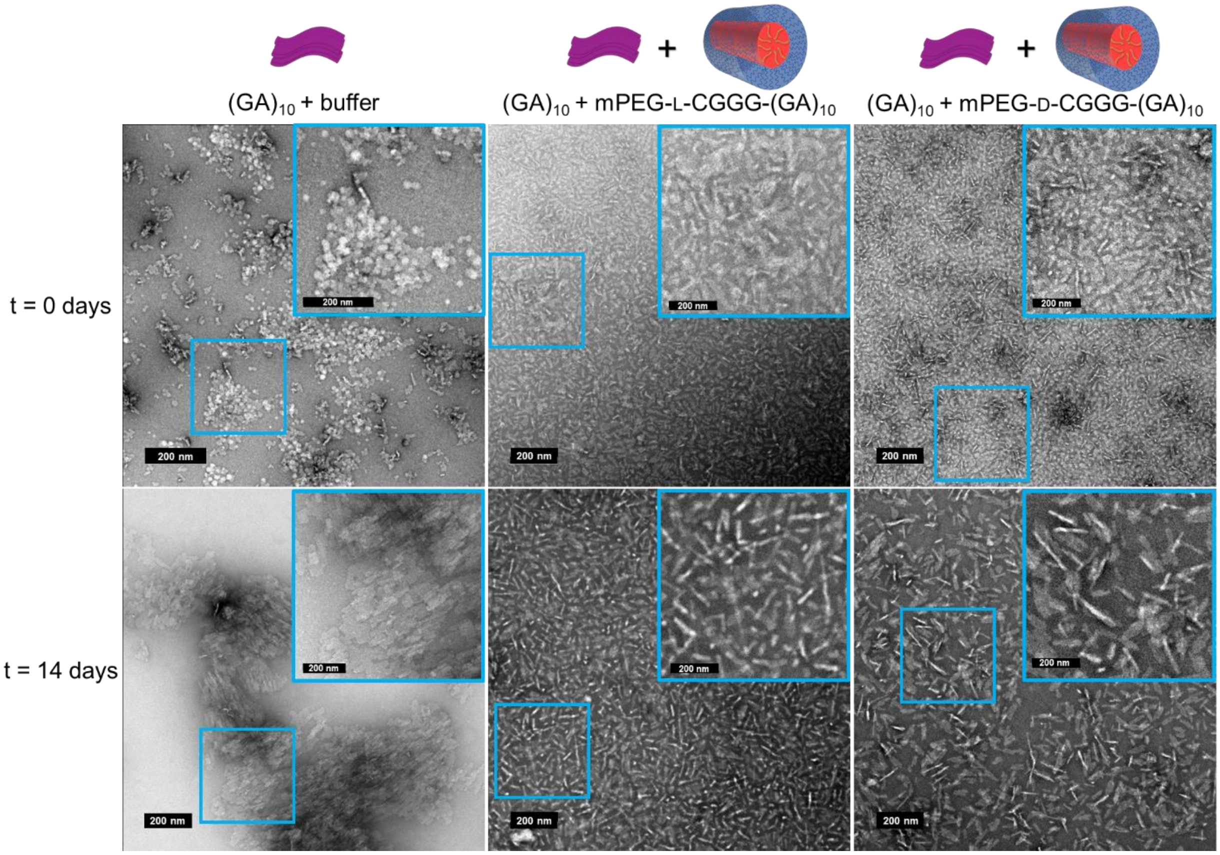

Figure 4.6. TEM images of $(GA)_{10}$ incubated in buffer alone, 7 mg/mL mPEG-L-CGGG-$(GA)_{10}$, and 7 mg/mL mPEG-D-CGGG-$(GA)_{10}$ immediately after incubation began and after 14 days of incubation. In the buffer treatment group, small aggregates of $(GA)_{10}$ are observed coming together to form larger aggregates at the beginning of the experiment, while at the end of the experiment much larger aggregates are observed. For both conjugate conditions, small $(GA)_{10}$ aggregates are observed at the beginning and end of the experiment, but the conjugate treatment prevents them from forming large-scale aggregates as observed for $(GA)_{10}$ incubated in buffer alone.

4.2.5. Disaggregation of $(GA)_{10}$ in the presence of conjugates is concentration-dependent

To test the effects of conjugate concentration on $(GA)_{10}$ aggregation prevention, we repeated the previous turbidity experiment with three different concentrations of mPEG-

L-CGGG-$(GA)_{10}$: 7 mg/mL (same as previous experiment), 0.35 mg/mL (5x lower concentration, ~0.2 mM conjugate and ~0.05 mM peptide content), and 35 mg/mL (5x higher concentration, ~5 mM conjugate and ~1.2 mM peptide content) (**Figure 4.7**). For this experiment, we decided to take turbidity data at earlier timepoints (t = 3 h, t = 6 h, and t = 12 h) to capture some data points during the sharp drop in turbidity we observed over the first 24 h for 7 mg/mL mPEG-L-CGGG-$(GA)_{10}$ in the last experiment. We chose to use mPEG-L-CGGG-$(GA)_{10}$ here because it broke up the $(GA)_{10}$ aggregates in the previous turbidity experiment faster than the mPEG-D-CGGG-$(GA)_{10}$. We found that the turbidity of $(GA)_{10}$ in buffer alone again increases over time and becomes more heterogeneous with time. For 35 mg/mL mPEG-L-CGGG-$(GA)_{10}$, the turbidity starts low and stays low. By comparing the initial t = 0 h turbidity of 35 mg/mL mPEG-L-CGGG-$(GA)_{10}$ to the buffer alone, we can see that the 35 mg/mL treatment group prevented initial aggregation of $(GA)_{10}$ to a significant degree ($p < 0.005$). On the other hand, the initial turbidity of the $(GA)_{10}$ incubated with 7 mg/mL mPEG-L-CGGG-$(GA)_{10}$ is similar to the initial turbidity of the $(GA)_{10}$ incubated with buffer alone and then decreases with time to a final turbidity similar to the final turbidity of the 35 mg/mL treatment group. Finally, the turbidity of $(GA)_{10}$ in the 0.35 mg/mL mPEG-L-CGGG-$(GA)_{10}$ treatment group is initially higher than all the other treatment groups, then experiences a small increase after 3 h, and stays at the same turbidity for the duration of the study. These data indicate a concentration-dependent response of $(GA)_{10}$ aggregation to mPEG-L-CGGG-$(GA)_{10}$, where at a higher concentration (35 mg/mL) with similar peptide content on the conjugate to free $(GA)_{10}$ in solution, the conjugate prevents most of the aggregation of $(GA)_{10}$ from happening at all. At a middle concentration (7 mg/mL) with an order of magnitude lower concentration of conjugate peptide content compared to free (GA)$_{10}$, the conjugate does not prevent initial aggregation, but does break up the aggregates that form. At a lower concentration (0.35 mg/mL) with two orders of magnitude lower conjugate peptide content concentration compared to free (GA)$_{10}$, the conjugate neither prevents initial aggregation nor breaks up the aggregates that are present, but it does prevent the aggregates from growing like what is observed for (GA)$_{10}$ in buffer alone.

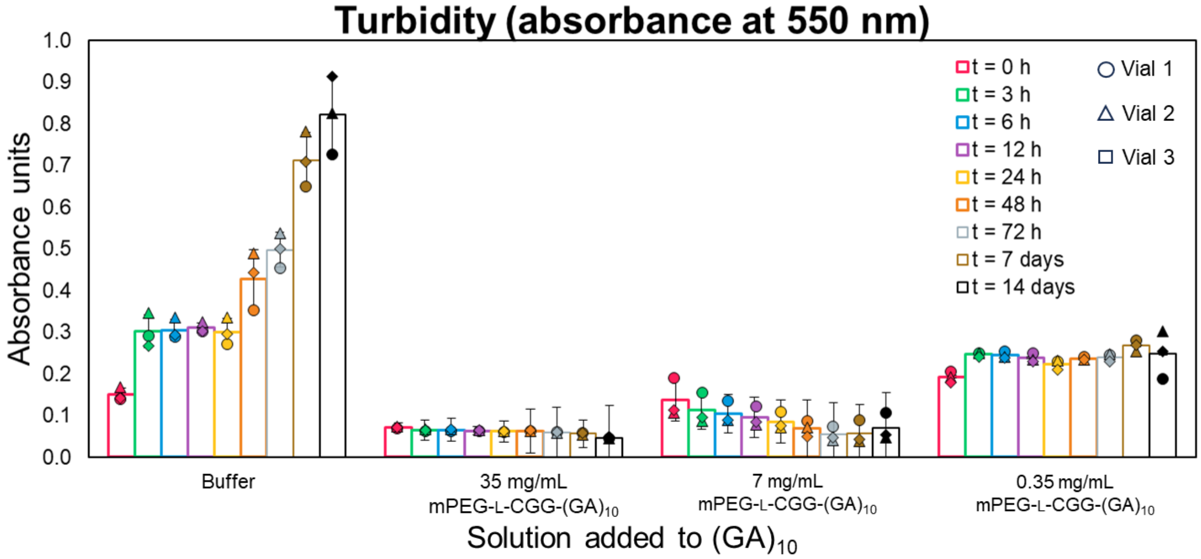

Figure 4.7. Turbidity over time for (GA)$_{10}$ treated with buffer or three different concentrations of mPEG-L-CGGG-(GA)$_{10}$. As previously observed, the turbidity of the (GA)$_{10}$ incubated in buffer alone continually increases over time. The (GA)$_{10}$ treated with 35 mg/mL mPEG-L-CGGG-(GA)$_{10}$ has low turbidity initially and remains low, indicating that it prevents most aggregation from occurring at all. The 7 mg/mL mPEG-L-CGGG-(GA)$_{10}$ treatment condition has an initially higher turbidity that drops over time, indicating that some aggregates formed and were subsequently broken up by the conjugate. Finally, the (GA)$_{10}$ treated with 0.35 mg/mL mPEG-L-CGGG-(GA)$_{10}$ starts with a higher turbidity than the other conditions, has an increase

over the first 3 h, but then remains stable for the next 14 days, suggesting that aggregates form and are not broken up, but the conjugate also does not allow them to grow.

4.2.6. Incubation of mPEG-CGGG-$(GA)_{10}$ conjugates with pre-aggregated $(GA)_{10}$

To better reflect the disease state in ALS, we designed an experiment where $(GA)_{10}$ was allowed to freely aggregate before application of the treatment groups. $(GA)_{10}$ was incubated in 10 mM phosphate buffer for 7 days before either PEG-ME, mPEG-L-CGGG-$(GA)_{10}$, or mPEG-D-CGGG-$(GA)_{10}$ were added to the sample in powder form. Similar to previous experiments, the polymer or conjugates were added at a concentration of 7 mg/mL and a control was run where nothing further was added to the buffer. The turbidity of the solutions was monitored over a period of 28 days after adding PEG-ME or conjugate to observe the continued aggregation behavior of $(GA)_{10}$ (**Figure 4.8**). As expected, the $(GA)_{10}$ incubated in buffer alone or with PEG-ME alone continued to aggregate over time, as evidenced by the continual increase in turbidity over time in this experiment. For the two conjugate treatment groups, we observed a sharp increase in turbidity over the first 2 days, after which the turbidity consistently decreased. Interestingly, whereas for the co-incubation experiment we observed a difference in the aggregation behavior of $(GA)_{10}$ for treatment with mPEG-L-CGGG-$(GA)_{10}$ compared to mPEG-D-CGGG-$(GA)_{10}$, for this experiment the two conjugate treatments lead to very similar responses in $(GA)_{10}$ aggregation behavior. We note that the starting turbidities for the buffer and PEG-ME treatment groups were significantly different from the starting turbidities for the mPEG-L-CGGG-$(GA)_{10}$ and mPEG-D-CGGG-$(GA)_{10}$ treatment groups, even though for the first week they were all just $(GA)_{10}$ incubating in buffer. We attribute this to the use of differently shaped stir bars between the first two treatment groups and the second two treatment groups. Despite the different starting turbidities, it is clear that the (GA)$_{10}$ in buffer and PEG-ME aggregates unchecked, while the conjugate-treated (GA)$_{10}$ aggregation initially accelerates but is then stopped and reversed. This is supported by calculating a percent change from t = 0 days after pre-aggregation to t = 28 days after pre-aggregation. The (GA)$_{10}$ treated with buffer experienced a 141% increase in turbidity over this time period, the (GA)$_{10}$ treated with PEG-ME experienced a 99% increase in turbidity, the (GA)$_{10}$ treated with mPEG-L-CGGG-(GA)$_{10}$ experienced a 49% decrease in turbidity, and the (GA)$_{10}$ treated with mPEG-D-CGGG-(GA)$_{10}$ experienced a 37% decrease in turbidity.

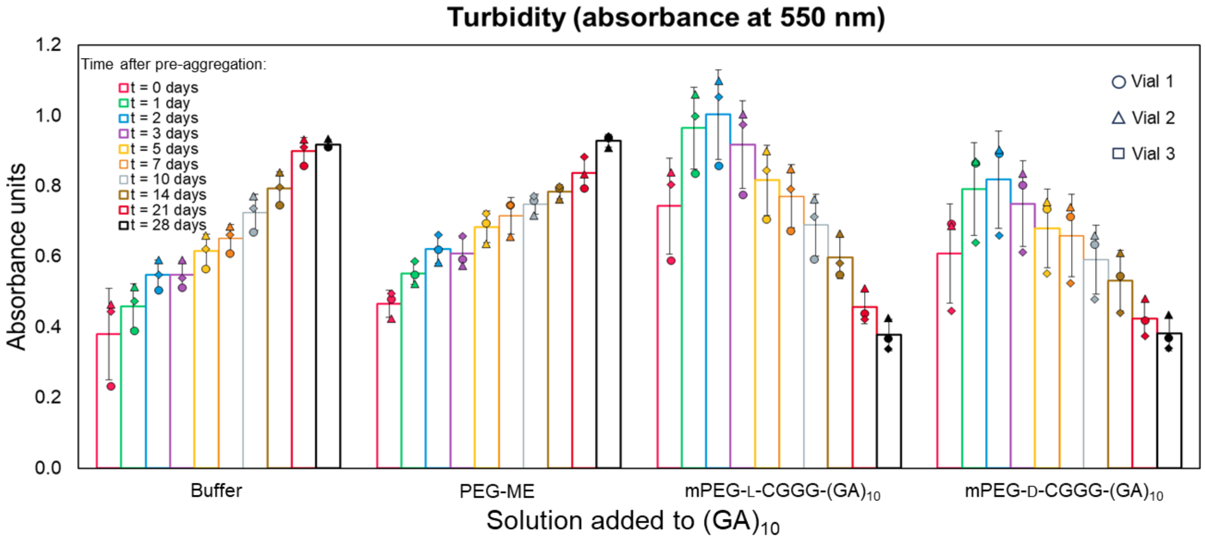

Figure 4.8. Turbidity over time for (GA)$_{10}$ aggregated for 7 days, then treated with no further additives, 7 mg/mL PEG-ME, 7 mg/mL mPEG-L-CGGG-(GA)$_{10}$, or 7 mg/mL mPEG-D-CGGG-(GA)$_{10}$. The time indicates the days since treatment was added, rather than total days of aggregation. The (GA)$_{10}$ incubated with buffer or PEG-ME continually increase in turbidity over time. However, the (GA)$_{10}$ incubated with mPEG-L-CGGG-(GA)$_{10}$ or mPEG-D-CGGG-(GA)$_{10}$ see an initial increase in turbidity for the first two days, then the turbidity decreases over time, indicative of the conjugates breaking up the aggregates that formed.

4.2.7. Morphological behavior of pre-aggregated $(GA)_{10}$ upon addition of PEG-ME and mPEG-CGGG-$(GA)_{10}$ conjugates

In an analogous manner to the first co-incubation turbidity study, we acquired TEM images of the $(GA)_{10}$ solutions with different treatment groups at the end of the experiment (28 days), as well as the end of the pre-aggregation period (**Figure 4.9, Figures C21-C25**). We observed that small $(GA)_{10}$ aggregates were coming together into larger aggregates after the pre-aggregation period but were not yet the large-scale aggregates that we observed 28 days after the pre-aggregation period. The $(GA)_{10}$ that was treated with PEG-ME had a similar morphology to the $(GA)_{10}$ that was incubated in buffer alone, with large-scale aggregates similar in size to those observed in buffer alone. For the two conjugate-treated conditions, there again is no evidence of the large-scale $(GA)_{10}$ aggregates observed for the $(GA)_{10}$ incubated in PEG-ME or buffer. However, there are some smaller aggregates observed that are still present after 28 days, which may still be broken up by the conjugates over time, considering that the turbidity was still steadily decreasing and had not leveled off at the end of the experiment.

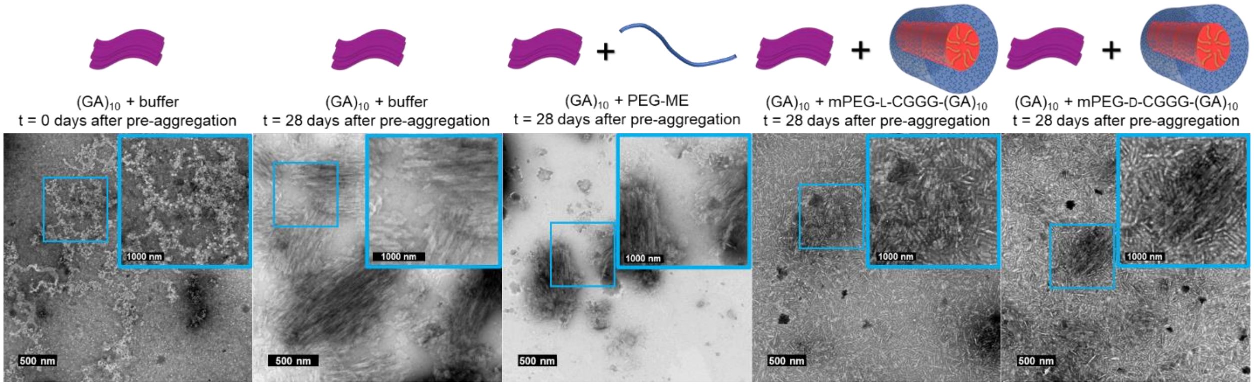

Figure 4.9. TEM images of $(GA)_{10}$ incubated in buffer alone, with PEG-ME, with mPEG-L-CGGG-$(GA)_{10}$, and with mPEG-D-CGGG-$(GA)_{10}$ 28 days after a 7 day pre-aggregation period, compared to $(GA)_{10}$ at the

end of the 7 day pre-aggregation period. Matching the trends in the turbidity data, $(GA)_{10}$ incubated in buffer or PEG-ME forms large-scale aggregates, while $(GA)_{10}$ incubated in mPEG-L-CGGG-$(GA)_{10}$ or mPEG-D-CGGG-$(GA)_{10}$ show no evidence of similar large-scale aggregates. Scale bars are 500 nm.

4.2.8. Incubation of mPEG-L-CGGG-$(GA)_{10}$ and mPEG-D-CGGG-$(GA)_{10}$ conjugates with $(GA)_{20}$

In the disease state, $(GA)_n$ is expected to be tens to thousands of repeats in length.[20,37] As such, it will be important to understand the relationship between the length of the peptide that is a component of the conjugate and the length of the $(GA)_n$ that it is targeting. To this end, we synthesized $(GA)_{20}$, which is double the length of the peptide component of the conjugates. As 40 amino acids is pushing the limits of the maximum peptide length achievable via automated, microwave-assisted peptide synthesis, we used mass spectrometry to check the mass of the $(GA)_{20}$ we synthesized (**Figure C26**). We found that the mass we observed in mass spectrometry corresponds to $(GA)_{20}$ with four alanine deletions and three glycine additions, so the $(GA)_{20}$ peptide is really $(GA)_{16}G$. For the purposes of this experiment, this is not a problem as we simply want to test our mPEG-CGGG-$(GA)_{10}$ conjugates against a $(GA)_n$ longer in length than ten repeats.

We studied the effects of coincubation of PEG-ME and mPEG-L-CGGG-$(GA)_{10}$ on $(GA)_{20}$ aggregation compared to aggregation in buffer alone (**Figure 4.10**) and the effects on $(GA)_{20}$ aggregation of adding mPEG-L-CGGG-$(GA)_{10}$ or mPEG-D-CGGG-$(GA)_{10}$ to $(GA)_{20}$ that was pre-aggregated for one week (**Figure 10**). For $(GA)_{20}$ incubated in buffer alone, there is an increase in turbidity over the first day, then there isn't much change until Day 15, after which there is a drop in turbidity on Days 30 and 44 that are similar to the starting turbidity (**Figure 4.10**). When $(GA)_{20}$ is preaggregated for 7 days before turbidity is measured, there is little difference in the turbidities observed over time (**Figure 4.11**). These data taken together may indicate that $(GA)_{20}$ aggregates very quickly over 1 day to form stable aggregates in solution that don't grow any larger. When $(GA)_{20}$ is co-incubated with PEG-ME, the same trends are observed: there is an increase in turbidity over the first day of co-incubation and there are little changes in turbidity with time until a drop in turbidity back to the starting value is observed after 30 days (**Figure 4.10**). For the co-incubation of $(GA)_{20}$ with mPEG-L-CGGG-$(GA)_{10}$, a nearly identical trend is observed, with a notable difference being that after 30 days, there is a larger drop in turbidity that is less turbid than the starting solution (**Figure 4.10**). Further experimentation would be required to confirm that the conjugate is having a significant impact on aggregation at these late time points. When mPEG-L-CGGG-$(GA)_{10}$ is incubated with pre-aggregated $(GA)_{20}$, however, no changes in turbidity are observed, very similar to the $(GA)_{20}$ incubated in buffer, so there are no indications that mPEG-L-CGGG-$(GA)_{10}$ is effective at dispersing pre-formed aggregates (**Figure 4.11**). Finally, incubation of mPEG-D-CGGG-$(GA)_{10}$ with pre-aggregated $(GA)_{20}$ also does not affect the turbidity of the solutions over time, leading to the same conclusion that mPEG-D-CGGG-$(GA)_{10}$ is not effective at dispersing $(GA)_{20}$ aggregates.

As the mPEG-CGGG-$(GA)_{10}$ conjugates seem to be less effective against $(GA)_{20}$ compared to $(GA)_{10}$, we sought design changes that might increase the effectiveness of the conjugates in preventing and dispersing longer aggregates. As a potential method to mediate this loss of effectiveness, we next explored increase the valency of the peptide presentation on the conjugates.

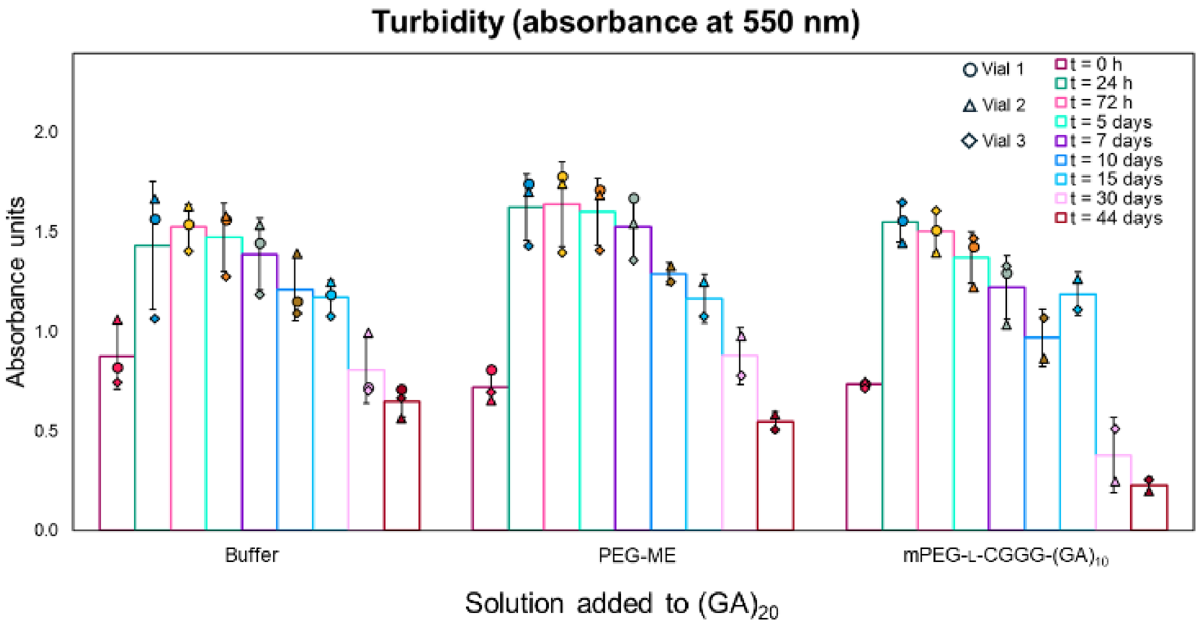

Figure 4.10. Turbidity over time for $(GA)_{20}$ treated with buffer, 7 mg/mL PEG-ME, or 7 mg/mL mPEG-L-CGGG-$(GA)_{10}$. There is little difference in turbidity over time between the three treatment conditions, indicating that mPEG-L-CGGG-$(GA)_{10}$ did not affect the aggregation of $(GA)_{20}$ over this time period.

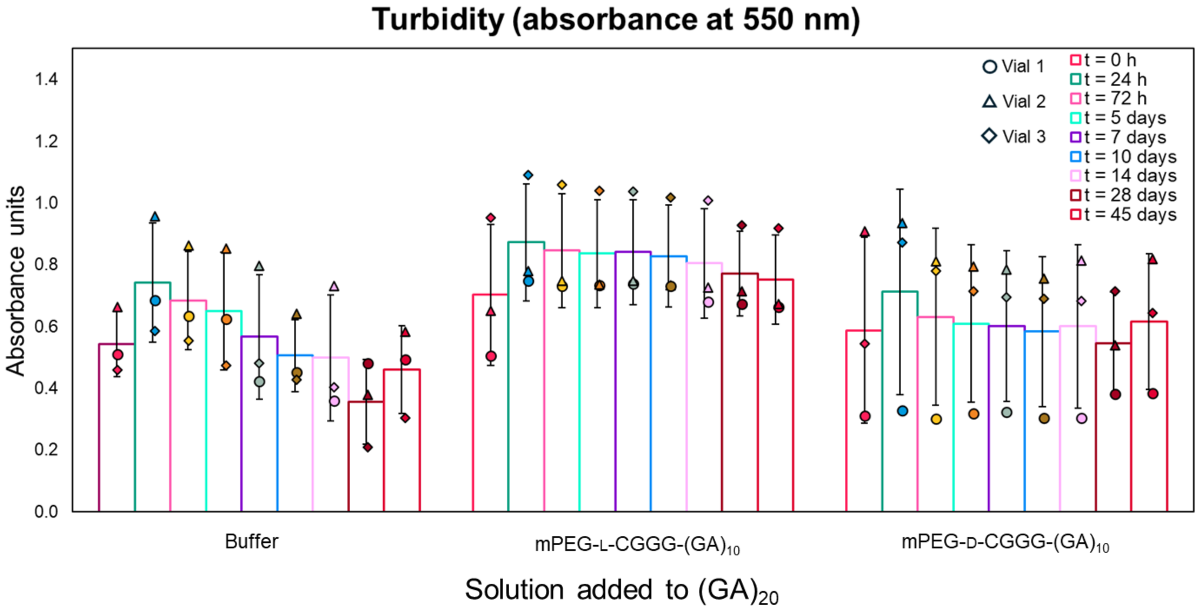

Figure 4.11. Turbidity over time for $(GA)_{20}$ aggregated for 7 days, then treated with no further additives, 7 mg/mL mPEG-L-CGGG-$(GA)_{10}$, or 7 mg/mL mPEG-D-CGGG-$(GA)_{10}$. The time indicates the days since treatment was added, rather than total days of aggregation. There is little difference in turbidity between

the three treatment conditions, indicating that mPEG-L-CGGG-$(GA)_{10}$ and mPEG-D-CGGG-$(GA)_{10}$ did not affect the aggregation of $(GA)_{20}$ over this time period.

4.2.9. Multivalent presentation of peptide content on star-shaped conjugates

Changing the architecture of the polymer-peptide conjugate is expected to change the presentation of the peptide component to the environment, and therefore may change the efficiency of the conjugate's interaction with $(GA)_n$ in solution. We prepared conjugates on 4-arm PEG-maleimide (20k) and 4-arm PEG-maleimide (10k) to alter both the presentation style and the ratio of polymer to peptide in the conjugate. If full conversion is achieved for these conjugations (all 4 arms of the polymer react with one peptide each), then the 20k polymer would have the same polymer: peptide ratio as the linear conjugate (20k: 4 peptides compared to 5k: 1 peptide). Meanwhile, the density of peptide on the conjugate would be twice as high for full conversion of the 10k polymer. Conjugates with both 4-arm polymers were prepared using the same reaction conditions as the linear conjugates (1 mM each of peptide and polymer in 7 M urea, 2: 1 volume ratio of peptide: polymer, 1 h reaction at room temperature) and purified by dialysis in a 3.5 kDa dialysis membrane against deionized water. However, after purification, we found that each of these conjugates was insoluble in aqueous solution even at concentrations as low as 0.5 mg/mL (**Figure C27**). Changing the peptide presentation had a significant effect on the aggregation behavior of the conjugates themselves, regardless of whether the polymer: peptide ratio of the 4-arm conjugate was the same as the polymer: peptide ratio of the linear conjugate. We hypothesize that the dramatic decrease in solubility for the 4-arm conjugates is due to a lack of flexibility required for the hydrophilic PEG component to fully wrap the hydrophobic peptide and form a hydrophilic shell. The linear conjugate, despite having the same polymer: peptide ratio as the conjugates of the 20k 4-arm PEG, has a more flexible PEG component that likely more easily forms a hydrophilic shell around the peptide, giving it the cylindrical micelle shape observed in TEM. Without the hydrophilic shell to solubilize the 4-arm conjugates, they aggregate in aqueous solution at much lower concentrations than the linear conjugates. To make multivalent conjugates that are effective as therapeutics, a balance will need to be struck where a more hydrophobic peptide component will drive stronger interactions with $(GA)_n$ but lead to a greater propensity for the conjugate to aggregate. Finding a different polymer component, whether that be a longer PEG chain or a different, more hydrophilic polymer (perhaps a zwitterion, for example poly(sulfobetaine methacrylate)), will be an important piece of this balance.

4.3 Conclusions

This work demonstrates a synthetic system designed to target toxic, aggregating $(GA)_n$ DPRs that are implicated in amyotrophic lateral sclerosis. Polymer-peptide conjugates with a hydrophilic PEG polymer component and a hydrophobic $(GA)_{10}$ peptide component not only stop the aggregation of a model DPR, $(GA)_{10}$, but are also capable of breaking up aggregates that have already formed. This is supported by decreases in the turbidity of $(GA)_{10}$ solutions incubated with D- or L-conjugates over time, whereas the turbidity of $(GA)_{10}$ solutions incubated with polymer alone or buffer alone increase over time. Additionally, TEM images reveal significant morphological differences, with a much more advanced aggregation state for $(GA)_{10}$ incubated in buffer or with polymer alone compared to $(GA)_{10}$ incubated with conjugates. While we expected that using conjugates with D-peptides might be more effective than conjugates with L-peptides due to previous reports of β-sheet peptides that form stronger interactions between D and L, we saw little difference in the effectiveness of our D- and L-conjugates in preventing and dispersing aggregation, leaving open questions about the design rules of stereochemistry-directed interactions. These data represent a unique middle ground where the D-peptides in the conjugate clearly interact with the L-$(GA)_{10}$, but don't interact more strongly than L-conjugates. In previous examples with other peptide systems, heterochiral interactions were either stronger than homochiral or did not occur at all; the unique interaction between D- and L-$(GA)_{10}$ deserves further investigation to further elucidate the design rules for stereochemistry-directed interactions. While both conjugates were effective against $(GA)_{10}$, they were less effective in breaking up aggregates of a longer model DPR, $(GA)_{20}$. Since native toxic $(GA)_n$ DPRs are hundreds to thousands of repeats in length, further investigation into a method that allows shorter length peptide components to effectively disaggregate longer $(GA)_n$ is critical. Going forward, focus should be turned to finding conjugate components that will allow for multivalent conjugates, whether as 4-arm star-shaped, comb-shaped, or another form of conjugate to expand knowledge of the relationship between polymer architecture and $(GA)_n$ targeting. The design of a synthetic therapeutic that is effective at both preventing and disrupting aggregation is a crucial step toward optimizing therapeutics that are less difficult/expensive to produce and less cold chain-dependent than current biologics, and this work represents an important foundation building toward that goal.

4.4 Materials and methods

4.4.1. Materials

Potassium phosphate dibasic (≥98%), potassium phosphate monobasic (≥99.0%), sodium hydroxide (NaOH, 97%) pellets, acetonitrile (HPLC grade), trifluoracetic acid (TFA, 99%), hydrochloric acid (37 wt%), dimethylformamide (DMF, ≥99.8%), diethyl ether (≥99.0%, contains butylated hydroxytoluene as inhibitor), triisopropylsilane (98%), piperidine (≥99%), 2,2′-(ethylenedioxy)diethanethiol (95%), diisopropyl carbodiimde (99%), methoxypolyethylene glycol maleimide 5,000 (≥90%), 4arm-PEG20K-Maleimide, and 4arm-PEG10K-Maleimide were purchased from Sigma-Aldrich. Urea (99.0-100.5%) was purchased from Avantor. Fmoc-Gly-OH, Fmoc-Ala-OH, and Fmoc-Cys(Trt) were purchased from Advanced ChemTech. Water purified by reverse osmosis (RO water) was obtained from an in-house supply and ultrapure water (18.2 MΩ cm) was obtained from a Thermo Scientific Smart2Pure water purification system. All chemicals were used without further purification.

4.4.2. Peptide synthesis

$(GA)_{10}$, $(GA)_{20}$, L-CGGG-$(GA)_{10}$, and D-CGGG-$(GA)_{10}$ were synthesized on a CEM Corporation Liberty Blue automated, microwave-assisted peptide synthesizer. Synthesis was performed using standard Fmoc methods on a Rink amide resin SS (0.5 mmol/g substitution, 100-200 mesh, 1% divinylbenzene, Advanced ChemTech). First, the resin was swelled in DMF for 5 minutes, then two “dummy coupling” steps were performed, designed to add DMF to the reaction vessel and heat to 90 °C like a normal coupling method. These dummy couplings ensure that the instrument is fully warmed up and consistently hitting the target temperature before the actual coupling methods begin. To grow the chain, Fmoc-protected amino acids are added to the reaction vessel and the Fmoc protecting group is removed using 20% (v/v) piperidine in DMF. The coupling reaction is then performed by adding diisopropyl carbodiimide (1 M in DMF) and Oxyma Pure (1 M in DMF) to the reaction vessel and heating to 90 °C for 2 min. The same steps for Fmoc removal and coupling are repeated until the peptide is built from C-terminus to N-terminus.

The peptides were cleaved from the resin and Trt side chain protecting groups were removed from the Cys residues via a 3 h, room temperature reaction in a solution of 92.5% TFA, 2.5% triisopropylsilane, 2.5% 2,2′-(ethylenedioxy)diethanethiol, and 2.5% deionized water. Following the reaction, the mixture was precipitated in cold ether and centrifuged (4816 x g for 5 min at 4 °C) to obtain a peptide pellet. This pellet was suspended once more in cold ether and centrifuged under the same conditions, before being dried under vacuum for 45 minutes. Dried peptides were dissolved in RO water, frozen in liquid nitrogen, lyophilized, and stored as powders at -20 °C.

4.4.3. Nuclear magnetic resonance (NMR) spectroscopy

Peptides or conjugates were dissolved at 5-7 mg/mL in deuterium oxide (D_2O) or deuterated dimethyl sulfoxide (DMSO-d6). ^1H NMR spectroscopy was conducted on a 600 MHz Bruker Avance III spectrometer equipped with a 5 mm HCN Zpfg probe. Chemical shifts were referenced to the solvent residual peak (either 2.50 or 4.79 ppm for DMSO-d6 or D_2O, respectively).

4.4.4. Matrix-assisted laser desorption/ionization (MALDI) time-of-flight (TOF) mass spectrometry

MALDI-TOF samples were prepared in RO water at a concentration of ~1 mg/mL. Samples were mixed 1:1 with a 5 mg/mL solution of cyano-4-hydroxycinnamic acid (CHCA) matrix prepared in 70% (v/v) acetonitrile in water + 0.1% TFA by pipetting up and down 6 times (2 μL of sample + 2 μL of CHCA matrix). A 2 μL aliquot of this solution was pipetted onto a FlexiMass SR48 target plate (Shimadzu) and dried at room temperature. The dried sample was loaded into a Shimadzu 8030 MALDI-TOF instrument, which was calibrated using MALDI TOFMix (LaserBio Labs) calibrant before every use.

4.4.5. Analytical-scale high performance liquid chromatography (HPLC)

$(GA)_{10}$ was dissolved at 0.5 mg/mL in HPLC solvent (95% ultrapure water + 0.1% TFA, 5% acetonitrile + 0.1% TFA) and double filtered (0.45 μm polytetrafluoroethylene membranes, 13 mm, VWR) to obtain a clear solution and remove aggregates. D- and L-CGGG-$(GA)_{10}$ were dissolved at 1 mg/mL in HPLC solvent and double filtered to obtain a clear solution. Samples were loaded into 2 mL vials and HPLC was performed on a Waters Alliance e2695 HPLC system with a 2998 photodiode array detector with separation achieved using an XBridge C18 reverse-phase column (4.6 x 75 mm, 3.5 μm particle size). Peptides were eluted using a 1 mL/min linear gradient from 5-95% (v/v) acetonitrile + 0.1% TFA in water + 0.1% TFA over 9 min with the column operating at 35 °C. Elution was monitored by absorbance at 214 nm.

4.4.6. Conjugation of CGGG-$(GA)_{10}$ peptides to poly(ethylene glycol)

Thiol-maleimide chemistry was used to conjugate D- or L-CGGG-$(GA)_{10}$ to poly(ethylene glycol) (PEG). The same reaction conditions were used for linear methoxy poly(ethylene glycol) (5,000), 4-arm poly(ethylene glycol) (20,000), and 4-arm poly(ethylene glycol) (10,000). Both peptide and polymer were dissolved at a concentration of 1 mM in 7 M urea dissolved in ultrapure water. Each sample was vortexed for 30 s and sonicated in a sonication bath for 15 s to fully dissolve the peptide or polymer. The pH was then adjusted to 6.5-6.9 for both solutions using 1-5 µL of 1 M NaOH or 1 M HCl. The pH was kept in this range to favor the thiol-maleimide reaction over an amine-maleimide reaction that becomes more favorable at higher pH. Peptide and polymer solutions were mixed at a volume ratio of 2:1 peptide: polymer (6.6 mL of peptide solution to 3.3 mL of polymer solution) to drive the reaction to completion (see Appendix C4.1). The mixture was stirred for 30 s on a Heidolph Hei-plate magnetic stir plate before the pH was checked again to ensure it remained between 6.5-6.9. The reaction mixture was allowed to stir for 1 h at room temperature before purification. For the 4-arm conjugates, purification was achieved by dialysis using a 3.5 kDa dialysis membrane dialyzed against RO water. For the linear conjugates, purification was achieved using preparative-scale HPLC. Preparative-scale HPLC was not used for 4-arm conjugates due to low yields (~5%).

4.4.7. mPEG-CGGG-$(GA)_{10}$ conjugate purification by preparative-scale HPLC

After 1 h of reaction, the reaction mixture described above was double filtered and directly loaded into the injection loop of a Waters 2545 HPLC system with an attached

2489 photodiode array detector and Waters Fraction Collector III collection system. The mixture was separated on an XBridge C18 reverse-phase column (30 x 150 mm, 5 µm particle size) using a gradient from 5% to 30% acetonitrile in water + 0.1% TFA from 2.22 to 4 min and 30% to 60% acetonitrile in water + 0.1% TFA from 4 min to 18 min. Fractions of eluent were collected in glass culture tubes (13 x 100 mm, VWR) and fractions that eluted from the desired peak were combined and lyophilized. The powders obtained from lyophilization were stored at -20 °C.

4.4.8. Turbidity experiments: co-incubation

For turbidity experiments, 3.6 mg of peptide powder was added to 7 mL vials. Separately, solutions of polymer or conjugate were prepared at concentrations of 35, 7, or 0.35 mg/mL and vortexed to dissolve. To start the experiment, 1.2 mL of buffer, polymer, or conjugate solution was added to the vials containing peptide. A stir bar (either 4.3x9.4 mm egg-shaped or 3.1x12.7 mm cylindrical) was added and solutions were stirred at 300 rpm on a Heidolph Hei-plate magnetic stir plate at room temperature. At the designated time points, 3 aliquots of 200 µL were added to a 96 well plate from each vial. Absorbance at 550 nm was measured on a Tecan Infinite M Plex plate reader. After the absorbance measurement, the 200 µL aliquots were returned to stirring in their original vials until the next time point. The values reported are the average of three 200 µL aliquots per vial subtracted by the average absorbance of three 200 µL aliquots of 10 mM phosphate buffer.

4.4.9. Turbidity experiments: pre-aggregation

The turbidity experiments probing pre-aggregation were conducted in the same way as the co-incubation experiments, with the exception that 1.2 mL of buffer was added to all vials of peptide. From that time, the solutions were stirred under the same conditions for 7 days to allow $(GA)_{10}$ or $(GA)_{20}$ to aggregate naturally without any added polymer or conjugate. After 7 days of incubation in buffer, the proper amount of polymer or conjugate was added directly to the vials in powder form. The values reported are the average of three 200 μL aliquots per vial subtracted by the average absorbance of three 200 μL aliquots of 10 mM phosphate buffer.

4.4.10. Thioflavin T fluorescence

For $(GA)_{10}$ thioflavin T fluorescence, we prepared $(GA)_{10}$ solutions at 3, 1.5, 0.75, 0.35, 0.15, and 0.04 mg/mL in 10 mM phosphate buffer. Each solution was prepared separately rather than by dilution because $(GA)_{10}$ is not fully soluble at all of these concentrations, so a dilution would not be reliable. We then prepared a 10 mM stock solution of thioflavin T and diluted the stock solution into each $(GA)_{10}$ solution to yield a final concentration of 10 μM thioflavin T in each vial. The vials were stirred for 75 min, then fluorescence was measured on a Tecan Infinite M Plex plate reader with an excitation wavelength of 450 nm and an emission wavelength of 482 nm.

For thioflavin T fluorescence measured during the turbidity study, we prepared a fresh stock solution of thioflavin T at 1 mM for each day a measurement was taken and then diluted this stock to 100 μM. After absorbance at 550 nm was measured for turbidity, 20 μL of the 100 μM stock solution was added to each 200 μL well in the 96 well plate, for a final concentration of 10 μM thioflavin T in each well. Fluorescence was measured at the same time points as the turbidity experiment on a Tecan Infinite M Plex plate reader with an excitation wavelength of 450 nm and an emission wavelength of 482 nm.

4.4.11. TEM imaging

To monitor morphological changes during the turbidity experiment, 10 μL aliquots were taken from one vial from each condition at the same time points as the turbidity experiments and frozen at -20 °C until sample grids were ready to be prepared. Samples were prepared on carbon-coated copper grids (300 mesh, Electron Microscopy Sciences), which were pretreated in a plasma cleaner with 20% v/v $O2_{(g)}$ and 80% v/v $Ar_{(g)}$ for 30 s. To apply the samples to the grids, 3 μL of sample were pipetted onto the grids and left for 1 min, blotted with filter paper by placing the filter paper at the edge of the grid to wick away excess solution, and washed three times by dabbing and blotting off 10 μL of RO water. Washed grids were dried for 1 min before adding 3 μL of 2% aqueous uranyl acetate staining solution for 1 min. Excess uranyl acetate solution was blotted with filter paper and the samples were air dried. Samples were imaged on an FEI Titan instrument operating at an accelerating voltage of 120 kV at magnifications ranging from 8,100x to 34,000x.

4.5 References

(1) Taylor, J. P.; Brown, R. H.; Cleveland, D. W. Decoding ALS: From Genes to Mechanism. *Nature* **2016**, *539*, 197–206. https://doi.org/10.1038/nature20413.

(2) Simmons, Z. Patient-Perceived Outcomes and Quality of Life in ALS.

Neurotherapeutics **2015**, *12*, 394–402. https://doi.org/10.1007/s13311-014-0322-x.

(3) Al-chalabi, A.; Hardiman, O. The Epidemiology of ALS : A Conspiracy of Genes , Environment and Time. *Nat. Rev. | Neurol.* **2013**, *9*, 617–628. https://doi.org/10.1038/nrneurol.2013.203.

(4) Arthur, K. C.; Calvo, A.; Price, T. R.; Geiger, J. T.; Chiò, A.; Traynor, B. J. Projected Increase in Amyotrophic Lateral Sclerosis from 2015 to 2040. *Nat. Commun.* **2016**, *7*, 12408. https://doi.org/10.1038/ncomms12408.

(5) Miller, R. G.; Mitchell, J. D.; Lyon, M.; Moore, D. H. Riluzole for Amyotrophic Lateral Sclerosis (ALS)/Motor Neuron Disease (MND). *Cochrane Database Syst. Rev.* **2012**, No. 3, CD001447. https://doi.org/10.1002/14651858.CD001447.pub2.

(6) Abe, K.; Aoki, M.; Tsuji, S.; Itoyama, Y.; Sobue, G.; Togo, M.; Hamada, C.; Tanaka, M.; Akimoto, M.; Nakamura, K.; Takahashi, F.; Kondo, K.; Yoshino, H.; Abe, K.; Aoki, M.; Tsuji, S.; Itoyama, Y.; Sobue, G.; Togo, M.; Hamada, C.; Sasaki, H.; Yabe, I.; Doi, S.; Warita, H.; Imai, T.; Ito, H.; Fukuchi, M.; Osumi, E.; Wada, M.; Nakano, I.; Morita, M.; Ogata, K.; Maruki, Y.; Ito, K.; Kano, O.; Yamazaki, M.; Takahashi, Y.; Ishiura, H.; Ogino, M.; Koike, R.; Ishida, C.; Uchiyama, T.; Mizoguchi, K.; Obi, T.; Watanabe, H.; Atsuta, N.; Aiba, I.; Taniguchi, A.; Sawada, H.; Hazama, T.; Fujimura, H.; Kusaka, H.; Kunieda, T.; Kikuchi, H.; Matsuo, H.; Ueyama, H.; Uekawa, K.; Tanaka, M.; Akimoto, M.; Ueda, M.; Murakami, A.; Sumii, R.; Kudou, T.; Nakamura, K.; Morimoto, K.; Yoneoka, T.; Hirai, M.; Sasaki, K.; Terai, H.; Natori, T.; Matsui, H.; Kotani, K.; Yoshida, K.;

Iwasaki, T.; Takahashi, F.; Kondo, K.; Yoshino, H. Safety and Efficacy of Edaravone in Well Defined Patients with Amyotrophic Lateral Sclerosis: A Randomised, Double-Blind, Placebo-Controlled Trial. *Lancet Neurol.* **2017**, *16*, 505–512. https://doi.org/10.1016/S1474-4422(17)30115-1.

(7) Miller, R. G.; Appel, S. H. Introduction to Supplement: The Current Status of Treatment for ALS. *Amyotroph. Lateral Scler. Front. Degener.* **2017**, *18*, 1–4. https://doi.org/10.1080/21678421.2017.1361447.

(8) Majounie, E.; Renton, A. E.; Mok, K.; Dopper, E. G. P.; Waite, A.; Rollinson, S.; Chiò, A.; Restagno, G.; Nicolaou, N.; Simon-Sanchez, J.; van Swieten, J. C.; Abramzon, Y.; Johnson, J. O.; Sendtner, M.; Pamphlett, R.; Orrell, R. W.; Mead, S.; Sidle, K. C.; Houlden, H.; Rohrer, J. D.; Morrison, K. E.; Pall, H.; Talbot, K.; Ansorge, O.; Hernandez, D. G.; Arepalli, S.; Sabatelli, M.; Mora, G.; Corbo, M.; Giannini, F.; Calvo, A.; Englund, E.; Borghero, G.; Floris, G. L.; Remes, A. M.; Laaksovirta, H.; McCluskey, L.; Trojanowski, J. Q.; Van Deerlin, V. M.; Schellenberg, G. D.; Nalls, M. A.; Drory, V. E.; Lu, C. S.; Yeh, T. H.; Ishiura, H.; Takahashi, Y.; Tsuji, S.; Le Ber, I.; Brice, A.; Drepper, C.; Williams, N.; Kirby, J.; Shaw, P.; Hardy, J.; Tienari, P. J.; Heutink, P.; Morris, H. R.; Pickering-Brown, S.; Traynor, B. J.; Adamson, G.; Bayer, A. J.; Beck, J.; Callister, J. B.; Blake, D. J.; Blumen, S. C.; Collinge, J.; Dunckley, T.; Ealing, J.; East, S.; Elman, L.; Gerhard, A.; Guerreiro, R. J.; Gwinn, K.; Halliwell, N.; Hamdalla, H. H.; Hewitt, C.; Ince, P.; Jablonka, S.; James, C.; Kent, L.; Knock, J. C.; Lynch, T.; Mahoney, C.; Mann, D.; Neal, J.; Norris, D.; O’Dowd, S.; Richardson, A.; Rossor, M.; Rothstein, J.; Scholz, S. W.; Snowden, J.; Stephan, D. A.; Toulson, G.; Turner, M. R.; Warren, J. D.;

Young, K.; Weng, Y. H.; Kuo, H. C.; Lai, S. C.; Huang, C. L.; Camuzat, A.; Entraingues, L.; Guillot-Noël; Verpillat, P.; Clerget-Darpoux, F.; Corcia, P.; Couratier, P.; Didic, M.; Dubois, B.; Duyckaerts, C.; Guedj, E.; Golfier, V.; Habert, M. O.; Hannequin, D.; Lacomblez, L.; Meininger, V.; Salachas, F.; Levy, R.; Michel, B. F.; Pasquier, F.; Puel, M.; Thomas-Anterion, C.; Sellal, F.; Vercelletto, M.; Moglia, C.; Cammarosano, S.; Canosa, A.; Gallo, S.; Brunetti, M.; Ossola, I.; Marinou, K.; Papetti, L.; Pisano, F.; Pinter, G. L.; Conte, A.; Luigetti, M.; Zollino, M.; Lattante, S.; Marangi, G.; la Bella, V.; Spataro, R.; Colletti, T.; Battistini, S.; Ricci, C.; Caponnetto, C.; Mancardi, G.; Mandich, P.; Salvi, F.; Bartolomei, I.; Mandrioli, J.; Sola, P.; Lunetta, C.; Penco, S.; Monsurrò, M. R.; Tedeschi, G.; Conforti, F. L.; Gambardella, A.; Quattrone, A.; Volanti, P.; Floris, G.; Cannas, A.; Piras, V.; Marrosu, F.; Marrosu, M. G.; Murru, M. R.; Pugliatti, M.; Parish, L. D.; Sotgiu, A.; Solinas, G.; Ulgheri, L.; Ticca, A.; Simone, I.; Logroscino, G. Frequency of the C9orf72 Hexanucleotide Repeat Expansion in Patients with Amyotrophic Lateral Sclerosis and Frontotemporal Dementia: A Cross-Sectional Study. *Lancet Neurol.* **2012**, *11*, 323–330. https://doi.org/10.1016/S1474-4422(12)70043-1.

(9) Renton, A. E.; Majounie, E.; Waite, A.; Simón-Sánchez, J.; Rollinson, S.; Gibbs, J. R.; Schymick, J. C.; Laaksovirta, H.; van Swieten, J. C.; Myllykangas, L.; Kalimo, H.; Paetau, A.; Abramzon, Y.; Remes, A. M.; Kaganovich, A.; Scholz, S. W.; Duckworth, J.; Ding, J.; Harmer, D. W.; Hernandez, D. G.; Johnson, J. O.; Mok, K.; Ryten, M.; Trabzuni, D.; Guerreiro, R. J.; Orrell, R. W.; Neal, J.; Murray, A.; Pearson, J.; Jansen, I. E.; Sondervan, D.; Seelaar, H.; Blake, D.; Young, K.;

Halliwell, N.; Callister, J. B.; Toulson, G.; Richardson, A.; Gerhard, A.; Snowden, J.; Mann, D.; Neary, D.; Nalls, M. A.; Peuralinna, T.; Jansson, L.; Isoviita, V. M.; Kaivorinne, A. L.; Hölttä-Vuori, M.; Ikonen, E.; Sulkava, R.; Benatar, M.; Wuu, J.; Chiò, A.; Restagno, G.; Borghero, G.; Sabatelli, M.; Heckerman, D.; Rogaeva, E.; Zinman, L.; Rothstein, J. D.; Sendtner, M.; Drepper, C.; Eichler, E. E.; Alkan, C.; Abdullaev, Z.; Pack, S. D.; Dutra, A.; Pak, E.; Hardy, J.; Singleton, A.; Williams, N. M.; Heutink, P.; Pickering-Brown, S.; Morris, H. R.; Tienari, P. J.; Traynor, B. J. A Hexanucleotide Repeat Expansion in C9ORF72 Is the Cause of Chromosome 9p21-Linked ALS-FTD. *Neuron* **2011**, *72*, 257–268. https://doi.org/10.1016/j.neuron.2011.09.010.

(10) DeJesus-Hernandez, M.; Mackenzie, I. R.; Boeve, B. F.; Boxer, A. L.; Baker, M.; Rutherford, N. J.; Nicholson, A. M.; Finch, N. C. A.; Flynn, H.; Adamson, J.; Kouri, N.; Wojtas, A.; Sengdy, P.; Hsiung, G. Y. R.; Karydas, A.; Seeley, W. W.; Josephs, K. A.; Coppola, G.; Geschwind, D. H.; Wszolek, Z. K.; Feldman, H.; Knopman, D. S.; Petersen, R. C.; Miller, B. L.; Dickson, D. W.; Boylan, K. B.; Graff-Radford, N. R.; Rademakers, R. Expanded GGGGCC Hexanucleotide Repeat in Noncoding Region of C9ORF72 Causes Chromosome 9p-Linked FTD and ALS. *Neuron* **2011**, *72*, 245–256. https://doi.org/10.1016/j.neuron.2011.09.011.

(11) Zu, T.; Gibbens, B.; Doty, N. S.; Gomes-Pereira, M.; Huguet, A.; Stone, M. D.; Margolis, J.; Peterson, M.; Markowski, T. W.; Ingram, M. A. C.; Nan, Z.; Forster, C.; Low, W. C.; Schoser, B.; Somia, N. V.; Clark, H. B.; Schmechel, S.; Bitterman, P. B.; Gourdon, G.; Swanson, M. S.; Moseley, M.; Ranum, L. P. W. Non-ATG-

Initiated Translation Directed by Microsatellite Expansions. *Proc. Natl. Acad. Sci.* **2011**, *108* (1), 260–265. https://doi.org/10.1073/pnas.1013343108.

(12) Zu, T.; Liu, Y.; Bañez-Coronel, M.; Reid, T.; Pletnikova, O.; Lewis, J.; Miller, T. M.; Harms, M. B.; Falchook, A. E.; Subramony, S. H.; Ostrow, L. W.; Rothstein, J. D.; Troncoso, J. C.; Ranum, L. P. W. RAN Proteins and RNA Foci from Antisense Transcripts in C9ORF72 ALS and Frontotemporal Dementia. *Proc. Natl. Acad. Sci.* **2013**, *110* (51), E4968–E4977. https://doi.org/10.1073/pnas.1315438110.

(13) Waite, A. J.; Bäumer, D.; East, S.; Neal, J.; Morris, H. R.; Ansorge, O.; Blake, D. J. Reduced C9orf72 Protein Levels in Frontal Cortex of Amyotrophic Lateral Sclerosis and Frontotemporal Degeneration Brain with the C9ORF72 Hexanucleotide Repeat Expansion. *Neurobiol. Aging* **2014**, *35*, 1779.e5-1779.e13. https://doi.org/10.1016/j.neurobiolaging.2014.01.016.

(14) Zu, T.; Gibbens, B.; Doty, N. S.; Gomes-Pereira, M.; Huguet, A.; Stone, M. D.; Margolis, J.; Peterson, M.; Markowski, T. W.; Ingram, M. A. C.; Nan, Z.; Forster, C.; Low, W. C.; Schoser, B.; Somia, N. V.; Clark, H. B.; Schmechel, S.; Bitterman, P. B.; Gourdon, G.; Swanson, M. S.; Moseley, M.; Ranum, L. P. W. Non-ATG-Initiated Translation Directed by Microsatellite Expansions. *Proc. Natl. Acad. Sci.* **2011**, *108* (1), 260–265. https://doi.org/10.1073/pnas.1013343108.

(15) Zhang, Y. J.; Gendron, T. F.; Grima, J. C.; Sasaguri, H.; Jansen-West, K.; Xu, Y. F.; Katzman, R. B.; Gass, J.; Murray, M. E.; Shinohara, M.; Lin, W. L.; Garrett, A.; Stankowski, J. N.; Daughrity, L.; Tong, J.; Perkerson, E. A.; Yue, M.; Chew, J.; Castanedes-Casey, M.; Kurti, A.; Wang, Z. S.; Liesinger, A. M.; Baker, J. D.;

Jiang, J.; Lagier-Tourenne, C.; Edbauer, D.; Cleveland, D. W.; Rademakers, R.; Boylan, K. B.; Bu, G.; Link, C. D.; Dickey, C. A.; Rothstein, J. D.; Dickson, D. W.; Fryer, J. D.; Petrucelli, L. C9ORF72 Poly(GA) Aggregates Sequester and Impair HR23 and Nucleocytoplasmic Transport Proteins. *Nat. Neurosci.* **2016**, *19* (5), 668–677. https://doi.org/10.1038/nn.4272.

(16) Zhang, Y. J.; Jansen-West, K.; Xu, Y. F.; Gendron, T. F.; Bieniek, K. F.; Lin, W. L.; Sasaguri, H.; Caulfield, T.; Hubbard, J.; Daughrity, L.; Chew, J.; Belzil, V. V.; Prudencio, M.; Stankowski, J. N.; Castanedes-Casey, M.; Whitelaw, E.; Ash, P. E. A.; DeTure, M.; Rademakers, R.; Boylan, K. B.; Dickson, D. W.; Petrucelli, L. Aggregation-Prone C9FTD/ALS Poly(GA) RAN-Translated Proteins Cause Neurotoxicity by Inducing ER Stress. *Acta Neuropathol.* **2014**, *128*, 505–524. https://doi.org/10.1007/s00401-014-1336-5.

(17) Quaegebeur, A.; Glaria, I.; Lashley, T.; Isaacs, A. M. Soluble and Insoluble Dipeptide Repeat Protein Measurements in C9orf72-Frontotemporal Dementia Brains Show Regional Differential Solubility and Correlation of Poly-GR with Clinical Severity. *Acta Neuropathol. Commun.* **2020**, *8*, 184. https://doi.org/10.1186/s40478-020-01036-y.

(18) Zhou, Q.; Lehmer, C.; Michaelsen, M.; Mori, K.; Alterauge, D.; Baumjohann, D.; Schludi, M. H.; Greiling, J.; Farny, D.; Flatley, A.; Feederle, R.; May, S.; Schreiber, F.; Arzberger, T.; Kuhm, C.; Klopstock, T.; Hermann, A.; Haass, C.; Edbauer, D. Antibodies Inhibit Transmission and Aggregation of C9orf72 Poly-GA Dipeptide Repeat Proteins . *EMBO Mol. Med.* **2017**, *9* (5), 687–702. https://doi.org/10.15252/emmm.201607054.

(19) Khosravi, B.; Hartmann, H.; May, S.; Möhl, C.; Ederle, H.; Michaelsen, M.; Schludi, M. H.; Dormann, D.; Edbauer, D. Cytoplasmic Poly-GA Aggregates Impair Nuclear Import of TDP-43 in C9orf72 ALS/FTLD. *Hum. Mol. Genet.* **2017**, *26* (4), 790–800. https://doi.org/10.1093/hmg/ddw432.

(20) Darling, A. L.; Breydo, L.; Rivas, E. G.; Gebru, N. T.; Zheng, D.; Baker, J. D.; Blair, L. J.; Dickey, C. A.; Koren, J.; Uversky, V. N. Repeated Repeat Problems: Combinatorial Effect of C9orf72-Derived Dipeptide Repeat Proteins. *Int. J. Biol. Macromol.* **2019**, *127*, 136–145. https://doi.org/10.1016/j.ijbiomac.2019.01.035.

(21) Nguyen, L.; Montrasio, F.; Pattamatta, A.; Tusi, S. K.; Bardhi, O.; Meyer, K. D.; Hayes, L.; Nakamura, K.; Banez-Coronel, M.; Coyne, A.; Guo, S.; Laboissonniere, L. A.; Gu, Y.; Narayanan, S.; Smith, B.; Nitsch, R. M.; Kankel, M. W.; Rushe, M.; Rothstein, J.; Zu, T.; Grimm, J.; Ranum, L. P. W. Antibody Therapy Targeting RAN Proteins Rescues C9 ALS/FTD Phenotypes in C9orf72 Mouse Model. *Neuron* **2020**, *105* (4), 645-662.e11. https://doi.org/10.1016/j.neuron.2019.11.007.

(22) Jiang, J.; Zhu, Q.; Gendron, T. F.; Saberi, S.; McAlonis-Downes, M.; Seelman, A.; Stauffer, J. E.; Jafar-nejad, P.; Drenner, K.; Schulte, D.; Chun, S.; Sun, S.; Ling, S. C.; Myers, B.; Engelhardt, J.; Katz, M.; Baughn, M.; Platoshyn, O.; Marsala, M.; Watt, A.; Heyser, C. J.; Ard, M. C.; De Muynck, L.; Daughrity, L. M.; Swing, D. A.; Tessarollo, L.; Jung, C. J.; Delpoux, A.; Utzschneider, D. T.; Hedrick, S. M.; de Jong, P. J.; Edbauer, D.; Van Damme, P.; Petrucelli, L.; Shaw, C. E.; Bennett, C. F.; Da Cruz, S.; Ravits, J.; Rigo, F.; Cleveland, D. W.; Lagier-Tourenne, C. Gain of Toxicity from ALS/FTD-Linked Repeat Expansions in C9ORF72 Is Alleviated by Antisense Oligonucleotides Targeting GGGGCC-Containing RNAs. *Neuron* **2016**,

90, 535–550. https://doi.org/10.1016/j.neuron.2016.04.006.

(23) Awwad, S.; Angkawinitwong, U. Overview of Antibody Drug Delivery. *Pharmaceutics* **2018**, *10* (83), 1–24. https://doi.org/10.3390/pharmaceutics10030083.

(24) Harding, F. A.; Stickler, M. M.; Razo, J.; DuBridge, R. B. The Immunogenicity of Humanized and Fully Human Antibodies: Residual Immunogenicity Resides in the CDR Regions. *MAbs* **2010**, *2* (3), 256–265. https://doi.org/10.4161/mabs.2.3.11641.

(25) Yu, Y. B.; Briggs, K. T.; Taraban, M. B.; Brinson, R. G.; Marino, J. P. Grand Challenges in Pharmaceutical Research Series: Ridding the Cold Chain for Biologics. *Pharm. Res.* **2021**, *38*, 3–7. https://doi.org/10.1007/s11095-021-03008-w.

(26) Song, Y.; Cheng, P.-N.; Zhu, L.; Moore, E. G.; Moore, J. S. Multivalent Macromolecules Redirect Nucleation-Dependent Fibrillar Assembly into Discrete Nanostructures. *J. Am. Chem. Soc.* **2014**, *136*, 5233–5236. https://doi.org/10.1021/ja501102f.

(27) Song, Y.; Moore, E. G.; Guo, Y.; Moore, J. S. Polymer–Peptide Conjugates Disassemble Amyloid β Fibrils in a Molecular-Weight Dependent Manner. *J. Am. Chem. Soc.* **2017**, *139* (12), 4298–4301. https://doi.org/10.1021/jacs.7b00289.

(28) Jiang, X.; Halmes, A. J.; Licari, G.; Smith, J. W.; Song, Y.; Moore, E. G.; Chen, Q.; Tajkhorshid, E.; Rienstra, C. M.; Moore, J. S. Multivalent Polymer − Peptide Conjugates: A General Platform for Inhibiting Amyloid Beta Peptide Aggregation.

ACS Macro Lett. **2019**, *8*, 1365–1371. https://doi.org/10.1021/acsmacrolett.9b00559.

(29) Soto, C.; Sigurdsson, E. M.; Morelli, L.; Kumar, R. A.; Castano, E. M.; Frangione, B. Beta-Sheet Breaker Peptides Inhibit Fibrillogenesis in a Rat Brain Model of Amyloidosis: Implications for Alzheimer's Therapy. *Nat. Med.* **1998**, *4* (7), 822–826.

(30) Swanekamp, R. J.; Dimaio, J. T. M.; Bowerman, C. J.; Nilsson, B. L. Coassembly of Enantiomeric Amphipathic Peptides into Amyloid-Inspired Rippled β-Sheet Fibrils. *J. Am. Chem. Soc.* **2012**, *134*, 5556–5559. https://doi.org/10.1021/ja301642c.

(31) Nagy, K. J.; Giano, M. C.; Jin, A.; Pochan, D. J.; Schneider, J. P. Enhanced Mechanical Rigidity of Hydrogels Formed From Enantiomeric Peptide Assemblies. *J Am Chem Soc* **2011**, *133* (38), 14975–14977. https://doi.org/10.1158/0008-5472.CAN-10-4002.BONE.

(32) Nagy-Smith, K.; Beltramo, P. J.; Moore, E.; Tycko, R.; Furst, E. M.; Schneider, J. P. Molecular, Local, and Network-Level Basis for the Enhanced Stiffness of Hydrogel Networks Formed from Coassembled Racemic Peptides: Predictions from Pauling and Corey. *ACS Cent. Sci.* **2017**, *3*, 586–597. https://doi.org/10.1021/acscentsci.7b00115.

(33) Yang, H.; Yang, S.; Kong, J.; Dong, A.; Yu, S. Obtaining Information about Protein Secondary Structures in Aqueous Solution Using Fourier Transform IR Spectroscopy. *Nat. Protoc.* **2015**, *10* (3), 382–396.

https://doi.org/10.1038/nprot.2015.024.

(34) Liu, X. Y.; Nothias, J. M.; Scavone, A.; Garfinkel, M.; Millis, J. M. Biocompatibility Investigation of Polyethylene Glycol and Alginate-Poly-l-Lysine for Islet Encapsulation. *ASAIO J.* **2010**, *56* (3), 241–245. https://doi.org/10.1097/MAT.0b013e3181d7b8e3.

(35) Joralemon, M. J.; McRae, S.; Emrick, T. PEGylated Polymers for Medicine: From Conjugation to Self-Assembled Systems. *Chem. Commun.* **2010**, *46*, 1377–1393. https://doi.org/10.1039/b920570p.

(36) Monera, O. D.; Kay, C. M.; Hodges, R. S. Protein Denaturation with Guanidine Hydrochloride or Urea Provides. *Protein Sci.* **1994**, *3* (11), 1984–1991.

(37) Yin, S.; Lopez-Gonzalez, R.; Kunz, R. C.; Gangopadhyay, J.; Borufka, C.; Gygi, S. P.; Gao, F. B.; Reed, R. Evidence That C9ORF72 Dipeptide Repeat Proteins Associate with U2 SnRNP to Cause Mis-Splicing in ALS/FTD Patients. *Cell Rep.* **2017**, *19*, 2244–2256. https://doi.org/10.1016/j.celrep.2017.05.056.

Chapter 5. Investigating peptide candidates to target toxic charged proteins implicated in amyotrophic lateral sclerosis

5.1 Introduction

In this chapter, we rationally design peptides to target charged proteins that are implicated in ALS and investigate their thermodynamic properties by isothermal titration calorimetry to inform future studies into polymer-peptide conjugate therapeutics.

Amyotrophic lateral sclerosis (ALS) is a deadly neurodegenerative disease without effective treatment strategies.[1–3] A genetic mutation of the *C9orf72* gene causes one of the most prevalent forms of the disease,[1,4,5] which manifests in accumulation of repeating hexanucleotide RNA foci,[4] loss of the C9orf72 protein,[6] and the production of five dipeptide repeat proteins (DPRs): glycine-alanine $(GA)_n$, glycine-arginine $(GR)_n$, proline-arginine $(PR)_n$, glycine-proline $(GP)_n$, and proline-alanine $(PA)_n$.[7,8] In Chapter 4 we focused on the $(GA)_n$ DPR, but that is not the only DPR produced that is toxic to cells. In particular, the highly cationic $(GR)_n$ and $(PR)_n$ DPRs are highly toxic to neuronal cells when added to cells in culture or expressed in model systems, including fly, mouse, yeast, and worm models.[9–11] $(GR)_n$ and $(PR)_n$ exhibit toxicity through a wide variety of mechanisms. For example, $(GR)_n$ and $(PR)_n$ accumulate in the nucleus (even when externally applied in cultured cells), where they interact with nucleoli and cause defects in RNA processing, ultimately leading to cell death.[12] $(GR)_n$ and $(PR)_n$ also bind to proteins in the nuclear pores, which prevents transport of macromolecules in and out of the nucleus and leads to cell death.[13,14] A variety of intercellular proteins interact with $(GR)_n$ and $(PR)_n$, such as RNA-binding proteins and proteins that are important to the assembly of membraneless organelles. These interactions change the way the proteins function and alter their phase separation, resulting in impaired protein function and contributing to cell death.[15] Given these widespread toxic mechanisms, targeting $(GR)_n$ and $(PR)_n$ for therapeutic intervention would likely have a positive effect across multiple areas of the cell and contribute to improved neuronal health.

Multiple recent reports demonstrate the utility of using antisense oligonucleotides, targeting the mutated region of the *C9orf72* gene, to reduce the levels of $(GR)_n$ and/or $(PR)_n$.[16,17] In cell culture, antisense oligonucleotides reduced the concentration of $(GR)_n$ present in neuronal cells in a mouse model. The reduction of $(GR)_n$ corresponded to a reduction in neurodegeneration for treated mice.[17] Similarly, treatment of mice with the *C9orf72* genetic mutation with antisense oligonucleotides led to decreased levels of all DPRs, including $(GR)_n$ and $(PR)_n$, and treated mice recovered from behavioral deficits.[16] From this evidence, it is clear that reducing the levels of free $(GR)_n$ and $(PR)_n$ DPRs in cells is an effective measure to ameliorate their toxicity to neuronal cells.

As discussed in Chapter 4, while these treatments are promising for ALS therapy, there are several key challenges for the use of biologics as therapeutics. These include time- and cost-intensive production processes, susceptibility to physicochemical alterations during manufacture and transport,[18] enzymatic degradation,[18] undesirable immunogenic effects,[19] and the need for extensive use of cold-chain to deploy these treatments in developing countries.[20]

To address these limitations associated with biological therapeutics, we sought to develop a synthetic therapeutic to sequester $(GR)_n$ and $(PR)_n$ DPRs to prevent their toxic interactions in cells. In a similar manner to the polymer-peptide conjugate materials we developed to target $(GA)_n$ DPRs, we envision polymer-peptide conjugates including a hydrophilic, biocompatible polymer to prevent aggregation of the therapeutic and a $(GR)_n$/$(PR)_n$-binding peptide. In this chapter, we developed a set of peptides and utilized isothermal titration calorimetry (ITC) to determine the strongest binders to $(GR)_n$ and $(PR)_n$. We reasoned that taking advantage of electrostatics would be a way to drive interactions with cationic $(GR)_n$ and $(PR)_n$, so we designed and tested three anionic peptides: $(GE)_{10}$, $(PE)_{10}$, and E_{10}. $(GE)_{10}$ and $(PE)_{10}$ were designed to match the sequence structure of $(GR)_n$ and $(PR)_n$ while substituting the cationic R amino acids for anionic glutamic acids, while E_{10} is anionic with a greater charge density but the same number of charged groups.

This set of peptides is designed to answer several questions. First, do $(GR)_n$ and $(PR)_n$ bind preferentially to peptides that match their alternating sequence structure (*i.e.* does $(GR)_n$ bind mostly strongly to $(GE)_{10}$ and $(PR)_n$ bind most strongly to $(PE)_{10}$)? $(PR)_{12}$ has been reported to form small aggregates with a parallel double-helix structure despite a combination of hydrophilic and electrostatically-repulsive interactions contributed by the R residues, so it may be expected that the $(PR)_n$ DPRs would preferentially assemble with $(PE)_{10}$, driven by helix-helix assembly and leading to stronger binding for $(PE)_{10}$ compared to the other E peptides.[21] No such stable aggregates were observed for $(GR)_{12}$-, so $(GR)_n$ might not be expected to have a similar preference for an E peptide of the same sequence structure.[21]

This set of E peptides will also answer questions about the role of charge density in complexation. E_{10} contains the same number of charged amino acids as $(GE)_{10}$ and $(PE)_{10}$, but the charged amino acids are not separated by neutral amino acids. Charge patterning can have a profound effect on charge-based interactions, as evidenced by differences observed in the complex coacervation of E_{50} and different sequence patterns of GK peptides, where charged K residues are grouped in blocks of 2, 4, 8, or 16 residues (*i.e.* $(GK)_{25}$, $G(KKGG)_{12}K$, $G(K_4G_4)_6K$, and $G(K_8G_8)_3K$).[22] Complexes between E_{50} and GK peptides with larger groups of charged residues (more charge dense) are more stable than peptides having less charge density in both simulations and experiments. This sequence effect was attributed to a larger entropic driving force for complexation for more charge dense peptides, due to a more favorable entropy gain from the release of counterions from the surfaces of more charge dense peptides compared to peptides that are less charge dense. These results suggest that there may be a stronger driving force for $(GR)_n$ and $(PR)_n$ to complex with E_{10} compared to the less charge dense $(GE)_{10}$ and $(PE)_{10}$, but the effects of the sequence structure and charge density may compete against each other, leaving both questions open for this system.

This work will inform the design rules for targeted biomolecular interactions between charged peptides. With these design rules in hand, we can develop an effective polymer-peptide conjugate therapeutic to sequester toxic $(GR)_n$ and $(PR)_n$ DPRs similar to the polymer-peptide conjugates designed to sequester $(GA)_n$ DPRs in Chapter 4. Toward this goal, we report here the thermodynamic characterization of the interactions of $(GE)_{10}$, $(PE)_{10}$, and E_{10} with $(GR)_{10}$ and $(PR)_{10}$.

5.2 Results and discussion

We synthesized $(GE)_{10}$, $(PE)_{10}$, E_{10}, $(GR)_{10}$ and $(PR)_{10}$ in-house and assessed their purity by analytical-scale HPLC (**Figure D1**). $(GE)_{10}$, $(PE)_{10}$, $(GR)_{10}$, and $(PR)_{10}$ were purified by preparative-scale HPLC (**Figure D2**) and mass spectrometry was used to confirm the expected product after purification (**Figure D3**). E_{10} was used with no further purification and the expected product was confirmed using mass spectrometry (**Figure D3**).

5.2.1. Complexation of $(GE)_{10}$, $(PE)_{10}$, and E_{10} with $(GR)_{10}$

We used isothermal titration calorimetry (ITC) to compare the thermodynamics of complexation for the anionic $(GE)_{10}$, $(PE)_{10}$, and E_{10} peptides with cationic $(GR)_{10}$. Titrations were all performed in 10 mM phosphate buffer (pH 7.4) with a 2.5 mM solution of E peptide titrated into a 0.25 mM solution of $(GR)_{10}$. These concentrations were selected as they were found to provide a strong signal to noise ratio for data collected with our ITC. Each solution was pH corrected to pH 7.40 ± 0.05 to ensure that the heat rate observed in the thermogram is a result of peptide interaction and heats of dilution, without contributions from the heats of mixing solutions at different pH. For each titration, the heats of dilution associated with diluting E peptide into buffer and buffer into $(GR)_{10}$ were subtracted from the total heats obtained for the interaction.

The titration of $(GE)_{10}$ into $(GR)_{10}$ resulted in little to no interaction, as the binding that was observed was nearly entirely accounted for by the dilution of $(GE)_{10}$ into buffer, indicating that $(GE)_{10}$ only weakly interacts with $(GR)_{10}$ or does not interact at all (**Figure 5.1A**). On the other hand, a strong interaction was observed for the titration of $(PE)_{10}$ into

$(GR)_{10}$ (**Figure 5.1B**). Large endothermic heats of interaction are observed, which are counteracted by large exothermic heats of dilution for $(PE)_{10}$ diluted in buffer. After subtracting the heats of dilution from the heats of interaction observed, the final binding heats for the $(PE)_{10}$: $(GR)_{10}$ complex have a maximum of 18 kJ/mol, compared to a maximum of -1.9 kJ/mol for the $(GE)_{10}$: $(GR)_{10}$ interaction. For the interaction between E_{10} and $(GR)_{10}$, both small endothermic and exothermic heats are observed (**Figure 5.1C**). For the first several injections, until a molar ratio of ~0.7 E_{10}: $(GR)_{10}$, there is an endothermic domain. In the thermogram, small peaks can be observed that go both above and below the baseline for these injections, indicating a balance of both endothermic and exothermic interactions. When accounting for the heat of dilution of E_{10} into buffer, however, it is clear that these initial interactions are endothermic. At a molar ratio of ~0.7, the interaction becomes exothermic and slightly stronger than the heat of dilution, before matching the heat of dilution at higher molar ratio, indicating that no further interaction is occurring. Ultimately, when it comes to comparing the strength of this E_{10}: $(GR)_{10}$ complex to the $(PE)_{10}$: $(GR)_{10}$ complex, the $(PE)_{10}$: $(GR)_{10}$ complex is stronger as measured by binding heats (maximum endothermic binding heat of 6.5 kJ/mol and maximum exothermic binding heat of -3.0 kJ/mol for E_{10}: $(GR)_{10}$, compared to 18 kJ/mol for $(PE)_{10}$: $(GR)_{10}$). While it would be ideal to compare a thermodynamic parameter such as dissociation constant between groups to determine the strongest binders, none of these data fit well to existing binding models, so we use the relative magnitude of the binding heats to compare peptide-peptide interactions. These data indicate that $(PE)_{10}$ is the strongest binder of $(GR)_{10}$ and therefore would make the best peptide component of a polymer-peptide conjugate therapeutic designed to sequester $(GR)_{10}$ among the peptides studied here.

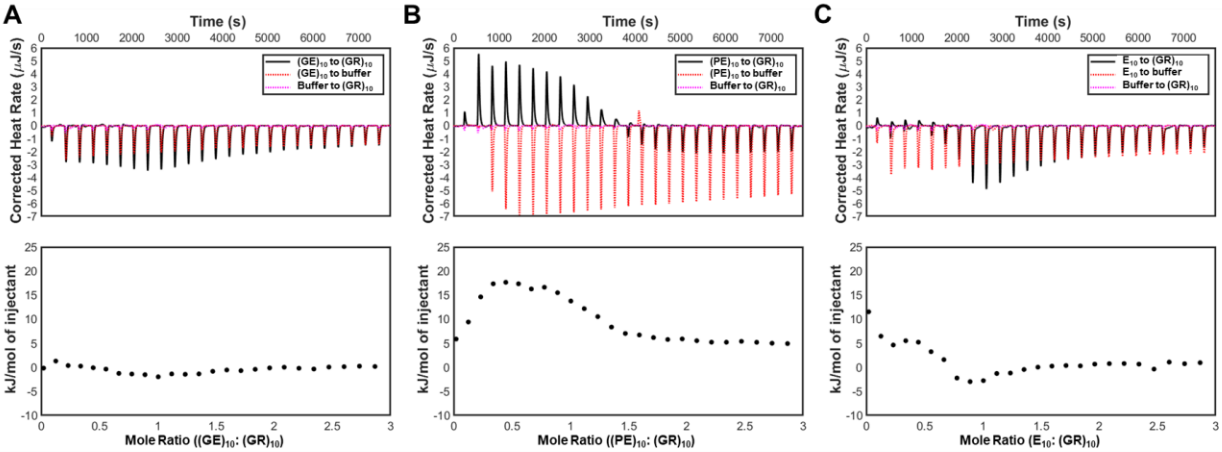

Figure 5.1. Baseline-subtracted thermograms and integrated binding heats of 2.5 mM A) $(GE)_{10}$, B) $(PE)_{10}$, and C) E_{10} titrated into 0.25 mM $(GR)_{10}$ in 10 mM phosphate buffer. Each titration results in a different binding profile.

5.2.2. Complexation of $(GE)_{10}$, $(PE)_{10}$, and E_{10} with $(PR)_{10}$

We used isothermal titration calorimetry (ITC) to compare the thermodynamics of complexation for the anionic $(GE)_{10}$, $(PE)_{10}$, and E_{10} peptides with cationic $(PR)_{10}$. Experiments were conducted similarly to titrations with $(GR)_{10}$: 2.5 mM E peptide was titrated into 0.25 mM $(PR)_{10}$, pH of each solution was corrected to pH 7.40 ± 0.05, and the heats of dilution of E peptide into buffer and buffer into $(PR)_{10}$ were subtracted from the total heats of the interaction.

For these titrations into $(PR)_{10}$, all interactions were observed to be endothermic whereas some were endothermic, some were exothermic, and some were both exothermic and endothermic for the titrations into $(GR)_{10}$ (**Figure 5.2**). The titration of

$(GE)_{10}$ into $(PR)_{10}$ resulted in small endothermic heats of interaction, with a maximum of 7 kJ/mol (**Figure 5.2A**). This suggests a relatively weak interaction between $(GE)_{10}$ and $(PR)_{10}$. On the other hand, a much larger endothermic interaction was observed for $(PE)_{10}$ and $(PR)_{10}$ (**Figure 5.2B**). After subtraction of the large exothermic heats of dilution of $(PE)_{10}$ in buffer, the $(PE)_{10}$: $(PR)_{10}$ interaction has maximum binding heat of 16 kJ/mol, which is similar to the largest binding heat we observed for the interactions with $(GR)_{10}$. In contrast to the mixture of exothermic and endothermic binding domains observed for the interaction of E_{10} with $(GR)_{10}$, the interaction of E_{10} with $(PR)_{10}$ is entirely endothermic, with a maximum binding heat of 11 kJ/mol (**Figure 5.2C**). We again used the magnitudes of the binding heats produced to compare the interactions of $(GE)_{10}$, $(PE)_{10}$, and E_{10} with $(PR)_{10}$ as these data do not fit well to existing binding models. From the maximum binding heats, we observe that $(PE)_{10}$ is the strongest binder of $(PR)_{10}$, with E_{10} being the second strongest and $(GE)_{10}$ having the weakest interaction.

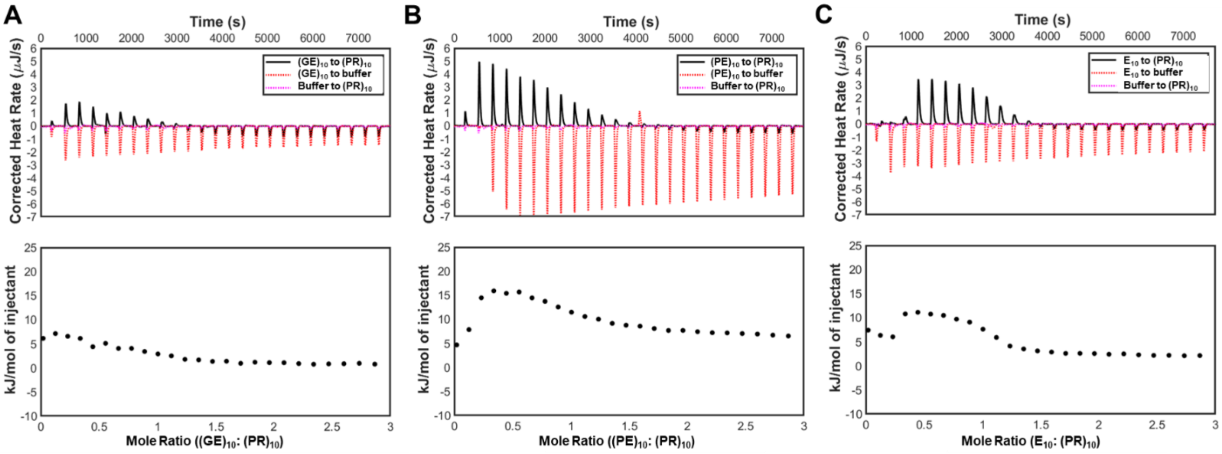

Figure 5.2. Baseline-subtracted thermograms and integrated binding heats of 2.5 mM A) $(GE)_{10}$, B) $(PE)_{10}$, and C) E_{10} titrated into 0.25 mM $(GR)_{10}$ in 10 mM phosphate buffer. These titrations all result in endothermic interactions with different magnitudes, where the endothermic binding heats for the interaction between $(PE)_{10}$ and $(PR)_{10}$ are the largest in magnitude.

5.3 Conclusions

These data demonstrate that $(PE)_{10}$ is the strongest binder to both $(GR)_{10}$ and $(PR)_{10}$ among the peptides tested here, answering questions about peptide structure and charge density. We expected that $(PE)_{10}$ might bind $(PR)_{10}$ most strongly as it has been shown to self-assemble into double helices even without an electrostatic driving force,[21] but it was less expected that the $(PE)_{10}$ would also bind $(GR)_{10}$ the most strongly. Matching sequence structure was clearly not a factor in the strongest binder to $(GR)_{10}$, as $(GE)_{10}$ interacted with it very weakly. Perhaps the $(PE)_{10}$ bound $(GR)_{10}$ strongly in part due to the large number of assembly-prone proline residues in the sequence. Future studies should investigate whether $(PE)_{10}$ forms stable structures in solution both alone and in the presence of $(GR)_{10}$ and $(PR)_{10}$, as such assembly may be entropically favorable to allow the release of structured water and ordered counterions from the surface of each peptide. Further understanding of these phenomena surrounding $(PE)_{10}$ will help inform the design rules for these interactions.

Charge density in these interactions seems to play less of a role than the peptide structure. E_{10}, having a higher charge density than $(GE)_{10}$ and $(PE)_{10}$ was expected to interact more strongly with $(GR)_{10}$ and $(PR)_{10}$. While E_{10} did interact with $(GR)_{10}$ and $(PR)_{10}$ more strongly than $(GE)_{10}$ interacted with either peptide, E_{10} did not bind either as strongly as $(PE)_{10}$. By the comparison between E_{10} and $(GE)_{10}$, it seems that the idea of higher charge density leading to stronger interactions holds true, but the effect of $(PE)_{10}$, whether it be structure-forming or something else, is a larger driver of peptide interaction than charge density.

Moving forward, it will be important to test the efficacy of these E peptides for sequestering $(GR)_{10}$ and $(PR)_{10}$ to corroborate the binding data presented here. E peptides can be conjugated to linear or multivalent polymers to yield conjugates that will remain soluble even if assemblies are formed, similar to the conjugates developed in Chapter 4. The potential to sequester toxic $(GR)_{10}$ and $(PR)_{10}$ DPRs is a promising therapeutic opportunity for ALS and could even be used in conjunction with the antisense oligonucleotide gene therapies that are currently being developed. The design rules explored here contribute to the understanding of how peptides bind to toxic DPRs to aid in the development of such therapeutics.

5.4 Materials and methods

5.4.1 Materials

Potassium phosphate dibasic (≥98%), potassium phosphate monobasic (≥99.0%), sodium hydroxide (NaOH, 97%) pellets, acetonitrile (HPLC grade), trifluoracetic acid (TFA, 99%), hydrochloric acid (37 wt%), dimethylformamide (DMF, ≥99.8%), diethyl ether (≥99.0%, contains butylated hydroxytoluene as inhibitor), triisopropylsilane (98%), piperidine (≥99%), 2,2′-(ethylenedioxy)diethanethiol (95%), and diisopropyl carbodiimde (99%) were purchased from Sigma-Aldrich. Fmoc-Gly-OH, Fmoc-Pro-OH, Fmoc-Arg(Pbf), and Fmoc-Glu(OBut)-OH were purchased from Advanced ChemTech. Water purified by reverse osmosis (RO water) was obtained from an in-house supply and ultrapure water (18.2 MΩ cm) was obtained from a Thermo Scientific Smart2Pure water purification system. All chemicals were used without further purification.

5.4.2 Peptide synthesis

$(GE)_{10}$, $(PE)_{10}$, E_{10}, $(GR)_{10}$, and $(PR)_{10}$ were synthesized on a CEM Corporation Liberty Blue automated, microwave-assisted peptide synthesizer. Synthesis was performed using standard Fmoc methods on a Rink amide resin SS (0.5 mmol/g substitution, 100-200 mesh, 1% divinylbenzene, Advanced ChemTech). First, the resin was swelled in DMF for 5 minutes, then two "dummy coupling" steps were performed, designed to add DMF to the reaction vessel and heat to 90 °C like a normal coupling method. These dummy couplings ensure that the instrument is fully warmed up and consistently hitting the target temperature before the actual coupling methods begin. To grow the chain, Fmoc-protected amino acids are added to the reaction vessel and the Fmoc protecting group is removed using 20% (v/v) piperidine in DMF. The coupling reaction is then performed by adding diisopropyl carbodiimide (1 M in DMF) and Oxyma Pure (1 M in DMF) to the reaction vessel and heating to 90 °C for 2 min. The same steps for Fmoc removal and coupling are repeated until the peptide is built from C-terminus to N-terminus.

The peptides were cleaved from the resin and Trt side chain protecting groups were removed from the Cys residues via a 3 h, room temperature reaction in a solution of 92.5% TFA, 2.5% triisopropylsilane, 2.5% 2,2′-(ethylenedioxy)diethanethiol, and 2.5% deionized water. Following the reaction, the mixture was precipitated in cold ether and centrifuged (4816 x g for 5 min at 4 °C) to obtain a peptide pellet. This pellet was suspended once more in cold ether and centrifuged under the same conditions, before being dried under vacuum for 45 minutes. Dried peptides were dissolved in RO water, frozen in liquid nitrogen, lyophilized, and stored as powders at -20 °C.

5.4.3 Matrix-assisted laser desorption ionization – time of flight mass spectrometry

MALDI-TOF samples were prepared in RO water at a concentration of ~1 mg/mL. Samples were mixed 1:1 with a 5 mg/mL solution of cyano-4-hydroxycinnamic acid (CHCA) matrix prepared in 70% (v/v) acetonitrile in water + 0.1% TFA by pipetting up and down 6 times (2 µL of sample + 2 µL of CHCA matrix). A 2 µL aliquot of this solution was pipetted onto a FlexiMass SR48 target plate (Shimadzu) and dried at room temperature. The dried sample was loaded into a Shimadzu 8030 MALDI-TOF instrument, which was calibrated using MALDI TOFMix (LaserBio Labs) calibrant **on each plate**.

5.4.4 Analytical-scale high performance liquid chromatography (HPLC)

Peptides were dissolved at 1 mg/mL in HPLC solvent (95% ultrapure water + 0.1% TFA, 5% acetonitrile + 0.1% TFA) and filtered (0.45 µm polytetrafluoroethylene membranes, 13 mm, VWR) to obtain a clear solution. Samples were loaded into 2 mL vials and HPLC was performed on a Waters Alliance e2695 HPLC system with a 2998 photodiode array detector with separation achieved using an XBridge C18 reverse-phase column (4.6 x 75 mm, 3.5 µm particle size). Peptides were eluted using 1 mL/min gradients that are listed with the characterization.

5.4.5 Peptide purification by preparative-scale HPLC

To purify peptides, 20-40 mg of peptide was dissolved in 10 mL HPLC solvent (95% ultrapure water + 0.1% TFA, 5% acetonitrile + 0.1% TFA) and twice filtered through 25 mm syringe filters with 0.45 µm polytetrafluoroethylene membranes. The filtered solution was loaded into the injection loop of a Waters 2545 HPLC system with an attached 2489 photodiode array detector and Waters Fraction Collector III collection system. The sample was separated on an XBridge C18 reverse-phase column (30 x 150 mm, 5 µm particle size). The gradients used to achieve separation are listed in Table D1. Eluent was collected in 13 x 100 mm glass culture tubes (VWR) and the fractions of eluent that eluted from the desired product peak were combined and lyophilized. The lyophilized powders were used to obtain HPLC chromatograms and mass spectra of purified peptides and then were stored as powders at -20 °C.

5.4.6 Isothermal titration calorimetry (ITC)

ITC experiments were performed on a standard volume Affinity ITC (TA Instruments). All peptide solutions were prepared at 2.5 mM or 0.25 mM in 10 mM phosphate buffer, pH corrected to 7.40 ± 0.05 by adding 1-10 µL of 1 M NaOH, and degassed for 5-10 min using a TA Instruments degassing station at 400 mm Hg. The titrant and titrand pH were always checked to ensure they were with pH 7.40 ± 0.05 immediately prior to experiments to avoid substantial heat contributions from the heat of mixing of solutions with different pH. Titrations consisted of an initial 2 µL injection followed by 24 10 µL injections of 2.5 mM titrant solution injected into 1.3 mL of 0.25 mM titrand solution. Following an initial delay of 200 s, injections were separated by 300 s. Experiments were performed at 25 °C with a stirring rate of 125 rpm. The reference cell was filled with 1.3 mL of degassed, deionized water that is exchanged weekly. The resulting thermograms were baseline-subtracted and heats of binding were obtained by integrating the area under each injection peak using NanoAnalyze (TA Instruments). The obtained heats of binding were then divided by moles of injectant. Heats of dilution (titrations of titrant into buffer and buffer into titrand) were analyzed similarly, and the molar heats of dilution were subtracted from the molar heats of binding to yield the final plots of kJ/mol of injectant vs. mole ratio for each titration.

5.5 References

(1) Taylor, J. P.; Brown, R. H.; Cleveland, D. W. Decoding ALS: From Genes to Mechanism. *Nature* **2016**, *539*, 197–206. https://doi.org/10.1038/nature20413.

(2) Simmons, Z. Patient-Perceived Outcomes and Quality of Life in ALS. *Neurotherapeutics* **2015**, *12*, 394–402. https://doi.org/10.1007/s13311-014-0322-x.

(3) Al-chalabi, A.; Hardiman, O. The Epidemiology of ALS : A Conspiracy of Genes , Environment and Time. *Nat. Rev. | Neurol.* **2013**, *9*, 617–628. https://doi.org/10.1038/nrneurol.2013.203.

(4) DeJesus-Hernandez, M.; Mackenzie, I. R.; Boeve, B. F.; Boxer, A. L.; Baker, M.; Rutherford, N. J.; Nicholson, A. M.; Finch, N. C. A.; Flynn, H.; Adamson, J.; Kouri, N.; Wojtas, A.; Sengdy, P.; Hsiung, G. Y. R.; Karydas, A.; Seeley, W. W.; Josephs, K. A.; Coppola, G.; Geschwind, D. H.; Wszolek, Z. K.; Feldman, H.; Knopman, D. S.; Petersen, R. C.; Miller, B. L.; Dickson, D. W.; Boylan, K. B.; Graff-Radford, N. R.; Rademakers, R. Expanded GGGGCC Hexanucleotide Repeat in Noncoding Region of C9ORF72 Causes Chromosome 9p-Linked FTD and ALS. *Neuron* **2011**, *72*, 245–256. https://doi.org/10.1016/j.neuron.2011.09.011.

(5) Renton, A. E.; Majounie, E.; Waite, A.; Simón-Sánchez, J.; Rollinson, S.; Gibbs, J.

R.; Schymick, J. C.; Laaksovirta, H.; van Swieten, J. C.; Myllykangas, L.; Kalimo, H.; Paetau, A.; Abramzon, Y.; Remes, A. M.; Kaganovich, A.; Scholz, S. W.; Duckworth, J.; Ding, J.; Harmer, D. W.; Hernandez, D. G.; Johnson, J. O.; Mok, K.; Ryten, M.; Trabzuni, D.; Guerreiro, R. J.; Orrell, R. W.; Neal, J.; Murray, A.; Pearson, J.; Jansen, I. E.; Sondervan, D.; Seelaar, H.; Blake, D.; Young, K.; Halliwell, N.; Callister, J. B.; Toulson, G.; Richardson, A.; Gerhard, A.; Snowden, J.; Mann, D.; Neary, D.; Nalls, M. A.; Peuralinna, T.; Jansson, L.; Isoviita, V. M.; Kaivorinne, A. L.; Hölttä-Vuori, M.; Ikonen, E.; Sulkava, R.; Benatar, M.; Wuu, J.; Chiò, A.; Restagno, G.; Borghero, G.; Sabatelli, M.; Heckerman, D.; Rogaeva, E.; Zinman, L.; Rothstein, J. D.; Sendtner, M.; Drepper, C.; Eichler, E. E.; Alkan, C.; Abdullaev, Z.; Pack, S. D.; Dutra, A.; Pak, E.; Hardy, J.; Singleton, A.; Williams, N. M.; Heutink, P.; Pickering-Brown, S.; Morris, H. R.; Tienari, P. J.; Traynor, B. J. A Hexanucleotide Repeat Expansion in C9ORF72 Is the Cause of Chromosome 9p21-Linked ALS-FTD. *Neuron* **2011**, *72*, 257–268. https://doi.org/10.1016/j.neuron.2011.09.010.

(6) Waite, A. J.; Bäumer, D.; East, S.; Neal, J.; Morris, H. R.; Ansorge, O.; Blake, D. J. Reduced C9orf72 Protein Levels in Frontal Cortex of Amyotrophic Lateral Sclerosis and Frontotemporal Degeneration Brain with the C9ORF72 Hexanucleotide Repeat Expansion. *Neurobiol. Aging* **2014**, *35*, 1779.e5-1779.e13. https://doi.org/10.1016/j.neurobiolaging.2014.01.016.

(7) Zu, T.; Gibbens, B.; Doty, N. S.; Gomes-Pereira, M.; Huguet, A.; Stone, M. D.; Margolis, J.; Peterson, M.; Markowski, T. W.; Ingram, M. A. C.; Nan, Z.; Forster, C.; Low, W. C.; Schoser, B.; Somia, N. V.; Clark, H. B.; Schmechel, S.; Bitterman, P.

B.; Gourdon, G.; Swanson, M. S.; Moseley, M.; Ranum, L. P. W. Non-ATG-Initiated Translation Directed by Microsatellite Expansions. *Proc. Natl. Acad. Sci.* **2011**, *108* (1), 260–265. https://doi.org/10.1073/pnas.1013343108.

(8) Zu, T.; Liu, Y.; Bañez-Coronel, M.; Reid, T.; Pletnikova, O.; Lewis, J.; Miller, T. M.; Harms, M. B.; Falchook, A. E.; Subramony, S. H.; Ostrow, L. W.; Rothstein, J. D.; Troncoso, J. C.; Ranum, L. P. W. RAN Proteins and RNA Foci from Antisense Transcripts in C9ORF72 ALS and Frontotemporal Dementia. *Proc. Natl. Acad. Sci.* **2013**, *110* (51), E4968–E4977. https://doi.org/10.1073/pnas.1315438110.

(9) Mizielinska, S.; Grönke, S.; Niccoli, T.; Ridler, C. E.; Clayton, E. L.; Devoy, A.; Moens, T.; Norona, F. E.; Woollacott, I. O. C.; Pietrzyk, J.; Cleverley, K.; Nicoll, A. J.; Pickering-brown, S.; Dols, J.; Cabecinha, M.; Hendrich, O.; Fratta, P.; Fisher, E. M. C.; Partridge, L.; Isaacs, A. M. C9orf72 Repeat Expansions Cause Neurodegeneration in Drosophila through Arginine-Rich Proteins. *Science (80-.).* **2014**, *345* (6201), 1192–1194.

(10) Wen, X.; Tan, W.; Westergard, T.; Krishnamurthy, K.; Markandaiah, S. S.; Shi, Y.; Lin, S.; Shneider, N. A.; Monaghan, J.; Pandey, U. B.; Pasinelli, P.; Ichida, J. K.; Trotti, D. Antisense Proline-Arginine RAN Dipeptides Linked to C9ORF72-ALS/FTD Form Toxic Nuclear Aggregates That Initiate Invitro and Invivo Neuronal Death. *Neuron* **2014**, *84*, 1213–1225. https://doi.org/10.1016/j.neuron.2014.12.010.

(11) Tang, X.; Toro, A.; Sahana, T. G.; Gao, J.; Chalk, J.; Oskarsson, B. E.; Zhang, K.; Zhang, K. Divergence, Convergence, and Therapeutic Implications: A Cell Biology Perspective of C9ORF72-ALS/FTD. *Mol. Neurodegener.* **2020**, *15*, 34.

https://doi.org/10.1186/s13024-020-00383-7.

(12) Kwon, I.; Xiang, S.; Kato, M.; Wu, L.; Theodoropoulos, P.; Wang, T.; Kim, J.; Yun, J.; Xie, Y.; McKnight, S. L. Poly-Dipeptides Encoded by the C9orf72 Repeats Bind Nucleoli, Impede RNA Biogenesis, and Kill Cells. *Science (80-.).* **2014**, *345* (6201), 1139–1145. https://doi.org/10.1126/science.1254917.

(13) Fallini, C.; Khalil, B.; Smith, C. L.; Rossoll, W. Traffic Jam at the Nuclear Pore: All Roads Lead to Nucleocytoplasmic Transport Defects in ALS/FTD. *Neurobiol. Dis.* **2020**, *140* (December 2019), 104835. https://doi.org/10.1016/j.nbd.2020.104835.

(14) Shi, K. Y.; Mori, E.; Nizami, Z. F.; Lin, Y.; Kato, M.; Xiang, S.; Wu, L. C.; Ding, M.; Yu, Y.; Gall, J. G.; McKnight, S. L. Toxic PR $_n$ Poly-Dipeptides Encoded by the *C9orf72* Repeat Expansion Block Nuclear Import and Export. *Proc. Natl. Acad. Sci.* **2017**, *114* (7), E1111–E1117. https://doi.org/10.1073/pnas.1620293114.

(15) Lee, K. H.; Zhang, P.; Kim, H. J.; Mitrea, D. M.; Sarkar, M.; Freibaum, B. D.; Cika, J.; Coughlin, M.; Messing, J.; Molliex, A.; Maxwell, B. A.; Kim, N. C.; Temirov, J.; Moore, J.; Kolaitis, R. M.; Shaw, T. I.; Bai, B.; Peng, J.; Kriwacki, R. W.; Taylor, J. P. C9orf72 Dipeptide Repeats Impair the Assembly, Dynamics, and Function of Membrane-Less Organelles. *Cell* **2016**, *167* (3), 774-788.e17. https://doi.org/10.1016/j.cell.2016.10.002.

(16) Jiang, J.; Zhu, Q.; Gendron, T. F.; Saberi, S.; McAlonis-Downes, M.; Seelman, A.; Stauffer, J. E.; Jafar-nejad, P.; Drenner, K.; Schulte, D.; Chun, S.; Sun, S.; Ling, S. C.; Myers, B.; Engelhardt, J.; Katz, M.; Baughn, M.; Platoshyn, O.; Marsala, M.; Watt, A.; Heyser, C. J.; Ard, M. C.; De Muynck, L.; Daughrity, L. M.; Swing, D. A.;

Tessarollo, L.; Jung, C. J.; Delpoux, A.; Utzschneider, D. T.; Hedrick, S. M.; de Jong, P. J.; Edbauer, D.; Van Damme, P.; Petrucelli, L.; Shaw, C. E.; Bennett, C. F.; Da Cruz, S.; Ravits, J.; Rigo, F.; Cleveland, D. W.; Lagier-Tourenne, C. Gain of Toxicity from ALS/FTD-Linked Repeat Expansions in C9ORF72 Is Alleviated by Antisense Oligonucleotides Targeting GGGGCC-Containing RNAs. *Neuron* **2016**, *90*, 535–550. https://doi.org/10.1016/j.neuron.2016.04.006.

(17) Cook, C. N.; Wu, Y.; Odeh, H. M.; Gendron, T. F.; Jansen-West, K.; del Rosso, G.; Yue, M.; Jiang, P.; Gomes, E.; Tong, J.; Daughrity, L. M.; Avendano, N. M.; Castanedes-Casey, M.; Shao, W.; Oskarsson, B.; Tomassy, G. S.; McCampbell, A.; Rigo, F.; Dickson, D. W.; Shorter, J.; Zhang, Y. J.; Petrucelli, L. C9orf72 Poly(GR) Aggregation Induces TDP-43 Proteinopathy. *Sci. Transl. Med.* **2020**, *12*, eabb3774. https://doi.org/10.1126/SCITRANSLMED.ABB3774.

(18) Awwad, S.; Angkawinitwong, U. Overview of Antibody Drug Delivery. *Pharmaceutics* **2018**, *10* (83), 1–24. https://doi.org/10.3390/pharmaceutics10030083.

(19) Harding, F. A.; Stickler, M. M.; Razo, J.; DuBridge, R. B. The Immunogenicity of Humanized and Fully Human Antibodies: Residual Immunogenicity Resides in the CDR Regions. *MAbs* **2010**, *2* (3), 256–265. https://doi.org/10.4161/mabs.2.3.11641.

(20) Yu, Y. B.; Briggs, K. T.; Taraban, M. B.; Brinson, R. G.; Marino, J. P. Grand Challenges in Pharmaceutical Research Series: Ridding the Cold Chain for Biologics. *Pharm. Res.* **2021**, *38*, 3–7. https://doi.org/10.1007/s11095-021-03008-

w.

(21) Zheng, S.; Sahimi, A.; Shing, K. S.; Sahimi, M. Molecular Dynamics Study of Structure, Folding, and Aggregation of Poly-PR and Poly-GR Proteins. *Biophys. J.* **2021**, *120*, 64–72. https://doi.org/10.1016/j.bpj.2020.11.2258.

(22) Chang, L. W.; Lytle, T. K.; Radhakrishna, M.; Madinya, J. J.; Vélez, J.; Sing, C. E.; Perry, S. L. Sequence and Entropy-Based Control of Complex Coacervates. *Nat. Commun.* **2017**, *8*, 1273. https://doi.org/10.1038/s41467-017-01249-1.

Chapter 6. Conclusions and outlook

Tuning biomaterials using specific biomolecular interactions represents a promising avenue to develop next-generation biomaterials with the increased complexity required to recapitulate the complex, dynamic nature of native tissues and develop effective therapeutics.[1] In this thesis, we explored the specific interactions of several peptides as therapeutics and components of biomaterials. In **Chapter 2**, we harnessed the specific, displaceable interactions between coiled coil peptides to develop biomaterials with spatiotemporal control over the presentation of biomolecules on the surface. We connected the specific coiled coil interactions to stereochemistry-directed interactions in **Chapter 3** by redesigning coiled coils to make them amenable to undergoing stereochemistry-directed interactions. We observed that employing stereochemistry-directed interactions in coiled coils combined the strong, specific interactions between coiled coils with the enhanced stability and tunable interaction strength of stereochemistry-directed interactions. With these design rules established, we designed a polymer-peptide conjugate biomaterial using to prevent aggregates of toxic proteins implicated in amyotrophic lateral sclerosis (ALS) in **Chapter 4**, where we also leveraged stereochemistry-directed interactions to develop design rules for a different peptide system. Both D- and L-conjugates dispersed aggregates with similar efficacy, raising questions about the stereochemistry-directed interactions between these peptides that warrant future exploration. Towards the goal of developing polymer-peptide conjugates to target a set of highly charged toxic proteins that are also implicated in ALS, we characterized the interactions between these toxic proteins and a set of peptides designed to interact with them electrostatically in **Chapter 5**. From this study, we selected candidates for future conjugation to polymers to prepare therapeutics.

A key takeaway from this work is the utility of coiled coil peptides in biomaterials, as the specific and displaceable interactions of coiled coils enabled the facile patterning and changing of biomolecule display on biomaterial surfaces. Additionally, we showed that the benefits reported for stereochemistry-directed interactions can be combined with the desirable features of coiled coil interactions through informed design. While initial attempts to access stereochemistry-directed interactions in coiled coils caused a disruption of coiled coil complexation, we demonstrated here that we can use peptide sequence design to prepare coiled coils with the same features that lead to specificity and strong complexation while also making them amenable to stereochemistry-directed interactions. As the design rules for stereochemistry-directed interactions are not well-established, such sequence design modifications may play an important role in adapting a wide variety of peptides to harness the enhanced stability and wider range of binding strengths afforded by stereochemistry-directed interactions.

From the polymer-peptide conjugate design work, we provided further evidence that the general design of a hydrophilic polymer combined with a peptide designed to bind a target protein is generalizable. We achieved comparable results for dispersal and prevention of aggregation to previous work using polymer-peptide conjugates to target $A\beta_{40}$, suggesting that this polymer-peptide approach may extend to other systems. Within this system, we further explored the stereochemistry-directed interaction design space by using both D- and L-peptides in our conjugates, where we expected the D-conjugates to be more effective at dispersing aggregates due to stronger binding afforded by stereochemistry-directed interactions. However, we observed little difference between the D- and L-conjugates, suggesting that such a driving force did not exist in this case. Further study of these peptides will provide important insight into the design rules for stereochemistry-directed interactions, as there are currently opposing examples that demonstrate that stereochemistry-directed interactions drive stronger binding[2–6] or don't drive binding at all,[7,8] but no examples as far as we know that establish no difference in interaction strength. Contingent upon further study to confirm that the peptides alone, when the polymer is not a factor, do not experience a difference in binding due to stereochemistry-directed interactions, the connection of peptide sequence features to the effect of stereochemistry-directed interactions will be a large part in the advancement of design rules.

The study of highly charged peptide interactions also highlighted the importance of peptide sequence and its connection to structure. We varied both charge density and sequence/structure in our peptides designed to target $(GR)_n$ and $(PR)_n$, two charged proteins implicated in ALS). The role of sequence and structure in $(GR)_n$/$(PR)_n$ binding strength was highlighted in our results, as the proline-based $(PE)_{10}$ had the strongest heats of interaction with both target peptides, even relative to the more charge-dense E_{10} peptide. This emphasized the importance of peptide assembly and sequence design when choosing a protein-targeting peptide for polymer-peptide conjugate biomaterials, especially since our other results indicate that the polymer-peptide conjugate design may become more generalized for protein-targeting therapeutics.

The results presented in this thesis showcase the potential of coiled coils and polymer-peptide conjugates and provide groundwork for future studies that will further expand their molecular design space and functionality. To expand the range of complexation strengths and stabilities of heterochiral coiled coils, future studies will optimize the newly designed peptide sequences to better balance charge and deliver the most favorable hydrophobic interactions. For polymer-peptide conjugates, there is a wide design space in terms of polymer composition and architecture. Future studies will probe alternative architectures that provide multivalent peptide presentation and consider the polymer composition to better balance the hydrophilicity of the conjugate while changing peptide presentation.

Taken together, in this thesis we have enhanced the tunability and functionality of materials by altering the tunability of specific peptide interactions using stereochemistry-directed interactions and conjugation to polymers. The findings presented here expand on the design rules for stereochemistry-directed interactions and polymer-peptide conjugates and can be used to inform the future design of next-generation biomaterials.

6.1 References

(1) Roach, P.; Eglin, D.; Rohde, K.; Perry, C. C. Modern Biomaterials: A Review - Bulk Properties and Implications of Surface Modifications. *J. Mater. Sci. Mater. Med.* **2007**, *18*, 1263–1277. https://doi.org/10.1007/s10856-006-0064-3.

(2) Nagy, K. J.; Giano, M. C.; Jin, A.; Pochan, D. J.; Schneider, J. P. Enhanced Mechanical Rigidity of Hydrogels Formed From Enantiomeric Peptide Assemblies. *J Am Chem Soc* **2011**, *133* (38), 14975–14977. https://doi.org/10.1158/0008-5472.CAN-10-4002.BONE.

(3) Swanekamp, R. J.; Dimaio, J. T. M.; Bowerman, C. J.; Nilsson, B. L. Coassembly of Enantiomeric Amphipathic Peptides into Amyloid-Inspired Rippled β-Sheet

Fibrils. *J. Am. Chem. Soc.* **2012**, *134*, 5556–5559. https://doi.org/10.1021/ja301642c.

(4) Swanekamp, R. J.; Welch, J. J.; Nilsson, B. L. Proteolytic Stability of Amphipathic Peptide Hydrogels Composed of Self-Assembled Pleated Β-Sheet or Coassembled Rippled Β-Sheet Fibrils. *Chem. Commun.* **2014**, *50*, 10133–10136. https://doi.org/10.1039/c4cc04644g.

(5) Nagy-Smith, K.; Beltramo, P. J.; Moore, E.; Tycko, R.; Furst, E. M.; Schneider, J. P. Molecular, Local, and Network-Level Basis for the Enhanced Stiffness of Hydrogel Networks Formed from Coassembled Racemic Peptides: Predictions from Pauling and Corey. *ACS Cent. Sci.* **2017**, *3*, 586–597. https://doi.org/10.1021/acscentsci.7b00115.

(6) Urban, J. M.; Ho, J.; Piester, G.; Fu, R.; Nilsson, B. L. Rippled β-Sheet Formation by an Amyloid-β Fragment Indicates Expanded Scope of Sequence Space for Enantiomeric β-Sheet Peptide Coassembly. *Molecules* **2019**, *24*, 1983. https://doi.org/10.3390/molecules24101983.

(7) Wadai, H.; Yamaguchi, K. I.; Takahashi, S.; Kanno, T.; Kawai, T.; Naiki, H.; Goto, Y. Stereospecific Amyloid-like Fibril Formation by a Peptide Fragment of Β2-Microglobulin. *Biochemistry* **2005**, *44* (1), 157–164. https://doi.org/10.1021/bi0485880.

(8) Koga, T.; Matsuoka, M.; Higashi, N. Structural Control of Self-Assembled Nanofibers by Artificial β-Sheet Peptides Composed of D- or L-Isomer. *J. Am. Chem. Soc.* **2005**, *127* (50), 17596–17597. https://doi.org/10.1021/ja0558387.

Appendix A: Supporting information for Chapter 2

List of Figures

A1. Peptide characterization

A1.1. Mass spectrometry of coiled coil peptides

Mass spectrometry was used to confirm the successful synthesis of the peptides used in this study. The observed m/z for each peptide corresponds to the $[M+H]^+$ ionization of the peptide (**Figure A1**).

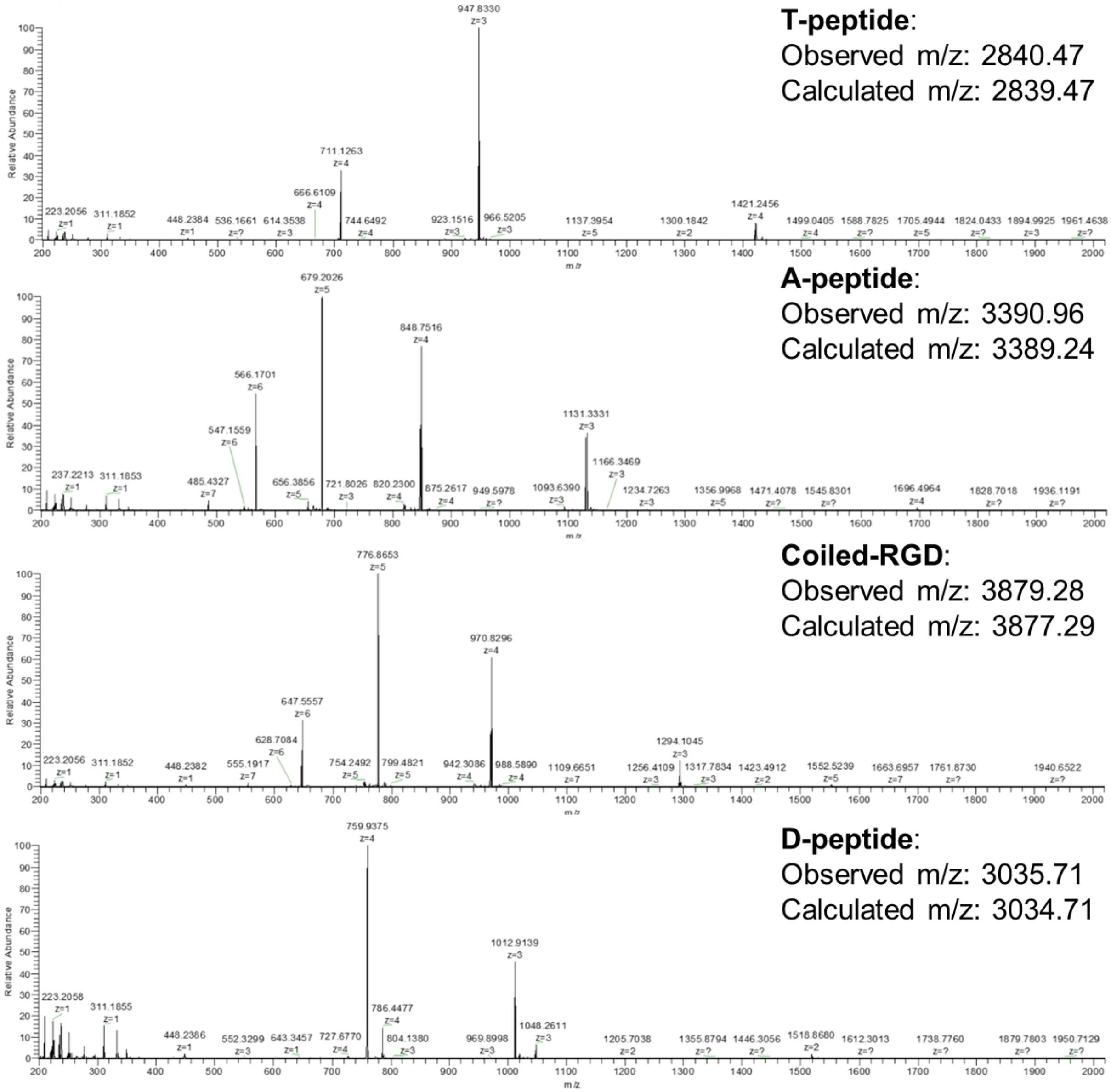

T-peptide:
Observed m/z: 2840.47
Calculated m/z: 2839.47

A-peptide:
Observed m/z: 3390.96
Calculated m/z: 3389.24

Coiled-RGD:
Observed m/z: 3879.28
Calculated m/z: 3877.29

D-peptide:
Observed m/z: 3035.71
Calculated m/z: 3034.71

Figure A1. Electrospray ionization mass spectrometry of coiled coil peptides used in this study. Each observed m/z corresponds to the $[M+H]^+$ ionization of the peptide.

A1.2. Analytical scale high performance liquid chromatography: purity of coiled coil peptides

To assess the purity of the peptides used in this study, we used high performance liquid chromatography (HPLC). The HPLC chromatograms indicate some presence of side products, but taken together with the mass spectrometry data confirming the expected molecular weight, we decided to use these peptides without further purification (**Figure A2**).

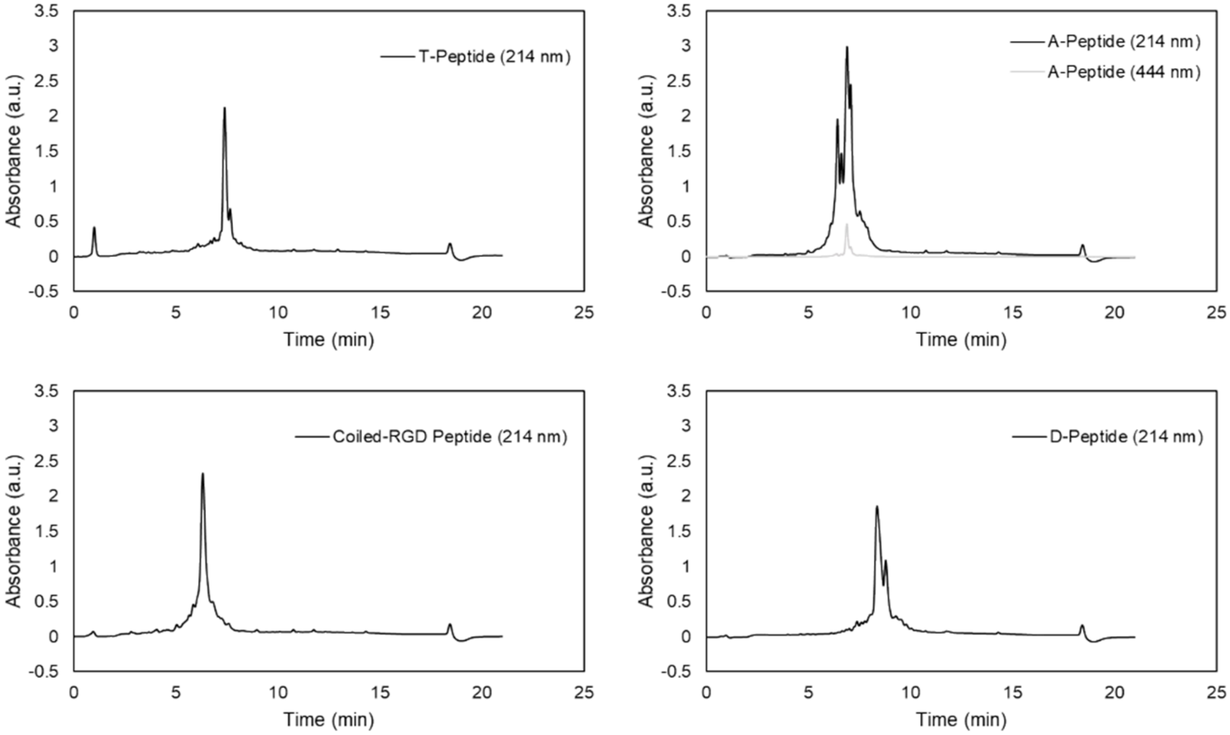

Figure A2. Analytical HPLC chromatograms of coiled coil peptides. The peptides were detected by absorbance at 214 nm and FAM absorbance on the A-peptide was detected by absorbance at 444 nm. The second peak in the A-peptide chromatogram that does not correspond to the FAM absorbance is likely A-peptide that is unlabeled. The peptide was eluted on a linear AB gradient from 5% to 95% B (v/v) over 10 minutes, where A is ultrapure water + 0.1% TFA and B is acetonitrile + 0.1% TFA.

A1.3. Secondary structure characterization of coiled coil peptides

Peptide secondary structure was determined by circular dichroism (CD) spectroscopy (**Figure A3**). The spectrum of the T-peptide (EIAALEK)$_3$G$_7$CG shows the peptide adopts a random coil structure. As the T-peptide behaved how we expected it to in forming coiled-coil complexes with release being dependent on the addition of the competing D-peptide, we hypothesize that the 7- glycine spacer added to provide physical space between the hydrogel/fiber substrates and the coiled domains might also consequently limit the overall helical nature of the peptide. However, the T-peptide still allowed for stable coiled-coil complexes to form on hydrogel/hydrogel fiber substrates that could easily be disrupted via the user-defined addition of the complementary D-peptide. This was unsurprising as randomly coiled peptides have been previously shown to adopt the helical secondary structure as they assemble into coiled-coil complexes – specifically when the sequence contains the necessary amino acid motifs to complex with the complementary strand as they do here (E/K complementary heptads).[1]

The spectrum of the Coiled RGD peptide GYGRGDSPG-$(KIAALKE)_4$ shows a modest helical structure based on the CD spectrum, with the addition of the bioactive RGD domain likely limiting the formation of the α-helix, as $(KIAALKE)_4$ itself has been previously shown to be α-helical.[2]

The spectra of the A-peptide FAM-$(KIAALKE)_4$ and the D-peptide $(EIAALEK)_4$ best match the CD signature of an α-helical structure. Overall, despite the peptides exhibiting varying degrees of α-helicity, they demonstrated the ability to form coiled coil complexes with their complements throughout this chapter.

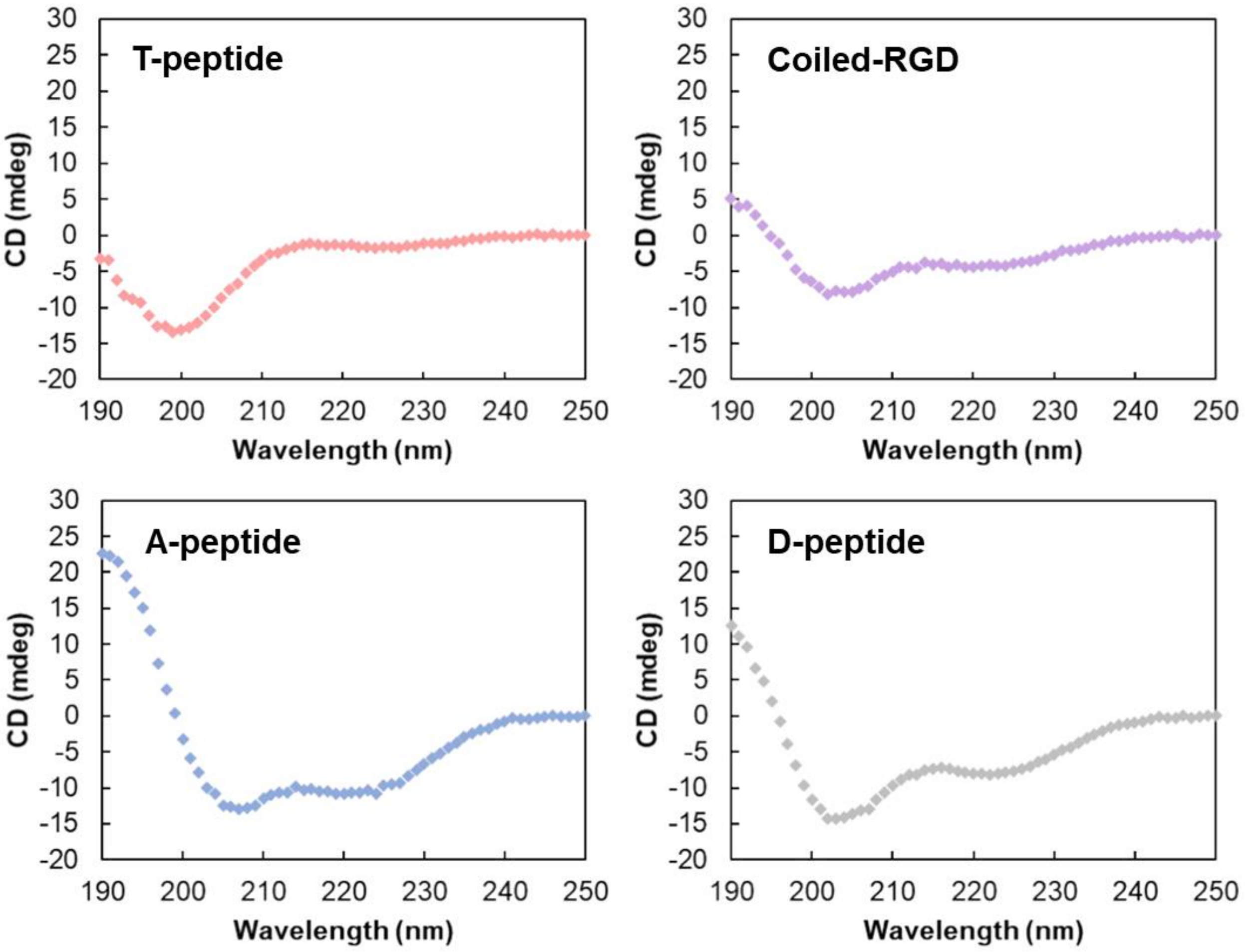

Figure A3. CD spectra of coiled coil peptides at 0.1 mg/mL in 10 mM PBS (pH 7.4). CD measurements were taken at 25 °C, with a data pitch of 0.1 nm and scanning speed of 50 nm/min. The spectra are shown as the average of 3 scans per sample.

A2. Additional ITC data

A2.1. Replicates of titration of T-peptide into coiled-RGD peptide in NIH 3T3 fibroblast medium

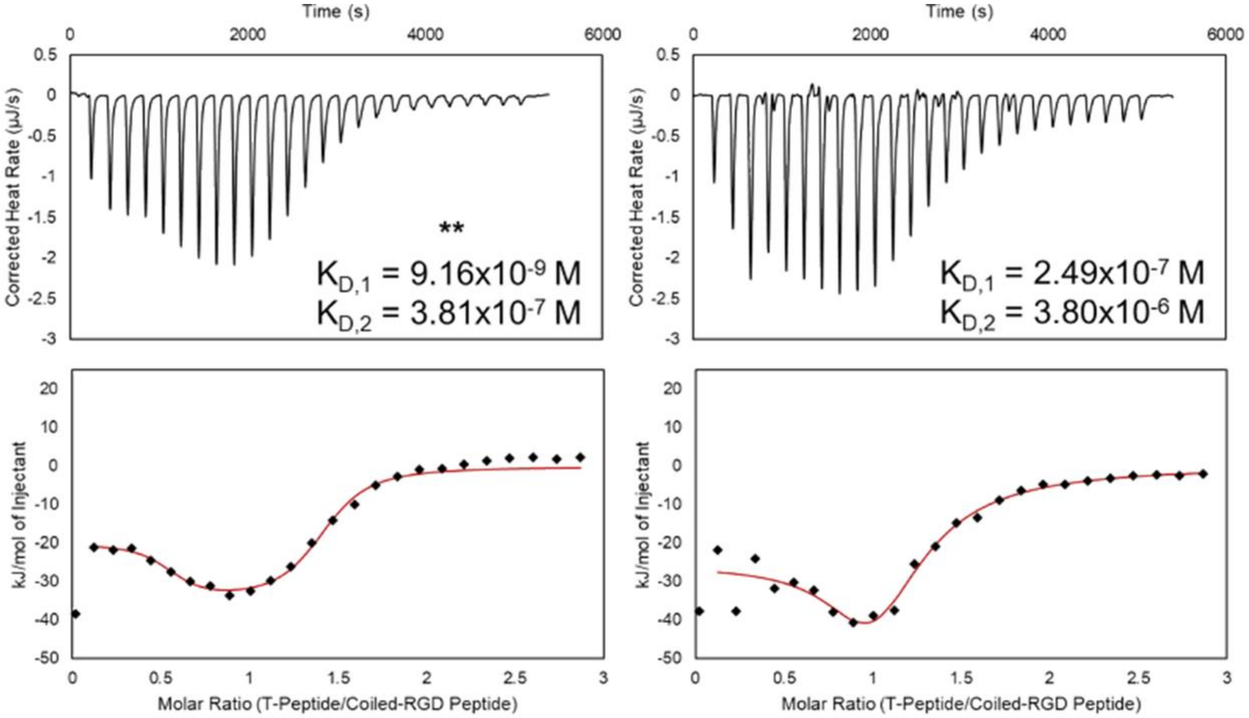

Figure A4. Thermogram and integrated binding heats from the titration of 200 μM T-peptide into 20 μM coiled-RGD peptide in fibroblast medium. The binding heats were fit to a two-site binding model (red line) and the associated K_D values calculated from that model are shown on the plot. ***Indicates that plot was included in Figure 2.2.*

A2.2. Replicates of titration of coiled-RGD peptide into D-peptide in NIH 3T3 fibroblast medium

For the titration of coiled-RGD peptide into D-peptide, both exothermic and endothermic peaks are observed as discussed in Chapter 2 (**Figure A5**). We attempted to fit these integrated heats to a two-site binding model (red lines), but the fit clearly does not match the data at early molar ratios, indicating that the parameters obtained from the model would not reliably represent the data.

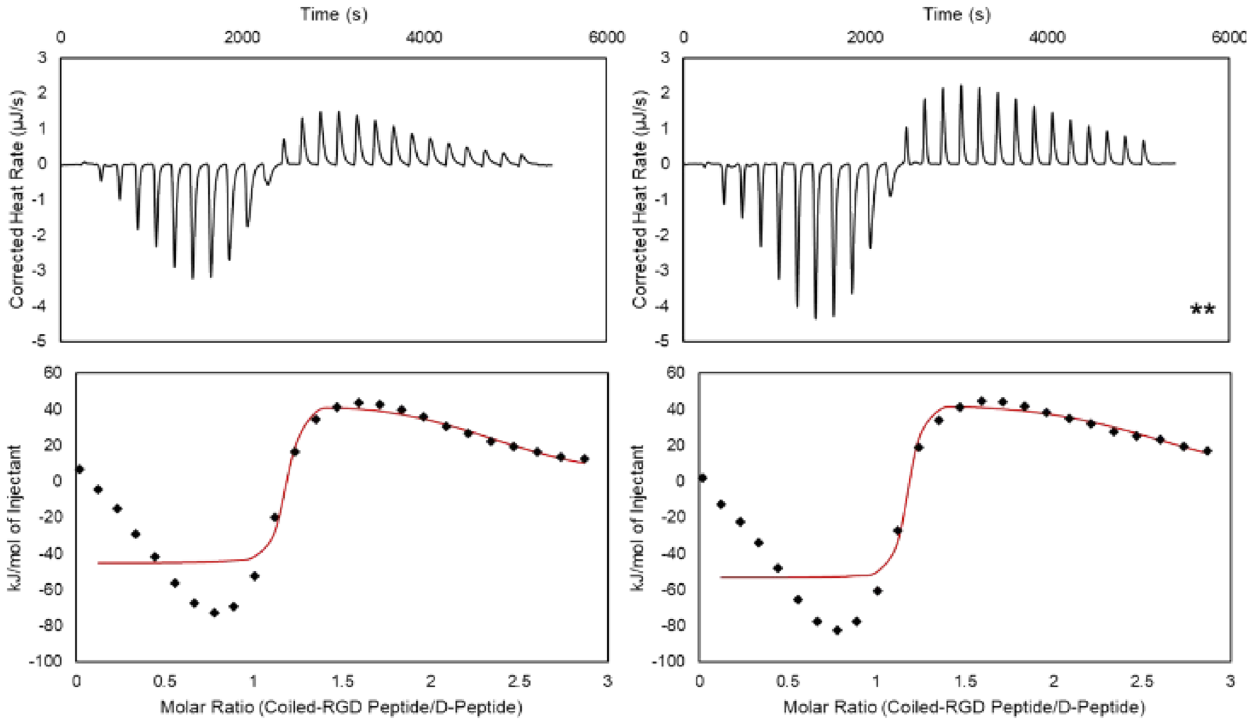

Figure A5. Thermogram and integrated binding heats from the titration of 200 μM coiled-RGD peptide into 20 μM D-peptide in fibroblast medium. The binding heats were attempted to be fit to a two-site binding model (red lines) but the model does not fit the data well. ***Indicates that plot was included in Figure 2.2.*

A2.3. Replicates of titration of T-peptide into D-peptide in NIH 3T3 fibroblast medium

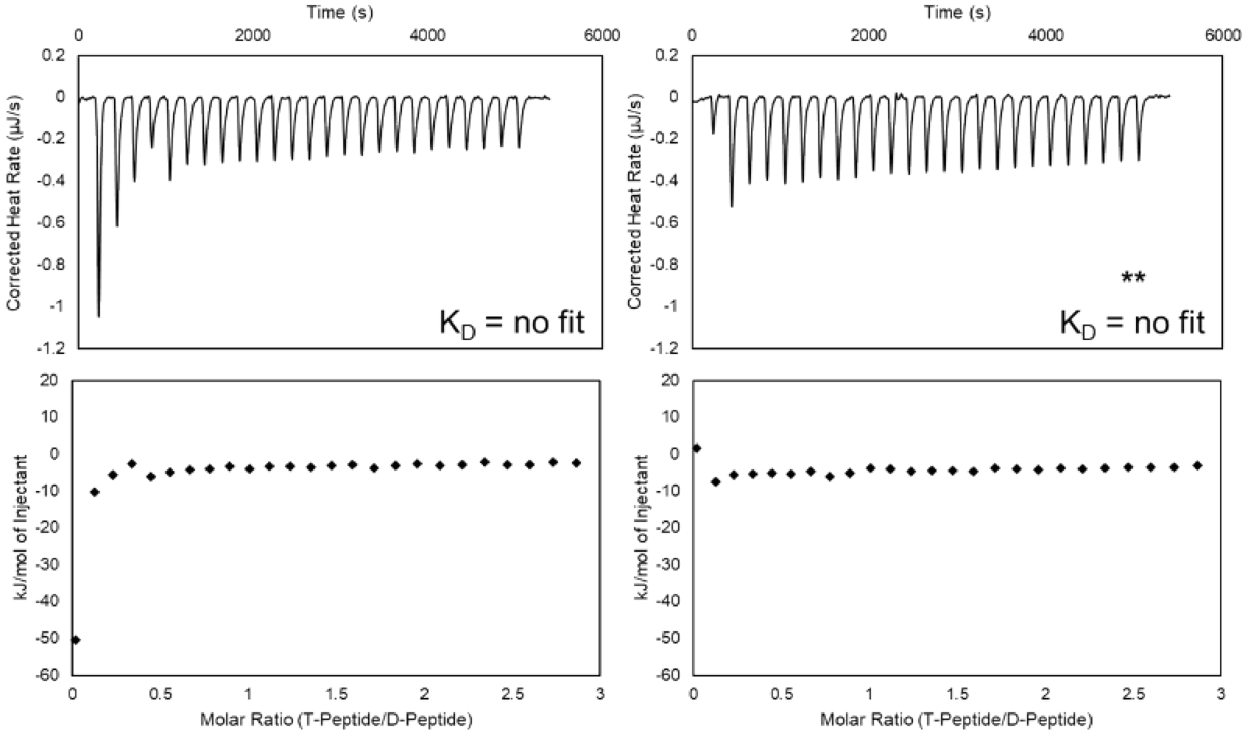

Figure A6. Thermogram and integrated binding heats from the titration of 200 µM T-peptide into 20 µM D-peptide in fibroblast medium. ***Indicates that plot was included in Figure 2.2.*

A2.4. Titrations of T-peptide into A-peptide in 1X PBS

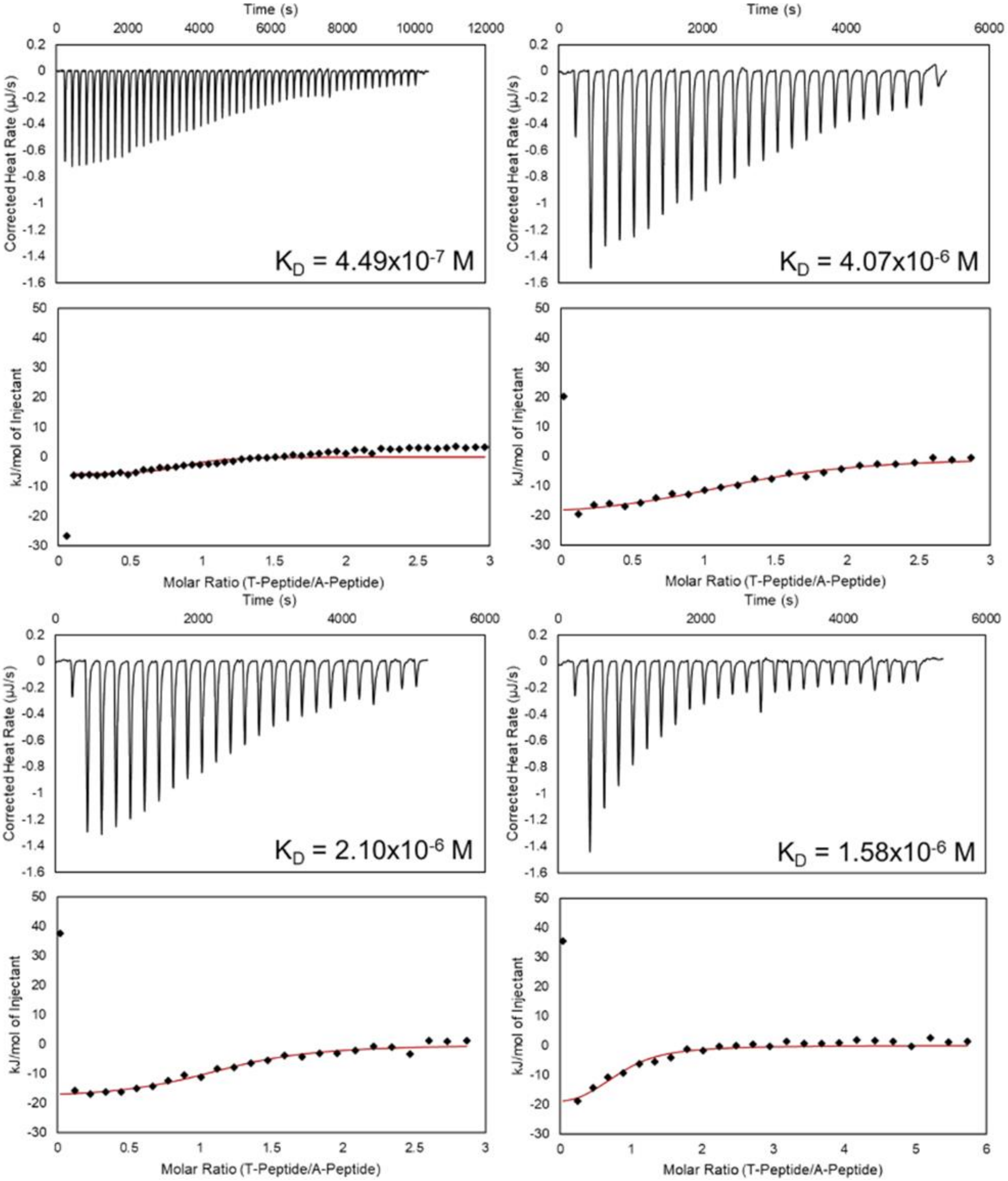

Figure A7. Thermogram and integrated binding heats from the titration of 200 μM T-peptide into 20 μM A-peptide in 1X PBS, with the exception of the bottom right titration which was performed with 200 μM T-peptide and 10 μM A-peptide. The top left titration was performed with 50 total injections, compared to 25 injections for the other titrations. The binding heats were fit to a single-site binding model and the associated K_D values calculated from that model are shown on the plot.

A2.5. Titrations of T-peptide into coiled-RGD peptide in 1X PBS

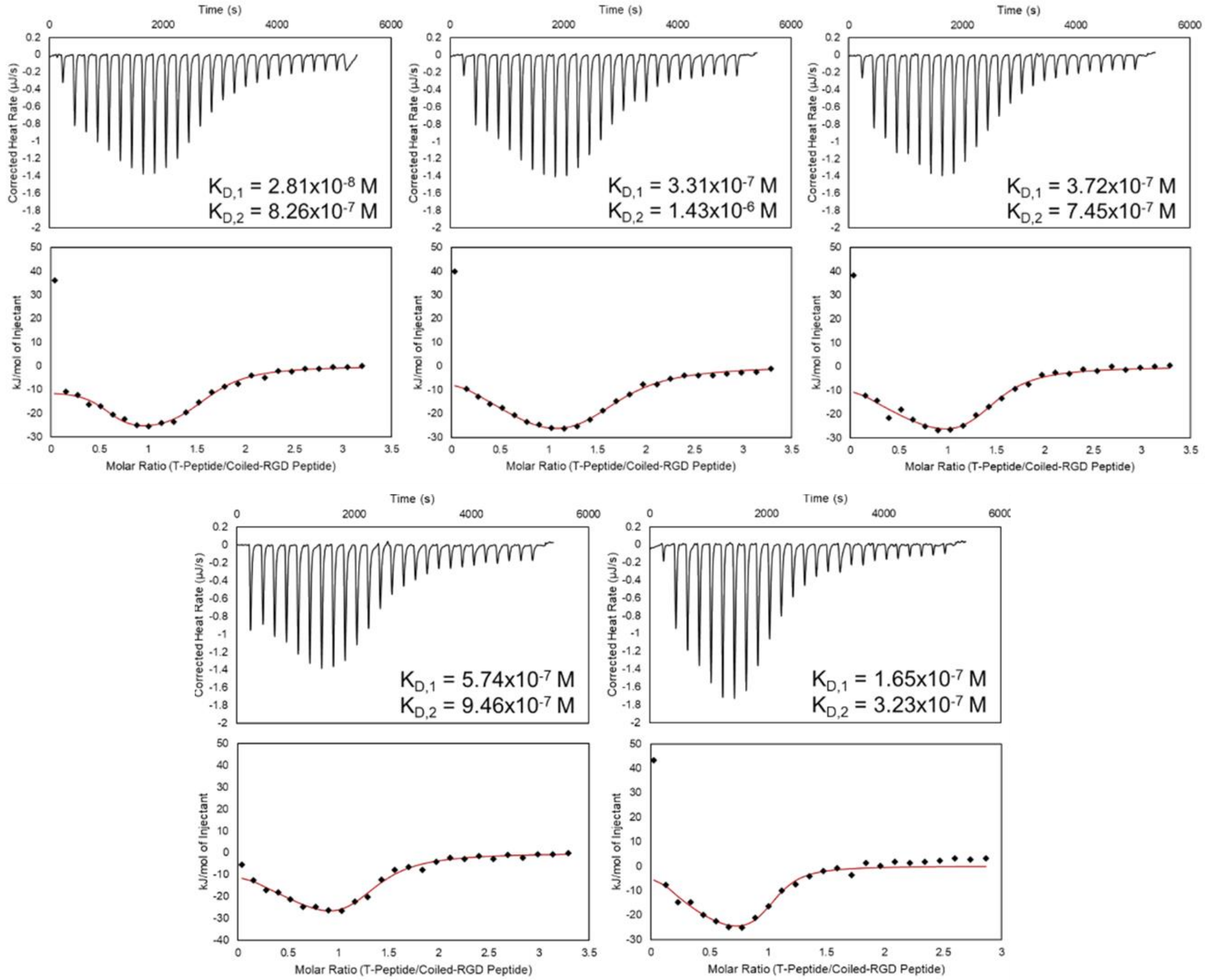

Figure A8. Thermogram and integrated binding heats from the titration of 200 μM T-peptide into 20 μM coiled-RGD peptide in 1X PBS. The binding heats were fit to a two-site binding model and the associated K_D values calculated from that model are shown on the plot.

A2.6. Titrations of A-peptide into D-peptide in 1X PBS

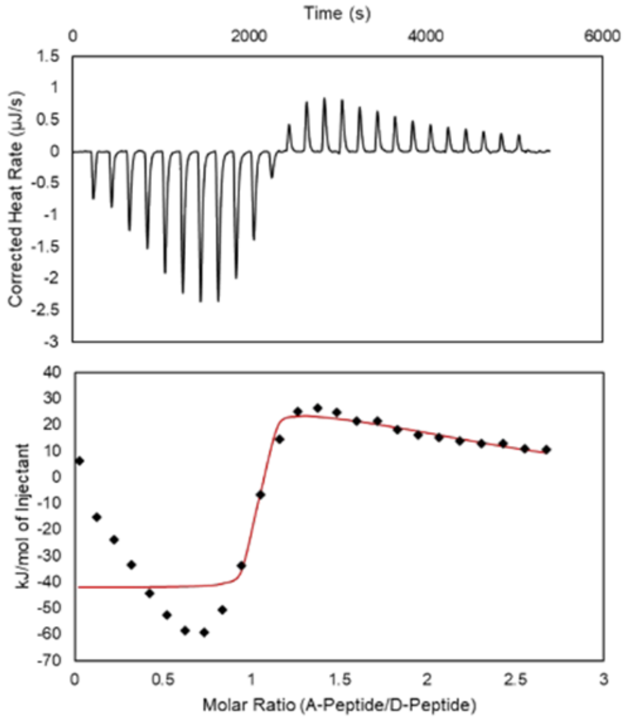

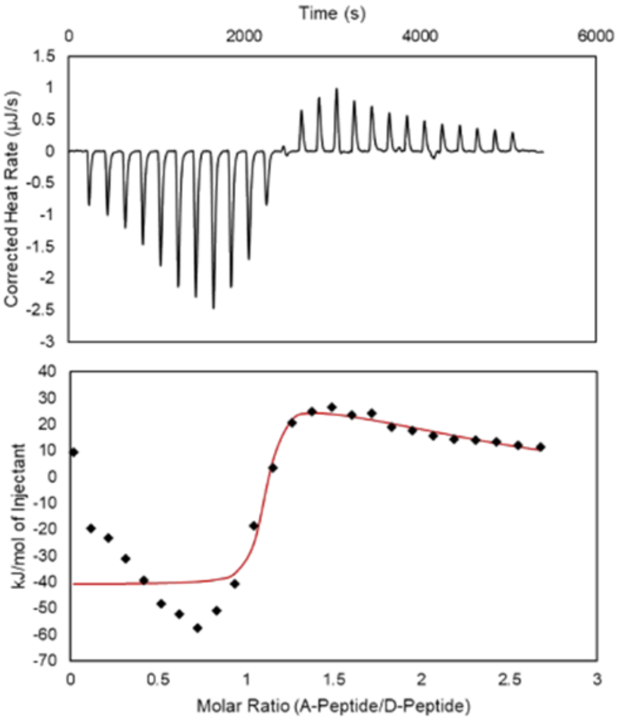

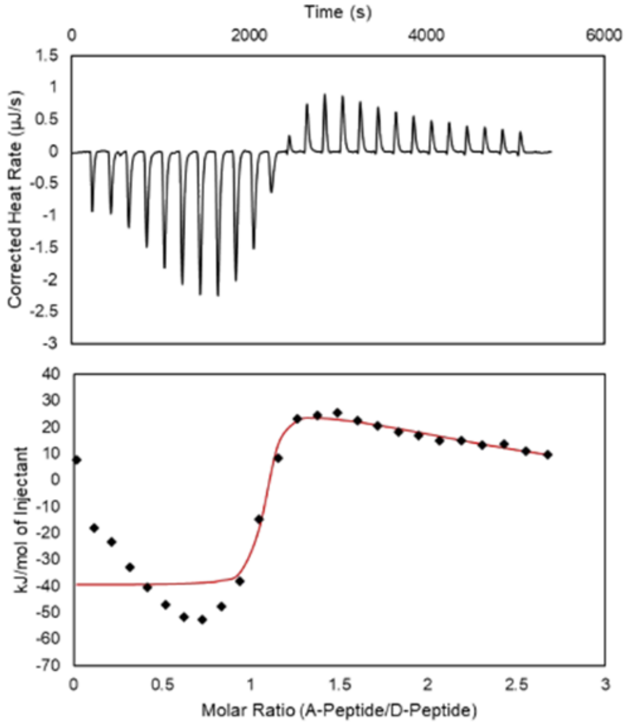

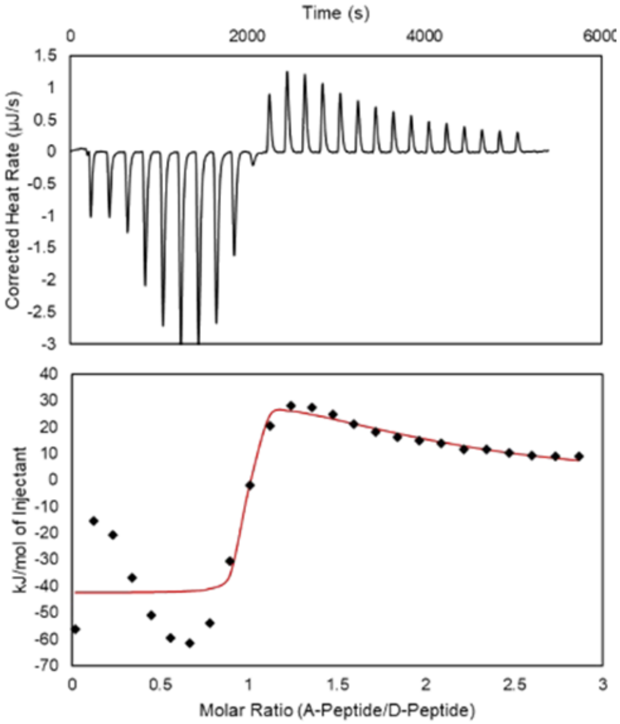

Figure A9. Thermogram and integrated binding heats from the titration of 200 μM A-peptide into 20 μM D-peptide in 1X PBS. The binding heats were attempted to be fit to a two-site binding model (red lines) but the model does not fit the data well.

A2.7. Titrations of coiled RGD-peptide into D-peptide in 1X PBS

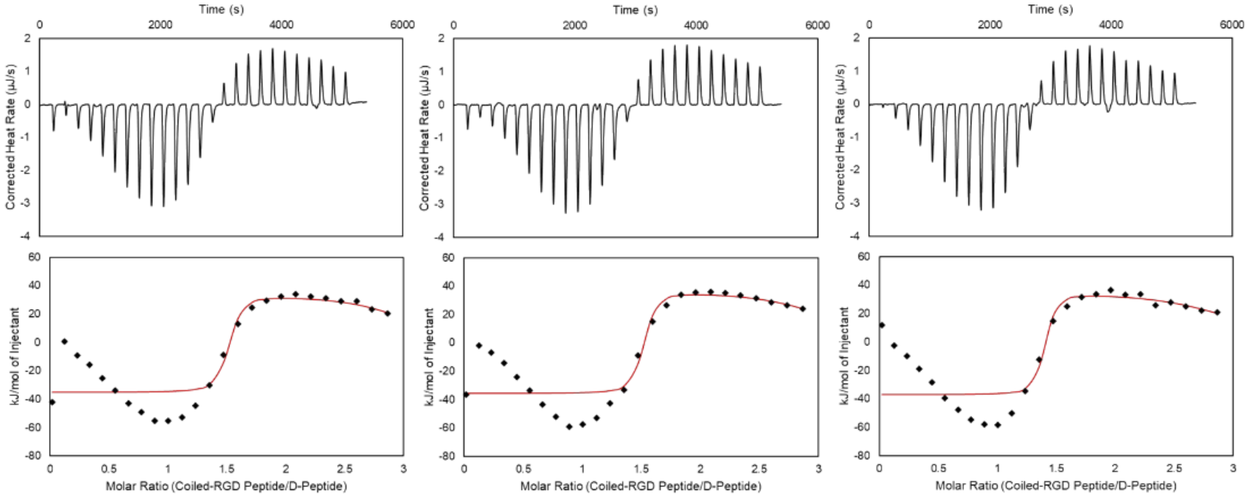

Figure A10. Thermogram and integrated binding heats from the titration of 200 μM coiled-RGD peptide into 20 μM D-peptide in 1X PBS. The binding heats were attempted to be fit to a two-site binding model (red lines) but the model does not fit the data well.

A2.8. Titrations of coiled T-peptide into D-peptide in 1X PBS

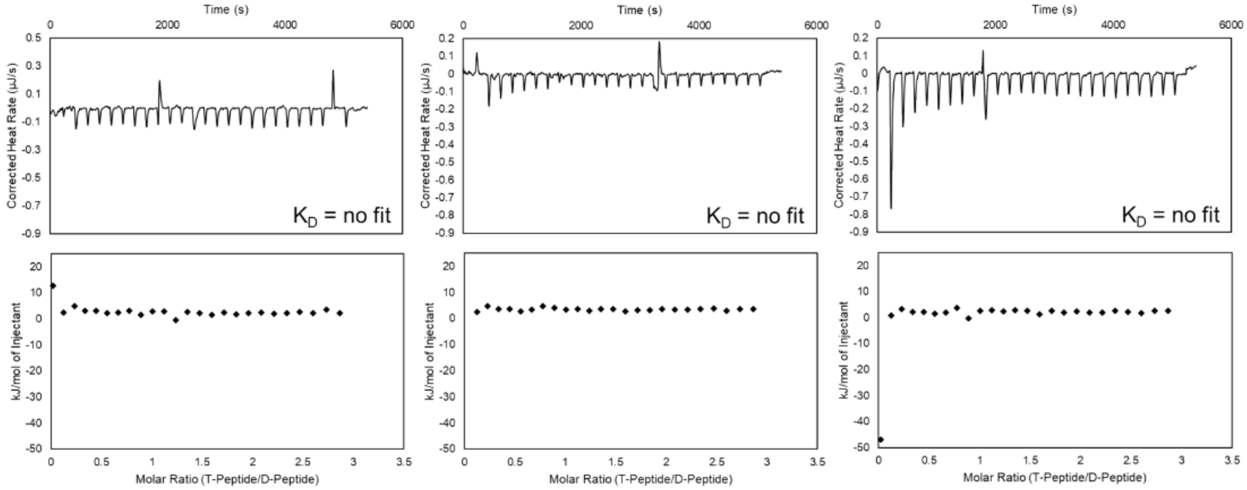

Figure A11. Thermogram and integrated binding heats from the titration of 200 μM T-peptide into 20 μM D-peptide in 1X PBS.

A3. References

(1) Apostolovic, B.; Danial, M.; Klok, H. A. Coiled Coils: Attractive Protein Folding Motifs for the Fabrication of Self-Assembled, Responsive and Bioactive Materials. *Chem. Soc. Rev.* **2010**, *39* (9), 3541–3575. https://doi.org/10.1039/b914339b.

(2) Litowski, J. R.; Hodges, R. S. Designing Heterodimeric Two-Stranded Alpha-Helical Coiled-Coils. *J. Biol. Chem.* **2002**, *277* (40), 37272–37279. https://doi.org/10.1074/jbc.M204257200.

Appendix B: Supporting information for Chapter 3

List of Figures

List of Tables

B1. Peptide Characterization

The coiled coil peptides used in this study were purified by preparative-scale HPLC using the binary gradients listed in Table S1 below. The following figures show chromatograms of crude and purified peptides, as well as MALDI-TOF mass spectra of each purified peptide.

Table B1. List of elution conditions for preparative-scale HPLC purification of coiled coils.

Peptide	Binary gradient (Solvent A = water + 0.1% TFA, Solvent B = acetonitrile + 0.1% TFA)
L-K_4^7	5 to 30% B from 2.22 to 4 min, 30 to 45% B from 4 to 32 min
D-K_4^7	5 to 30% B from 2.22 to 4 min, 30 to 45% B from 4 to 32 min
L-E_4^7	5 to 95% B from 4 to 32 min

L-K_3^{11}	5 to 30% B from 2.22 to 4 min, 30 to 60% B from 4 to 25 min
D-K_3^{11}	5 to 30% B from 2.22 to 4 min, 30 to 60% B from 4 to 25 min
L-E_3^{11}	5 to 30% B by 2.22 min, 30 to 95% B from 2.22 to 22 min
D-E_4^{7}	5 to 95% B from 4 to 32 min

B1.1 L-K_4^7

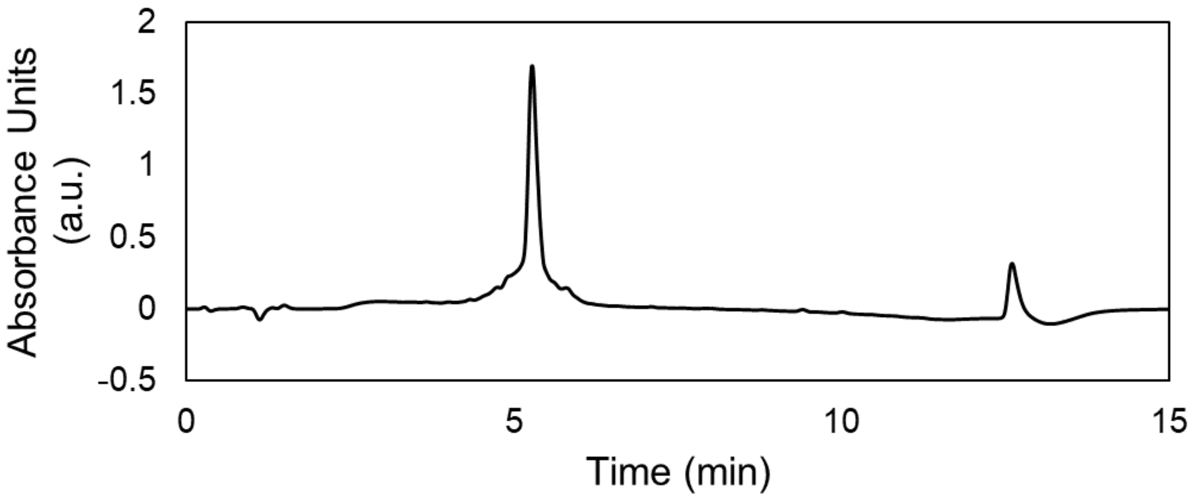

Figure B1. Analytical HPLC chromatogram of crude L-K_4^7. The peptide was eluted on a linear AB gradient from 5% to 95% B (v/v) over 9 minutes, where A is ultrapure water + 0.1% TFA and B is acetonitrile + 0.1% TFA.

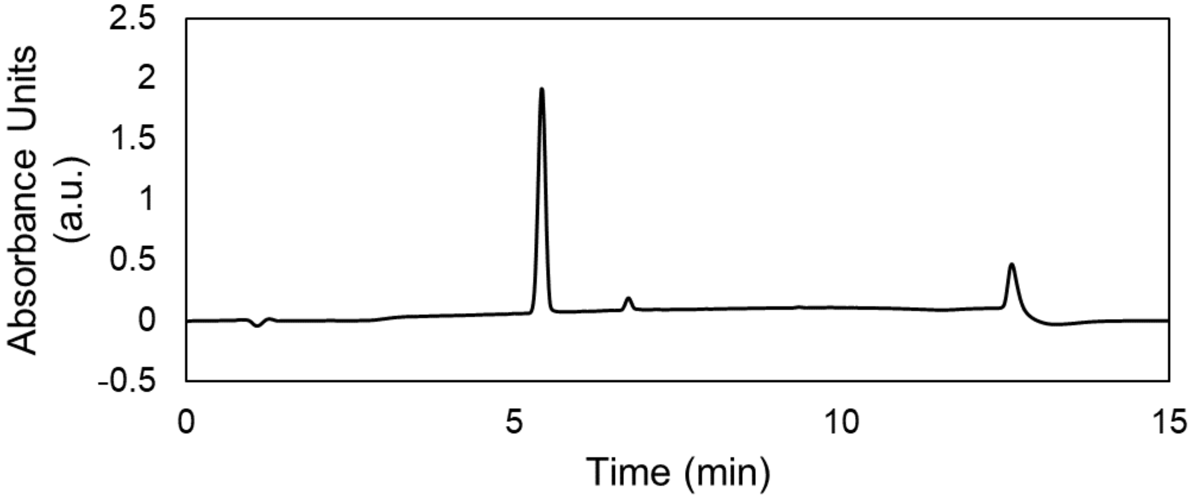

Figure B2. Analytical HPLC chromatogram of purified L-K_4^7. The primary peak corresponding to the purified peptide accounts for >96% of the total peak area. The peptide was eluted on a linear AB gradient from 5% to 95% B (v/v) over 9 minutes, where A is ultrapure water + 0.1% TFA and B is acetonitrile + 0.1% TFA.

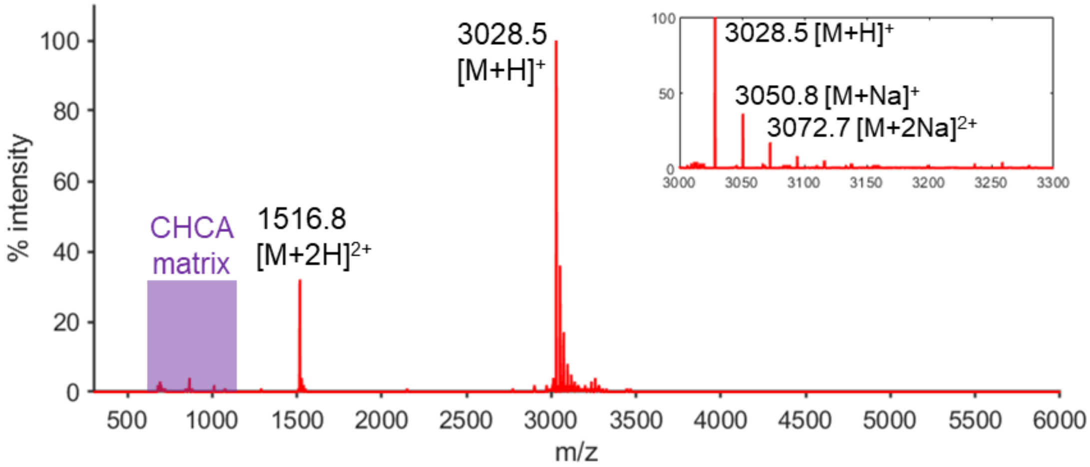

Figure B3. MALDI-TOF mass spectrum of purified L-K_4^7.

B1.2 D-K_4^7

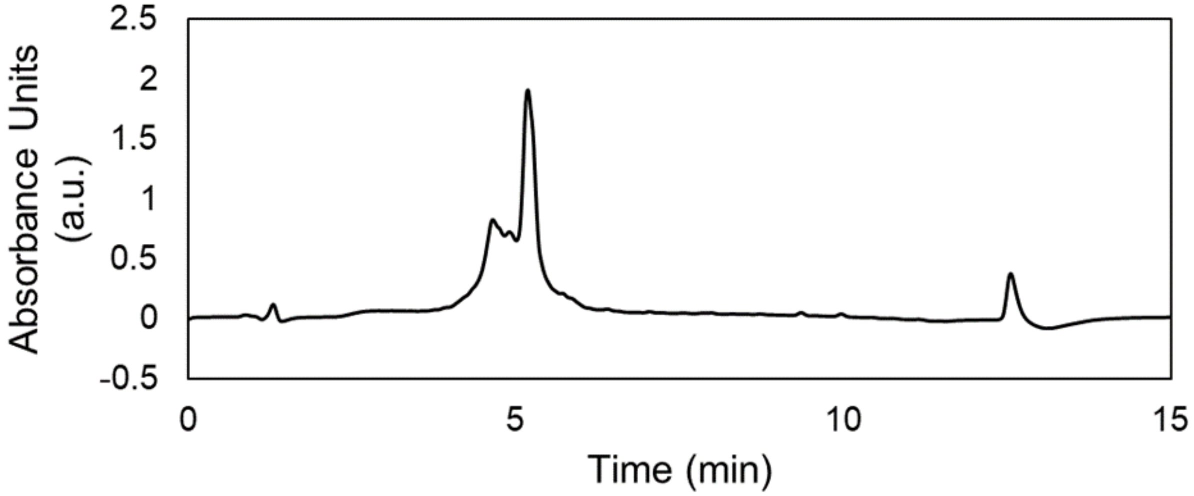

Figure B4. Analytical HPLC chromatogram of crude D-K_4^7. The peptide was eluted on a linear AB gradient from 5% to 95% B (v/v) over 9 minutes, where A is ultrapure water + 0.1% TFA and B is acetonitrile + 0.1% TFA.

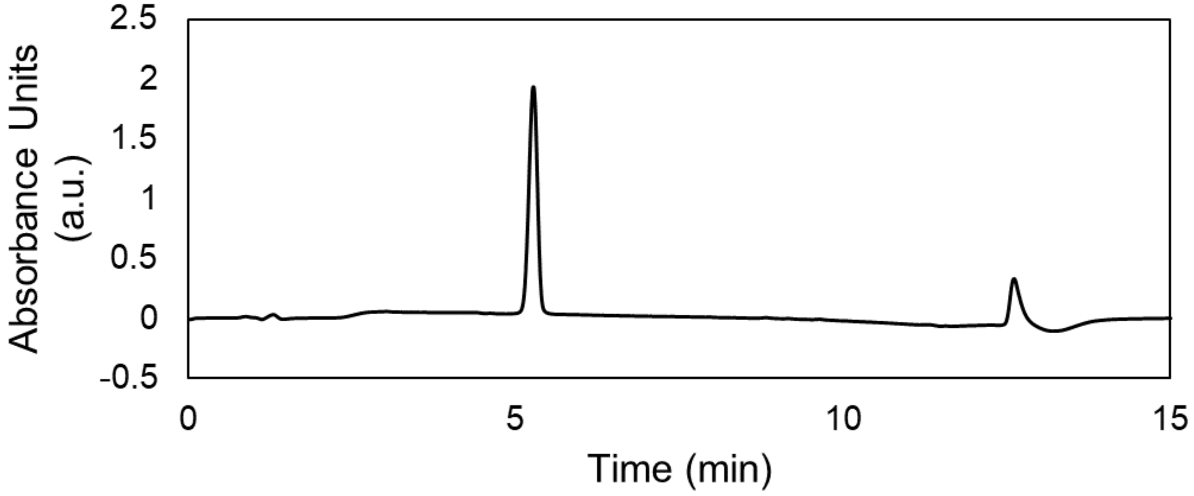

Figure B5. Analytical HPLC chromatogram of purified D-K_4^7. The primary peak corresponding to the purified peptide accounts for >99% of the total peak area. The peptide was eluted on a linear AB gradient from 5% to 95% B (v/v) over 9 minutes, where A is ultrapure water + 0.1% TFA and B is acetonitrile + 0.1% TFA.

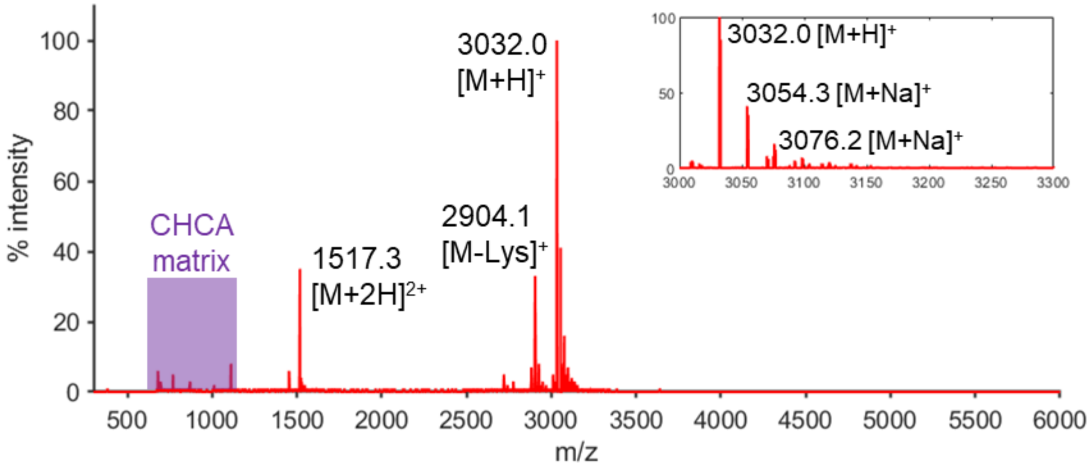

Figure B6. MALDI-TOF mass spectrum of purified D-K_4^7.

We note that the MALDI mass spectrum shows a Lys deletion. However, we see only one peak for D-K_4^7 in the analytical HPLC chromatogram for the purified peptide. Either the deletion is such a minor product that it is not detected on HPLC (which, despite the size of the peak in the mass spectrum, is possible because MALDI-TOF does not always convey relative abundance), or the deletion is not resolved from the main peptide peak under these HPLC conditions. Regardless, we used unpurified peptides to perform a titration of D-K_4^7 into L-E_4^7 (**Figure B7**), which yielded a thermogram and integrated heats of interaction that are very similar to the same titration performed with purified peptides (**Figure 3.2** and **Figure B21**). Therefore, even if the deletion is present in the purified D-K_4^7, it is unlikely to have affected the conclusions drawn from titrations using this peptide.

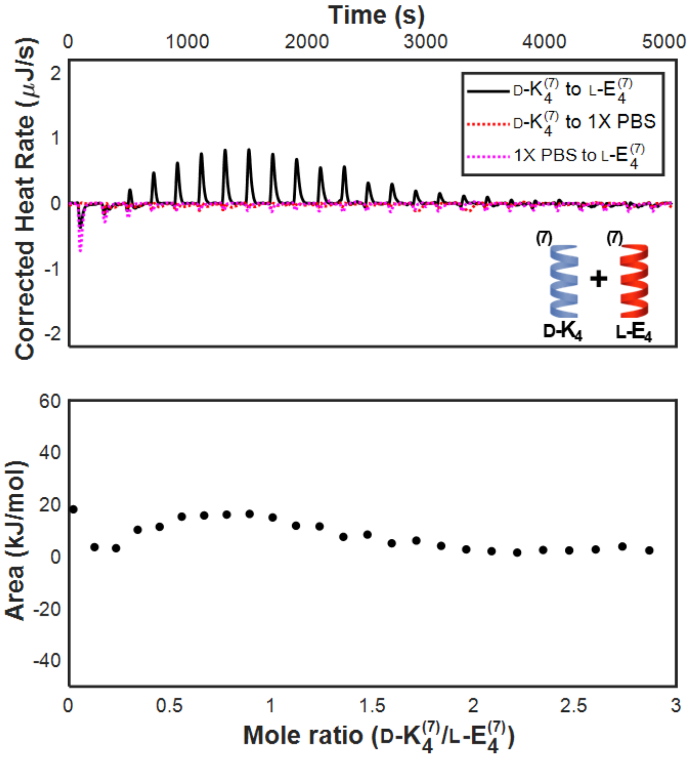

Figure B7. Thermogram and integrated binding heat from the titration of unpurified D-K$_4^7$ into L-E$_4^7$ at pH 7.4 in 1X PBS.

B1.3 L-E_4^7

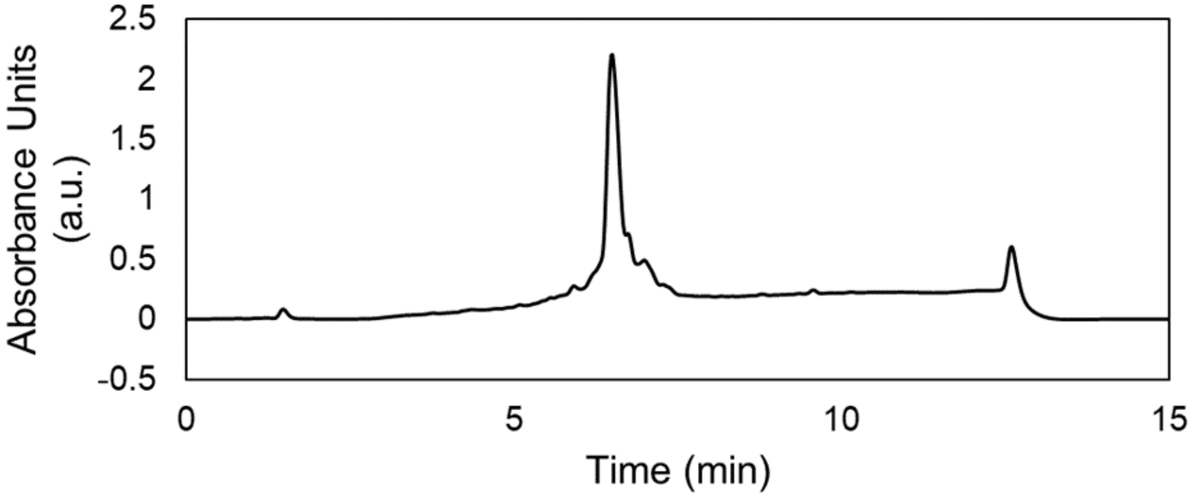

Figure B8. Analytical HPLC chromatogram of crude L-E_4^7. The peptide was eluted on a linear AB gradient from 5% to 95% B (v/v) over 9 minutes, where A is ultrapure water + 0.1% TFA and B is acetonitrile + 0.1% TFA.

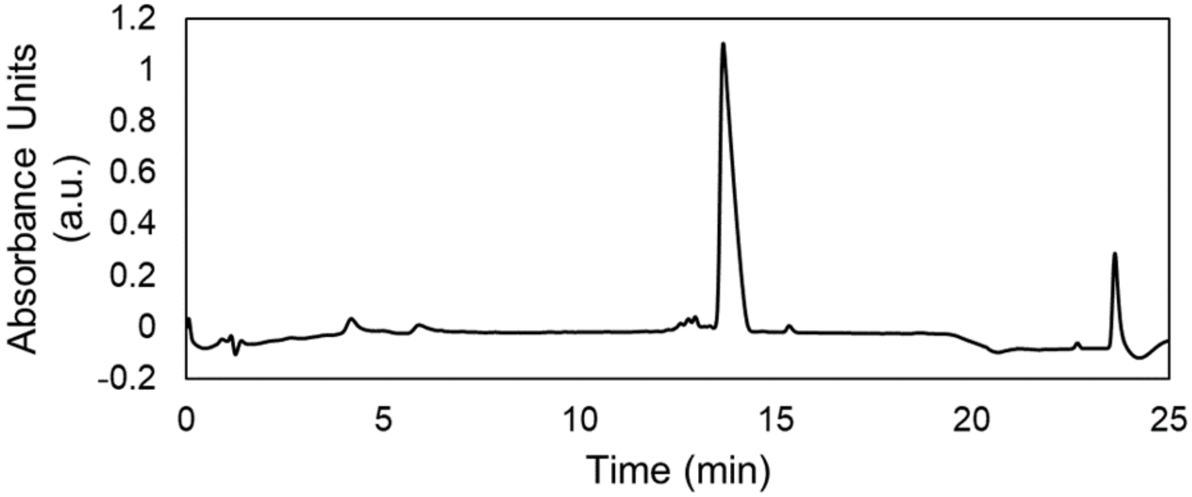

Figure B9. Analytical HPLC chromatogram of purified L-E_4^7. The primary peak corresponding to the purified peptide accounts for >93% of the total peak area. The peptide was eluted on a linear AB gradient from 5% to 62% B (v/v) over 17 minutes, where A is ultrapure water + 0.1% TFA and B is acetonitrile + 0.1% TFA.

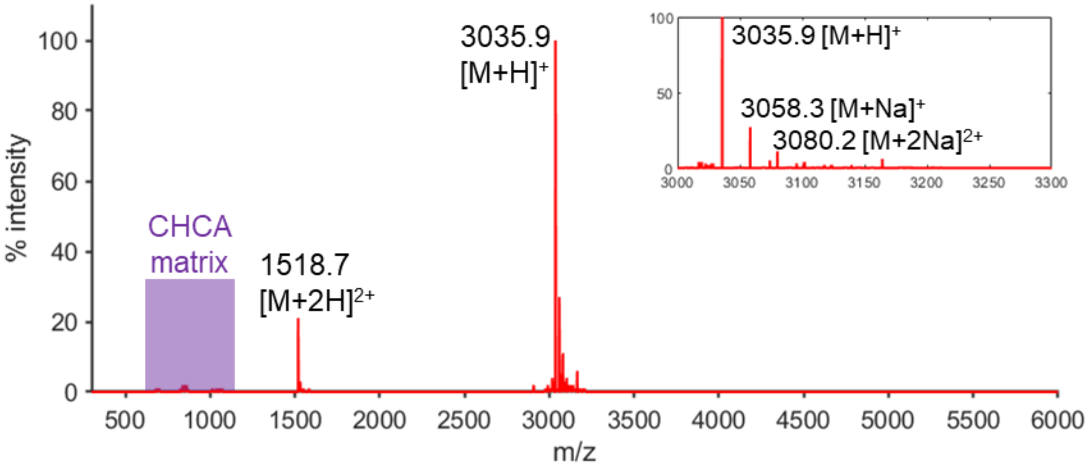

Figure B10. MALDI-TOF mass spectrum of purified L-E_4^7.

B1.4 L-K_3^{11}

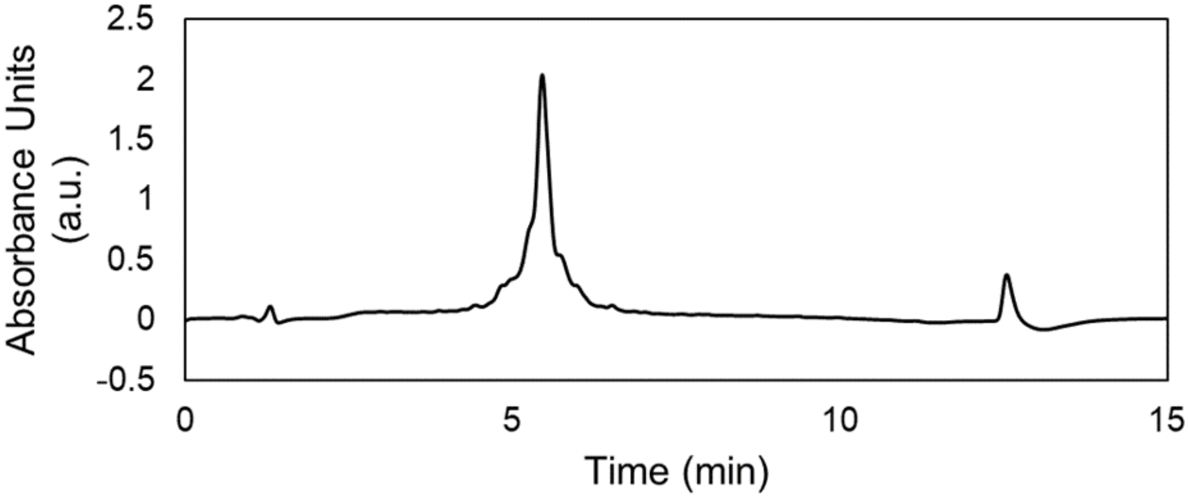

Figure B11. Analytical HPLC chromatogram of crude L-K_3^{11}. The peptide was eluted on a linear AB gradient from 5% to 95% B (v/v) over 9 minutes, where A is ultrapure water + 0.1% TFA and B is acetonitrile + 0.1% TFA.

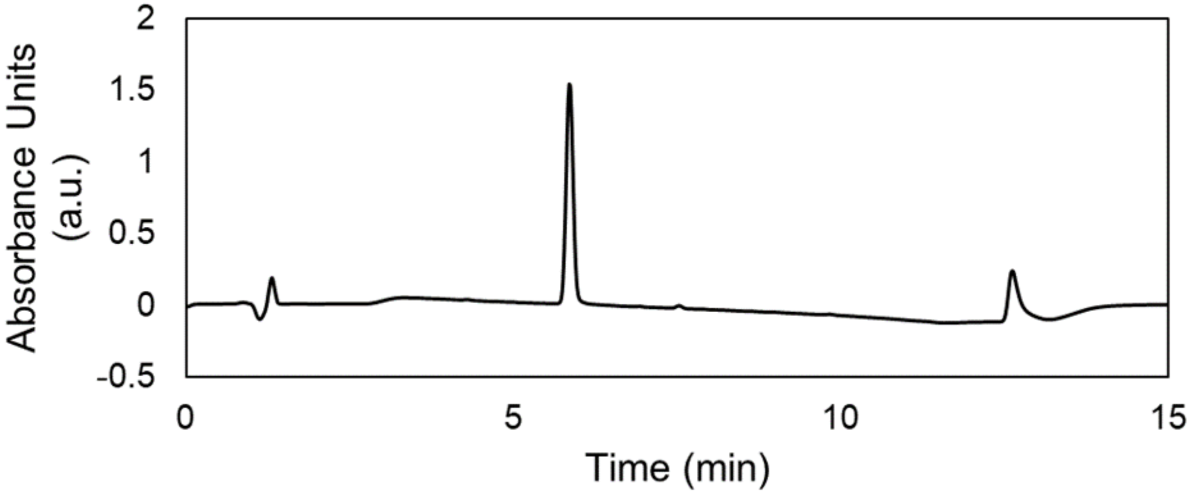

Figure B12. Analytical HPLC chromatogram of purified L-K_3^{11}. The primary peak corresponding to the purified peptide accounts for >99% of the total peak area. The peptide was eluted on a linear AB gradient from 5% to 95% B (v/v) over 9 minutes, where A is ultrapure water + 0.1% TFA and B is acetonitrile + 0.1% TFA.

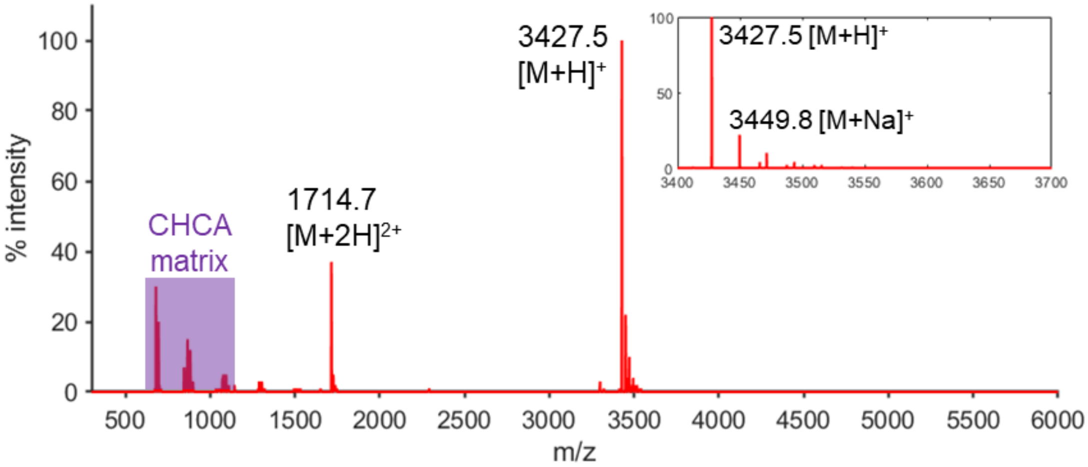

Figure B13. MALDI-TOF mass spectrum of purified L-K_3^{11}.

B1.5 D-K_3^{11}

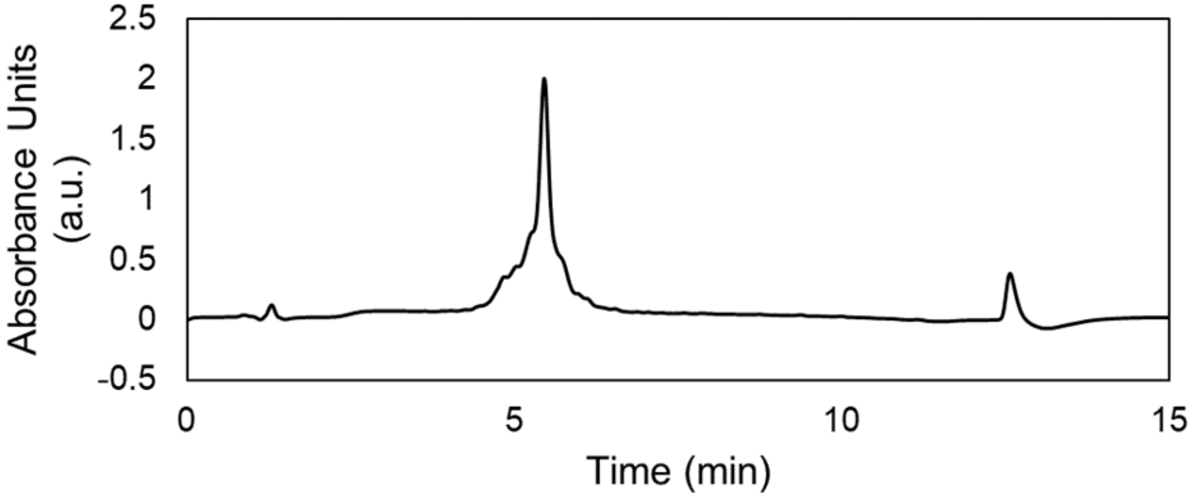

Figure B14. Analytical HPLC chromatogram of crude D-K_3^{11}. The peptide was eluted on a linear AB gradient from 5% to 95% B (v/v) over 9 minutes, where A is ultrapure water + 0.1% TFA and B is acetonitrile + 0.1% TFA.

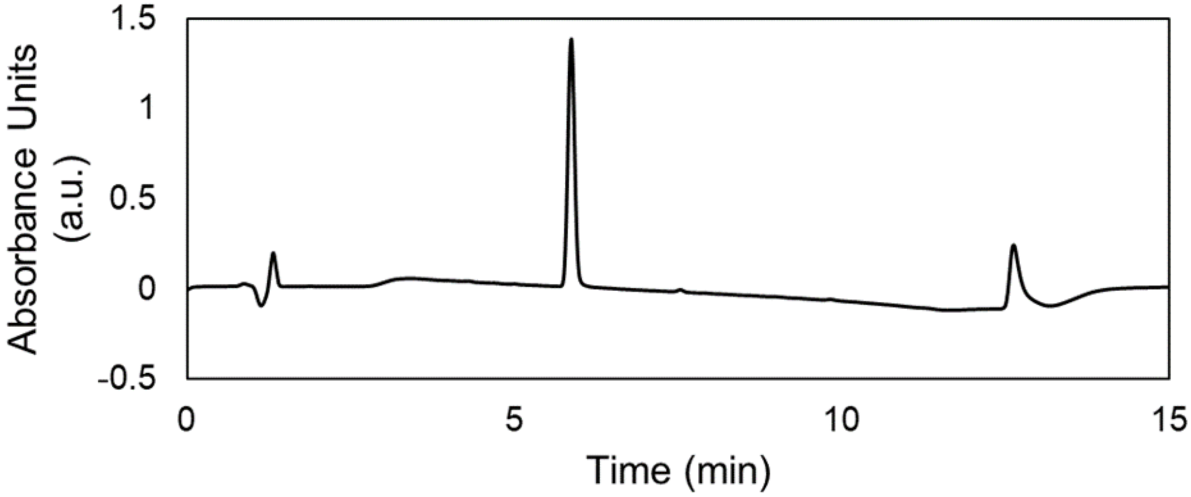

Figure B15. Analytical HPLC chromatogram of purified D-K_3^{11}. The primary peak corresponding to the purified peptide accounts for >99% of the total peak area. The peptide was eluted on a linear AB gradient from 5% to 95% B (v/v) over 9 minutes, where A is ultrapure water + 0.1% TFA and B is acetonitrile + 0.1% TFA.

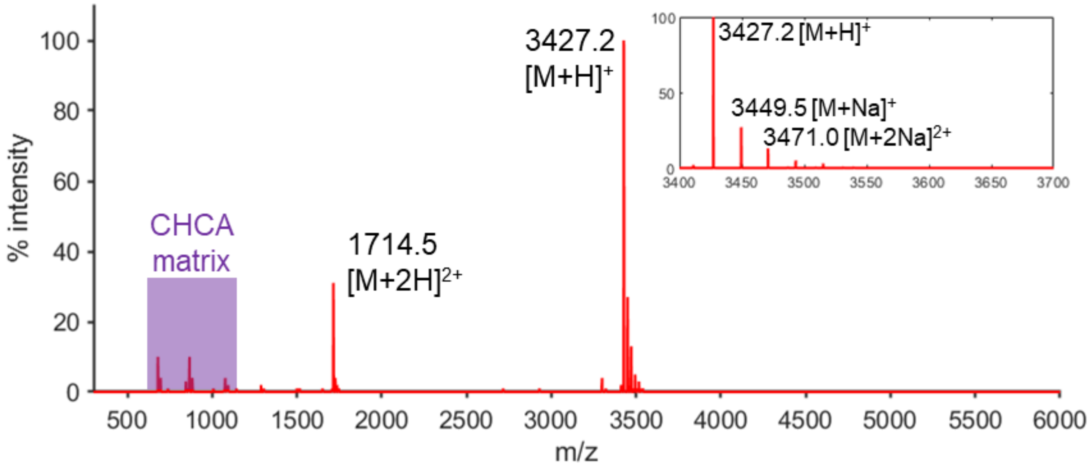

Figure B16. MALDI-TOF mass spectrum of purified D-K_3^{11}.

B1.6 L-E_3^{11}

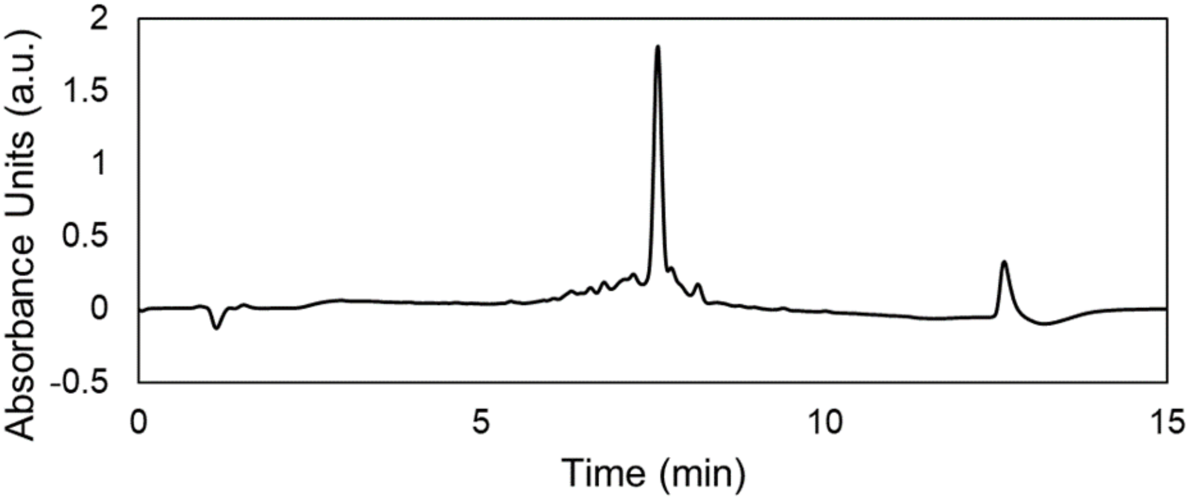

Figure B17. Analytical HPLC chromatogram of crude L-E_3^{11}. The peptide was eluted on a linear AB gradient from 5% to 95% B (v/v) over 9 minutes, where A is ultrapure water + 0.1% TFA and B is acetonitrile + 0.1% TFA.

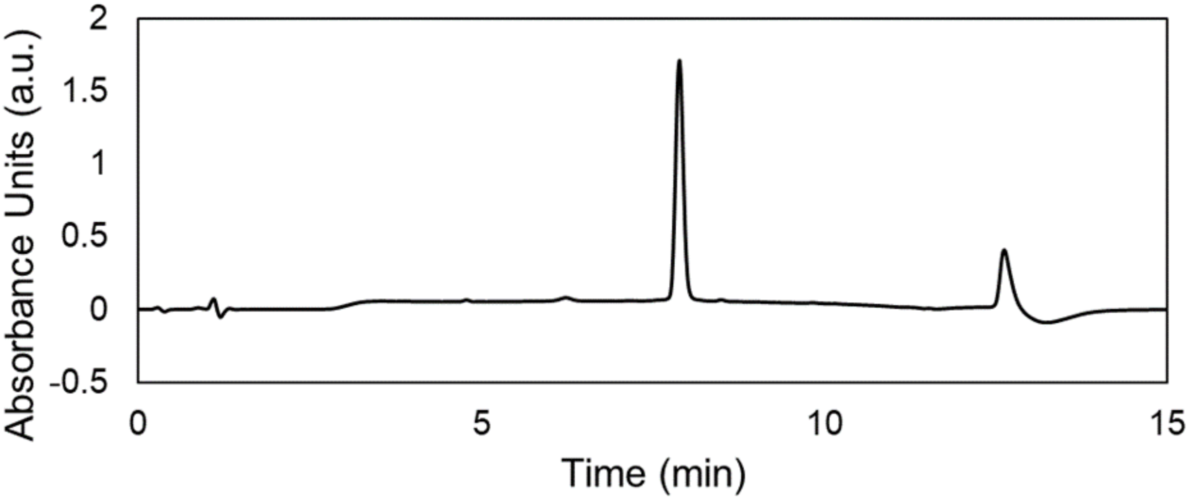

Figure B18. Analytical HPLC chromatogram of purified L-E_3^{11}. The primary peak corresponding to the purified peptide accounts for >97% of the total peak area. The peptide was eluted on a linear AB gradient from 5% to 95% B (v/v) over 9 minutes, where A is ultrapure water + 0.1% TFA and B is acetonitrile + 0.1% TFA.

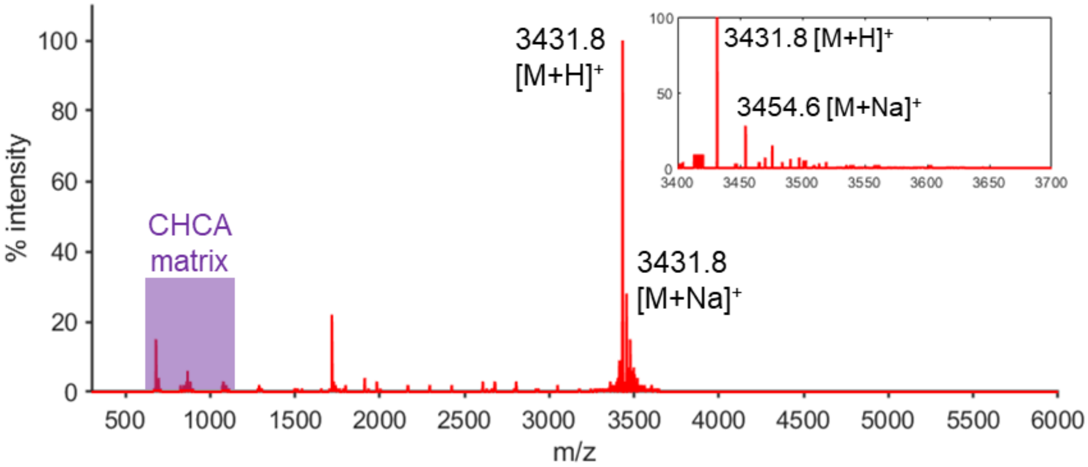

Figure B19. MALDI-TOF mass spectrum of purified L-E_3^{11}.

B1.7 MALDI of CHCA matrix

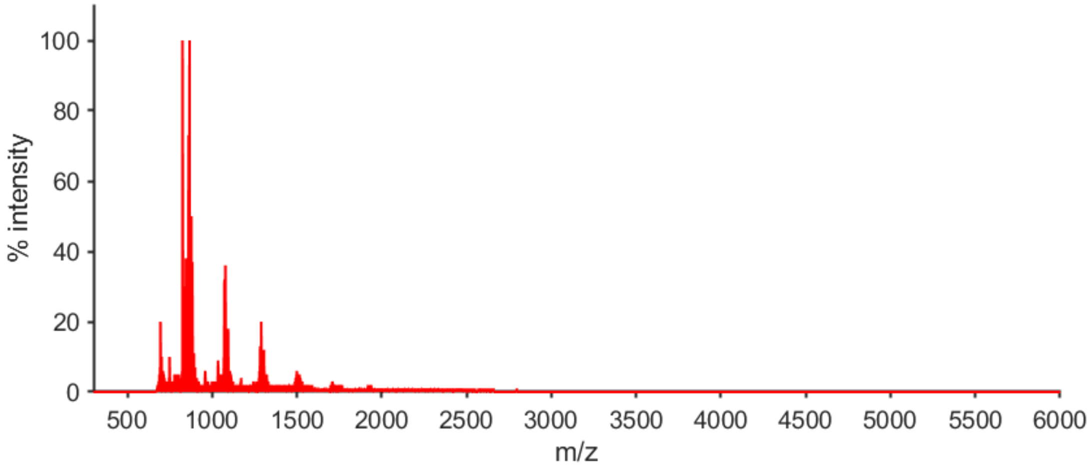

Figure B20. MALDI-TOF mass spectrum of CHCA matrix.

B2. Additional ITC thermograms

B2.1 Replicate of L-K_4^7 titrated into L-E_4^7

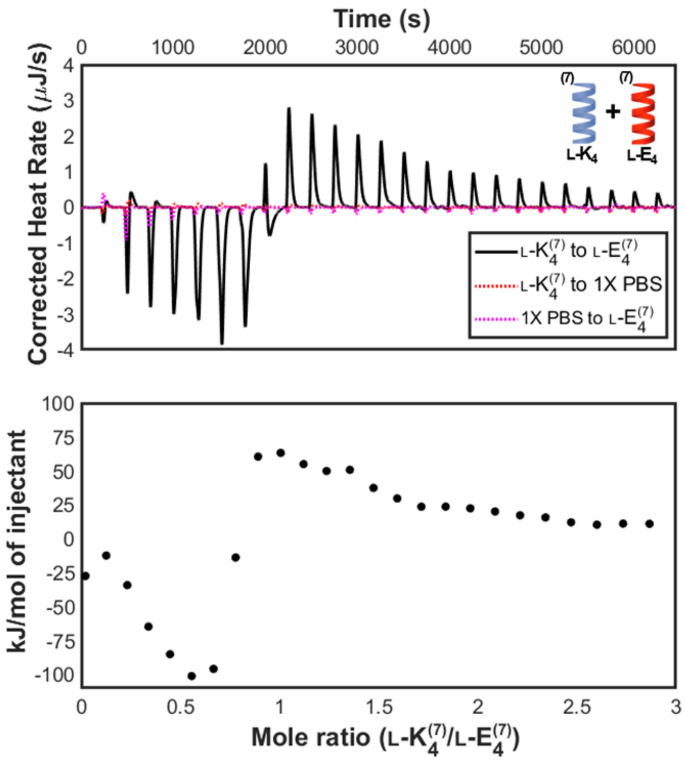

Figure B21. Thermogram and integrated binding heat from the titration of L-K_4^7 into L-E_4^7 at pH 7.4 in 1X PBS.

B2.2 Replicate of D-K_4^7 titrated into L-E_4^7

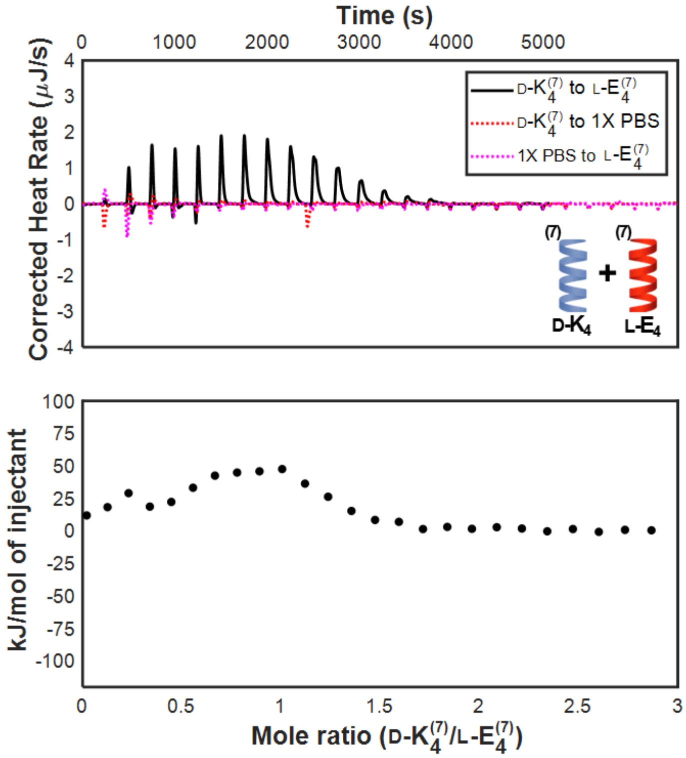

Figure B22. Thermograms and integrated binding heats from the titration of D-K_4^7 into L-E_4^7 at pH 7.4 in 1X PBS.

B2.3 Replicate of L-K_3^{11} titrated into L-E_3^{11}

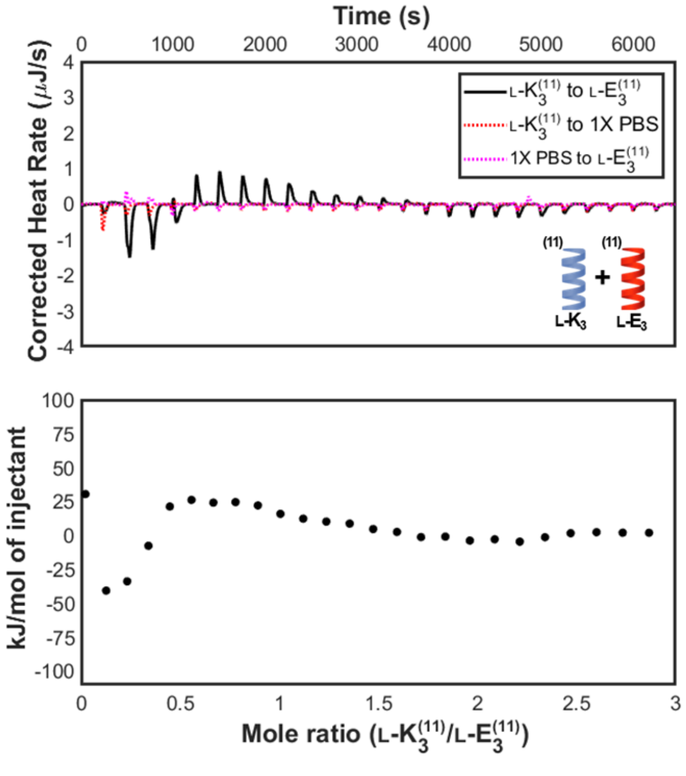

Figure B23. Thermograms and integrated binding heats from the titration of L-K_3^{11} into L-E_3^{11} at pH 7.4 in 1X PBS.

B2.4 Replicate of D-K_3^{11} titrated into L-E_3^{11}

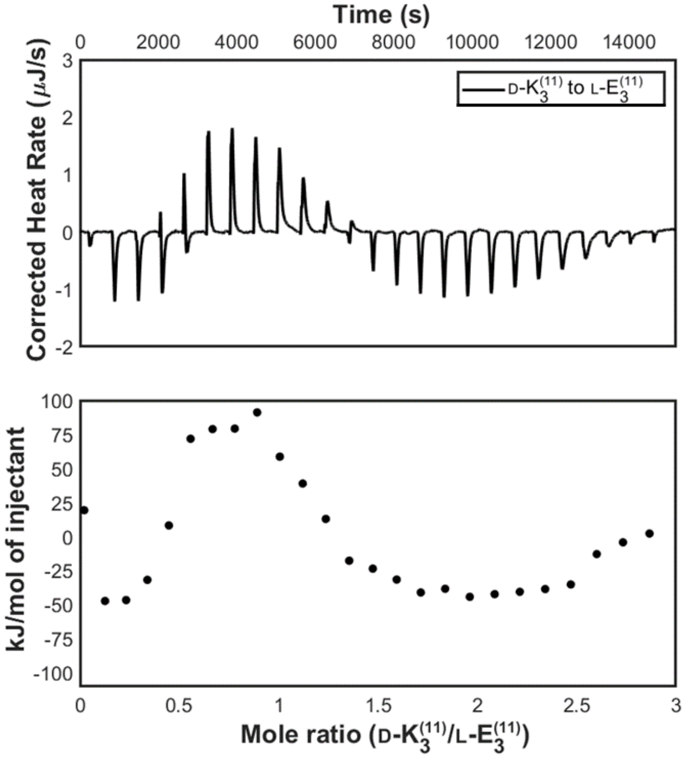

Figure B24. Thermogram and integrated binding heats from the titration of D-K_3^{11} into L-E_3^{11} at pH 7.4 in 1X PBS with 600 s spacing between injections.

B3. CD spectra of coiled coils

B3.1 Determination of CD spectroscopy conditions

The experimental parameters of cuvette path length, buffer concentration, and wavelength range were all varied to find the best experimental conditions for this system. There are three characteristic features of the CD spectrum of an α-helix, including (for an L-peptide), negative peaks at 222 nm and 208 nm as well as a positive peak at 193 nm. Therefore, we initially decided to collect data from 190 nm – 250 nm, choosing path length and buffer concentration based on obtaining quality data in this range. To this end, we observed the CD and high tension (HT) voltage signals for data collected in 1 mm and 0.1 mm cuvettes for 1X and 0.1X PBS. HT voltage is used to control the gain of the detector to obtain an ideal signal to noise ratio. When a sample absorbs too much light, the HT increases rapidly, and when HT is ≥ 700, the photons reaching the detector are not sufficient to provide reliable CD data. We found that, when using a path length of 1 mm and 1X PBS, the HT increased rapidly below 200 nm, leading to unreliable CD data, but for 0.1X PBS in a 1 mm cuvette or 1X PBS in a 0.1 mm cuvette, there were no problems with data reliability (**Figure B25**). Based on this data and in an attempt to keep the buffer concentration consistent with other experiments in this manuscript, we initially decided to use 1X PBS in a 0.1 mm cuvette to take CD measurements. However, we were surprised to find that under these conditions for a 25 µM solution of L-K_4^7, the CD spectrum displayed none of the characteristic peaks for an α-helix (**Figure B26, red**). For comparison, we also obtained a CD spectrum of 25 µM L-K_4^7 in 1X PBS in a 1 mm cuvette and observed the characteristic peaks at 222 nm and 208 nm (**Figure B26, black**). We also obtained CD spectra of L-K_4^7 in 0.1X PBS in both 1 mm and 0.1 mm cuvettes (**Figure B26, green and blue**) and found that characteristic α-helical peaks were only observed in the 1 mm cuvette. These data indicate that CD signal depends on path length. For this reason, and to keep the buffer concentration consistent with other experiments, we decided to move forward using the 1 mm cuvette and 1X PBS for wavelengths from 200 nm – 250 nm, relying on the two characteristic α-helical peaks at 222 nm and 208 nm to demonstrate helicity despite not having reliable data for the characteristic peak at 193 nm.

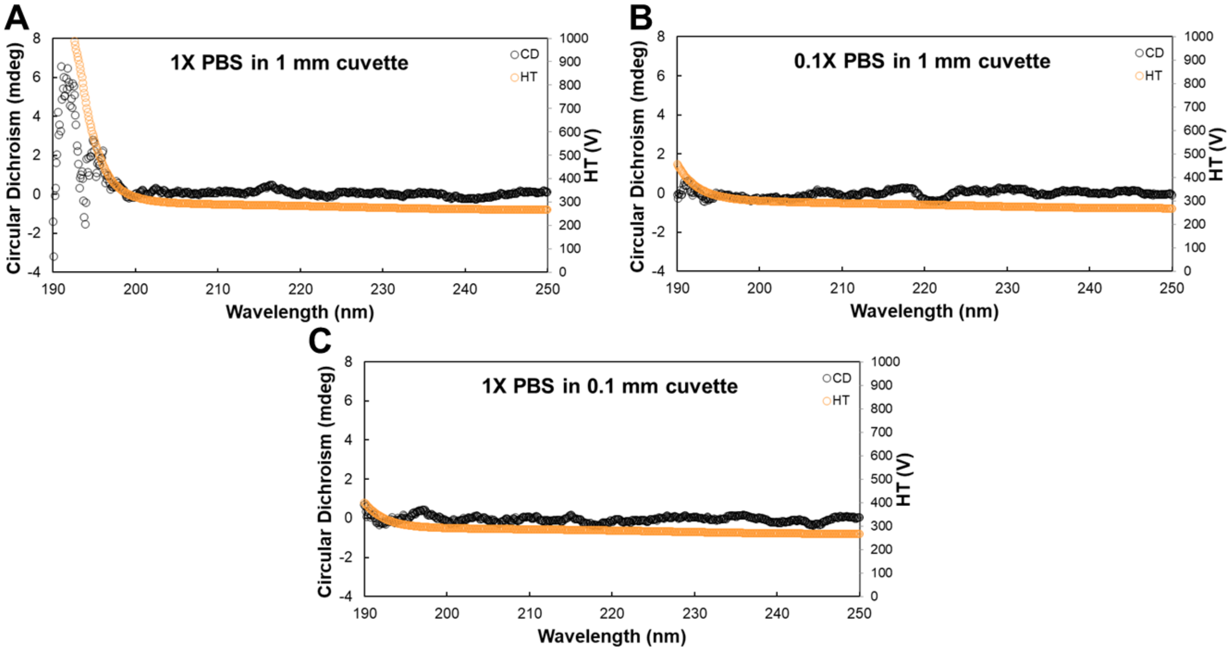

Figure B25. CD and HT voltage of A) 1X PBS in a 1 mm cuvette, B) 0.1X PBS in a 1 mm cuvette, and C) 1X PBS in a 0.1 mm cuvette. The HT voltage for the 1X PBS in a 1 mm cuvette increases rapidly between 200 nm – 190 nm, resulting in unreliable data. The HT voltage remains below 700 V for the other conditions, indicating that the data is reliable for the full range of 190 nm – 250 nm.

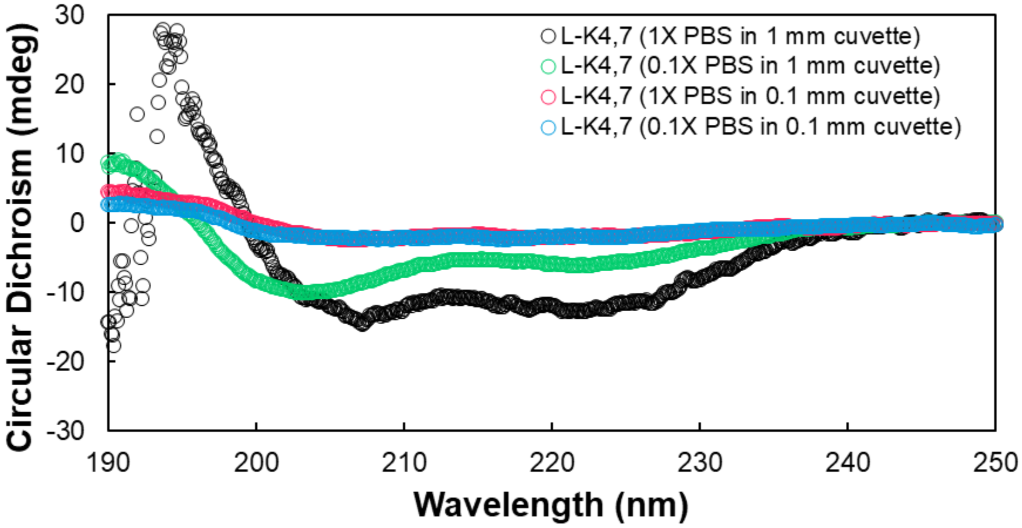

Figure B26. CD spectra of 25 μM L-K$_4^7$ in 1X PBS or 0.1X PBS measured in a 1 mm or 0.1 mm cuvette. Characteristic peaks for α-helices at 222 nm and 208 nm were only observed in samples measured in a 1 mm cuvette.

B3.2 CD spectroscopy of L-K$_4^7$, L-E$_4^7$, D-K$_4^7$, L-K$_3^{11}$, L-E$_3^{11}$, and D-K$_3^{11}$

CD spectroscopy was used to confirm the secondary structure and stereochemistry of the coiled coils used in this study. All coiled coils were helical at 100 μM in 1X PBS (evidenced by peaks at 222 nm and 208 nm), while D-coils exhibit mean residue ellipticities > 0 and L-coils exhibit mean residues ellipticities < 0, consistent with the expected stereochemistry (**Figure B27**).

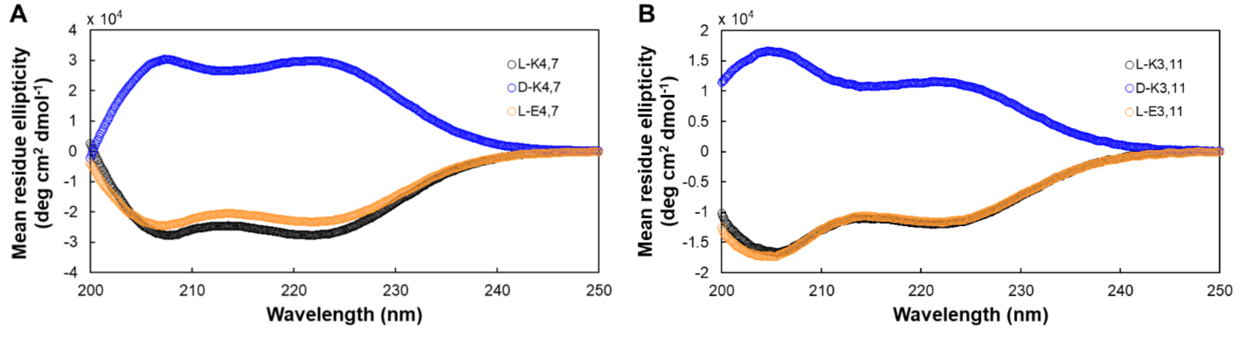

Figure B27. CD spectra of A) L-K$_4^7$, L-E$_4^7$, and D-K$_4^7$ and B) L-K$_3^{11}$, L-E$_3^{11}$, and D-K$_3^{11}$. All coils were helical and exhibited the expected stereochemistry.

B3.3 CD spectroscopy of blended coiled coils

Upon mixing homochiral or heterochiral blends of heptads and hendecads, we used CD spectroscopy to compare the secondary structure of the blended coiled coils to the individual coiled coils (**Figure B28**). For homochiral blends, the coiled coils with a heptad repeating sequence were found to have a slightly greater mean residue ellipticity at 208 nm and 222 nm, the wavelengths most associated with α-helicity. The hendecad coiled coils similarly exhibited greater mean residue ellipticities at 208 nm and 222 nm for homochiral blends. On the other hand, heterochiral blends of both heptad and hendecad coiled coils resulted in signals close to zero across the wavelength tested, due to the opposing stereochemistries of the blended peptides.

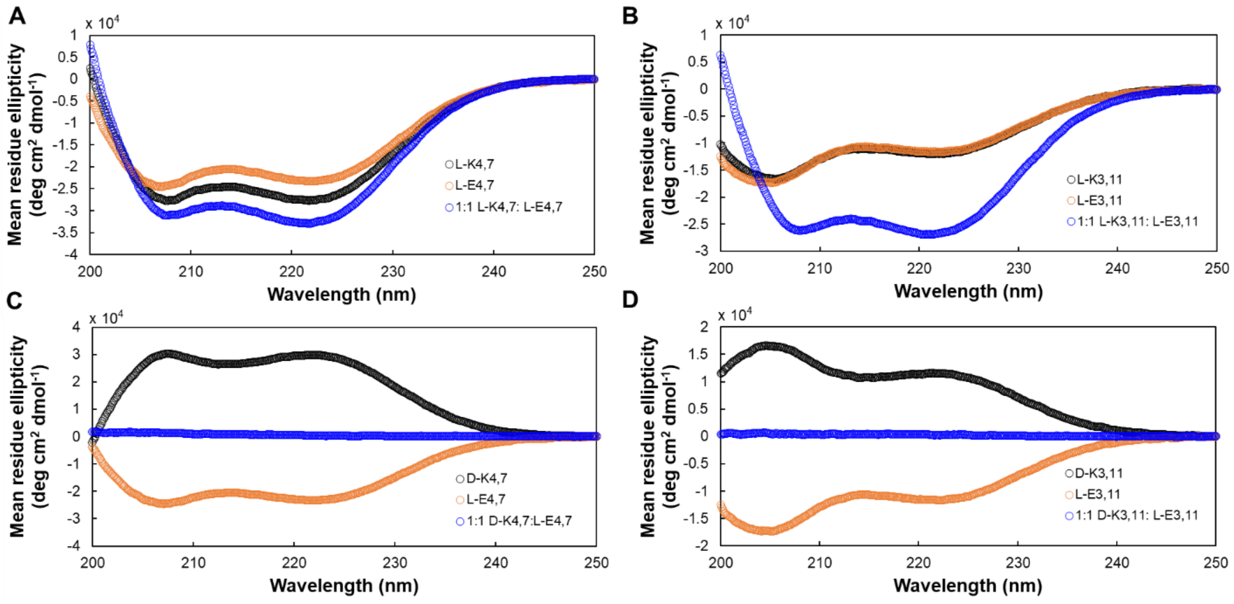

Figure B28. CD spectra of A) L-K$^7_4$, L-E$^7_4$, and 1:1 L-K$^7_4$: L-E$^7_4$, B) L-K$^{11}_3$, L-E$^{11}_3$, and 1:1 L-K$^{11}_3$: L-E$^{11}_3$, C) D-K$^7_4$, L-E$^7_4$, and 1:1 D-K$^7_4$: L-E$^7_4$, and D) D-K$^{11}_3$, L-E$^{11}_3$, and 1:1 D-K$^{11}_3$: L-E$^{11}_3$. All individual coils were helical as evidenced by peaks present at 208 nm and 222 nm. For the homochiral coiled coils, blending the heptad coiled coils (A) or hendecad coiled coils (B) resulted in a mixture with stronger helicity, as the mean residue ellipticity at these wavelengths was greater. Blending the heterochiral coiled coils (C and D) resulted in effectively no CD signal as the destructive interference of the equimolar peptides of opposing stereochemistry eliminates the signal.

B3.4 Thermal stability of L-K$_4^7$: L-E$_4^7$, D-K$_4^7$: L-E$_4^7$, L-K$_3^{11}$: L-E$_3^{11}$, and D-K$_3^{11}$: L-E$_3^{11}$ as measured by CD spectroscopy as a function of temperature

Temperature-dependent CD spectroscopy was used to assess the stability of homochiral and heterochiral heptad complexes. Solutions of 200 µM L-K$_4^7$, L-E$_4^7$, D-K$_4^7$, L-K$_3^{11}$, L-E$_3^{11}$, and D-K$_3^{11}$ were prepared in 1X PBS, then equal volumes of L-K$_4^7$ and L-E$_4^7$, D-K$_4^7$ and L-E$_4^7$, L-K$_3^{11}$ and L-E$_3^{11}$, or D-K$_3^{11}$ and L-E$_3^{11}$ were stirred together overnight to form an equimolar complex. CD spectra were taken of the complex solutions the next day from 5 °C to 90 °C in 5 °C increments. The homochiral heptads (**Figure B29 A**) and homochiral hendecads (**Figure B30 A**) maintained a helical conformation even at 90 °C, as evidenced by the retention of characteristic peaks at 222 nm and 208 nm, although the helical character of both complexes was reduced as measured by the increase in mean residue ellipticity at 222 nm (**Figure B29 A and Figure B30 A, bottom panel**). Unsurprisingly, the competing positive and negative CD signals of the D- and L-hendecad coils led to a lack of signal for both heterochiral heptads and heterochiral hendecads (**Figure B29 B and Figure B30 B**).

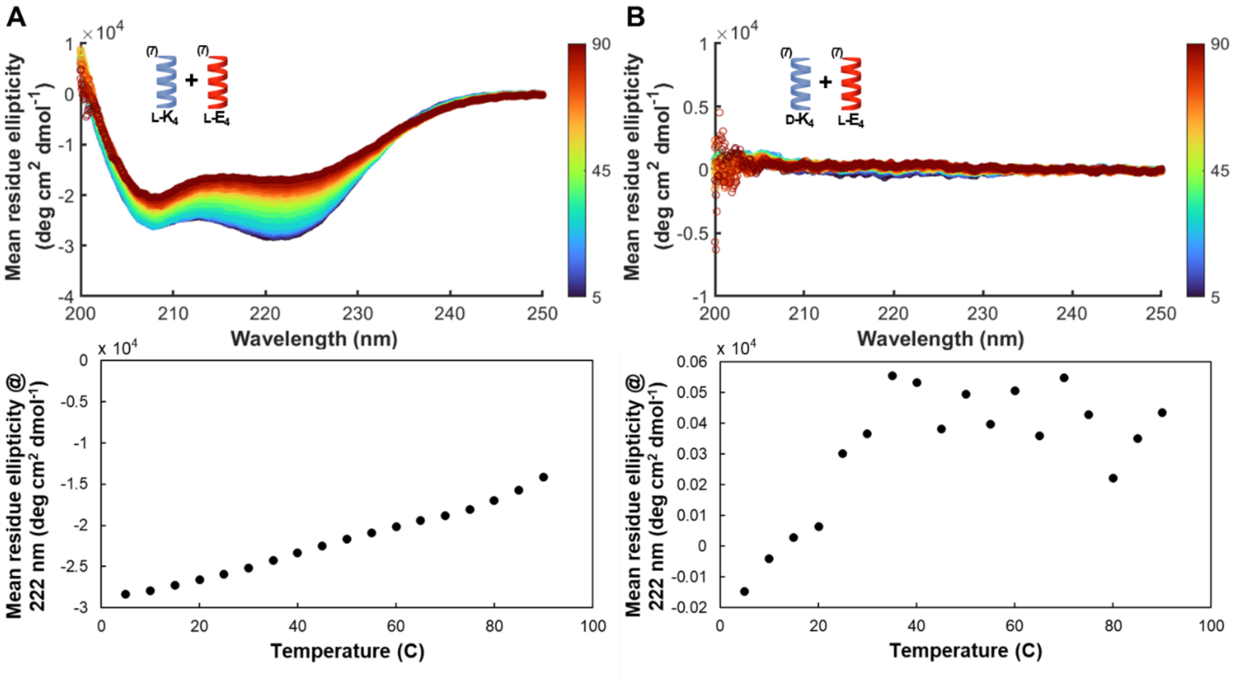

Figure B29. CD spectra as a function of temperature for A) L-K$_4^7$: L-E$_4^7$ and B) D-K$_4^7$: L-E$_4^7$. The top panel shows all CD spectra from 5 °C to 90 °C in intervals of 5 °C and the bottom panel shows just the mean residue ellipticity of the complex at 222 nm as a measure of helicity.

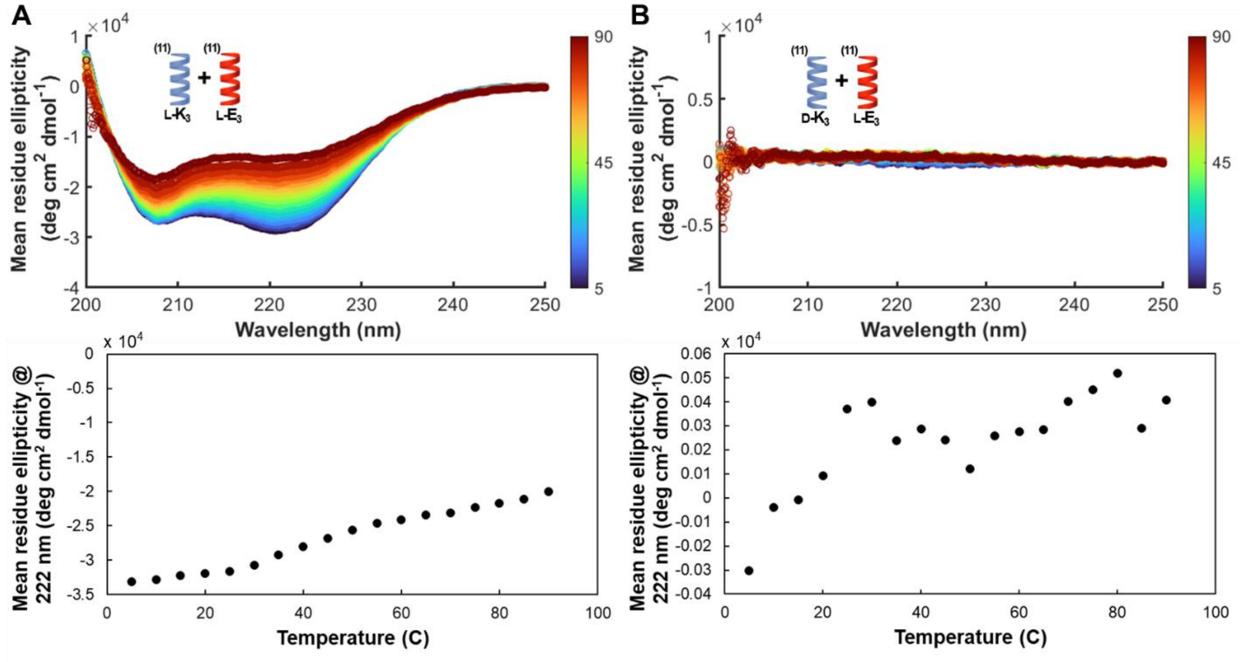

Figure B30. CD spectra of A) L-K$_3^{11}$: L-E$_3^{11}$ and B) D-K$_3^{11}$: L-E$_3^{11}$. The top panel shows all CD spectra from 5 °C to 90 °C in intervals of 5 °C and the bottom panel shows just the mean residue ellipticity of the complex at 222 nm as a measure of helicity.

B4. Additional degradation data

B4.1 Degradation of coiled coils in the absence of Proteinase K

As a control experiment, coiled coil complexes were incubated in 1X PBS following the same procedure as the degradation experiment without adding Proteinase K to test their stability in buffer. For heptad complexes (L-K$_4^7$: L-E$_4^7$ and D-K$_4^7$: L-E$_4^7$) and hendecad complexes (L-K$_3^{11}$: L-E$_3^{11}$ and D-K$_3^{11}$: L-E$_3^{11}$), the complexes remained stable out to 24 or 30 h (**Figure B31 and Figure B32**).

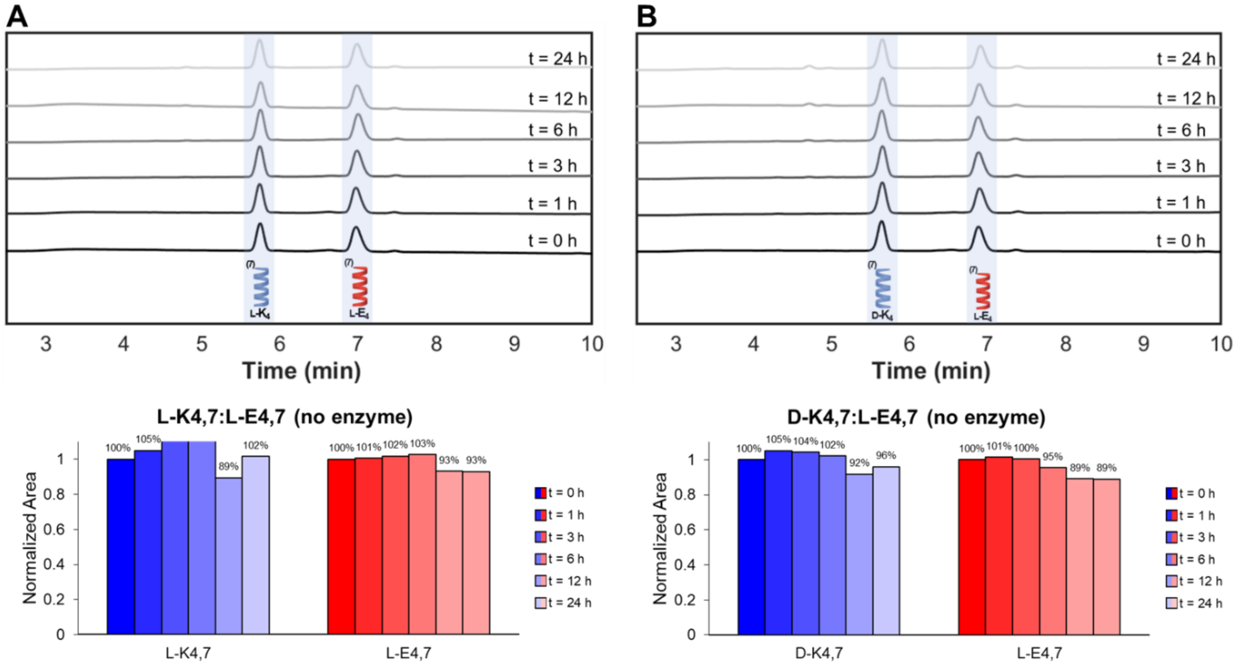

Figure B31. Stability of A) L-K_4^7: L-E_4^7 and B) D-K_4^7: L-E_4^7 upon incubation in 1X PBS.

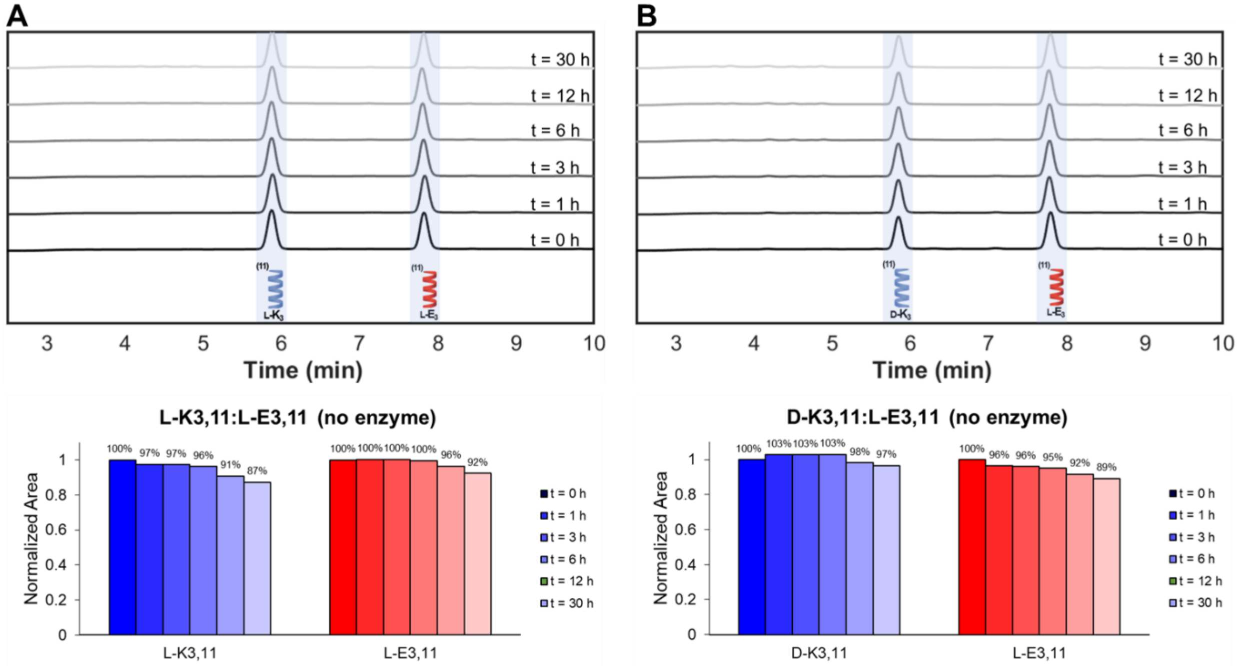

Figure B32. Stability of A) L-K_3^{11}: L-E_3^{11} and B) D-K_3^{11}: L-E_3^{11} upon incubation in 1X PBS.

4.2 Extended degradation of D-K$_3^{11}$: L-E$_3^{11}$ upon incubation with Proteinase K

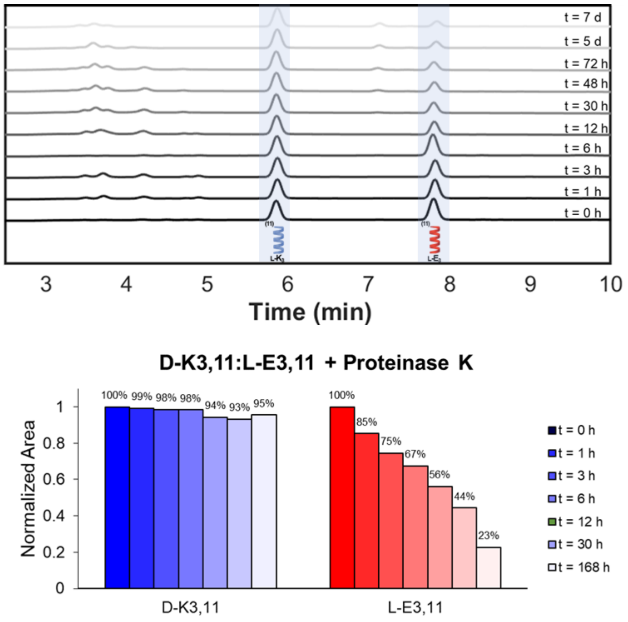

Figure B33. Proteolytic stability of D-K$_3^{11}$: L-E$_3^{11}$ in the presence of 5 μg/mL Proteinase K. HPLC chromatograms and percent intact K$_3^{11}$ and E$_3^{11}$ by peak area immediately after addition of and upon incubation for 1, 3, 6, 12, 30, 48, 72, 120, and 168 h with Proteinase K.

B5. MATLAB script to normalize elution time for degradation data

```
clear all
clc

% This code is intended to "normalize" HPLC data by lining up a peak in the plot at the
same x value for the entire set of data.  For example, I am
% creating this because I have degradation data, but the peaks shift slightly in elution
time for each time point run.  I want to align all of
% them so that the peak associated with one peptide always elutes at the same time.

% We start by reading in the data from a text file.
T = readtable('hplcdata.txt');
x(1,:) = transpose(table2array(T(1:height(T), 1)));
y(1,:) = transpose(table2array(T(1:height(T), 2)));
for i = 1:width(T)-1
   x(i,:) = x(1,:);
```

```
end
for j = 2:width(T)
   y(j-1,:) = transpose(table2array(T(1:height(T), j)));
end

% earlytime and latetime set the bounds for where the code will search for a peak in the data to align.  For example, I have a peak that elutes at
% ~5.8 min in every run, so I have the code search for the max value between the times of 5.5 min and 6.5 min.
earlytime = 5.5;
latetime = 6.5;

% Here, we crop the datasets to work with only the data between earlytime and latetime.  However, often the xdata (Time) from HPLC does not include
% whole numbers, so I search for any value that is without 0.001 of earlytime and latetime in the xdata and crop the datasets to that.
croppedx = x(1,find(x(1,:)>earlytime-0.001 & x(1,:)<earlytime+0.001):find(x(1,:)>latetime-0.001 & x(1,:)<latetime+0.001));
for k = 1:width(T)-1
   croppedy(k,:) = y(k,find(x(1,:)>earlytime-0.001 & x(1,:)<earlytime+0.001):find(x(1,:)>latetime-0.001 & x(1,:)<latetime+0.001));
end

% This code only cares about the index, or position, of the max value and doesn't need the actual value, so we use the ~ operator to discard the
% actual value, and I0-I# to store the index.  For cases where a dataset doesn't have a peak in the region of interest (bewteen earlytime and
% latetime), we just set the index to I(1) (giving it the same index as the first dataset, meaning we won't shift the data). This is because we don't
% want to shift the data based on random noise in the baseline.  The noise value can be set based on your data.
noise = 0.09;
for l = 1:width(T)-1
   if max(croppedy(l,:)) > noise
      [~,I(l)] = max(croppedy(l,:));
   else
      I(l) = I(1);
   end
end

% This is the code block that actually shifts the data.  We know the index of the peak in the first dataset that we want to align the others to
% (I0), so we take that x value and subtract the x value of the peak in the next dataset.  If the peaks elute at the same time, this value is 0.  If
% they elute at slightly different times, the value of (croppedx(I0)-croppedx(I#)) will be the value in x that the dataset needs
```

```
% to move.  We change the values of the x data for each dataset individually.
for m = 2:width(T)-1
    x(m,:) = x(m,:) + (croppedx(I(1))-croppedx(I(m)));
end

% To stack the data vertically, I am simply adding value to each subsequent dataset. y0
is plotted as is, y1 is plotted 1.5 y units above that, and
% so on.
for n = 2:height(y)
    y(n,:) = y(n,:) + 1.5*(n-1);
end

% Plot the data!
cmap = gray(height(y)+1);
for t = 1:height(y)
    plot(x(t,:),y(t,:), 'LineWidth', 1.75); axis([2.5 10 -3 9])
    hold on
end
% Modify the plot to make it look nicer
ax = gca;
ax.TickLength = [0,0];
ax.LineWidth = 2;
ax.FontName = 'Arial';
ax.FontSize = 16;
yticks([]);
xlabel('\bf Time (min)', 'Fontsize', 18);
w = 8;
h = 4;
set(gcf,'units','inches','position',[4,4,w,h]);
%legend('t = 0 h', 't = 1 h', 't = 3 h', 't = 6 h', 't = 12 h', 't = 30 h', 't = 48 h', 't = 72 h', 't =
120 h', 't = 168 h', 't = 240 h', 'Location', 'North', 'Orientation','horizontal', 'FontSize', 11);
%legend boxoff
colororder(cmap);
```

Appendix C: Supporting information for Chapter 4

List of Figures

C1. $(GA)_{10}$ characterization

C1.1 $(GA)_{10}$ structure and purity

The structure of $(GA)_{10}$ was confirmed by NMR spectroscopy performed in deuterated dimethyl sulfoxide and MALDI-TOF mass spectrometry, while the purity was determined by HPLC. The expected peaks are present in the expected abundance in NMR and the mass is as expected by MALDI, so we conclude that $(GA)_{10}$ was successfully synthesized. By HPLC, we do observe two peaks, with the primary peak accounting for >91% of the total peak area. Due to the low solubility of the $(GA)_{10}$ peptide, we did not attempt to purify by preparative-scale HPLC and instead used the peptide as synthesized.

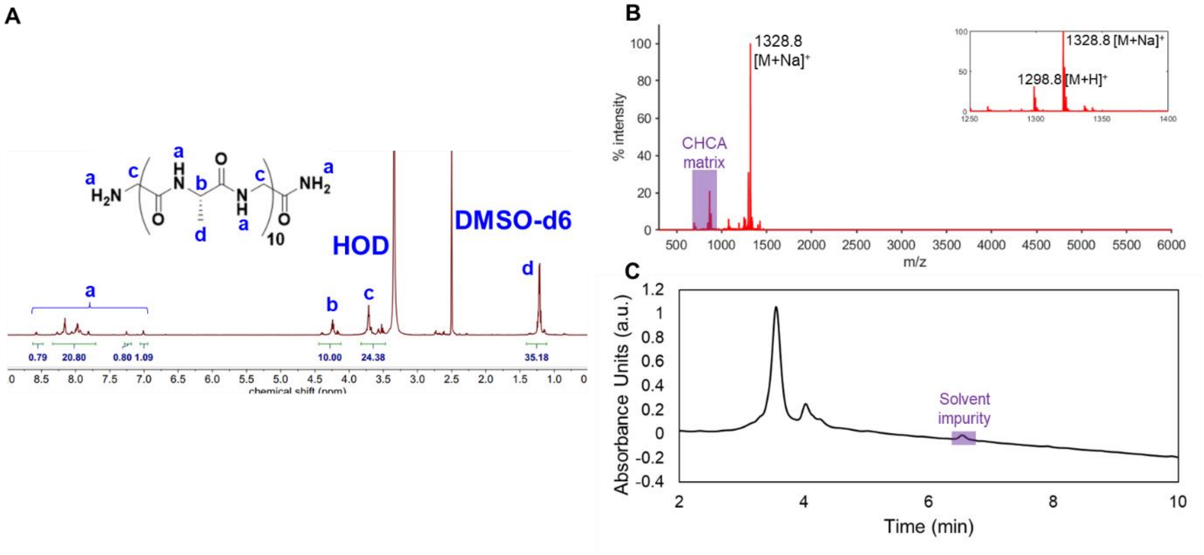

Figure C1. Structural and purity characterization of $(GA)_{10}$. A) NMR spectrum of $(GA)_{10}$, with expected peaks labeled. B) MALDI-TOF mass spectrum of $(GA)_{10}$ with $[M+H]^+$ and $[M+Na]^+$ peaks labeled. C) Analytical HPLC chromatogram of $(GA)_{10}$. The primary peak accounts for >91% of the total peak area. The peptide was eluted on a linear AB gradient from 5% to 95% B (v/v) over 9 minutes, where A is ultrapure water + 0.1% TFA and B is acetonitrile + 0.1% TFA.

C1.2 $(GA)_{10}$ secondary structure

IR spectroscopy was used to determine the secondary structure of $(GA)_{10}$ in both the powder form (**Figure C2**) and in 10 mM phosphate buffer (**Figure 2**). In both forms, a peak at 1624 cm^{-1} characteristic of β-sheet formation is present, indicating that $(GA)_{10}$ is rich in β-sheet.

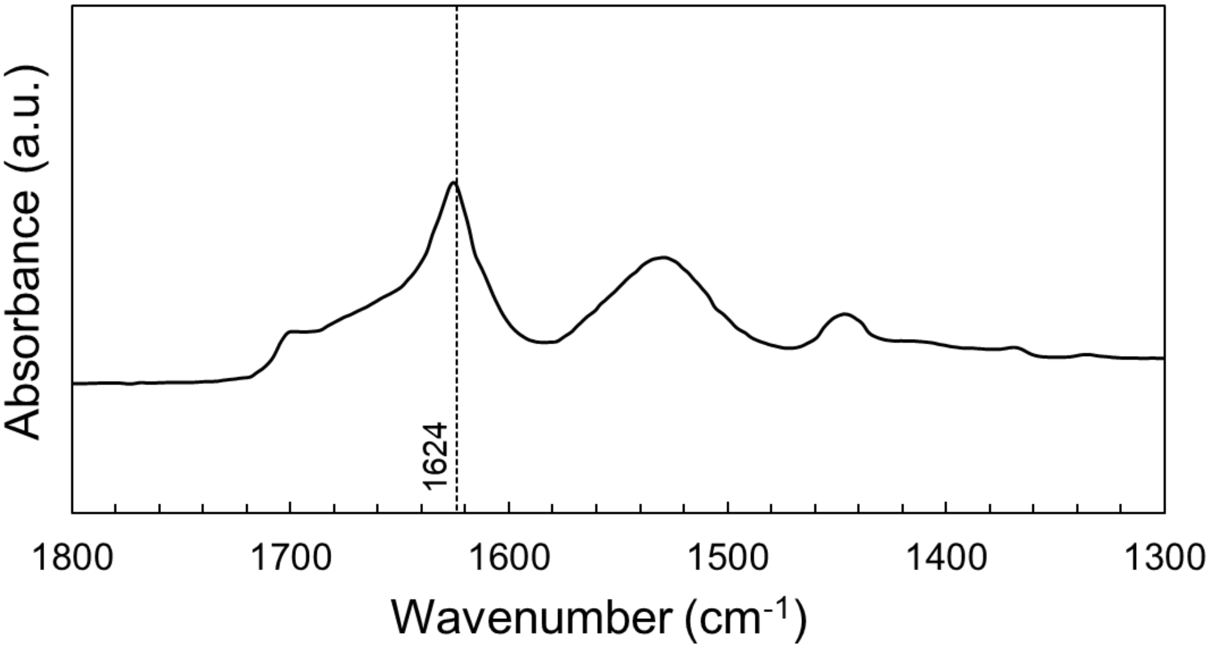

Figure C2. IR spectrum of powder $(GA)_{10}$. The characteristic β-sheet peak at 1624 cm^{-1} confirms the secondary structure of the peptide.

C1.3 $(GA)_{10}$ forms turbid solutions at 3 mg/mL in 10 mM phosphate buffer

Upon addition of $(GA)_{10}$ to 10 mM phosphate buffer at a concentration of 3 mg/mL, $(GA)_{10}$ immediately forms a turbid solution. The photos in **Figure C3** were taken within minutes of mixing $(GA)_{10}$ in the buffer.

Figure C3. Photos of $(GA)_{10}$ at 3 mg/mL in 10 mM phosphate buffer taken minutes after initial mixing.

C2. TEM images of 10 mM phosphate buffer

Images taken of 10 mM phosphate buffer indicate no structure formation, so none of the features observed in any of the TEM images of samples can be attributed to the buffer (**Figure C4**).

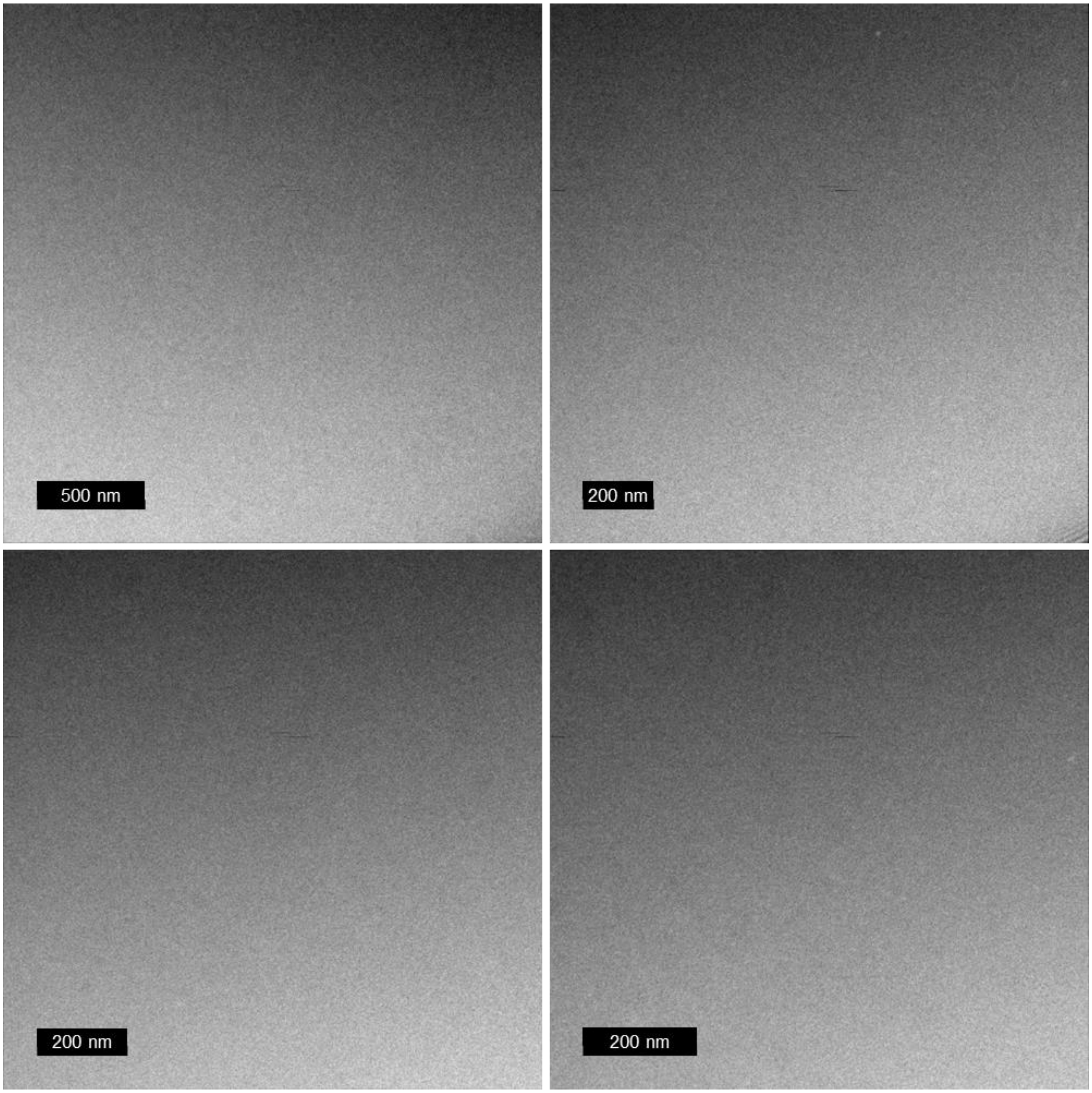

Figure C4. TEM images of 10 mM phosphate buffer show no signs of structure formation.

C3. Additional TEM images of GA)$_{10}$

All TEM images here are taken after overnight incubation of (GA)$_{10}$ in 10 mM phosphate buffer.

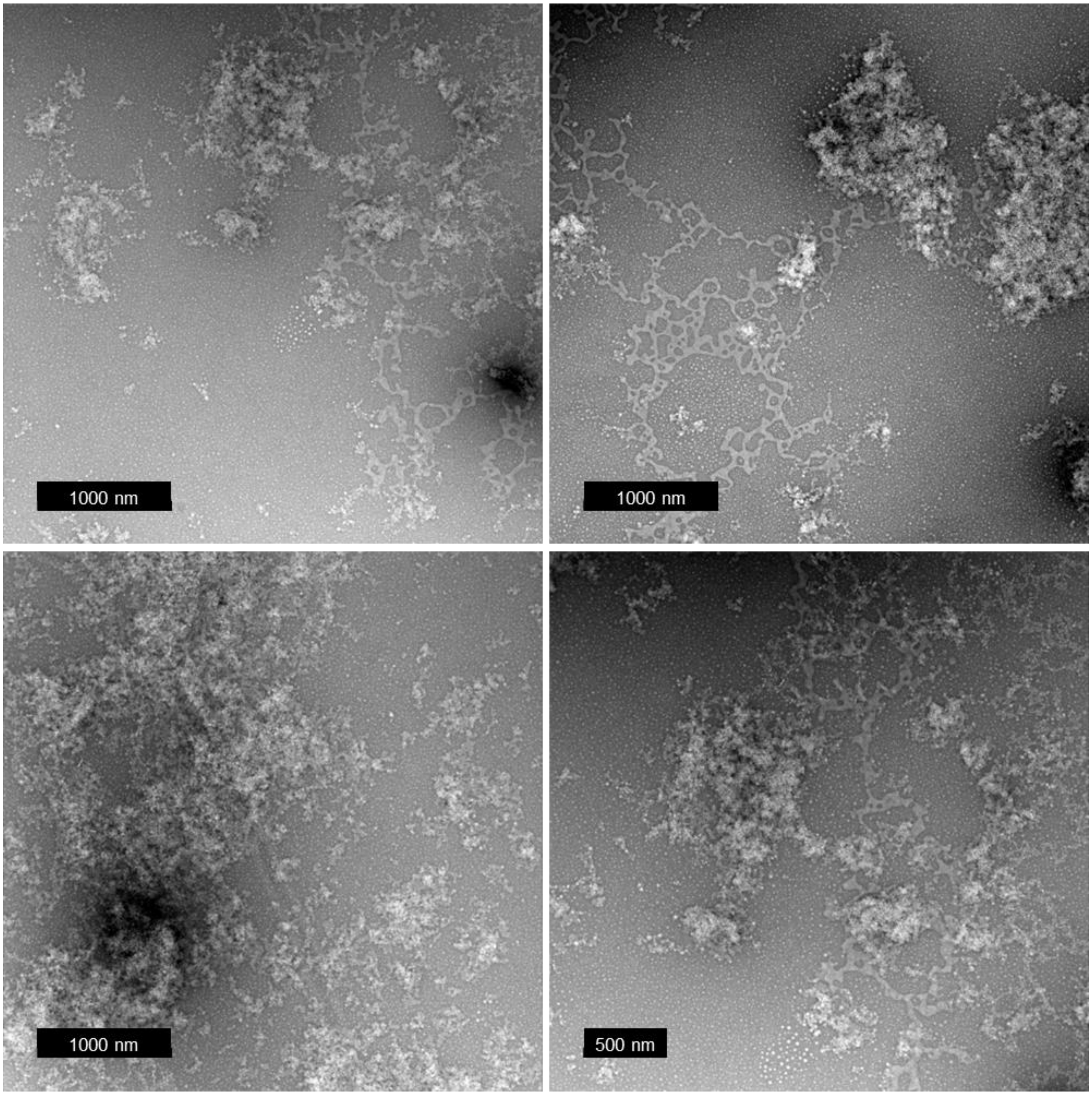

Figure C5. TEM images of $(GA)_{10}$ incubated in 10 mM phosphate buffer overnight. Aggregates of various sizes are observed, with smaller aggregates seemingly coming together to form larger aggregates.

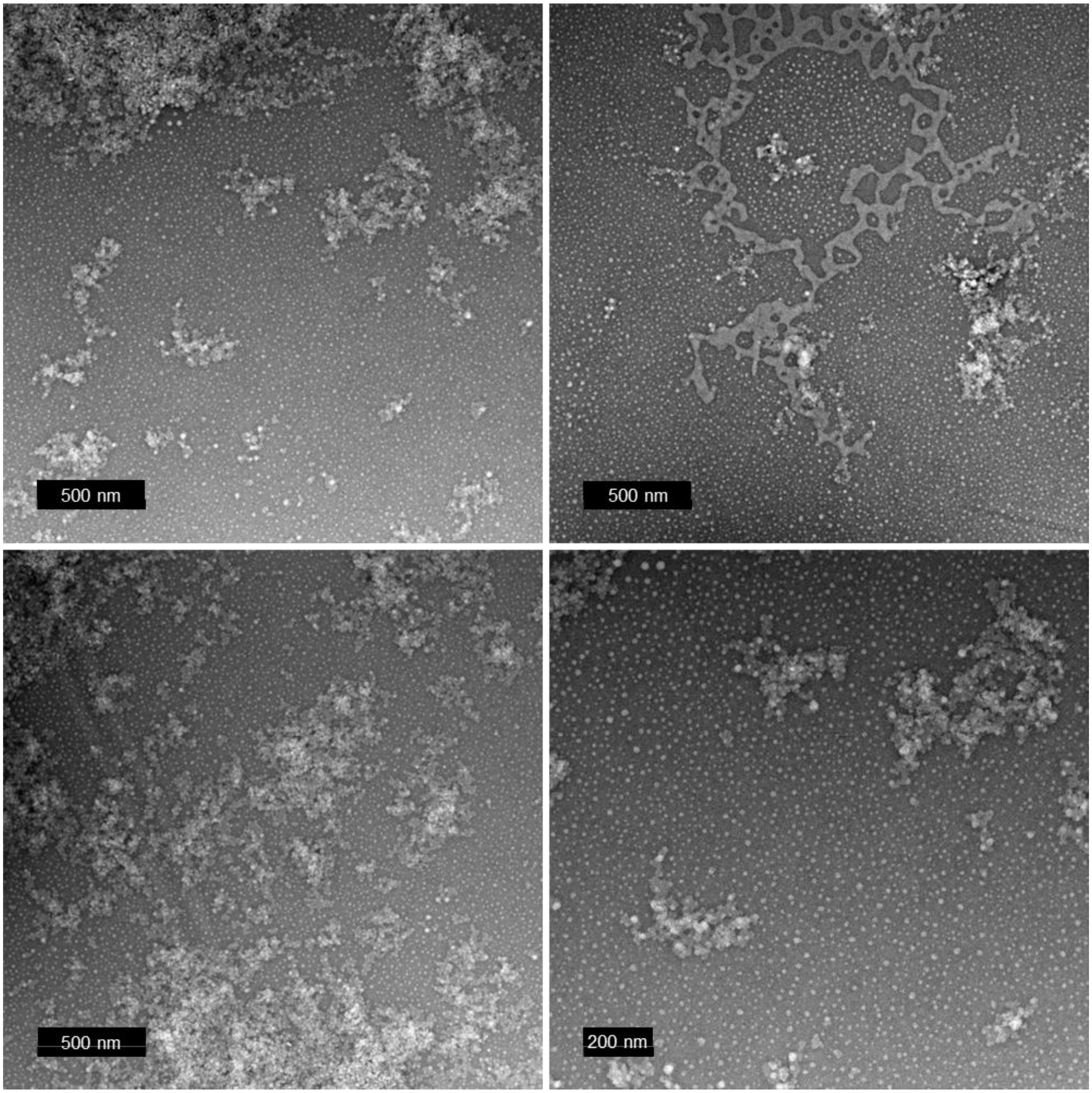

Figure C6. TEM images of $(GA)_{10}$ incubated in 10 mM phosphate buffer overnight. Aggregates of various sizes are observed, with smaller aggregates seemingly coming together to form larger aggregates.

C4. Characterization of mPEG-CGGG-$(GA)_{10}$ conjugates

C4.1 Mole ratio required for full conversion of thiol-maleimide conjugation reaction

The thiol-maleimide conjugation reaction proceeds quickly under these reaction conditions, but it does require a high molar ratio of peptide: polymer. By HPLC, we see four peaks in our reaction mixtures: one that corresponds to the peptide, one that corresponds to the polymer, one that corresponds to the newly formed conjugate, and another broad peak that elutes later than the polymer (**Figure C7**). We hypothesize that this broad peak is the result of conjugate that is targeting CGGG-$(GA)_{10}$ peptides in the reaction mixture before they react with the polymer. Since some amount of peptide reactant is consumed by this interaction, more peptide must be added to push the reaction to completion. Even at a molar ratio of 1.25:1 peptide: polymer, a large amount of unreacted polymer remains. However, when pushed to 2:1 peptide: polymer, we see nearly complete disappearance of the mPEG-mal polymer peak, indicating that we pushed the reaction to completion. We note that the L-CGGG-$(GA)_{10}$ peak doesn't seem to change across these conditions. This may be because all of the peptide is either reacted or interacting with the conjugate, or it could be that the hydrophobic peptide component of the reaction mixture is mostly filtered out before running HPLC. Additionally, there is a small peak that elutes just after the main polymer peak that does not change throughout the reaction. This is present in the chromatogram of the polymer alone as well. Likely, this is a small amount of polymer that does not have an active maleimide group (the supplied mPEG-maleimide from Aldrich has a purity of >90%).

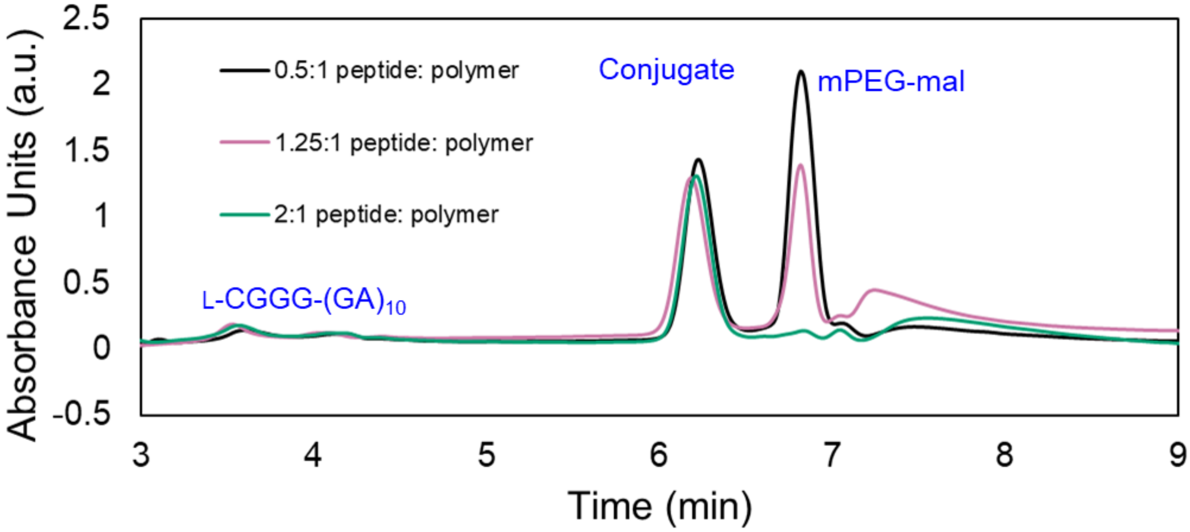

Figure C7. HPLC chromatograms of L-CGGG-$(GA)_{10}$ + mPEG-maleimide reaction mixtures at different peptide: polymer ratios. The peaks corresponding to the peptide, polymer, and newly formed conjugate are labeled. Only when reacted with a 2:1 excess of peptide: polymer is all of the polymer consumed. This may be due to the conjugate interacting with free peptide as it is formed, leading to the formation of the broad peak starting at ~7.3 min.

C4.2 Structure and purity of mPEG-CGGG-$(GA)_{10}$ conjugates

The conjugates purified by preparative-scale HPLC were analyzed by NMR spectroscopy to confirm the successful synthesis and SEC and HPLC to confirm purity. The expected peaks are present in the expected relative abundance, confirming the synthesis (**Figure C8A**). By SEC, only one peak corresponding to the conjugate is present, indicating that preparative-scale HPLC successfully separated the conjugate from any unreacted peptide or polymer (**Figure C8B**). Finally, HPLC confirms this purity as only one peak is observed (**Figure C8C**).

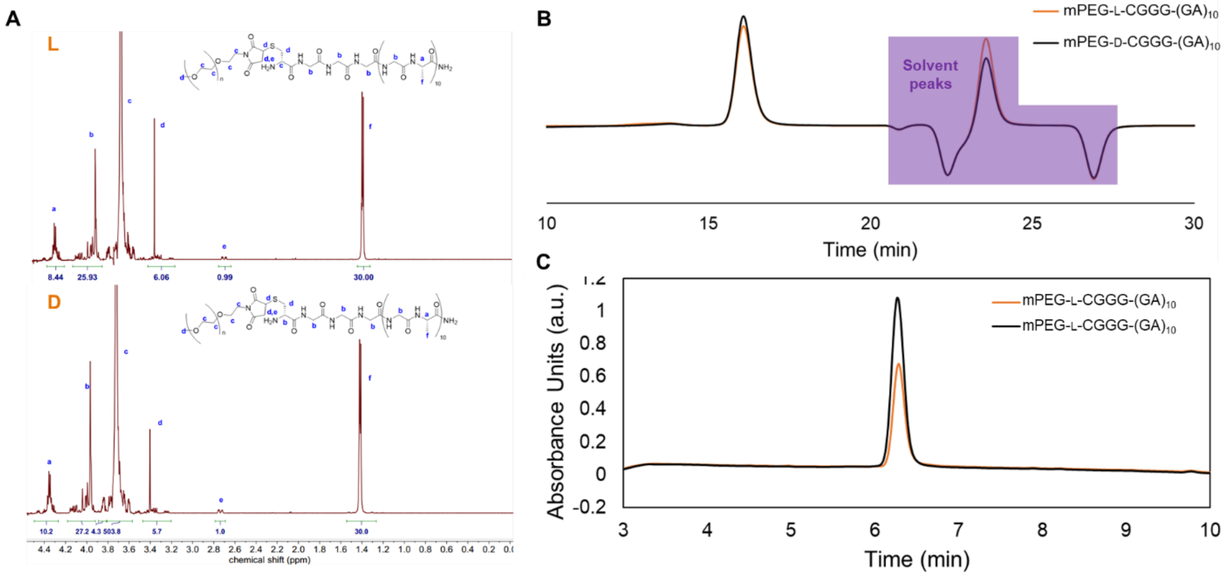

Figure C8. Characterization of mPEG-CGGG-(GA)10 conjugates. A) NMR spectrum of D- and L-CGGG-(GA)10 with peaks labeled. B) SEC chromatogram of D- and L-CGGG-(GA)10 eluting as a single peak with no unreacted polymer or peptide impurities. C) HPLC chromatogram of D- and L-CGGG-(GA)10 eluting as a single peak with no unreacted polymer or peptide impurities.

C4.3 Additional TEM images of mPEG-L-CGGG-(GA)10

All TEM images here are taken after overnight incubation in 10 mM phosphate buffer.

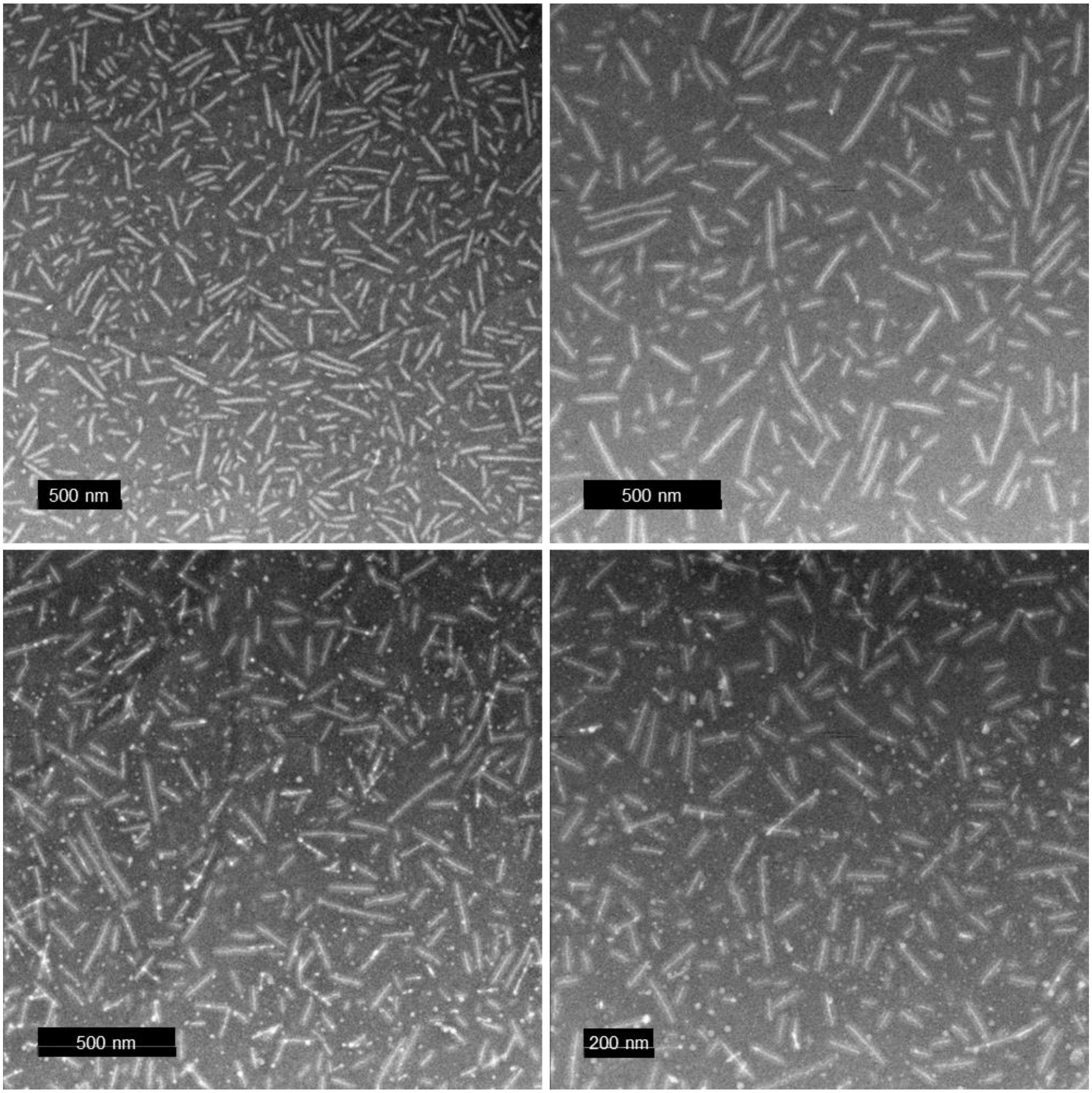

Figure C9. TEM images of mPEG-L-CGGG-(GA)$_{10}$ incubated overnight in 10 mM phosphate buffer. The most prevalent morphology is rod-like, leading to the proposed cylindrical micelle structure of the conjugates.

C4.4 Additional TEM images of mPEG-D-CGGG-(GA)$_{10}$

All TEM images here are taken after overnight incubation in 10 mM phosphate buffer.

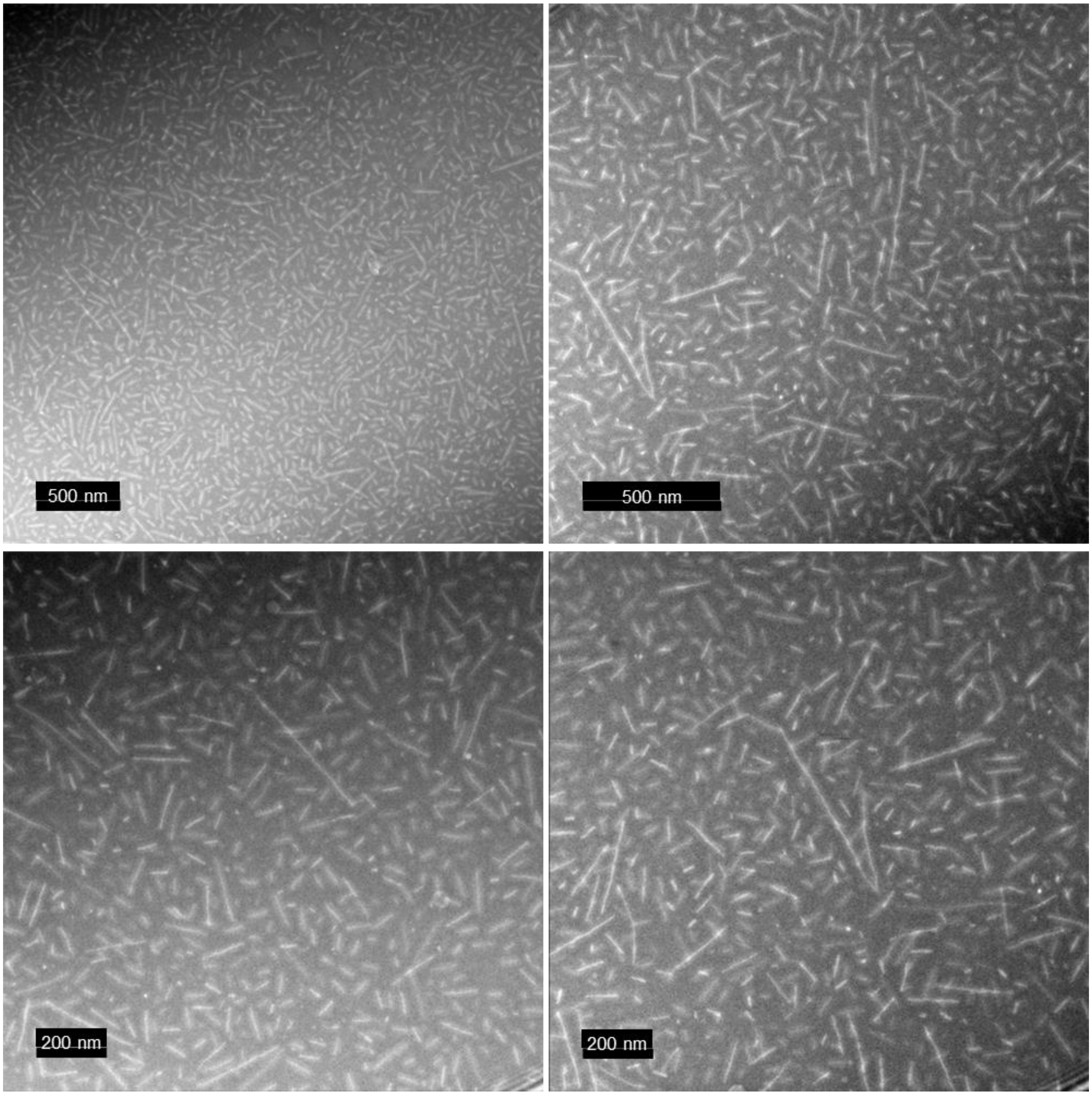

Figure C10. TEM images of mPEG-D-CGGG-(GA)$_{10}$ incubated overnight in 10 mM phosphate buffer. The most prevalent morphology is rod-like, leading to the proposed cylindrical micelle structure of the conjugates.

C5. Turbidity of mPEG-L-CGGG-(GA)$_{10}$ and mPEG-D-CGGG-(GA)$_{10}$ in 10 mM phosphate buffer

While the conjugates appear to fully dissolve by eye, we measured the turbidity of 7 mg/mL mPEG-L-CGGG-(GA)$_{10}$ and mPEG-D-CGGG-(GA)$_{10}$ dissolved in 10 mM phosphate buffer (**Figure C11**). Turbidity measurements were taken minutes after dissolution. The turbidity of the conjugate solutions was on the same order of magnitude as the buffer alone, which is two or more orders of magnitude lower than the turbidities we are measuring in the experiment. Therefore, the turbidity of the conjugates alone does not significantly contribute to the data collected in any of the turbidity studies conducted.

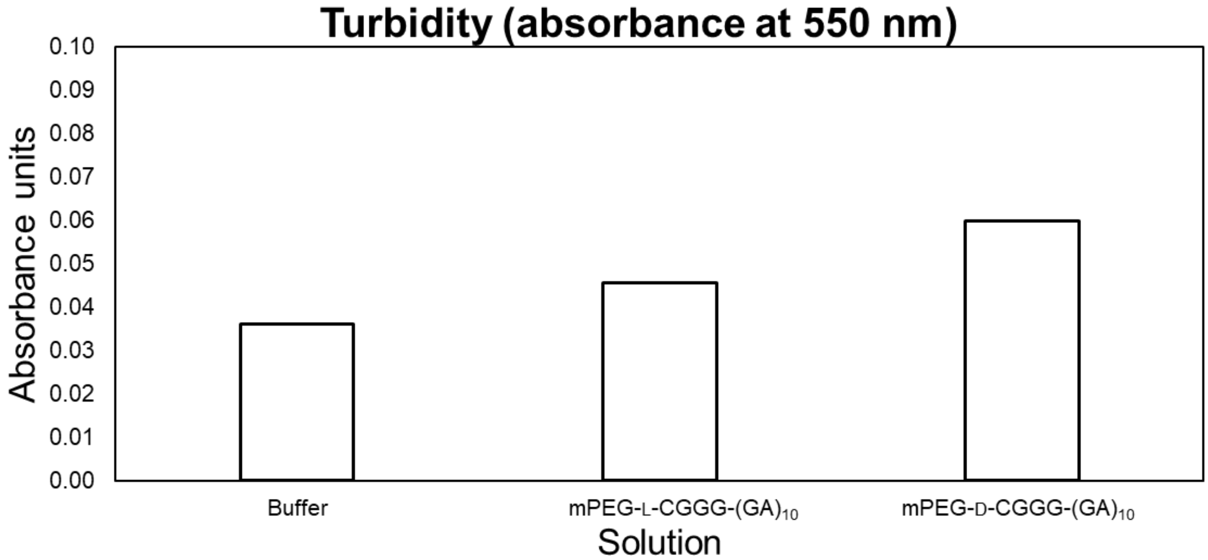

Figure C11. Turbidities of buffer, 7 mg/mL mPEG-L-CGGG-(GA)$_{10}$, and 7 mg/mL mPEG-D-CGGG-(GA)$_{10}$ in 10 mM phosphate buffer. These turbidities are multiple orders of magnitude lower than what is measured in the turbidity experiments.

C6. Turbidity of 10 mM phosphate buffer over 28 days

To test whether the turbidity of buffer solutions changes with time over the course of this experiment (due to, for example, the growth of bacteria/microbes in aqueous solution), we monitored the turbidity of a 10 mM phosphate buffer solution over 28 days (**Figure C12**). We observed little change over the 28 days of the experiment, indicating that turbidity is not artificially increased by changes to the solution over time rather than the aggregation of $(GA)_{10}$.

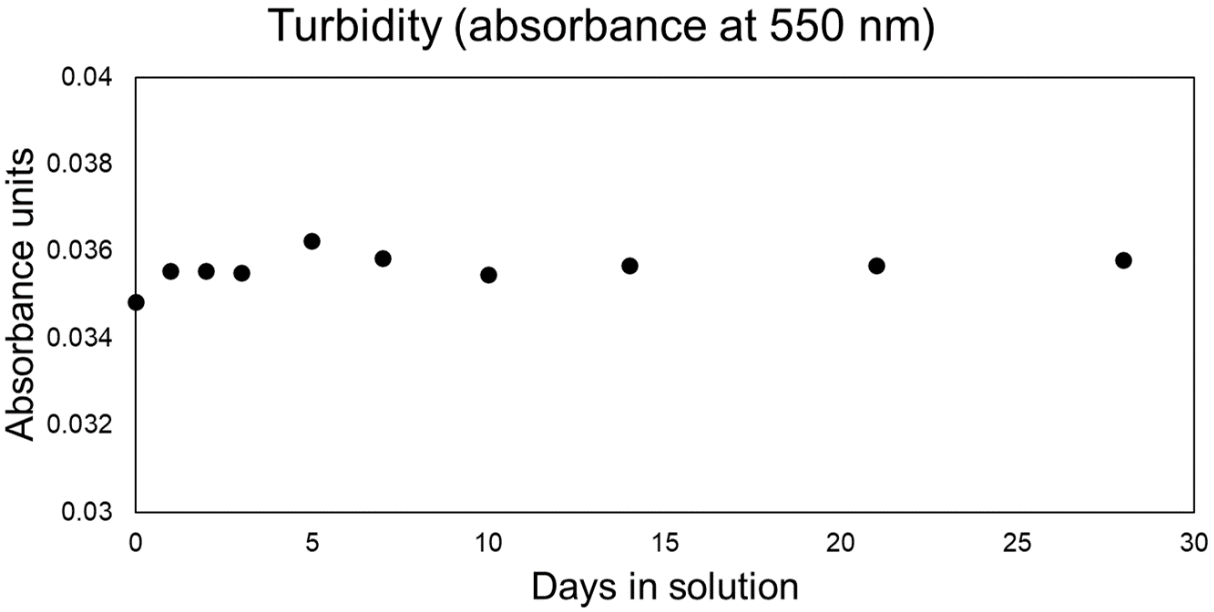

Figure C12. Turbidity of 10 mM phosphate buffer over 28 days. Little change is observed, indicating that changes in the buffer solution itself does not contribute to results observed in the turbidity experiments.

C7. Turbidity of $(GA)_{10}$ incubated with mPEG-mal and PEG-ME

To test whether the control over $(GA)_{10}$ aggregation observed for mPEG-mal was due to the maleimide functional group or the PEG itself, we compared the turbidity of $(GA)_{10}$ incubated with mPEG-mal 5,000 to the turbidity of $(GA)_{10}$ incubated with PEG-ME

5,000, which does not have a reactive functional group (**Figure C13**). We found that, similar to the (GA)10 incubated with mPEG-mal in the first turbidity experiment, (GA)10 incubated with mPEG-mal in this experiment initially experienced an increase in turbidity, then remained level for the rest of the experiment. On the other hand, (GA)10 incubated with PEG-ME continually increased in turbidity similar to what was observed for (GA)10 incubated in buffer alone, indicating that the maleimide reactive group contributes to preventing (GA)10 aggregation. As the conjugates we have designed do not have any reactive groups available, we decided to use PEG-ME as the polymer control moving forward, as it better represents the conjugate without peptide present.

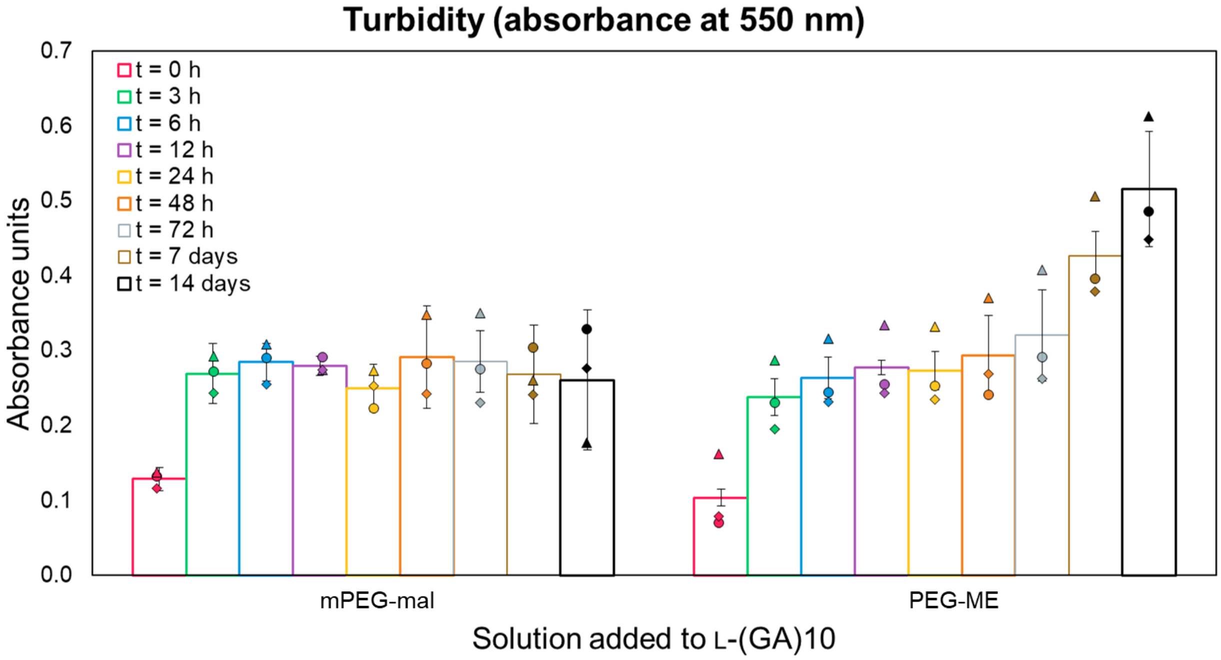

Figure C13. Turbidity of (GA)10 incubated with mPEG-mal or PEG-ME. The (GA)10 incubated with mPEG-mal initially increases in turbidity but then does not aggregate further, while the (GA)10 incubated with PEG-ME continually increases in turbidity. This indicates that the maleimide reactive group contributes to preventing aggregation, not the PEG itself.

C8. Thioflavin T fluorescence of $(GA)_{10}$ incubated with buffer, mPEG-mal, mPEG-L-CGGG-$(GA)_{10}$, or mPEG-D-CGGG-$(GA)_{10}$

Concurrently with the turbidity experiment, thioflavin T fluorescence was also measured for each vial (**Figure C14**). We observed little change in thioflavin T fluorescence with time after 2 days. Taken together with the turbidity data, this indicates that the thioflavin T either is able to diffuse into the conjugates and stain $(GA)_{10}$ present both there and in the bulk solution, or that the $(GA)_{10}$ remains in the outside solution at the same concentration at each time point but isn't able to come together to aggregate.

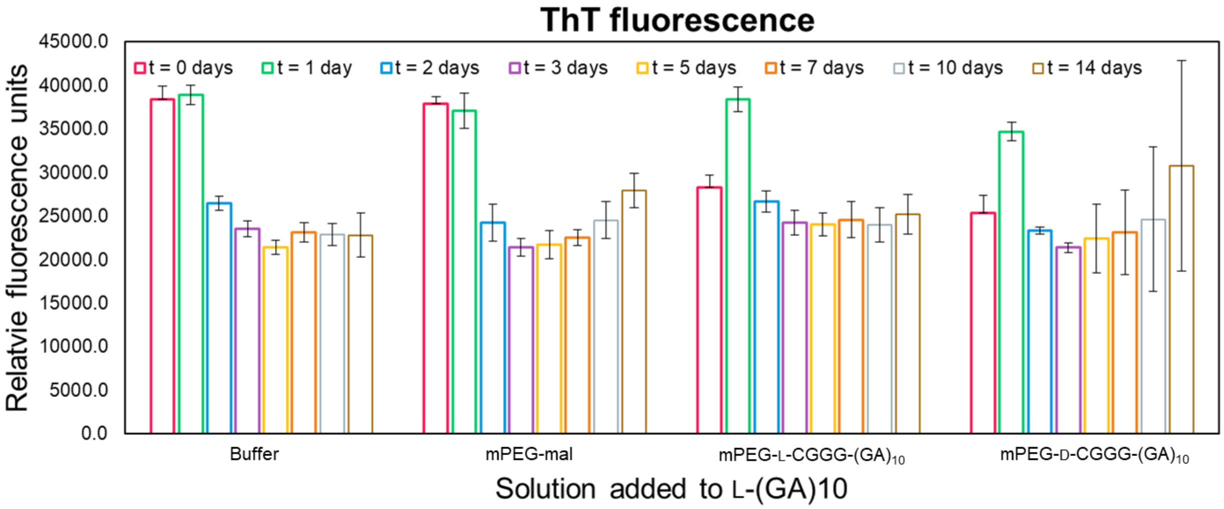

Figure C14. Thioflavin T fluorescence of $(GA)_{10}$ incubated with buffer, mPEG-mal, mPEG-L-CGGG-$(GA)_{10}$, or mPEG-D-CGGG-$(GA)_{10}$ in 10 mM phosphate buffer.

C9. Additional TEM images of coincubation study of (GA)$_{10}$ with buffer, mPEG-L-CGGG-(GA)$_{10}$, and mPEG-D-CGGG-(GA)$_{10}$

C9.1 Additional TEM images of (GA)$_{10}$ incubated in buffer at t = 0 days

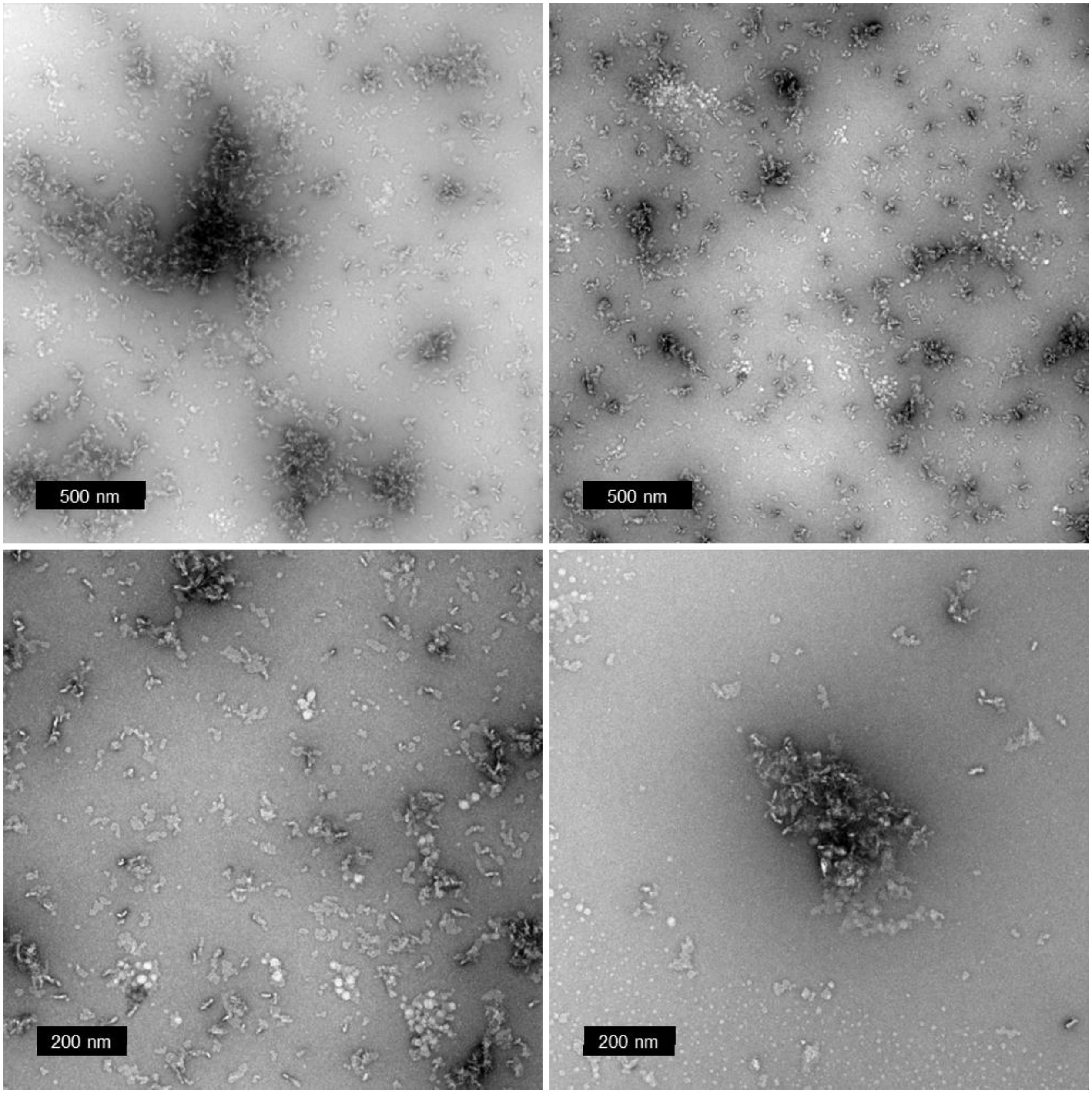

Figure C15. TEM images of $(GA)_{10}$ incubated in buffer for several minutes. Small aggregates are observed, some of which are coming together to form larger aggregates.

C9.2 Additional TEM images of $(GA)_{10}$ incubated in buffer at t = 14 days

Much larger aggregates are observed after 14 days. A couple examples were found of much larger, irregularly shaped objects such as the one in the center of the bottom right image. Further testing would be needed to confirm that this larger object is the result of $(GA)_{10}$ aggregation.

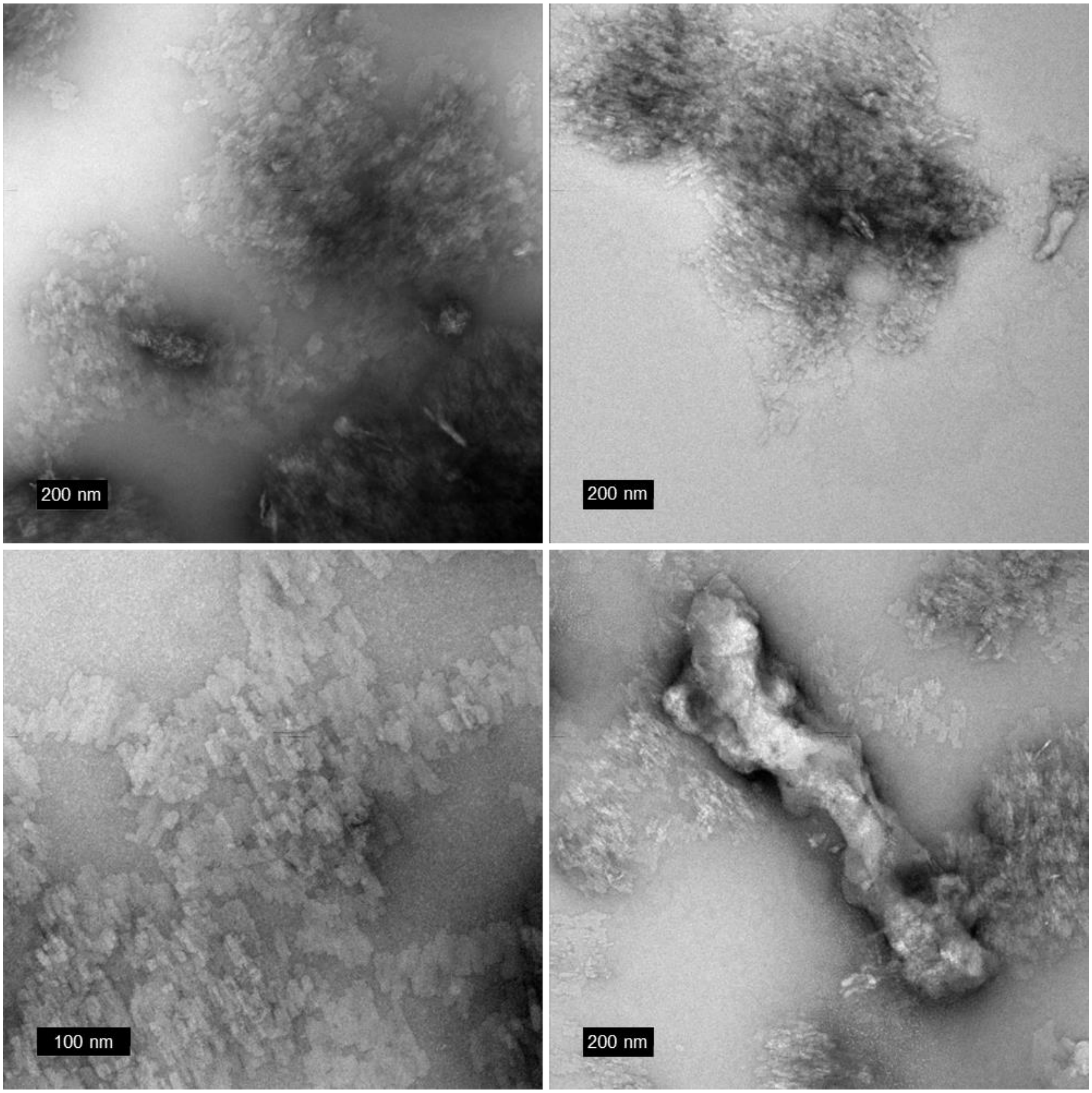

Figure C16. TEM images of $(GA)_{10}$ incubated in buffer for 14 days. Large aggregates are observed.

C9.3 Additional TEM images of $(GA)_{10}$ incubated with mPEG-L-CGGG-$(GA)_{10}$ at t = 0 days

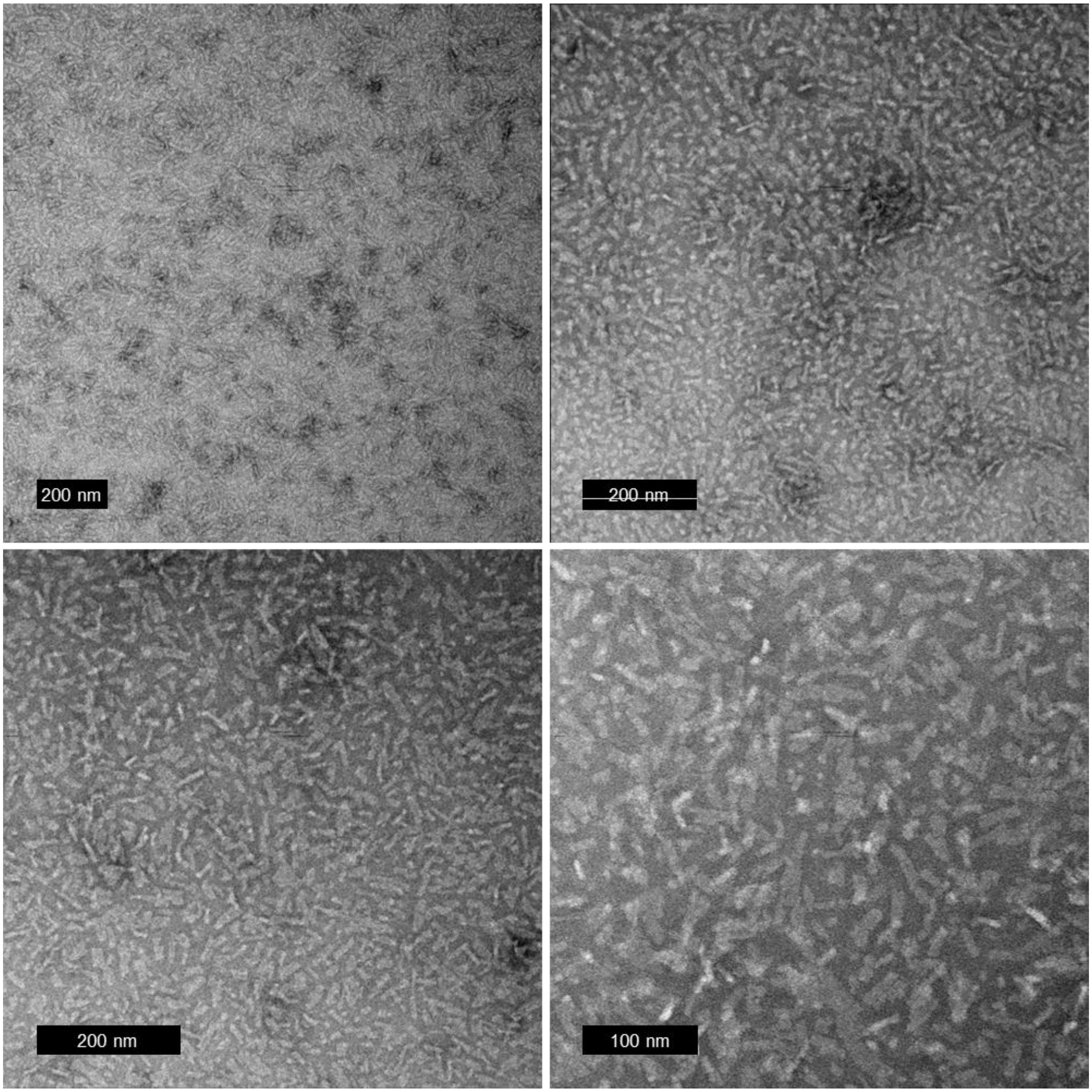

Figure C17. TEM images of $(GA)_{10}$ incubated in mPEG-L-CGGG-$(GA)_{10}$ for several minutes. A mixture of small aggregates and rod-like conjugates are observed.

C9.4 Additional TEM images of $(GA)_{10}$ incubated with mPEG-L-CGGG-$(GA)_{10}$ at t = 14 days

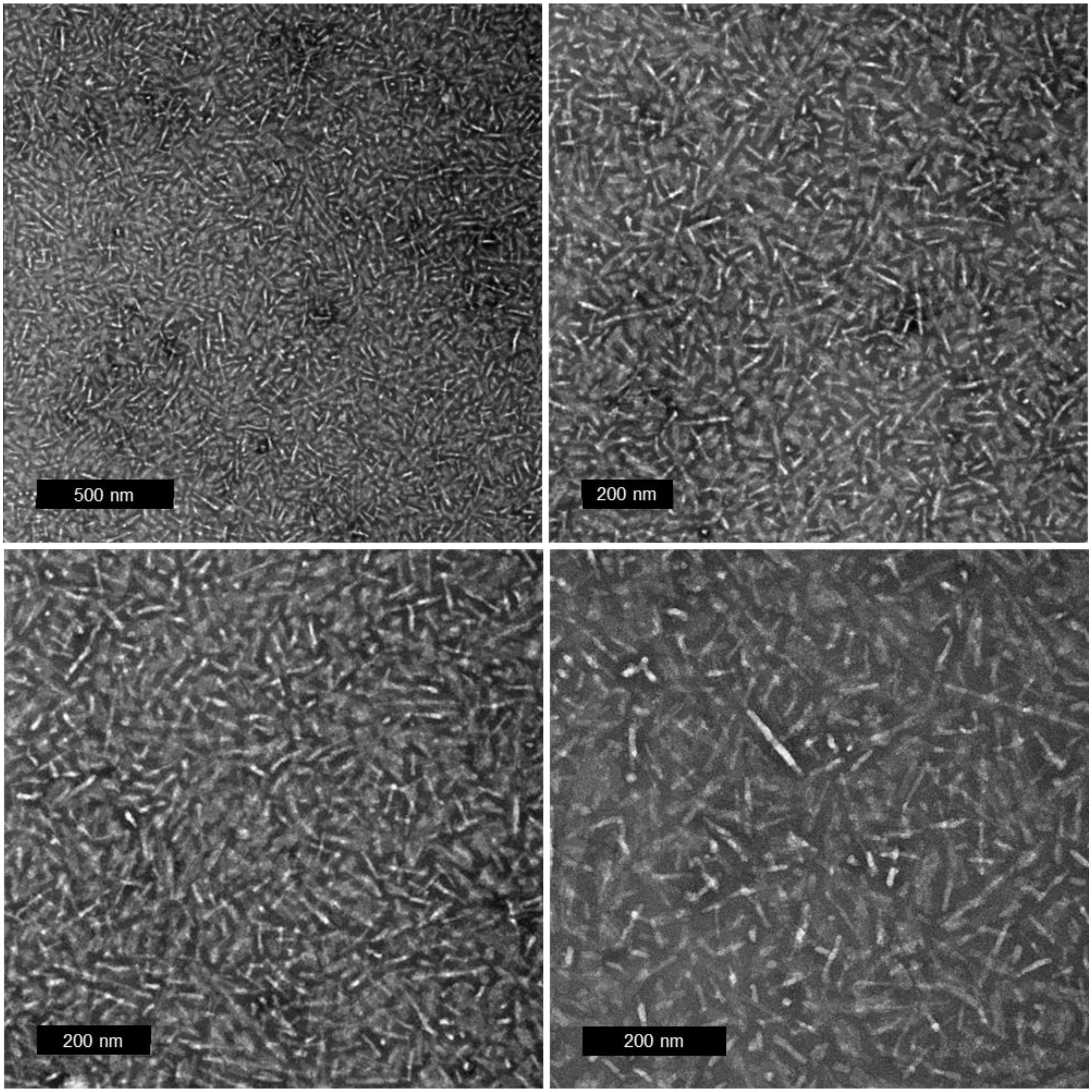

Figure C18. TEM images of $(GA)_{10}$ incubated in mPEG-L-CGGG-$(GA)_{10}$ for 14 days. A mixture of small aggregates and rod-like conjugates are still observed, but no large aggregates on the scale of what is seen when $(GA)_{10}$ is incubated in buffer alone.

C9.5 Additional TEM images of $(GA)_{10}$ incubated with mPEG-D-CGGG-$(GA)_{10}$ at t = 0 days

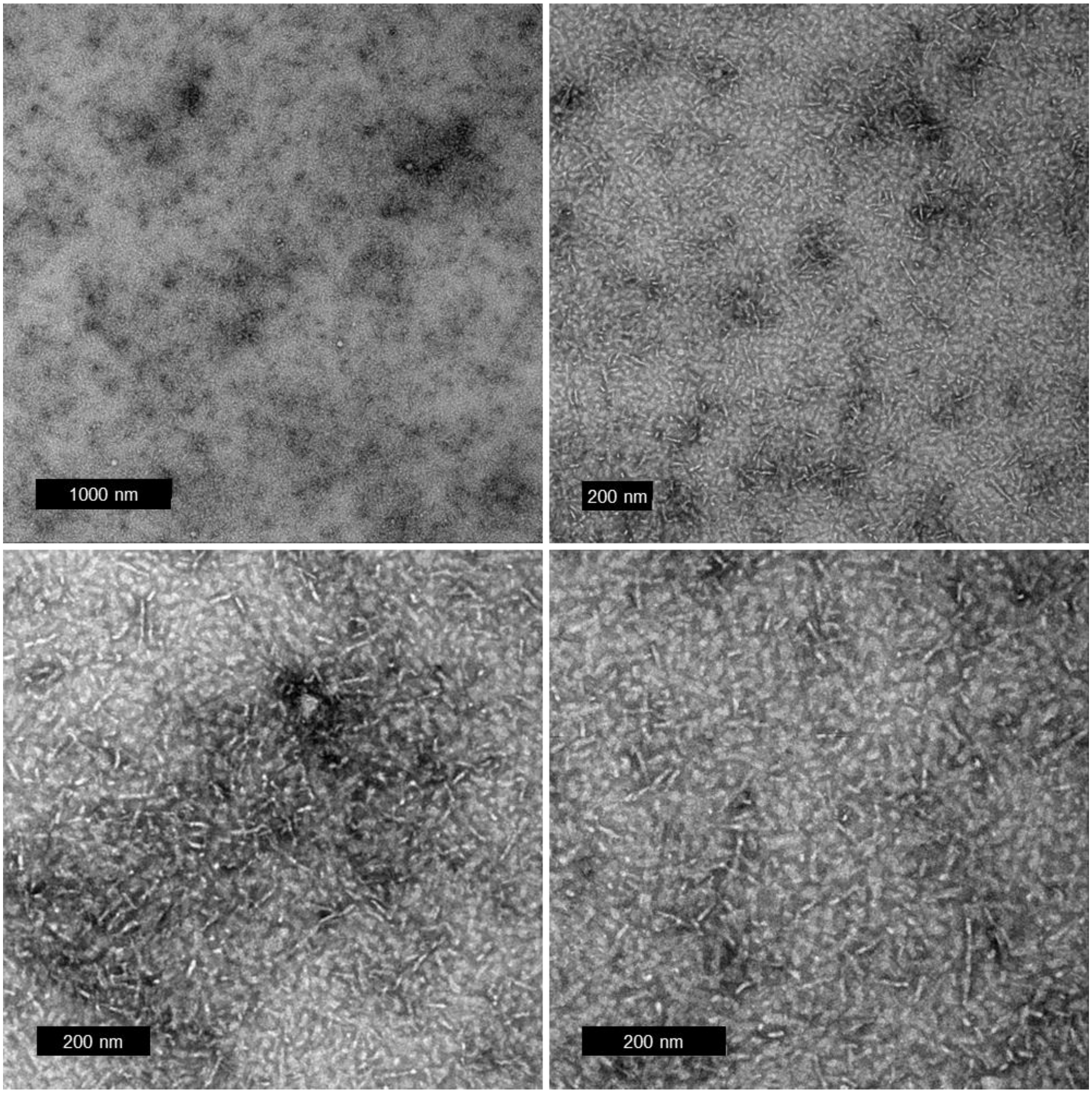

Figure C19. TEM images of $(GA)_{10}$ incubated in mPEG-D-CGGG-$(GA)_{10}$ for several minutes. A mixture of small aggregates and rod-like conjugates are observed.

C9.6 Additional TEM images of $(GA)_{10}$ incubated with mPEG-D-CGGG-$(GA)_{10}$ at t = 14 days

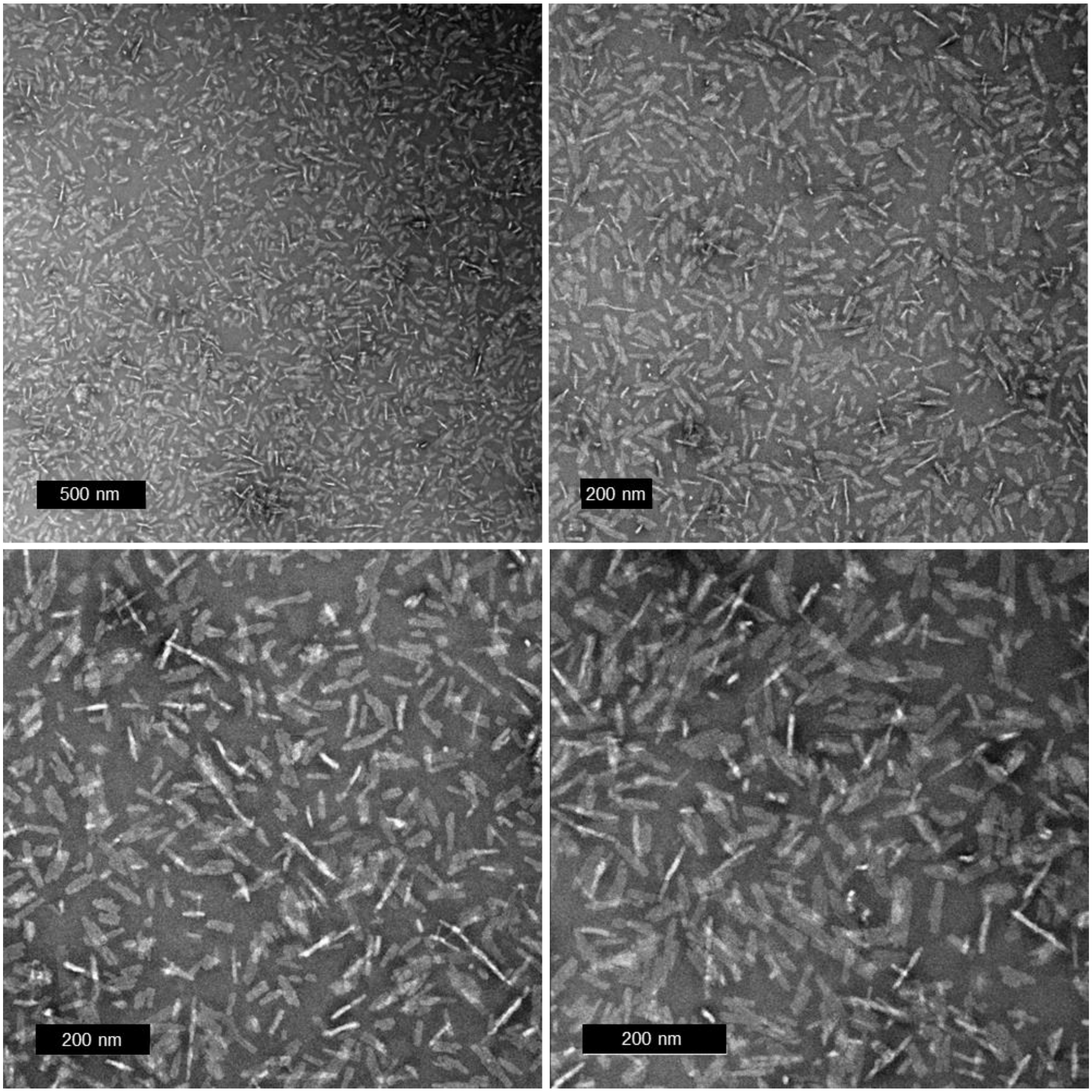

Figure C20. TEM images of $(GA)_{10}$ incubated in mPEG-D-CGGG-$(GA)_{10}$ for 14 days. A mixture of small aggregates and rod-like conjugates are still observed, but no large aggregates on the scale of what is seen when $(GA)_{10}$ is incubated in buffer alone.

C10. Additional TEM images of preaggregation study of $(GA)_{10}$ with buffer, PEG-ME, mPEG-L-CGGG-$(GA)_{10}$, and mPEG-D-CGGG-$(GA)_{10}$

C10.1 Additional TEM images of $(GA)_{10}$ preaggregated in buffer for 7 days

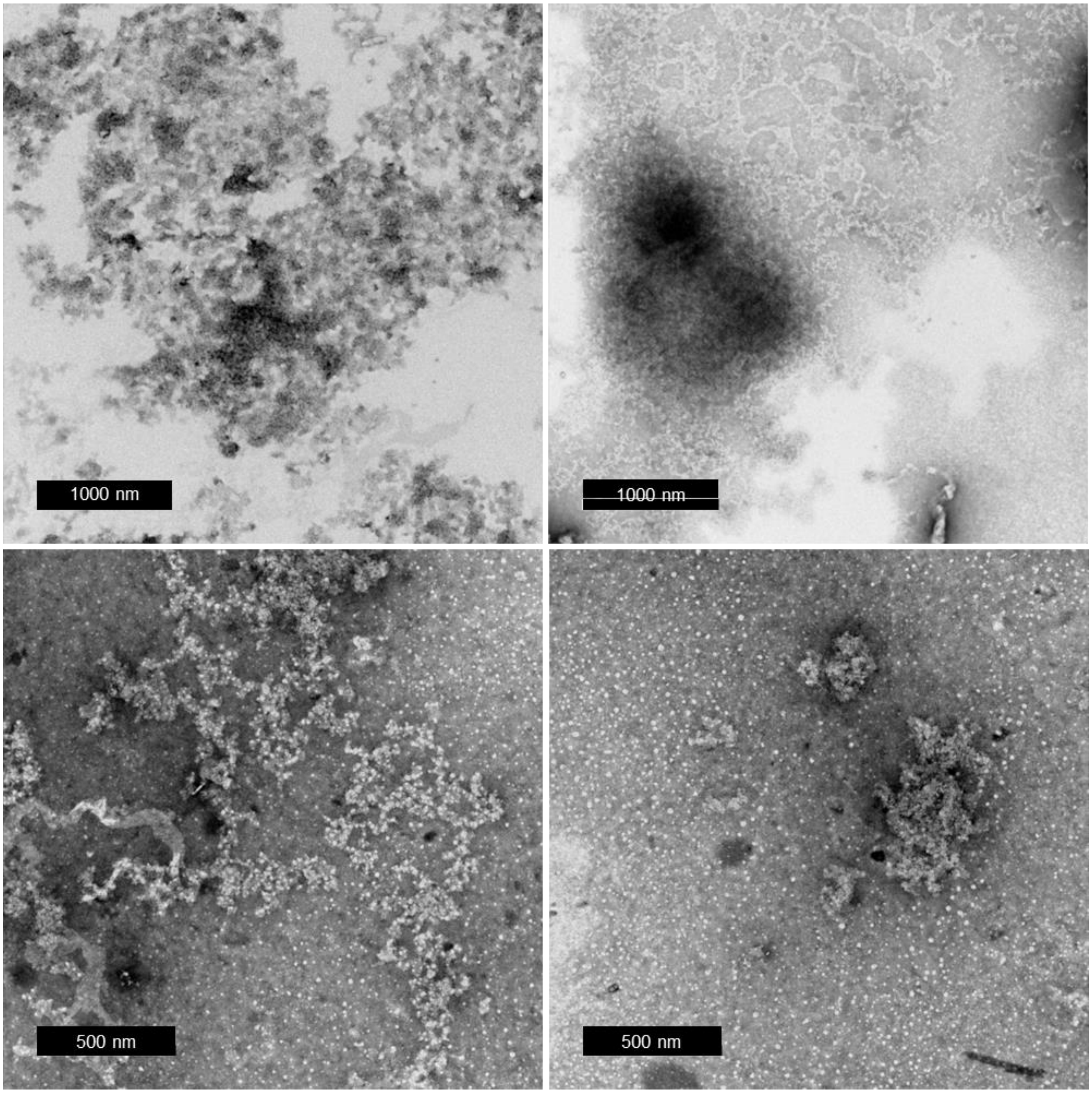

Figure C21. TEM images of $(GA)_{10}$ after 7 days of incubation in 10 mM phosphate buffer. A combination of small, medium, and large aggregates are observed, somewhere in between what was previously observed for $(GA)_{10}$ incubated in buffer for a few minutes and 14 days.

C10.2 Additional TEM images of preaggregated $(GA)_{10}$ treated with buffer for 28 days

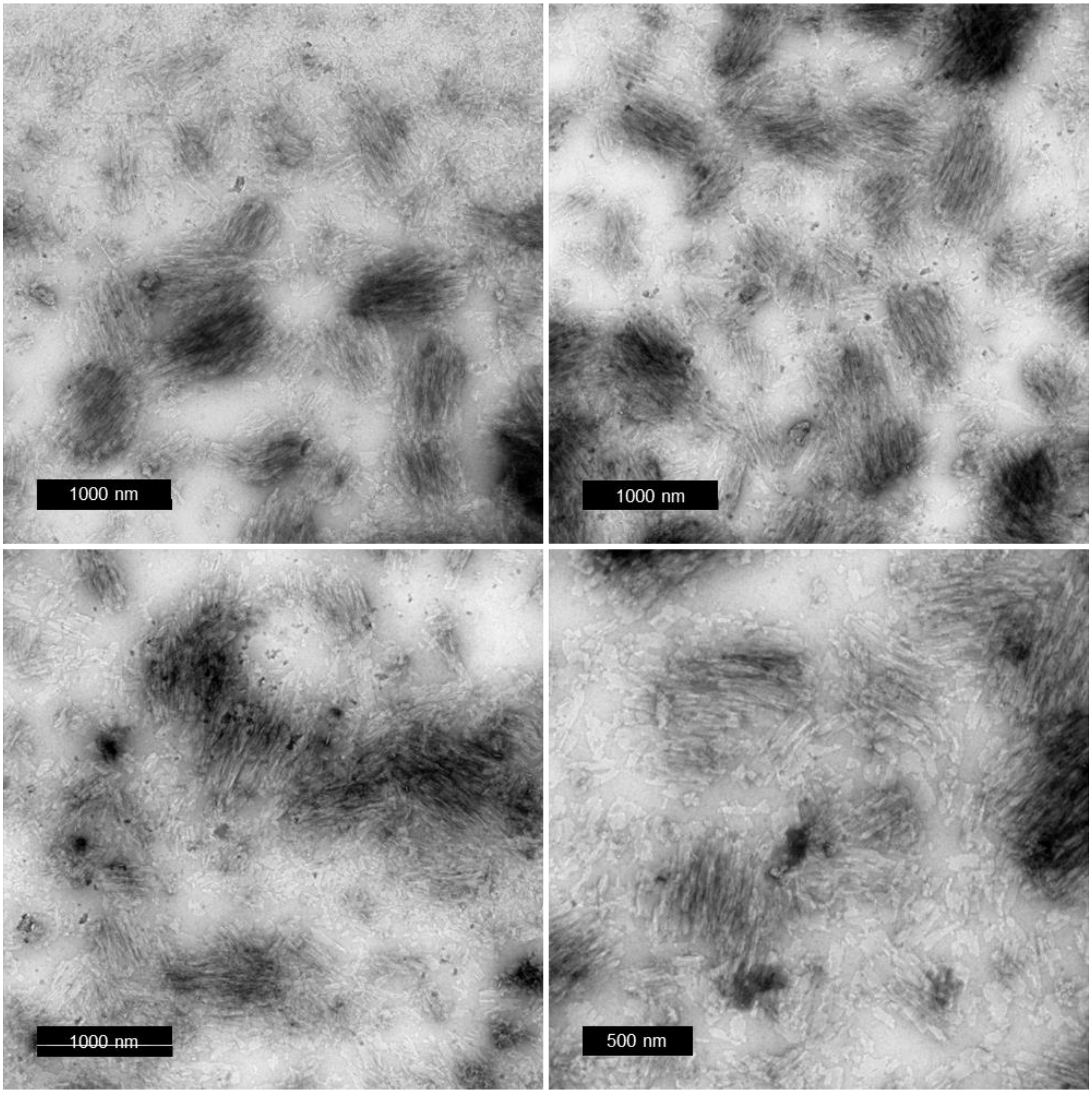

Figure C22. TEM images of preaggregated $(GA)_{10}$ incubated with buffer for 28 days. Large aggregates are observed.

C10.3 Additional TEM images of preaggregated $(GA)_{10}$ treated with PEG-ME for 28 days

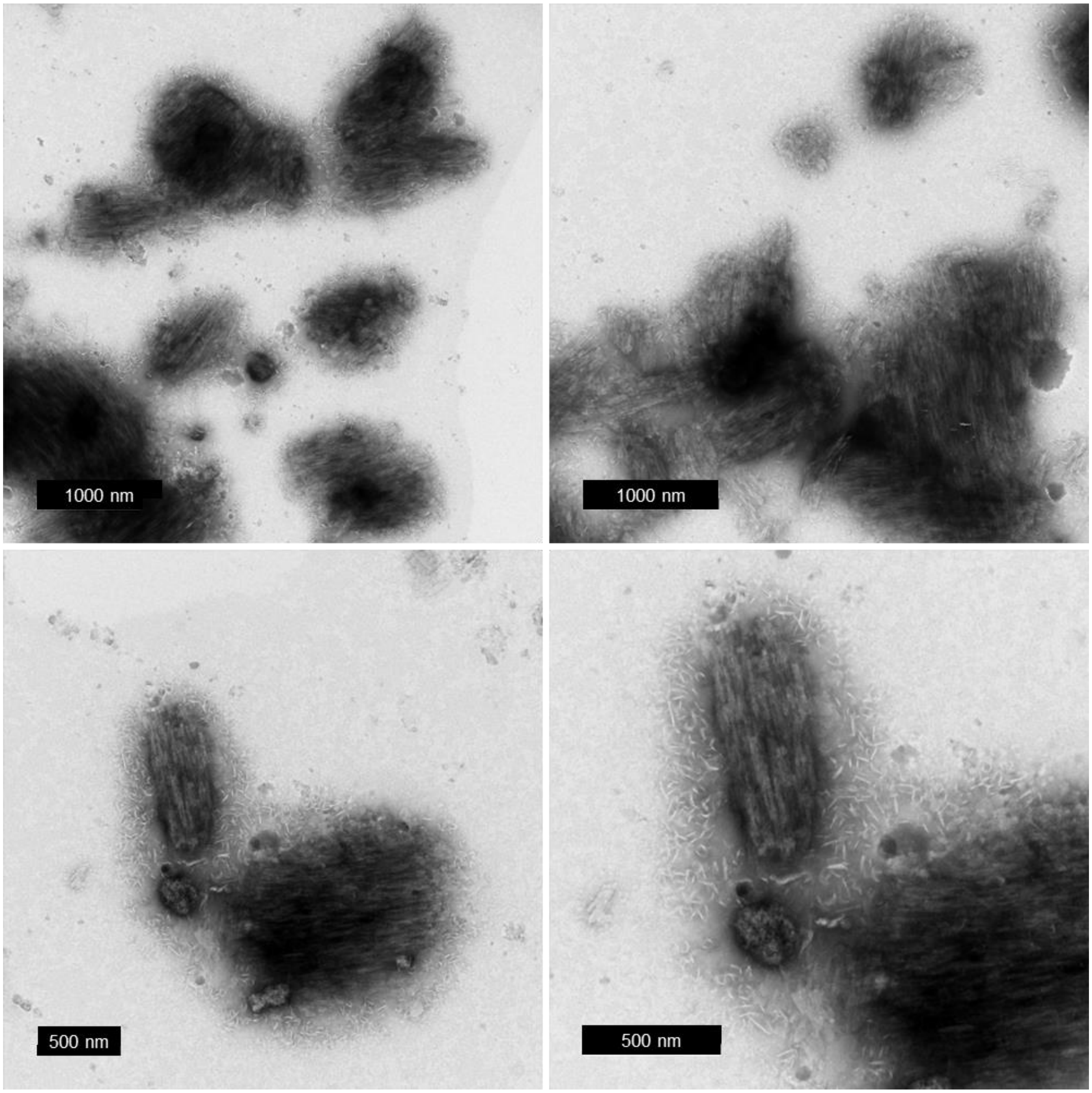

Figure C23. TEM images of preaggregated $(GA)_{10}$ incubated with PEG-ME for 28 days. Large aggregates are observed, similar in size to the aggregates observed for the preaggregated $(GA)_{10}$ treated with buffer.

C10.4 Additional TEM images of preaggregated $(GA)_{10}$ treated with mPEG-L-CGGG-$(GA)_{10}$ for 28 days

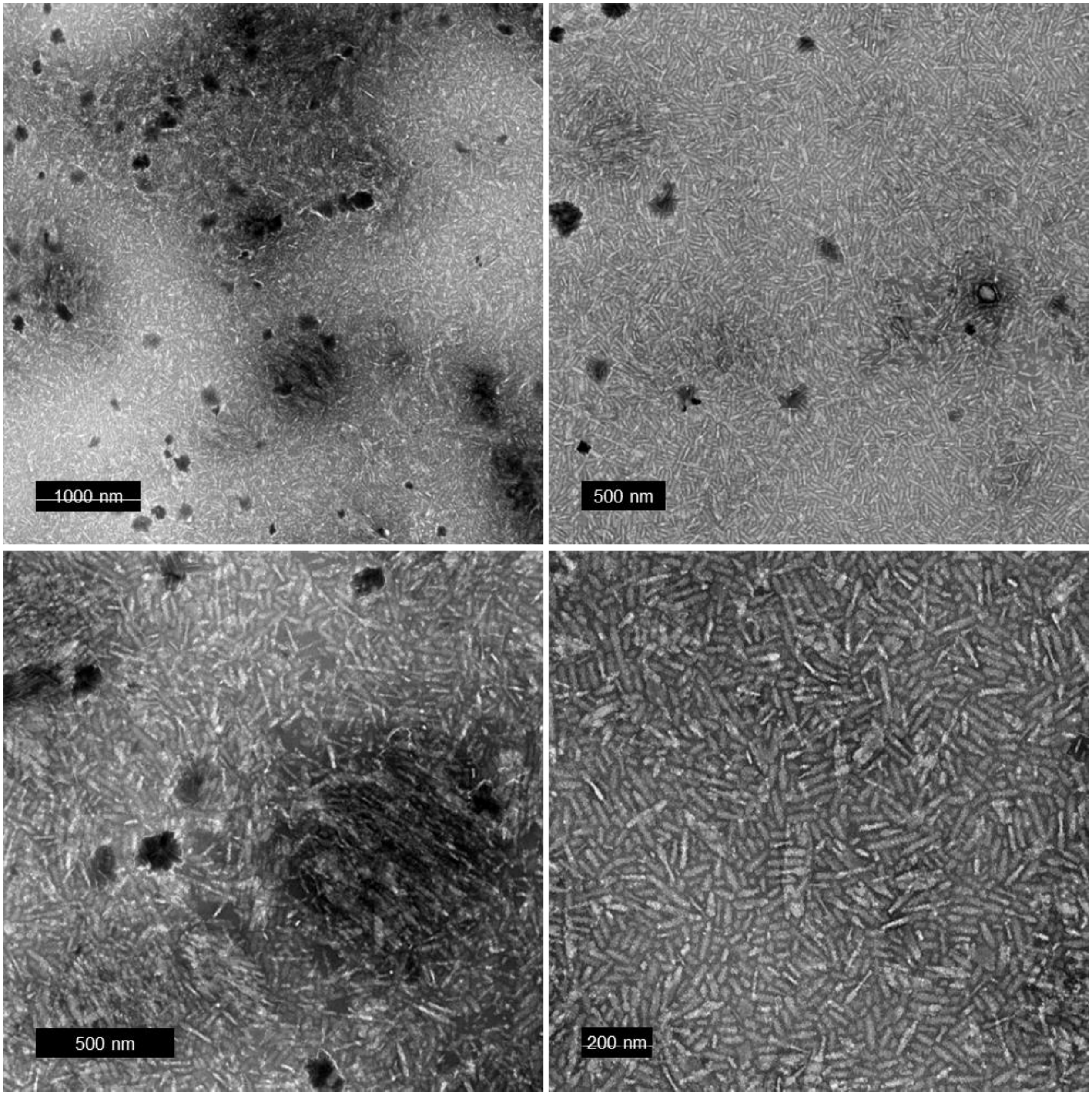

Figure C24. TEM images of preaggregated $(GA)_{10}$ incubated with mPEG-L-CGGG-$(GA)_{10}$ for 28 days. While the morphology is primarily rod-like micelles corresponding to the conjugate and some small aggregates, there are still areas with some larger aggregates present.

C10.5 Additional TEM images of preaggregated $(GA)_{10}$ treated with mPEG-D-CGGG-$(GA)_{10}$ for 28 days

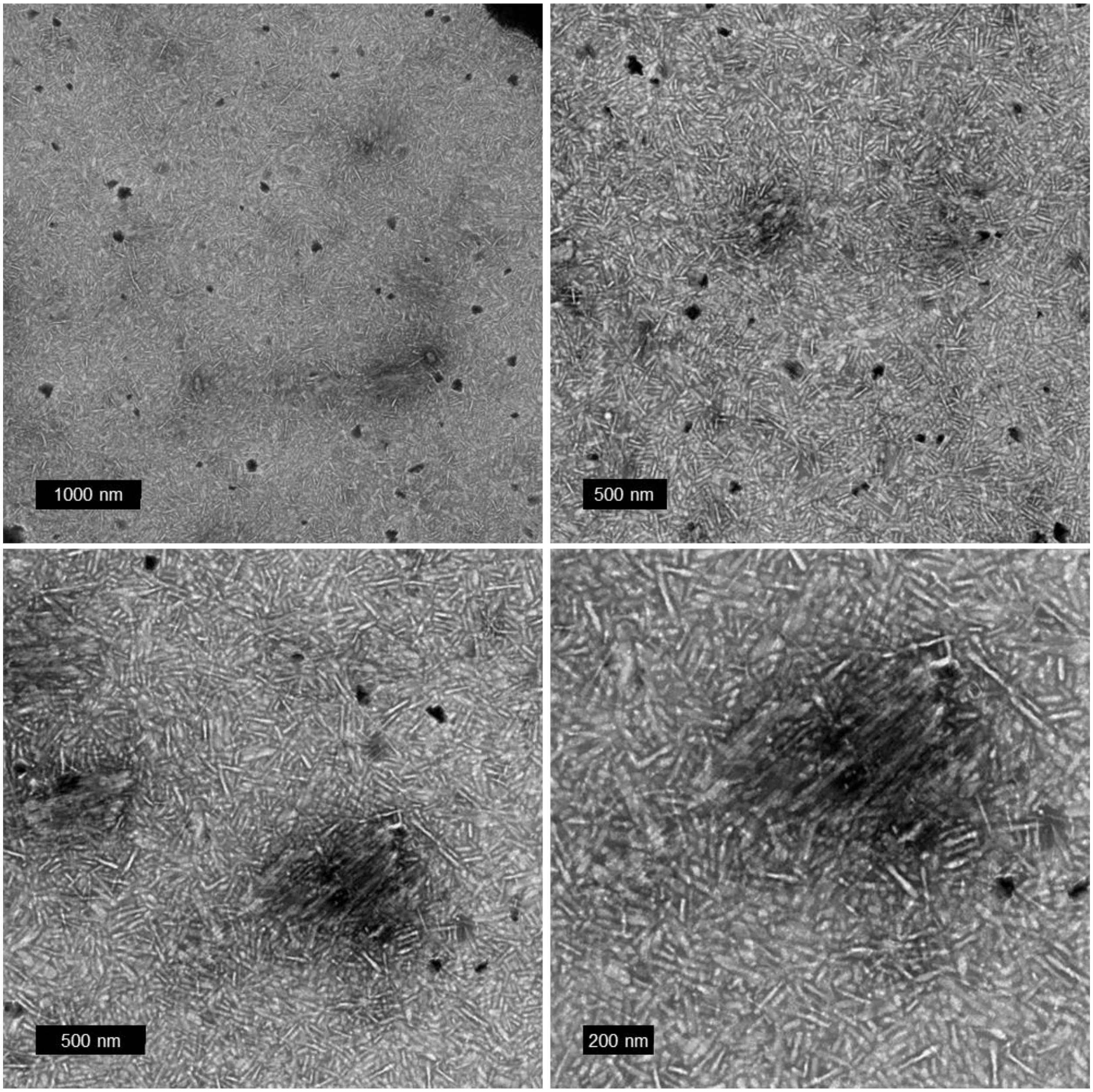

Figure C25. TEM images of preaggregated $(GA)_{10}$ incubated with mPEG-D-CGGG-$(GA)_{10}$ for 28 days. While the morphology is primarily rod-like micelles corresponding to the conjugate and some small aggregates, there are still areas with some larger aggregates present.

C11. $(GA)_{20}$ structural characterization

MALDI-TOF mass spectrometry was used to assess the synthesis of $(GA)_{20}$. The expected mass of 2578.2 was not observed, but a mass of 2150.0 was observed. We determined that this corresponded to the deletion of 4 A residues and 3 G residues, plus a sodium. Therefore, the $(GA)_{20}$ that we attempted to synthesize is actually $(GA)_{16}G$.

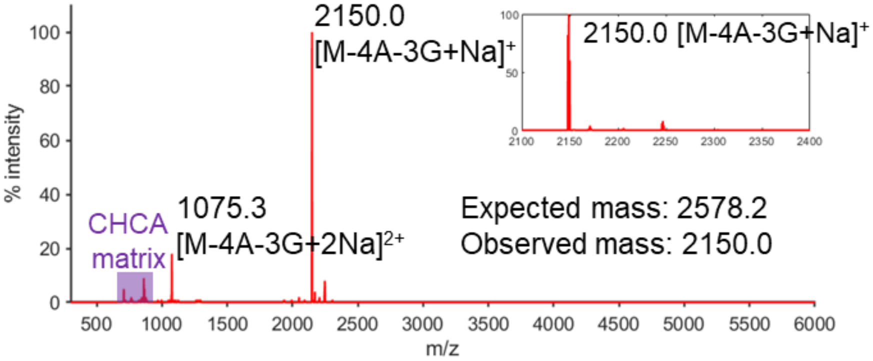

Figure C26. MALDI-TOF mass spectrum of $(GA)_{20}$. The expected mass of 2578.2 was not observed, rather a mass of 2150.0 was observed. We determined that this corresponded to the mass of $(GA)_{16}G$.

C12. 4-arm PEG-CGGG-$(GA)_{10}$ conjugate solubility

After synthesis and purification of 4-arm conjugates, we tested solubility in 10 mM phosphate buffer. Surprisingly, the 4-arm conjugates were insoluble at concentrations as low as 0.5 mg/mL. The 20k 4arm PEG-L-CGGG-$(GA)_{10}$ did not dissolve at all (**Figure C27, left,** insoluble aggregates circled in red), whereas the 10k 4arm PEG-L-CGGG-$(GA)_{10}$ resulted in a turbid solution (**Figure C27, right**). The same observations held true for the D-versions of these conjugates as well.

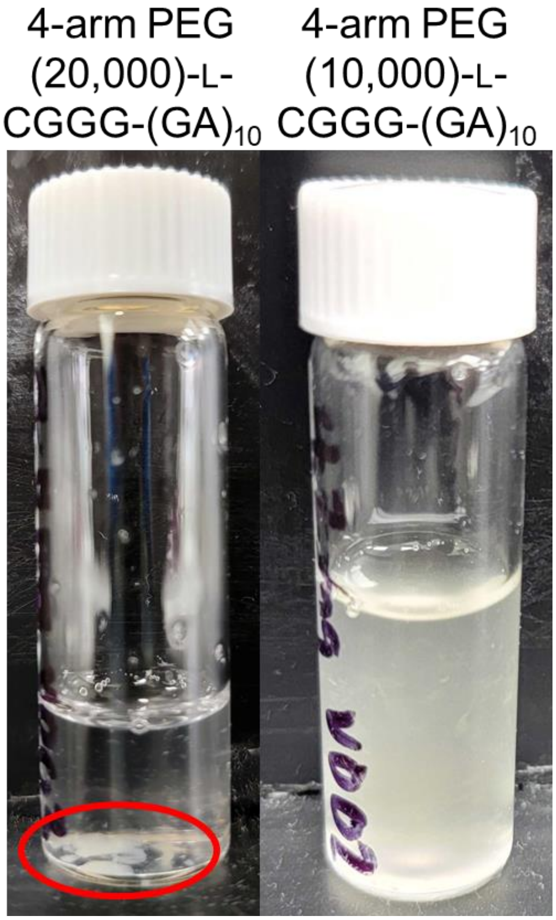

Figure C27. Insolubility of 4arm PEG conjugates in 10 mM phosphate buffer at 0.5 mg/mL. The 20k conjugate did not dissolve at all, resulting in an insoluble aggregate (red circle) whereas the 10k conjugate forms a very turbid solution.

Appendix D: Supporting information for Chapter 5

List of Figures

List of Tables

D1. Crude peptide HPLC

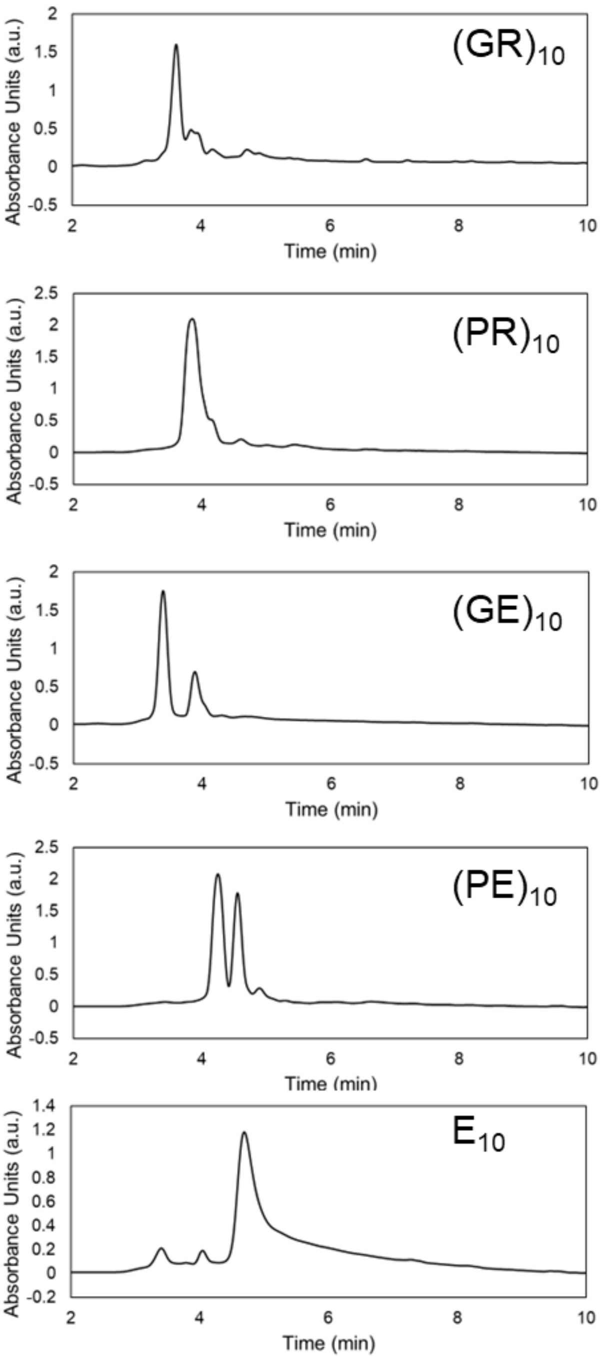

Figure D1. Analytical HPLC chromatograms of (GR)$_{10}$, (PR)$_{10}$, (GE)$_{10}$, (PE)$_{10}$, and E$_{10}$. (GR)$_{10}$, (PR)$_{10}$, (GE)$_{10}$, and (PE)$_{10}$ were purified further. E$_{10}$ was used as is, and the main peak in that chromatogram accounts for >90% of the total peak area. Peptides were eluted on a linear AB gradient from 5% to 95% B (v/v) over 9 minutes, where A is ultrapure water + 0.1% TFA and B is acetonitrile + 0.1% TFA.

D2. Peptide purification by preparative-scale HPLC

The peptides used in this study were purified by preparative-scale HPLC using the binary gradients listed in Table D1 below.

Table D1. List of elution conditions for preparative-scale HPLC purification of peptides.

Peptide	Binary gradient (Solvent A = water + 0.1% TFA, Solvent B = acetonitrile + 0.1% TFA)
$(GR)_{10}$	5 to 15% B from 2.22 to 4 min, 15 to 35% B from 4 to 18 min
$(PR)_{10}$	5 to 20% B from 2.22 to 4 min, 20 to 40% B from 4 to 25 min
$(GE)_{10}$	5 to 15% B from 2.22 to 16 min
$(PE)_{10}$	5 to 20% B from 2.22 to 4 min, 20 to 40% B from 4 to 25 min

The purified peptides obtained from this purification were analyzed by analytical-scale HPLC to determine their purity (**Figure D2**).

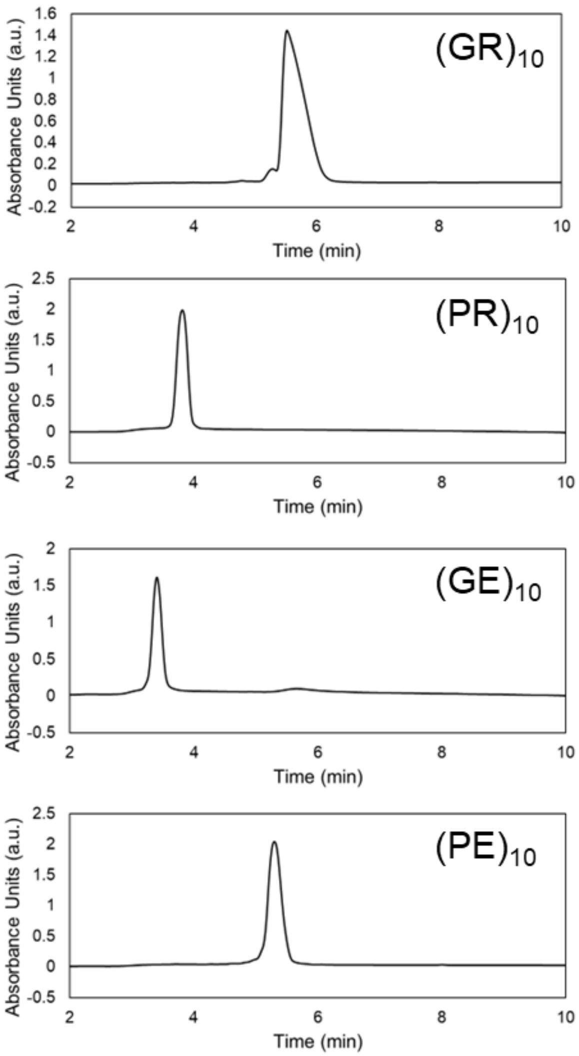

Figure D2. Analytical HPLC chromatograms of purified $(GR)_{10}$, $(PR)_{10}$, $(GE)_{10}$, and $(PE)_{10}$. The main peak in the $(GR)_{10}$ chromatogram accounts for >98% of the total peak area, the main peak in the $(PR)_{10}$ chromatogram accounts for >99% of the total peak area, the main peak in the $(GE)_{10}$ chromatogram accounts for >99% of the total peak area, and the main peak in the $(PE)_{10}$ chromatogram accounts for >99% of the total peak area. Peptides were eluted on a linear AB gradients, where A is ultrapure water + 0.1% TFA and B is acetonitrile + 0.1% TFA. $(GR)_{10}$ was eluted on a gradient from 5% to 25% B over 18 min, $(PR)_{10}$ and $(GE)_{10}$ were eluted on a gradient from 5% to 95% B over 9 min, and $(PE)_{10}$ was eluted on a gradient from 5% to 95% B over 18 min.

D3. Peptide mass spectrometry

Mass spectra were acquired for purified $(GR)_{10}$, $(PR)_{10}$, $(GE)_{10}$, and $(PE)_{10}$, and crude E_{10} to confirm their successful synthesis.

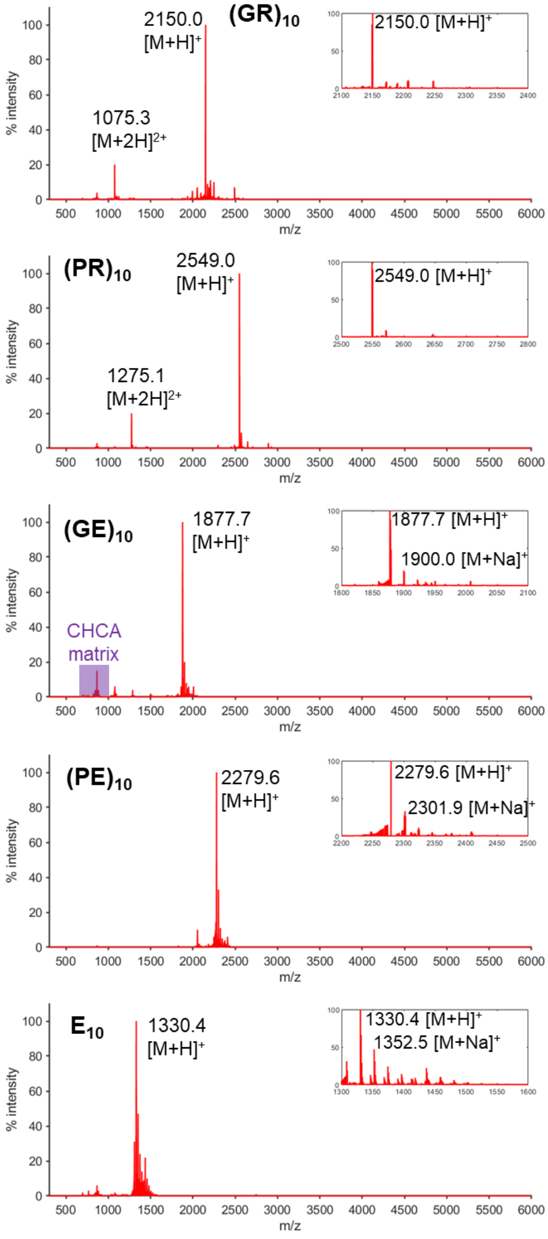

Figure D3. MALDI-TOF mass spectra of $(GR)_{10}$, $(PR)_{10}$, $(GE)_{10}$, $(PE)_{10}$, and E_{10}, with expected peaks labeled.